Mechanisms of melt migration in geodynamic processes: Theoretical and experimental modelling

A thesis submitted for the degree of

Doctor of Philosophy (Science) of

Jadavpur University

By

Dip Ghosh

Department of Geological Sciences
Jadavpur University
Kolkata-700032, India

July 2022

যাদবপুর বিশ্ববিদ্যালয়
কলকাতা - ৭০০০৩২, ভারত

JADAVPUR UNIVERSITY
KOLKATA-700 032, INDIA

FACULTY OF SCIENCE : DEPARTMENT OF GEOLOGICAL SCIENCES

CERTIFICATE FROM THE SUPERVISOR

This is to certify that the thesis entitled **"Mechanisms of melt migration in geodynamic processes: theoretical and experimental modelling"** submitted by **Sri Dip Ghosh** who got his name registered on 13/10/2015 for the award of **Ph.D. (Science)** degree of Jadavpur University, is absolutely based upon his own work under the joint supervision of **Professor Nibir Mandal** and **Dr. Sadhana M. Chatterjee** and that neither this thesis nor any part of it has been submitted for either any degree/ diploma or any other academic award anywhere before.

Sadhana M. Chatterjee
27/07/2022

(Signature of Supervisor & date with official seal)

Dr. Sadhana M Chatterjee
Associate Professor
Department of Geological Sciences
Jadavpur University
Kolkata-700 032

Nibir Mandal
27/07/2022

(Signature of Supervisor & date with official seal)

NIBIR MANDAL
Professor
Dept. of Geological Sciences
Jadavpur University
Kolkata - 700 032

Website : www.jaduniv.edu.in
E-mail : hod.geology@jadavpuruniversity.in

HOD Phone : 033 2457 2719
Office : 033 2457 2268

Dedicated to My Mother…

Acknowledgements

This thesis would not have come to be without the years of help and support of many people and some words of gratitude are very much due for their aspiring guidance, constructive criticisms and friendly advices throughout this period of my endeavour.

First of all, I would like to thank my supervisor Prof. Nibir Mandal for his unwavering support, guidance, and motivation during the course of my PhD. Not only he gave me the opportunity to continue doing scientific research after my master's thesis but also sparked my interest in solid earth geophysics by giving me the opportunity to broaden my scientific horizon by introducing me to new geodynamic problems. His continuous encouragement to break down complicated geodynamic problem using basic fluid dynamics elements to understand the underlying mechanism has largely shaped my research outlook. He also provided me with state of the art experimental geodynamics lab facilities. I would also like to thank my supervisor Dr. Sadhana M. Chatterjee for her interest and support in my research. Her constant enthusiasm and trust in my capabilities were instrumental in the production of this work.

This work would not have been possible without the cooperation from Dr. Giridas Maiti, Joyjeet Sen and Dr. Puspendu Saha, who helped me immensely in developing numerical and experimental setup. I am thankful to Anirban Das for conducting the initial experiments. I am grateful to Pradip Kar (Kar Babu) and Milan Mondal for providing me with state of the art experimental setups. I am indebted to the University Grants Commission, India for providing me with the research fellowship. I also extend my thanks to the supporting staffs of Jadavpur University especially that of the Department of Geological sciences.

I would like to sincerely acknowledge the support of each and every active and past members of JUGeodynamics Lab. My sincere thanks also goes to Dr. Shamik Sarkar, Dr. Amiya Baruah, Dr. Urmi Dutta, Dr. Sujoy Dasgupta, Dr. Pratik Das and Dr. Nilkamal Barai of our scientific group for providing me a range of constructive suggestions, guidance, and moral encouragement at different stages of my PhD work. I gratefully acknowledge the scientific discussions and friendly help from my lab mates at various stages of this thesis work. My sincere thanks goes to Dr. Ritabrata Dasgupta, Sudip Kumar Mondal, Manaska Mukhopadhyay, and Nandan Roy.

It has been a great pleasure to share my academic accomplishments and social life with friends and juniors, namely Uddalak Biswas, Pramit Chatterjee, Gouri Shankar Mukherjee and Ayan Patsa. All the informal talks with them motivated me freshly and energized my research work to a large extent. I would also like to thank Rudrani Chakraborty for her constant enthusiasm regarding my research.

Finally, I would like to thank my mother, who always supported me and helped me in difficult times, and Maadhushree Phukan, without whom I would not be the person I am now.

DIP GHOSH

Table of contents

Abstract

Rocks undergo partial melting in a wide range of geological conditions, such as ultra-high temperature metamorphism of crustal rocks, lithospheric subduction, adiabatic decompression of upwelling mantle beneath mid-oceanic ridges, and at the thermal boundary layer above core-mantle boundary (CMB). The partially molten materials generally ascend to Earth's surface under action of the buoyancy forces that act upon them due to their density difference with the ambience. Understanding the driving mechanisms of melt migration phenomena is one of the key challenges in solid earth geophysics, especially to address a number of questions: how do melts create their pathways, what control them to constitute a specific network of the pathways, and how does a melt network eventually produce melt pools? The present thesis primarily aims to study some of these phenomena through laboratory experiments and theoretical modelling.

Buoyancy driven melt transport phenomena play a critical role in dictating a range of geodynamic processes, such as arc volcanism in subduction zones. It is still enigmatic why volcanic spots in many arcs are spatially scattered, whereas some of them form well-defined trench-parallel linear chains. This present thesis investigates the mode of partial-melt transport under natural buoyancy, taking into account the effects of slab dip and the thickness of partially-molten layers, produced by dehydration melting in the mantle wedge above the slab. It is demonstrated from scaled laboratory experiments that Rayleigh-Taylor (RT) instability in the melt-rich layers controls the upwelling dynamics of the melt-bearing materials in the form of regular waves, ultimately to produce a set of plumes, often described as *cold plumes*. The experiments show a transition in the mode of RT instabilities (global to localized) at a critical slab dip, resulting in a change in spatially distributed plumes down the slab to focused plume activities at the up-dip region of the slab. The experimental findings are supported by real scale computational fluid dynamics (CFD) simulations. The thesis develops a theory within a framework of lubrication approximation to study the two competing processes: RT instability and slab-parallel advection in the melt-rich layer atop the subducting slab. The theoretical treatment invokes convective and absolute instabilities to determine the criticality of local versus global instability, which, in turn decides the locations of volcanoes on the surface. The 2D theoretical analysis is extended to 3D to obtain a complete picture of the instabilities at the interface, treating the 3D structures as a product of the interference between two waves trending along and across

the slab strike. The thesis also presents both linear and non-linear theories for RT instabilities to predict the three-dimensional interfacial geometry as a function of the inclination angle of the slab dip. Finally, the experimental and theoretical findings are used to explain varying volcano distributions observed in natural subduction zones, such as the presently active Mexican subduction system and the Java-Sumatra subduction system and the ancient subduction zones, e.g., the Andean subduction system. This study suggests that the time-dependent variation in subduction can be one of the factors to determine the evolution of contrasting volcano distribution patterns in different subduction zones or within the same subduction zones in their geological history.

Another direction of this thesis deals with the mechanism of melt migration through the mushy zone in mid oceanic ridges (MOR). The melts produced at divergent plate boundaries via adiabatic melting begin to ascend under buoyancy forces under critical dynamic states and eventually focus into the spreading center. Despite a significant advance in the MOR studies in recent time, the exact mechanics of melt migration and their accretion into the overlying lithosphere has remained a lively topic of research in geodynamics. The present study uses laboratory experiments to show the relative importance of the following competing dynamics: gravitational instability versus interfacial instability in deciding the modes of melt pathways in the porous system of mushy zones. The experimental results find the density contrast, viscosity ratio and the surface tension of the solid-melt system as the guiding factors. Increasing density contrast facilitates the pathways dominated by gravitational instability, whereas low density contrast and high surface tension favour the melt migration by interfacial instabilities.

The final part of this thesis is dedicated to explore the origin of the Deccan volcanism in a periodic fashion, established from geophysical and geochemical studies. The geodynamics of such pulsating volcanism is not yet understood. With the help of CFD simulations the present work provides a new geodynamic model to show the ascent dynamics of thermochemical plumes beneath the Deccan province during 70 to 60 Ma. The model suggests that plumes can ascend either in a continuous process to form a single large head or in a pulsating manner to produce multiple plume heads with a particular time gap between each pulse, depending upon a specific set of physical conditions. The model results are correlated with appropriate initial and boundary conditions prevailed in Deccan during 70-60 Ma to estimate the periodicity of pulsating plume formation, leading to a sequence of eruption events at a time interval of 0.4-0.7 Ma.

Chapter 1
Introduction

1.1 Plume dynamics: A historical perspective

Plate tectonics that emerged as a leading theory in the 1960s unified the two major geodynamic processes: mid-ocean ridge formation and arc volcanism in relation to plate boundaries. However, this theory did not account for the intra-plate volcanic activities recorded both in geological past and the present day across the globe. To bridge this gap, Wilson, (1963) introduced a mantle plume hypothesis that builds a connection of intra-plate hotspot volcanism and large-igneous provinces (LIPs) with mantle upwelling. He proposed that plumes are generated in the upper mantle at a depth of ~ 200 km (which he thought of as the centre of convective cycles to conceive a stable upwelling process). According to this plume model, the upwelling involves onset of melting at a shallow depth, ultimately giving rise to intraplate volcanism, described as a *hotspot*. In 1971, Morgan revisited this hypothesis, claiming that the distinct geochemical signatures of oceanic island basalts (OIBs) match with the primordial composition and thereby proposed plumes to originate from much deeper sources (Morgan, 1971). He thought mantle plumes as a product of purely thermal upwelling, forming typically a wide head (~1000 km) trailing into a slender tail (~100 km). His hypothesis is extended later to show the possible link of continental break-up with the initial plume head which subsequently generates the hotspot tracks (Morgan, 1972). However, the validity of such a proposition demands geophysical, geochemical and petrological evidences, which were lacking at the time of this conceptual development. The first convincing evidence came in conjunction with laboratory modelling by Whitehead and Luthor in 1975, who demonstrated from a series of scaled experiments the ascent dynamics of plumes. Their models provided a complete picture of the plume evolution in a thin low-density layer resting below a denser material of very high thickness for different viscosity contrast between the two layers. The experimental results consolidated the idea of large bulbous head and narrow tail for the mantle plumes. Using a linear stability analysis they established a relation between the growth rate of instability and wavenumber (Whitehead and Luther, 1975). With the advent of computers and

development of various robust numerical methods, the plume study then took a new turn. In 1978, Richter used mantle convection model to show the formation of thermal plumes with prominent head and tail structure (Richter, 1978). This study led to a leap in the understanding of plume dynamics. Yuen and Peltier, (1980) theorized the origin of plumes in terms of gravitational instabilities in the D" layer due to lowering in its density and viscosity by the heat influx from the outer core. Olson and Singer, (1985) modified Whitehead and Luthor's theory to propose that when the plume viscosity is significantly lower than the surrounding mantle, the plume tail acts as channels for plume material that flows from the core-mantle boundary. On the other hand, Griffiths and Campell, (1990) recognized thermochemical plumes and their characteristic features. This kind of plumes is driven by the chemically buoyant upwelling dynamics. They form circular heads, and entrain the surrounding material, resulting in a flattening of the plume head to a torus and giving the impression of a mushroom shaped plume. A comparison of geometry between thermal and thermochemical plumes is shown in Figure 1.1. The topography generated by such plumes were first investigated by Farnetani and Richards in 1994, who showed from numerical models that an excess temperature of > 300 K within a plume is necessary to generate melt volume similar to LIPs (Farnetani and Richards, 1994). Their model also generated a surface uplift on several kilometres scales above rising plume heads. Later van Keken, (1997) showed that the plume geometry and entrainment significantly changes if stress dependent rheology is considered.

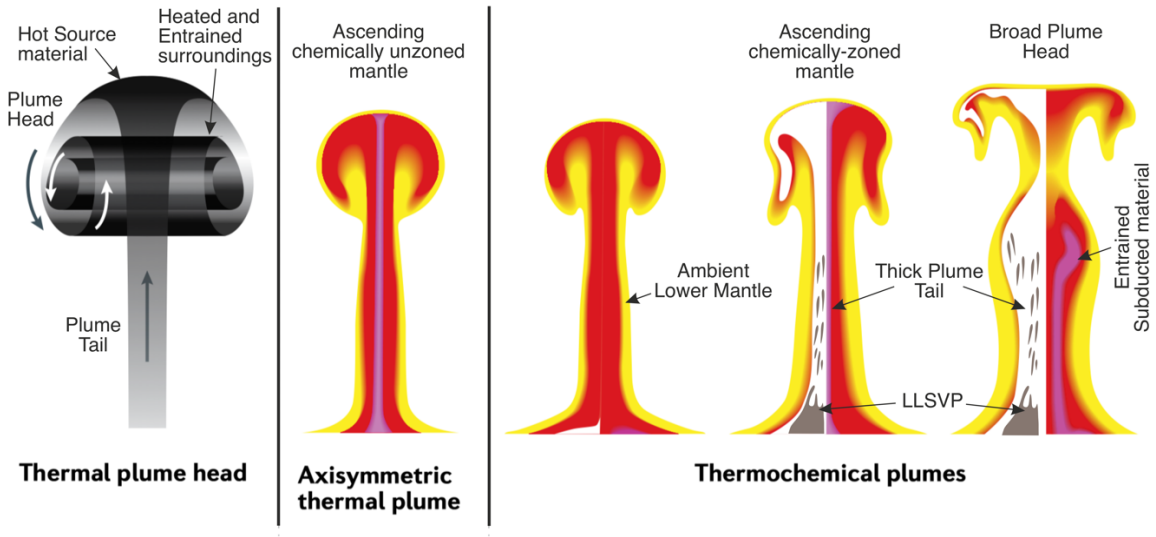

Figure 1.1: Representations of rising thermal and thermochemical plume: an ideal thermal plume head connected to its tail; an axisymmetric thermal plume; three thermochemical plumes (colours representing temperature differences). Modified from Koppers et. al., (2021)

Late 1990s and early 2000s witnessed a leaping advancement in the geophysical methods of seismic tomography that opened a new ground to capture detailed structures of Earth's lower mantle. For example, the first seismic tomographic model (S20RTS) detected the high-resolution structures above the CMB (Ritsema et al., 2011; Ritsema and van Heijst, 2002), which revealed lower than-average seismic velocities beneath the present day Africa and Pacific (Figure 1.2). The two regions, generally described as Large Low Shear-wave Velocity Provinces (LLSVPs) in literature, are thought to be the primary sources of thermochemical plume generation, which are located beneath ancient subduction zones. Interestingly, seismic tomographic studies suggest that in many regions, e.g., the Pacific margin of the Americas, subducted lithospheric slabs penetrate down into the lower mantle (Li et al., 2008), providing strong evidence against a layered mantle, as hypothesized earlier from geochemical observations.

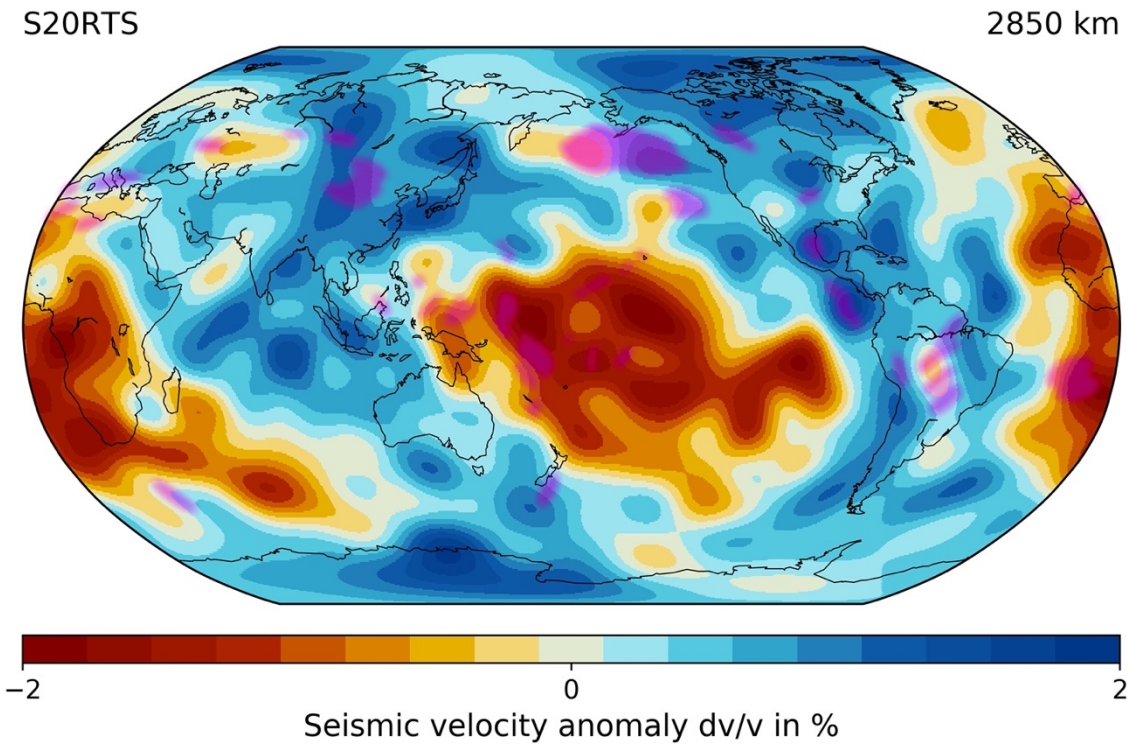

Figure 1.2: Seismic tomography model S20RTS showing map view of shear-wave velocity variation at 2850 km depth. Presence of large low shear-wave velocity provinces (LLSVPs) beneath Africa and the Pacific is clearly visible. Created using submachine.

During this time geoscientists discovered another type of plumes (often called cold plumes) in subduction zones, which are entirely chemical in nature and originate without any direct thermal contributions to their dynamics, e.g., thermal buoyancy (Flück et al.,

2003; Tamura et al., 2002; Zhao et al., 2009, 2002). Both petrological and geodynamic models suggest that cold plumes originate from dehydration melting in the mantle wedge, catalysed by fluids released from the subducting slabs. Such partial melting forms a distinct melt-rich layer above the slab, setting in an inverted density stratification that eventually forms cold plumes by gravitational instabilities. The plumes ascend across the lithosphere-asthenosphere boundary to generate arc-volcanism (Gerya and Yuen, 2003a).

1.2 Mantle plume and hotspot

Hotspots are thought to be a surface manifestation of plumes that originate at great depths. They generally record remarkable volcanic activities, producing mafic magmas in enormous volumes ($> 0.1 \times 10^6$ km^3) in a small region, that too within a geologically short time period, without any direct connection to tectonic activity. Their global distributions show their occurrences entirely within tectonic plates as well as at plate boundaries. Figure 1.3 presents the global distribution of well-established hotspots. Their population size is estimated to be > 40 (Koppers et al., 2021). The principal characteristic features of hotspots are:

- Unusually high crustal thickness.
- Topographic swell of > 1000 m marked by a geoid anomaly.
- Extrusive package thickness > 1 km,
- High melt production rates
- Very high mass flux ($300-6300$ kg/s) and heat flux (high excess temperature of > 300 K and buoyancy flux)
- Pulsating nature of the emplacement events.
- Distinct petrological and geochemical signatures, compared to those produced by plate-tectonics driven magmatism, such as arc volcanisms.
- Low seismic velocities, sometimes traceble down to the lower mantle.

According the plume hypothesis of hotspots, the ascending plumes undergo partial melting in the uppermost regions of their heads at a critical depth, and the melts generated thereby segregate to produce huge magmas that eventually erupt through the lithosphere to form large igneous provinces (LIPs) on Earth's surface. The Deccan Trap in India is thought to be a typical example of a LIP. Geological records suggest that LIPs generally evolve through a sequence of melt pulses of much shorter time scale ($\sim 0.2 - 0.3$ Ma), giving rise to a cumulative volume $> 0.1 \times 10^6$ km^3 of extrusive volcanism on an areal extent $>$

0.1×10^6 km^2. Geochronological studies indicate that more than 75% of the total volume accumulates in a time frame of approximately 1 Ma. Some geologists have postulated the timing of different LIPs to coincide with various mass extinction events. For example, Siberian Traps is often correlated with the largest known mass extinction event at the Permo/Triassic boundary (Bond and Wignall, 2014). Similarly, the Deccan Traps in India is thought to mark the KT mass extinction event (Petersen et al., 2016). To explain the temporal correlation between the LIP and mass extinction event, Wignall, (2001) has hypothesized that a huge volume of gases, such as CO_2 , SO_2 and HCl released during such volcanisms might resulted to a dramatic change in the global temperature that greatly modified the atmospheric environments, leading to an catastrophic event in the biological world.

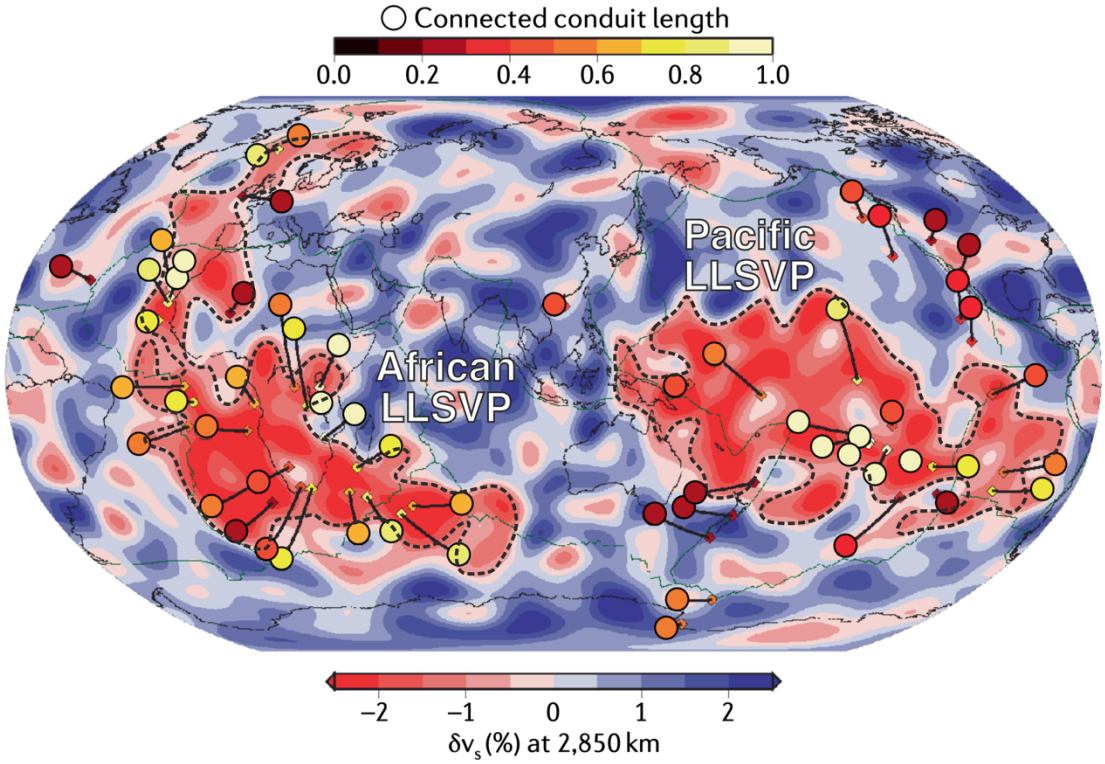

Figure 1.3: Location of surface hotspots (circles) with their depth-projected source locations (diamonds). The background colour (blue and red) represents the seismic shear velocity anomaly at 2,850-km depth. The two LLSVPs can be seen in red beneath the Africa and the Pacific. Most plumes are seen to originate above these LLSVPs expect for a few forming away from them. The upper bar indicates the normalized plume conduit length estimated from tomographic studies. Modified from Koppers et. al., (2021).

These LIPs mark the inception of hotspot tracks defined by an age-progressive volcanic events to form a chain-like distribution in the direction of plate motion. The most

acceptable tectonic model conceptualized that a plume at a fixed location in the mantle generates successive volcanic pulses to the moving plate at regular intervals, forming a chain of volcanic spots trailing the latest LIP (Richards et al., 1989). Geochronological and other geological proxies suggest that a hotspot tract forms over a time scale of million years, but in a pulsating fashion at an interval of > 1 Ma. The most spectacular example of hotspot track is the volcanic chain associated with the Réunion hotspot, where the Deccan traps marks the onset of hotspot activity, followed by the hotspot tract stretching to its present day position, the Réunion Island (Discussed in detail in Chapter 6). The Hawaiian-Emperor seamount chain is another remarkable example of hotspot tract, but it lacks the primary LIP which is thought to have subducted with the plate motion. Hotspots often show more complex structures with no hotspot track or LIP, e.g., the Canary Island or the Iceland. The distribution and dimensions of volcanic provinces associated with hotspot volcanism is shown in Figure 1.4 (flood basalts are marked in red and their corresponding hotspot tracks are shown in blue) (Coffin et al., 2006).

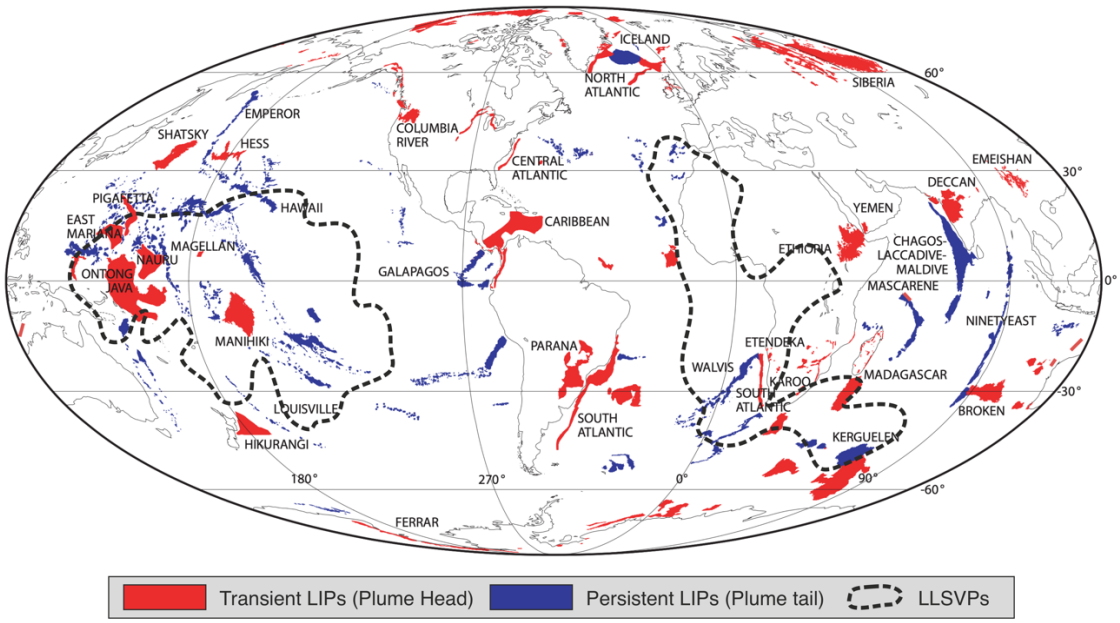

Figure 1.4: Distribution and extent of LIPs (Red) along with their hotspot tracts (Blue). Modified coffin et. al., (2006)

In the description of the plume hypothesis of LIPs, the plume excess temperature and the surface expression (dynamic topography) of plume activity are the two important considerations for plume modelling. Estimated excess temperatures are found to vary on a wide range. For example, petrological calculations provide an estimate of $175 - 195$ K

(Putirka, 2008) whereas the geochemistry of MgO content of LIPs and OIBs, suggests an excess temperature of $250 - 300$ K in the plume (Herzberg and Gazel, 2009). Considering a plume to originate from the thermal boundary layer (TBL) at CMB, the initial excess temperature of the plume must be > 1500 K as the thermal diffusion is a sluggish process, failing to cool the plume head in order to thermally equilibrate with the ambience during their ascent (Farnetani, 1997). The concept that assumes most plumes to originate from the edge of LLSVP can be an explanation as it hinders the lowermost part of the layer from rising, thus effectively reducing the plume temperature. The other arguments relate the excess temperature to radiogenic heat production, forming a thermal setting of a subadiabatic mantle with an adiabatically rising plume. This kind of thermal model accounts for a more effective decrease of the plume excess temperature.

LIP events generally witness a significant premagmatic domal uplift, depending on the type and characteristics of plume, due to upward forces of the hot, buoyant upwelling plume head. Laboratory model experiments show a maximum uplift of $500–1000$ m (Griffiths and Campell, 1990) whereas numerical model results varies from ~ 1500 m (for thermochemical plumes) (Dannberg and Sobolev, 2015) to > 4000 m (for purely thermal plumes). Using geological evidences, such as surface erosion, radiating drainage pattern, and sediment facies change, the workers have estimated the surface uplift and compare them with their models. Some LIPs, such as Yellowstone and Deccan record prominent premagmatic surface uplifts of $1000 - 2000$ m. In contrast, several LIPs, such as the Siberian trap show subsidence prior to magma emplacement. The Emeishan Traps, on the other hand, are reported to have undergone localized uplift (Sun et al., 2010). Despite these disagreements, most of the available data suggest the magnitude of maximum uplift in the order of 2×10^3 m, which poses a serious challenge to the classical thermal plume model. The updated model considers a thermochemical nature of the plume, fed by high density LLSVP (described in the next section) that reasonably explains the observed topography.

1.3 Deep Mantle Structures

1.3.1 Large low shear-wave velocity provinces

High-resolution tomographic images reveal two distinct zones in the lowermost mantle. Some of these anomalous regions show higher-than-average seismic wave speeds, often correlated with the old subducted lithospheric slabs as they are cooler and denser than the ambient mantle. The other kind of anomalous regions have lower-than-average wave

speeds, and they often lie beneath hotspots. There are two such antipodal, large low shear-wave velocity provinces (LLSVPs): one beneath the southwestern region of the Pacific Ocean, showing an elliptical outline in the map view, whereas the second one beneath the Atlantic Ocean, covering the western and southern parts of the African continent, and a significant part of the southern Indian Ocean. It describes an elongate outline in the east-west direction (Figure 1.2). The vertical extent of LLSVPs is traced down to a depth 1200 km above the CMB, in places.

LLSVPs are often identified as zones of low S wave as well as P wave velocities, although the P-wave velocity signature is much weaker than the other. Decomposition of these signals into spherical harmonics show degree two structure with minor degree three contribution (Garnero et al., 2016). They also often have a negative correlation between shear and compressional wave velocities, which probably indicates compositional heterogeneities in the LLSVPs (Antolik et al., 2003). Such heterogeneity is attributed to horizontal layering within the LLSVPs that originates either due to bridgmanite to post-perovskite transformation or to the phase transition of subducted material to post-perovskite and to seifertite. Moreover, studies on normal modes suggest higher density than the ambience in these lower mantle structures (Ishii and Tromp, 2004). Deschamps et al., (2011) correlated the aforementioned variation of compressional waves and density with the enrichment of iron and perovskite within the LLSVP structures. Other notable feature is the presence of sharp lateral V_S gradient along LLSVP boundaries. These sharp gradients are identified by a broadening of the waveform on a seismogram. This is implemented by performing a travel-time analysis and a waveform modelling from data along an array of seismic stations such that the waves encompasses both the LLSVPs and regions outside them. The estimates suggest that LLSVPs cover roughly an area of 30% of the CMB. It is also reported from this analysis that both the LLSVPs have sharp top boundaries at places. Tomographic studies often show increased shear wave splitting in SKS or SKKS waves that exit the core and travel up along the sides of LLSVPs. This can be a result of preferential alignment of compositional heterogeneity and/or lattice-preferred orientation along the edges of LLSVP caused by increased strain rate due to interaction of convective flow with the thermochemical piles at its margin.

The LLSVPs have some enigmatic features of their internal structure and geometry. It is still unknown whether these structures are simply an amalgamation of hot thermal upwelling anomalies near CMB in an isochemical lower mantle, or they are chemically distinct piles with intrinsically more-dense mantle material that have accumulated at the

base of large-scale, global upwelling regions. Garnero et al., (2016) predicted four possibilities related to the structure of LLSVPs:

- The earliest interpretation of LLSVPs was that they are large thermal megaplumes or poorly imaged clusters of thermal mantle plumes (Figure 1.5a). Although the seismic tomography can portray a blur image of the thermal plume cluster, it is evident from the conventional Earth-like convective model that the cluster would have a much smaller lateral dimension and thermal anomalies that can hardly explain the strong low-wavelength character of LLSVPs.
- The LLSVPs might originate from primordial thermochemical piles, and they can be of one of the following types, depending on their intrinsic density difference with the background mantle that primarily controls their vertical stability. In case of low density contrast between pile and the surrounding mantle, the piles can form domal structures with a vertically rise of ~1000 km from the CMB (Figure 1.5b). This concept led to the idea of *superplumes* in the lower mantle. The major problem with this concept is that it fails to explain the stability of LLSVPs over geologic timescales because they would be entrained with the ambient mantle, potentially decreasing their volume with time.
- If the density contrasts were thought to be high, the geodynamic setting would produce a *stable pile* structure (Figure 1.5c), remaining in the lowermost mantle due to their negative buoyancy. The pile would hardly interact with the ambience and thus persist over longer geologic timescales. A major drawback of this model is that it cannot readily explain the origin of thermochemical plumes without accounting for external factors, such as, convergent flow as subducted plate reaches CMB) owing to the high density of the piles.
- Thermochemical pile material are thought to have different bulk modulus as compared to the background mantle. This leads to a different pressure dependence than the surrounding, causing a depth-dependent density contrast. The result might be a *metastable pile* (Figure 1.5d), with a deeper buoyant portion overlain by a denser upper portion, producing upright piles with steep sides compared to a stable pile. Models show that they are in a time-dependent state where the mass exchange at the plume roots enhances the entrainment rates in a positive feedback process, reducing its size. On the other hand, downwelling processes results in accumulation of LLSVPs by supplying heavier materials to the pile.

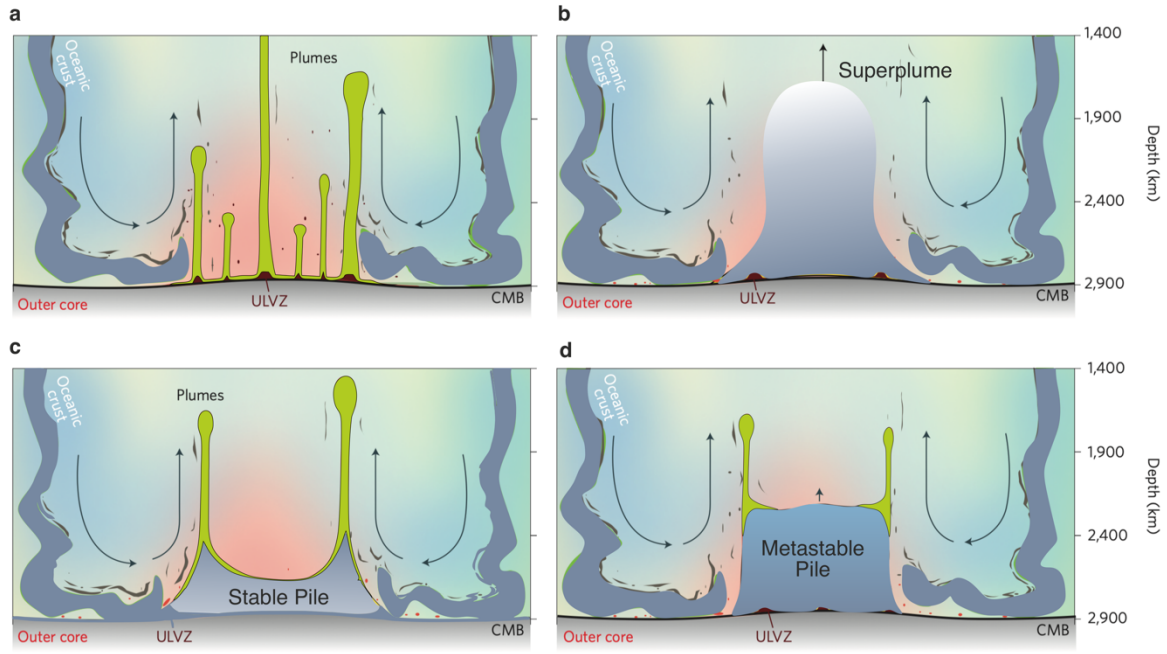

Figure 1.5: Types of geometry (interpreted) for LLSVPs. (a) Cluster of plumes, (b) Superplume, (c) Stable thermochemical pile, (d) Metastable thermochemical piles. Predicted locations of ULVZs are also shown. Modified from Garnero et. al., (2016)

Any hypothesis that attempts to explain the origin of LLSVPs should be consistent with the geophysical observations such as its sharp margin, anticorrelation of shear and compressional wave velocity, the stability on a geological time scale, as well as the presence of hotspots above them. Following McNamara, (2019) the main cause of LLSVPs can be one of the following:

1. Thermal (isochemical)
    a. Megaplumes
    b. Plume clusters
2. Thermochemical
    a. Primordial
        i) Domes and thermochemical superplumes (active, rising and sinking structures)
        ii) Primordial thermochemical piles (passive, negatively buoyant structures)
    b. Crustal accumulation

It is important to note that all the possibilities listed above constitute a two end-member scenario. The actual case is likely to fall somewhere in between.

Earlier studies correlated the origin of LLSVPs to upwelling of large megaplumes in the mantle. Using temperature dependent viscosity (Thompson and Tackley, 1998) or high thermal conductivity in the lowermost mantle (Matyska et al., 1994) the studies proposed a geodynamic model of megaplumes initiated at CMB. But as stated earlier, this proposition does not account for any geophysical signature or the stability of LLSVPs. (Bull et al., 2009) performed isochemical geodynamical calculations, using the plate motions of previous 120 million years to generate downwellings in the proper paleo-locations of subduction zones and showed the formation of plume clusters beneath present day Africa and the Pacific (Figure 1.6a). They used S20RTS model to apply a tomographic filter to seismic velocities to blur it, similar to the tomographic inversion to demonstrate that the thermal anomalies become blurred too, giving an apparent impression of plumes as much larger objects.

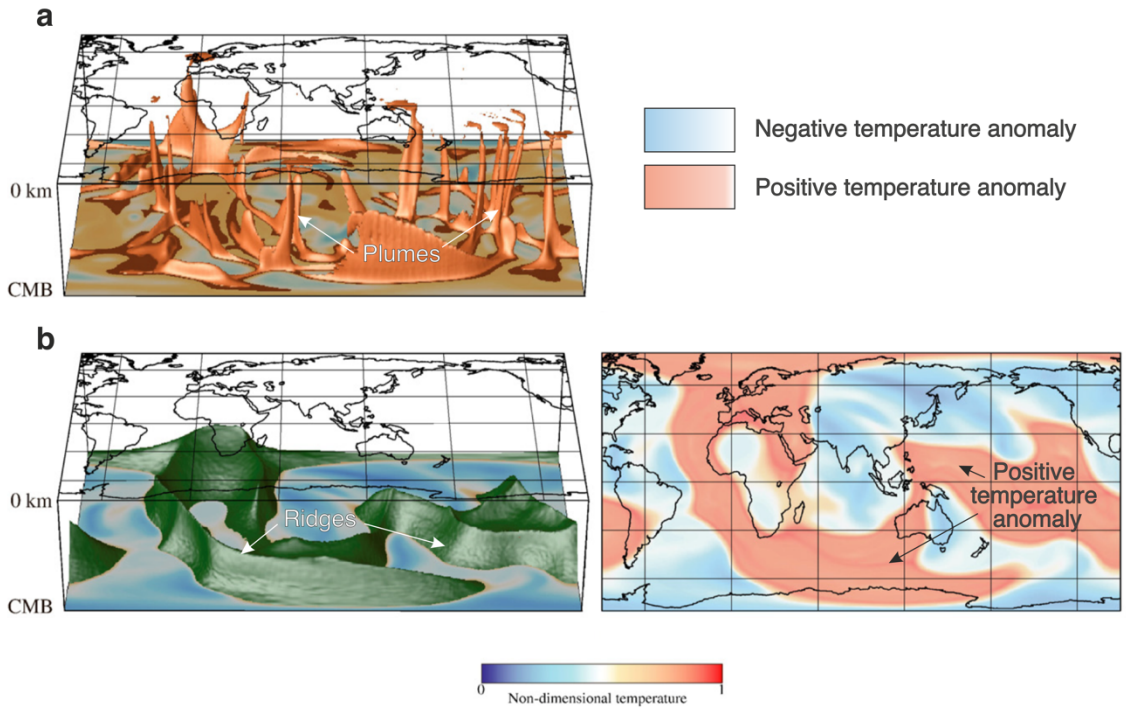

Figure 1.6: Two end member hypothesis for the origin and dynamics of LLSVPs. (a) Thermal model showing plume clusters leading to upwelling beneath Africa and Pacific. (b) Thermochemical model showing ridge-like structures beneath Africa and superposition of multiple ridges beneath southern Pacific. Modified from Bull et. al., (2009)

The simplest thermochemical model, on the other hand, is the presence a compositionally distinct reservoir at the CMB owing to its high density since very early in

Earth's history with no interaction with mantle convection whatsoever (Figure 1.6b). The common hypotheses on the formation of this ancient reservoir are:

- Remnants of a basal magma ocean (Labrosse et al., 2007)
- Accumulation of dense melts during Earth's differentiation (Lee et al., 2010)
- Accumulation of crust formed on the very early Earth due to various downwelling processes (Tolstikhin and Hofmann, 2005)

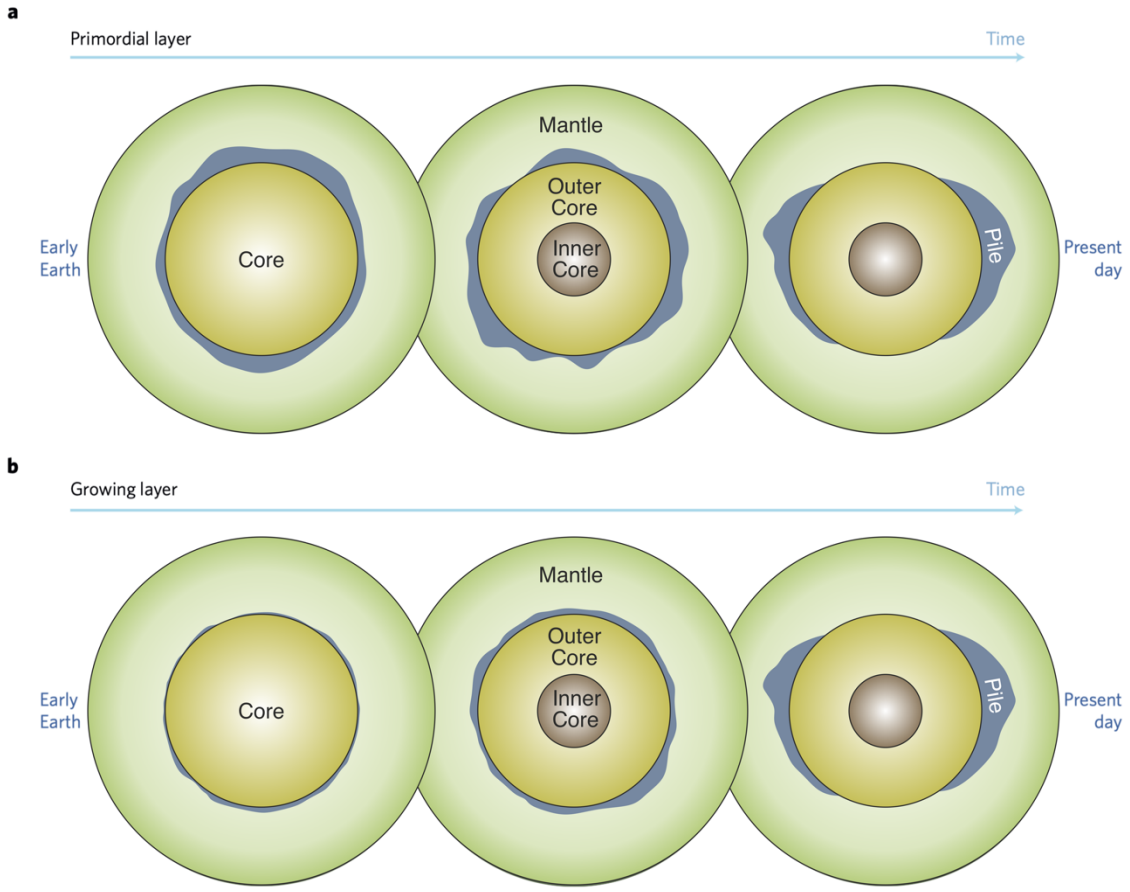

Figure 1.7: Two end-member model for the evolution of thermochemical piles. (a) Primordial layer due as a result of early differentiation and remnant of magma ocean. (b) Development of piles over geologic time due to various downwelling process. Modified from Garnero et al., (2016).

These are referred to as "basal mélange" (Tackley, 2012) or primordial thermochemical piles Owing to the higher intrinsic density they tend to remain stable or become periodically unstable and then stable again. Although these structures have negative buoyancy, they are pushed away from the subduction regions as they weigh less than the slabs (Lassak et al., 2010) and can in fact be shaped by mantle flow. The alternative hypothesis, primarily backed up by mineral physics studies, envisages accumulation of subducted oceanic crust

at the CMB over time due to its higher density, compared to the background mantle materials in the lower mantle condition (Hirose et al., 2005). It is shown that the crust must separate from the lithosphere, otherwise it would get assimilated into the ambient mantle (Li and McNamara, 2013). If, on the other hand, post-perovskite is rheologically weak, it will greatly enhance the segregation of the crust from the lithosphere (Ammann et al., 2010). The separated crust then move towards the laterally convergent regions along the CMB to accumulate as piles over geological time. There are two basic differences between the two aforementioned hypothesis: firstly, in the primordial model, the entrainment with the ambient mantle is much lower compared to the slab accumulation model. Secondly, because of its isolated nature, primordial model piles can only transport heat via conduction with little mass flux, resulting is sharp edges. Whereas in slab accumulation model, heat and mass are advected into the system during horizontal accumulation of the slabs and advected out of the system thought the top mostly via thermochemical plumes. The difference between the two model is shown in Figure 1.7

1.3.2 Ultra-Low Velocity Zones

Ultra-low velocity zones (ULVZs) are small-scale ($\sim 100 - 1000$ km wide and $\sim 10 - 40$ km thick) patches above the CMB, characterized by $\sim 30\%$ and $\sim 10\%$ reduction in S- and P- wave velocities, respectively. The seismic signature of ULVZs represent a density increase of $\sim 10\%$ compared to its ambience and they are found occur as scattered patches sparsely distributed along the entire CMB.

The basic way to identify ULVZs is to use long-wavelength diffracted waves such as SPdKS and SKPdS (Figure 1.8a). These waves can detect the existence of ULVZs, but fail to provide the exact location or the number of ULVZs present with reasonable certainty. Furthermore, they hardly give any information about their shape and size. A more precise way to locate ULVZs is to use pre-cursors and post-cursors to core-reflected waves (Rost et al., 2006) (Figure 1.8b). Seismograms receive a pre-cursor when a fraction of the wave front energy is reflected from the ULVZ top before reflecting off the core. On the other hand, they record post-cursors as energy produced by the core reflection is bounced off the ULVZ top from below, and then to encounter the core and reflect again. These pre- and post-cursors from an array of nearby seismic stations allow seismologists to find the geometry and dimension of the ULVZ. To summarize this approach, there are a limited

number of earthquake sources and seismic stations to interrogate the global CMB with sufficient high precision.

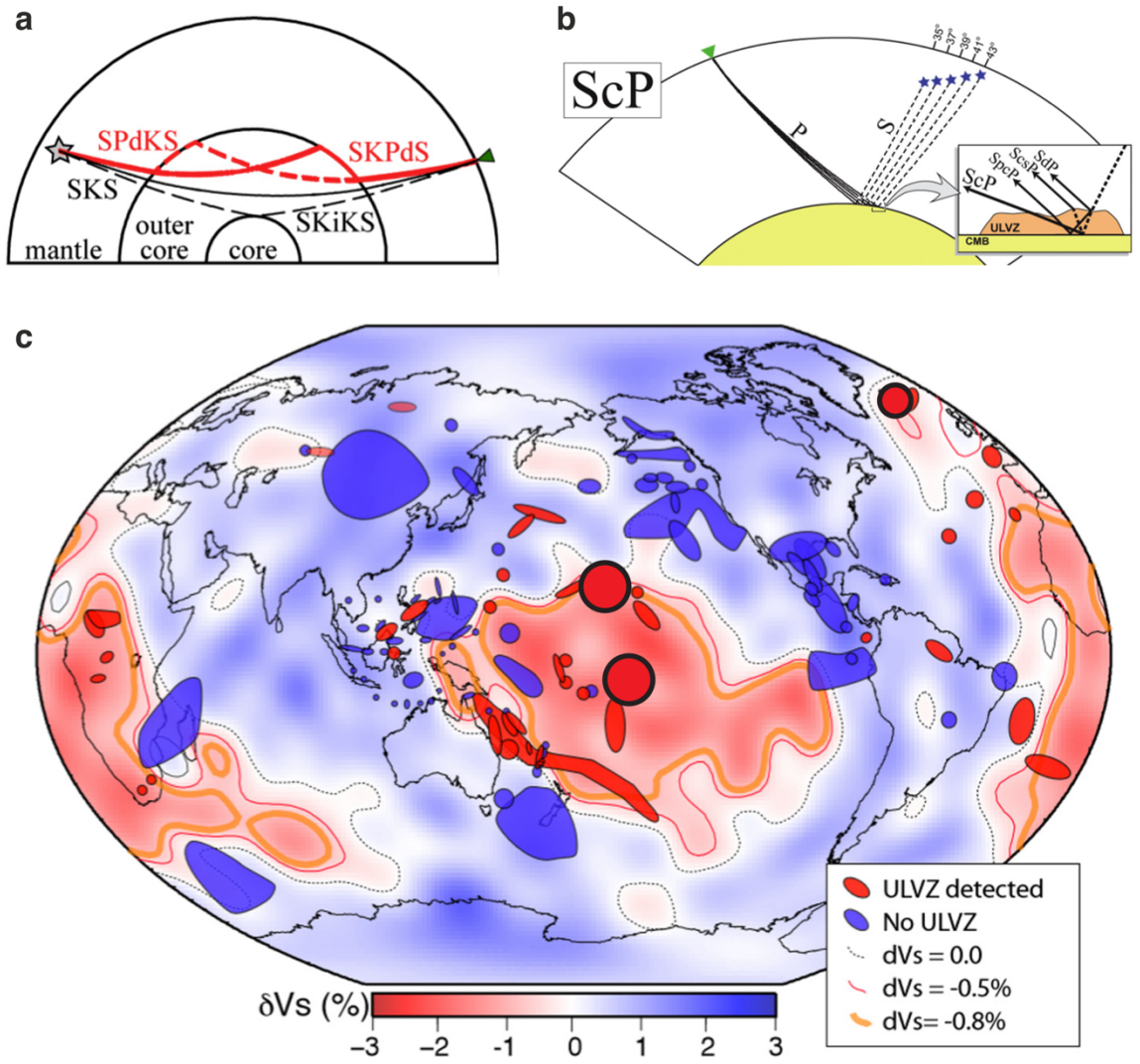

Figure 1.8: Identification and locations of ULVZs. (a) Probing of ULVZs using long-wavelength core diffracted waves such as SPdKS and SKPdS. (b) Probing via short-wavelength pre-cursors and post-cursors to core-reflected phases such as ScP. (c) Location of presence and absence of ULVZs superimposed on S20RTS model as background. Taken from McNamara, (2019).

Figure 1.8 shows the global distribution of ULVZs (dark red denotes the confirmed ULVZs locations and dark blue regions of no ULVZs). It is evident from this image that the CMB is not fully explored with a sufficient resolution to accurately detect the presence or the absence of ULVZs. One of the early explanations identifies the ULVZs them as the regions of dense partial melt patches (Williams et al., 1998). This hypothesis can be valid only when the melt sources significantly differ from the ambience in their initial chemical compositions, and thereby different melting temperatures. Secondly, the molten materials

must be denser in order to escape from the viscous stirring with the surrounding mantle. The source of the ULVZ material can be core derived iron oxides (Wicks et al., 2017), remnants of banded iron formations that were subducted (Dobson and Brodholt, 2005), core derived silicate sediment (Buffett et al., 2000), post-perovskite phase with iron enrichment (Mao et al., 2006), and FeO_2 component present within the structure of pyrite (Hu et al., 2016).

1.4 Plume Geochemistry

One of the most common tools that geologists use to differentiate various types of magma and their source regions includes a range of trace elements and isotope geochemistry. Geochemical signatures are generally heterogeneities that primarily originate from partial melting as this process results in partitioning of various elements depending on their compatibility, and a different composition of the residual solid. Elemental chemistry thus provides an excellent tool to evaluate the melt fraction, origin and the various processes involved in forming geochemical heterogeneity. The geochemical clues also provide a range of information, such as the location, length- and timescales of various geochemical domains in the deep mantle, and how geochemically and geographically zoned hotspot trails might reflect heterogeneity within mantle plumes.

Geochemical signatures, such as low abundance of incompatible elements suggest that mid oceanic ridge basalts (MORBs) are derived from depleted mantle (DMM or DM) materials. Ocean island basalts (OIBs), in contrast, are derived from enriched mantle (EM) and they show opposite geochemical trends, enrichment in incompatible elements and gradual decrease in enrichment with increase in compatibility. Another characteristic geochemical trend of Pb, Ti and Nb in all MORB and OIBs show depletion in Pb, as compared to arc-magmas (Hofmann, 2007). During subduction, Pb is transported to the mantle wedge due to dehydration reactions, leaving immobile elements, Ti and Nb in the slab. The Pb-rich melts produced by hydration melting in the mantle wedge give rise to arc-volcanism with magmas rich in Pb, but depleted in Ti and Nb. On the other hand, old subducting slabs reach CMB, which subsequently take part in plume formation that generates melts enriched with Ti and Nb, but low in Pb. These opposite geochemical trends suggest that the OIBs are generated from a source that contains subducted material, with the most obvious choice being LLSVP at the CMB (Sobolev et al., 2011). However, the hypothesis has been debated with an argument that subducted slabs are expected to be quite

dense. Alternatively, peridotite is postulated to be the predominant lithology to participate in melting beneath plume-fed hotspots. However, several studies show that the major element geochemistry of OIBs, eclogite and pyroxenite are indeed needed ((Koppers et al., 2021)). And the two LLSVP regions at the CMB seem to be the potential storage of dense, viscous slab materials that themselves from vigorous mantle convection.

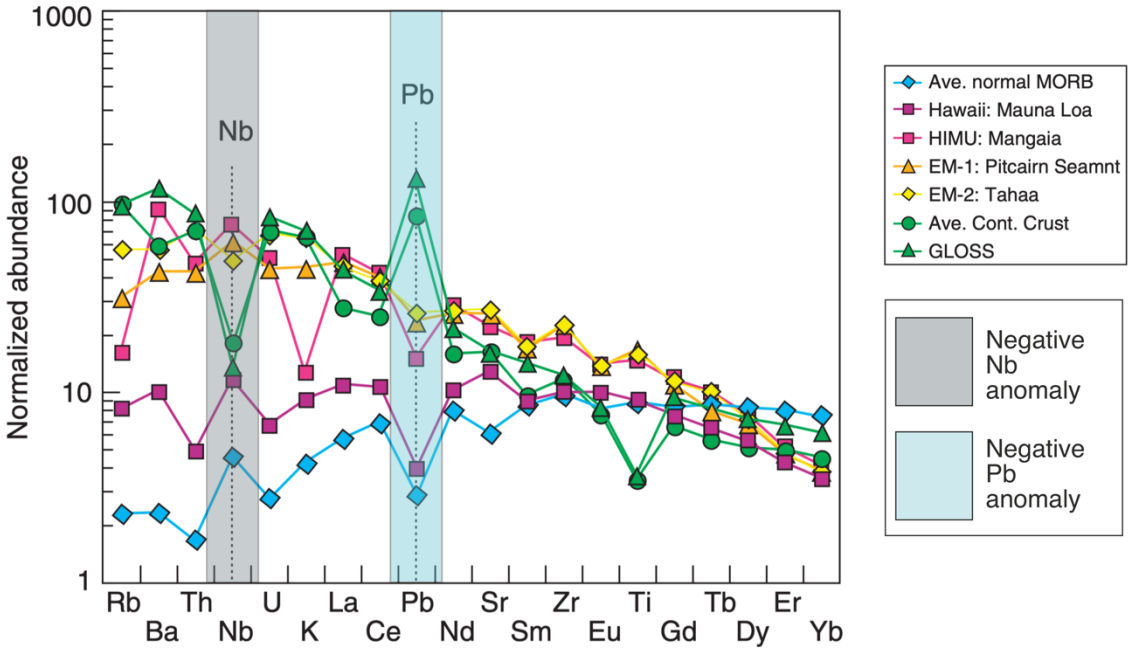

Figure 1.9: Spiderdgrams for different trace element abundance that are normalized with respect to primitive-mantle. Modified from Hofmann, (2007)

Geoscientists extensively use radiogenic to non-radiogenic isotope ratios of specific elements to identify mantle reservoirs and various fractionation events. In addition, they provide first-order evidence of lithosphere recycling in subduction zones and material transports from deep source regions to the surface by mantle plumes and other processes. Any fractionation processes affect the amount of radiogenic daughter isotopes based on their compatibility. The most commonly used isotopic pairs are $^{147}Sm/^{143}Nd$ and $^{87}Rb/^{87}Sr$ whose geochemical behaviour is exactly opposite as Sm is more compatible than Nd whereas Sr is more compatible than Rb. ^{147}Sm decays to ^{143}Nd and ^{87}Rb decays to ^{87}Sr where both the daughters are radiogenic. We divide them by its stable counterpart: ^{144}Nd and ^{86}Sr, respectively. A high value of $^{143}Nd/^{144}Nd$ indicates a depletion event where a high $^{87}Sr/^{86}Sr$ values indicates an enrichment event. As the isotopes of an element have similar geochemical affinities, the ratios $^{143}Nd/^{144}Nd$ and $^{87}Sr/^{86}Sr$ does not get affected by any

new melting or crystallization events and thus record the enrichment/depletion of the source itself. As shown in Figure 1.10a, OIBs has lower $^{143}Nd/^{144}Nd$ but higher $^{87}Sr/^{86}Sr$ ratios as compared to the MORBs, indicating a more enriched source for the OIBs. The various distinct trends of OIB isotopic signature are thought to represent various mantle reservoir such as EM1(Enriched Mantle 1: originated from delamination of lower continental crust of subducted pelagic sediments), EM2 (Enriched Mantle 2: originated from upper continental crust or oceanic crust with low sediment content or metasomatized oceanic mantle lithosphere) and HIMU (High μ: originated from magmatically enriched oceanic lithosphere or recycled oceanic crust) all connected to the PREMA (Prevalent Mantle: Material from the lower mantle). Some of them may represent a mixing of the aforementioned reservoirs with the depleted mantle (DM, the source of MORB) to generate a characteristic isotopic signature. The differences between various reservoir are also found in similar plots with Pb isotopes (Figure 1.10b-d) (Niu, 2018).

Ancient short-lived isotope systems are often used to identify the presence early-formed mantle reservoirs in the deep mantle. Common examples are $^{129}Xe/^{130}Xe$, $^{182}W/^{184}W$ and $^{142}Nd/^{144}Nd$ ratios which are typically restricted to the Hadean. Because of rapid radioactive decay (due to short half-lives from 8.9 to 103 million years), the radioactive parent isotopes for ^{129}Xe or ^{142}Nd were exhaused in the early stages of the Earth's formation. For example, a marked difference in $^{129}Xe/^{130}Xe$ ratio (^{129}I is converted to ^{129}Xe but ^{130}Xe is stable) between Earth's mantle and atmosphere indicates that such signature is present in the mantle since Hadean time despite vigorous convection. Similarly, $^{182}W/^{184}W$ (due to decay of ^{182}Hf) and $^{142}Nd/^{144}Nd$ (due to decay of ^{146}Sm) ratios of mantle and presence of ^{182}W and ^{142}Nd anomalies in OIBs suggests presence of Hadean generated mantle signatures in modern mantle. The presence of ^{182}W anomalies are more controversial and probably reflect a contribution from Earth's core, which has a very low $\mu^{182}W$ value (Figure 1.11a). During the differentiation, tungsten was preferably partitioned in the core due to its moderately siderophile nature whereas ^{182}Hf being lithophile remained in the mantle. It is probable that the core material are partitioned back into the lowermost mantle within ULVZs aided by silicate melting.

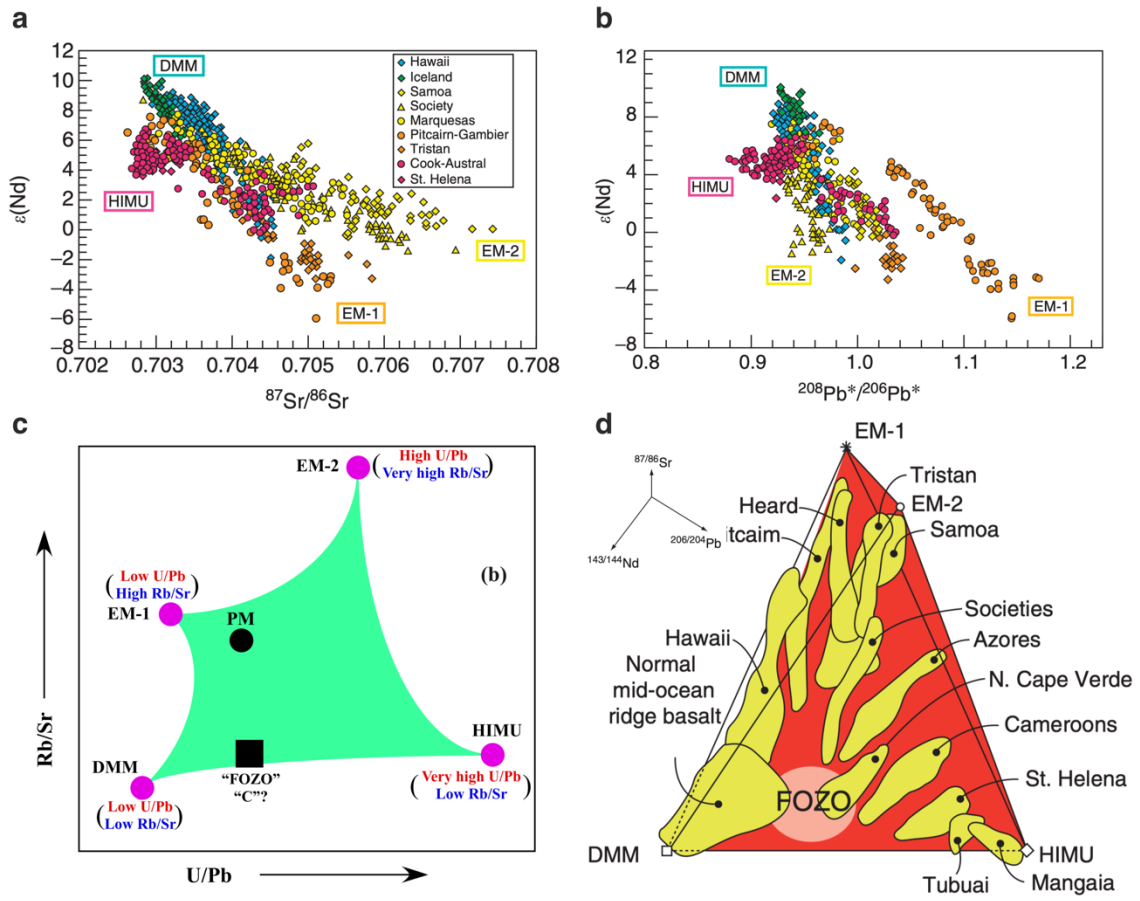

Figure 1.10: Isotopic variations in different mantle reservoirs. ε(Nd) versus $^{87}Sr/^{86}Sr$ (a) and radiogenic $^{208}Pb/^{206}Pb$ (b) plots for various OIBs; (c) Rb/Sr versus U/Pb showing various end-member geodynamic reservoirs; (d) 3D projection of various OIBs based on $^{87}Sr/^{86}Sr$, $^{143}Nd/^{144}Nd$ and $^{206}Pb/^{204}Pb$. Figure modified from Hofmann, (2007) and Niu, (2018).

Plume-fed hotspots can also provide important clues about the link of OIBs with the LLSVPs. Geochemical studies show that hotspots with highest $^{3}He/^{4}He$ ratios appear to be positioned over the LLSVPs although the high $^{3}He/^{4}He$ ratio is not restricted to LLSVPs, e.g., Yellowstone Hotspot, suggesting existence of primordial mantle outside the LLSVPs (Figure 1.11b) (Williams et al., 2015). Although the short-lived isotopes datasets (^{129}Xe, ^{142}Nd and ^{182}W) are too small to conclusively link enriched mantle to LLSVPs, Sr–Nd–Pb isotope datasets do confirm a geochemical linkage between the two (e.g., LLSVP always reflect low $^{143}Nd/^{144}Nd$). Alternative views suggest that hotspots with higher radiogenic Pb isotopes ($^{206}Pb/^{204}Pb$) are not related to LLSVPs. This is highly unlikely as enriched mantle domains are likely to have formed via subduction and recycling of ancient lithosphere. ULVZs, on the other hand, cannot be readily separated from LLSVPs purely based on geochemistry. Although a few plumes, such as Hawaii, Iceland and Marquesas are linked

with the ULVZ, no conclusion can be drawn until they are thoroughly mapped using seismic images.

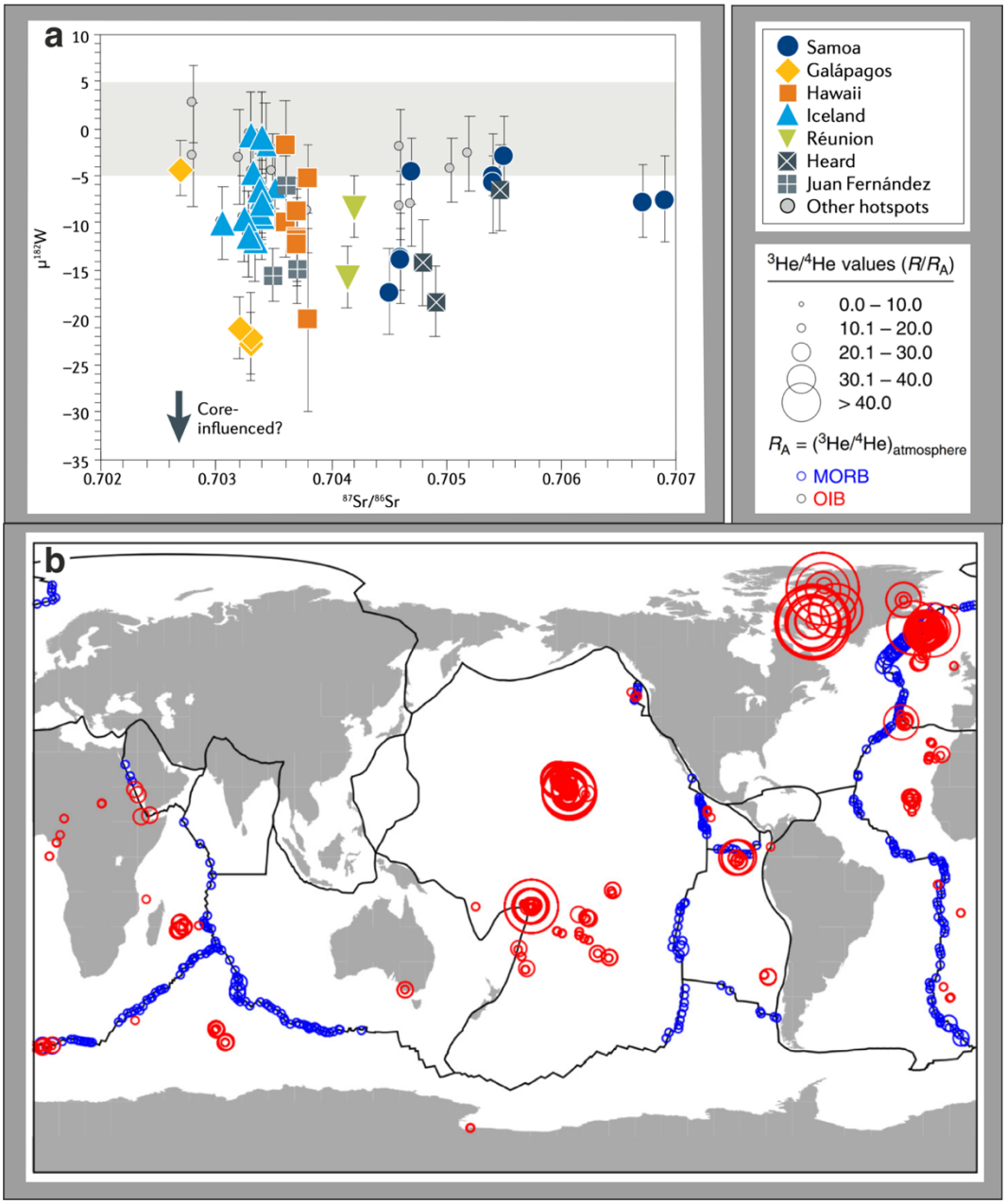

Figure 1.11: Different isotopic ratios to distinguish OIBs from MORBs. (a) Plot of $\mu^{182}W$ versus $^{87}Sr/^{86}Sr$ for various hotspot derived magmas. Modified Koppers, (2021); (b) Distribution of $^{3}He/^{4}He$ from various MORBs and OIBs. Modified from Williams et al., (2015).

The Geochemical surface expressions of OIBs often shows bilateral zoning or striping on million year scale. They can be results of the variation of plume source itself or their interaction with the lithosphere or change in plate kinematics. Overall the imprint can be subdivided into unzoned, concentrically zoned and bilaterally zones plumes. The

unzoned plume are heterogeneous in nature and generally explained by plumes with no internal zonation and typically shows temperature profile of the conduit and melting rate and on the refectory nature of elements to explain the variation in isotopic composition. The double-track volcanism is then explained by the change in direction of the overriding plate. When plume tilt and plate movement direction are aligned then both melt sources overlie each other, and as a result, there will be no zonation. Due to a change in the plate motion, the lithospheric motion may become faster and ascending plumes fail to adjust. As a result, there will be a geographic separation of deeply sourced peridotite melt and shallower secondary pyroxenite melts formed from eclogitic melt reactions. It is important to note that this model infers that double tracks only appear during periods of significate plate motion change. Concentrically zoned plumes, on the other hand, forms as densest and hottest material are concentrated towards the centre of the plume at the CMB or higher degree of partial melting towards the axis of the plume as compared to its boundary region. Since concentric zonation is identified by $^{3}He/^{4}He$ ratio, an alternative idea is that the more primitive material (high $^{3}He/^{4}He$) ascends vertically faster than the rest of the plume material causing the concentric geochemical signature and it has nothing to do with the underlying plume composition. Finally, bilateral zonation is thought to be the result of separate component with the plume, one derived mainly from enriched LLSVPs or ULVZs and the other dominated by depleted ambient mantle component. This results in two distinct chemical domains within the plume that results in the bilateral chemical zonation as they erupt.

The existence of such geochemical trend was first discovered form the Hawaiian Islands within the subparallel Loa and Kea volcanic tracks (Jones et al., 2016; Weis et al., 2011). Higher $^{208}Pb/^{206}Pb$ ratios in the southern Loa region represent the incorporation of enriched LLSVP material, northern Kea component, on the other hand, has lower $^{208}Pb/^{206}Pb$ ratio that possibly represents contribution of ambient lower mantle material that are common in most Pacific plumes (Koppers et al., 2021) (Figure 1.12). The other important observation is the absence of a Loa component prior to ~5 Ma which is often attributed to the change in Pacific plate motion around 6 Ma.

Since the discovery of plume zonation in Huwaii, these double-track trends have been observed in many other hotspot tracks, such as Cape Verde, Easter, Galápagos, Marquesas, Samoa, Society, Tristan-Gough and Rurutu. But the zonation is often more complex and can only be described by a combination of the aforementioned mechanisms. Therefore,

multiple petrological, chemical and physical parameters need to be considered when further refining and testing models of plume structure.

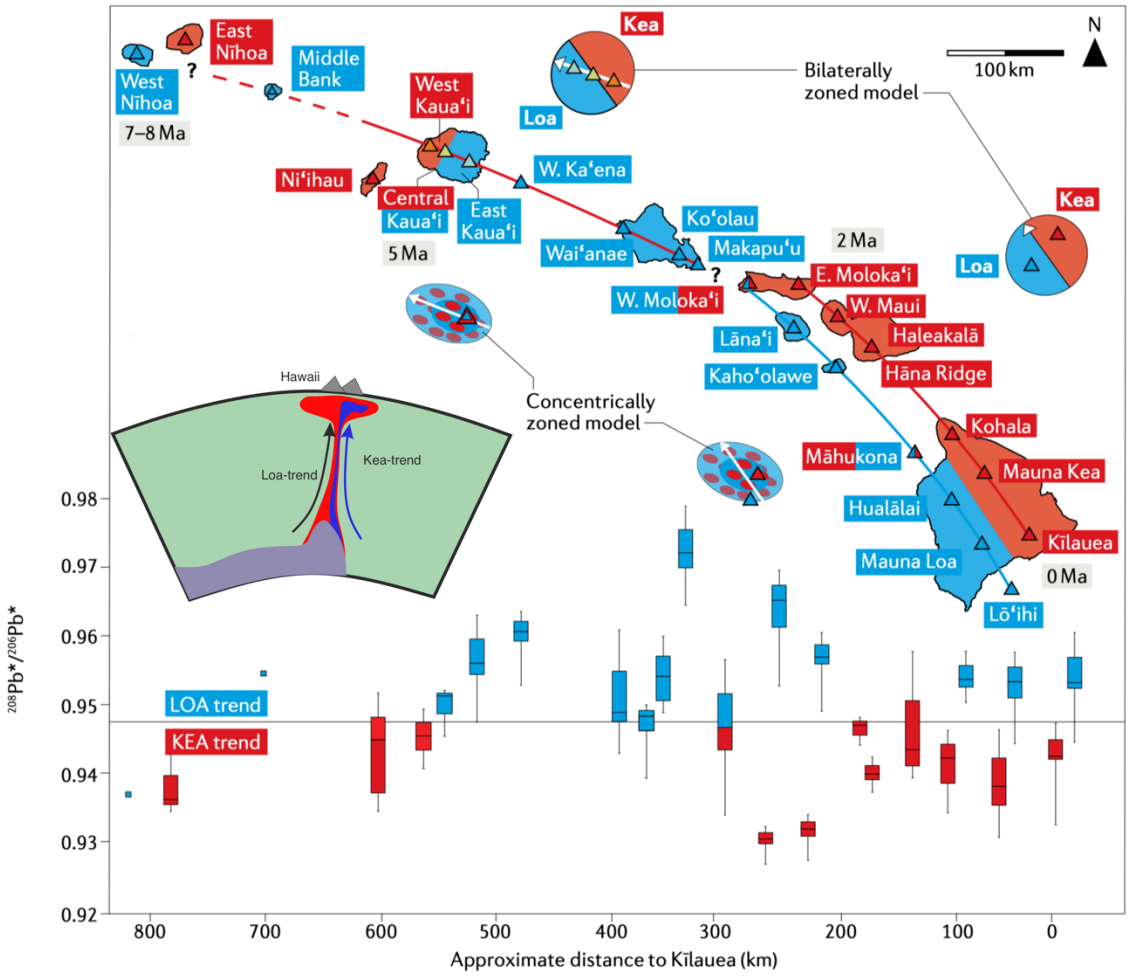

Figure 1.12: Double-track isotopic zonation in Hawaii showing two separate tracks: the Loa trend (blue) and the Kea trend (red). Modified from Koppers et al., 2021.

1.5 Imaging of plume

Geochemical studies are useful to track the source and the history of plumes; however, they cannot predict their structures and states or sources. Seismic tomography are found to be an excellent tool for imaging both the plumes and their source region.

Low seismic velocities underneath the LIPs are generally assumed to be an indicator of a plume structure. However, due to lack of coverage (more so in the ocean due to lack of earthquake sources and receiver stations in the ocean basins) of tomographic studies, the resolution of such tomographic models are limited. Moreover, wave-front healing (French and Romanowicz, 2015) can also musk the narrow channel and lead to difficulty in

detecting plume tail down to the lower mantle. Using synthetic experiments, seismologists soon realized that these hidden signatures can be appreciated only when they account for a full waveform analysis to resolve the plume conduits. For example, initial studies on Hawaii plume detected a broad, inclined upwelling that disappeared below 1500 km, but higher-resolution models in later years suggested the presence of at least 400 km wide conduits in the lower mantle beneath major hotspots, which appear to be rooted near the core–mantle boundary (Suetsugu et al., 2009) (Figure 1.13a). Recent tomographic investigations reveal a similar scenario beneath the Réunion plume (Figure 1.13b) (Tsekhmistrenko et al., 2021). Thermochemical plume conduits are generally found to be wider than that of a thermal plume due to the lower buoyancy. Thus, conduits width > 500 km in from tomographic studies indicates presence of thermochemical plumes, and most of them are observed over the LLSVPs. One major difference between the tomographic images and the numerical studies of the plume is that unlike the numerical plume where the conduits is straight throughout the mantle, seismic images of conduits often show strong tilts above 1000 km depth. This is attributed to the horizontal flow in the mantle, which is often not considered in numerical modelling. It is now thought that the flow is restricted below 1000 km and straight conduits thus occur mostly in the lower mantle at depths $>$ 1000 km. Tomography also detect downgoing slabs, sometimes heading to CMB. It might indicate the presence of a phase transition of ringwoodite to high pressure bridgmanite or other oxide phases at 1000 km that leads to change in physical properties, such as density, viscosity etc.

Based on the lower mantle seismic data, the existence of two LLSVPs were first hypothesized (Lay and Garnero, 2011). These antipodal regions have lower seismic velocities than the ambient lower mantle, and their spatial locations can be tomographically well-correlated with the present day position of hotspots. For example, a recent tomographic study of the Réunion hotspot shows a close link with the present day eastern flank of African LLSVP (Tsekhmistrenko et al., 2021). Moreover, as stated earlier, the LLSVPs are also considered as a slab graveyard, which is assumed to be a potential location for the thermochemical plume generation. In fact, this correlation is established from tomographic models showing plumes to rise from the edges of LLSVPs (French and Romanowicz, 2015).

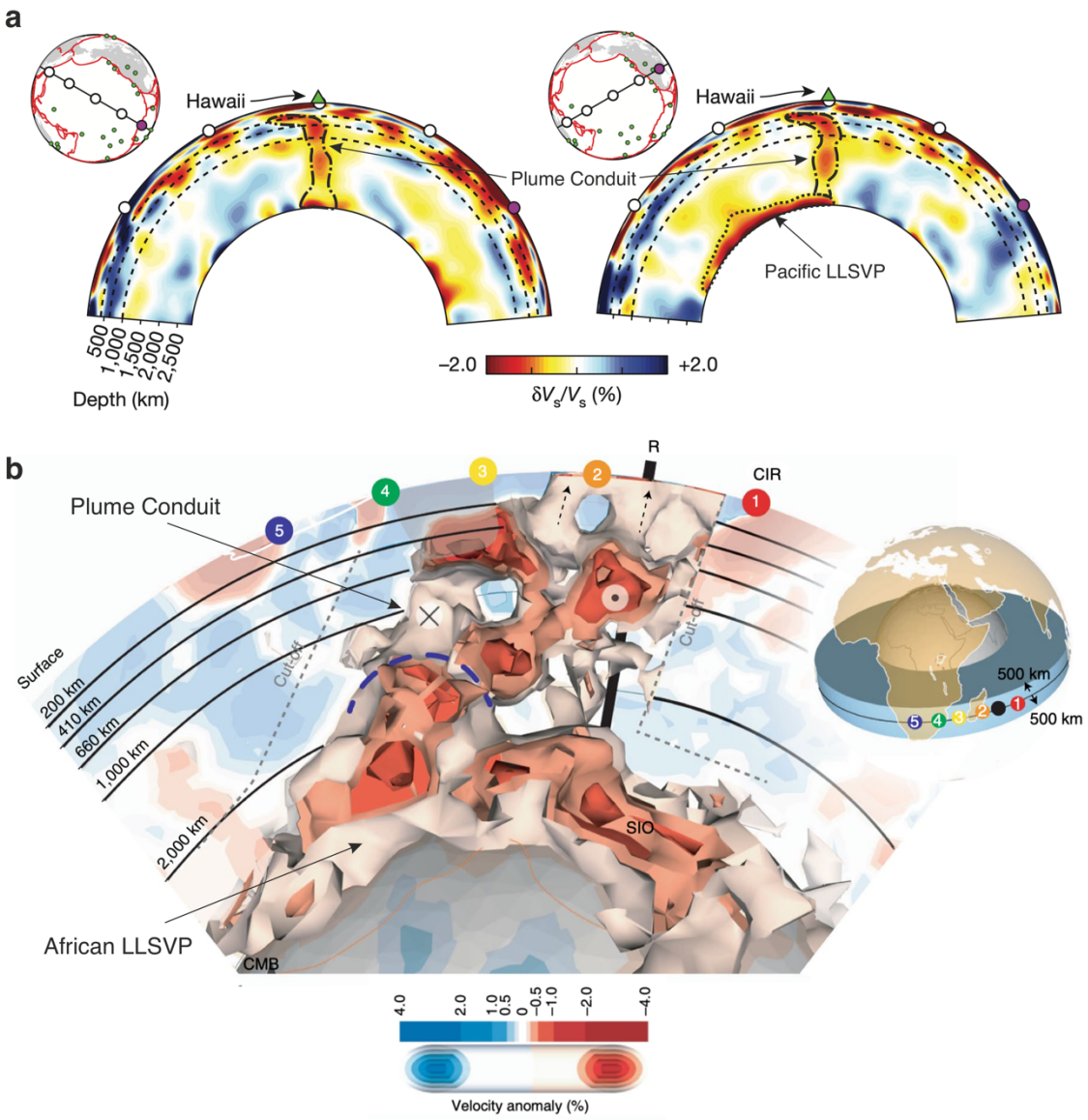

Figure 1.13: Seismic imaging of deep mantle plumes. (a) Tomographic images of Hawaiian plume and pacific LLSVP. Modified from French and Romanowicz, (2015); (b) 3D rendered p wave velocity model beneath La Réunion. Modified from Tsekhmistrenko et al., (2021).

1.6 Present views of mantle plume

Numerical studies show that thermal plumes are commonplace within mantle where convection (driven via bottom heating) is the main process to transfer mass and heat to the surface (van Keken, 1997). To make it more realistic, composition-driven density variation and temperature-dependent viscosity are incorporated to explain thermochemical instabilities at the CMB (Lin and Van Keken, 2006). With time, some of these instabilities form mature plumes, and under a favourable condition, they reach Earth's surface to form

hotspots. As described in the preceding section, tomographic studies show that hotspots concentrate mostly at the edges of LLSVPs (Figure 1.3), which needs a proper explanation.

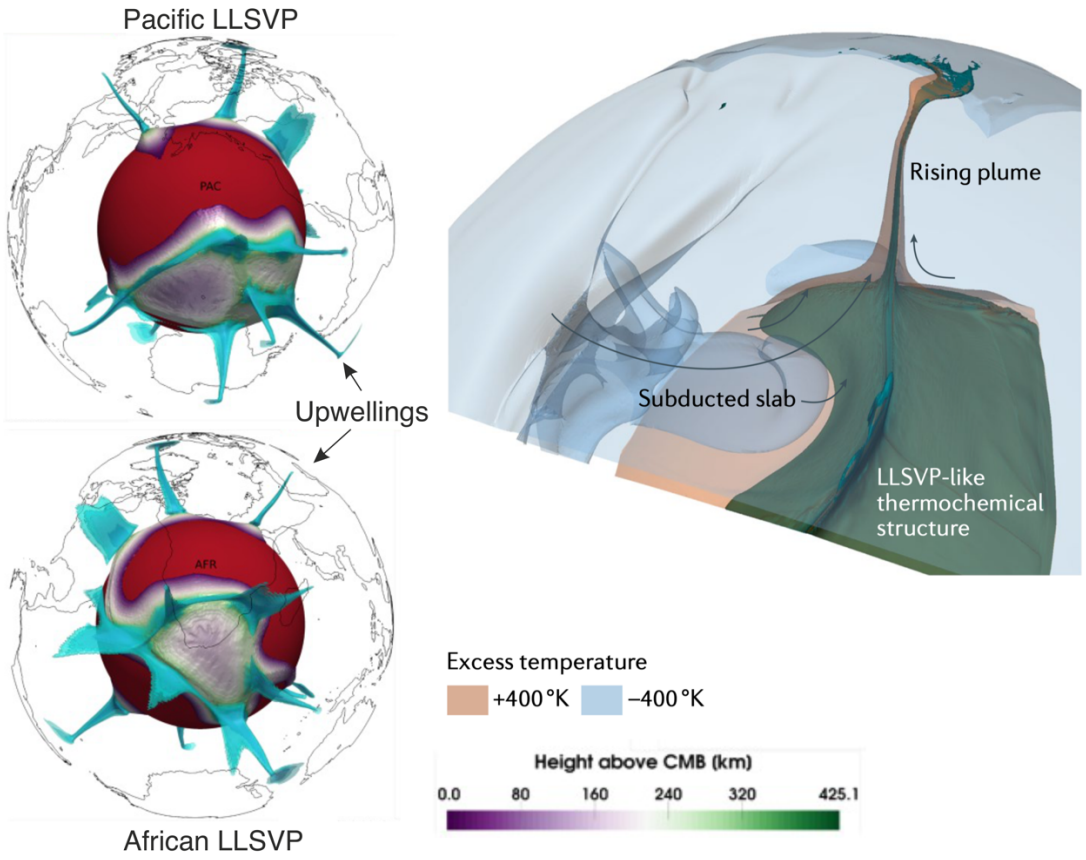

Figure 1.14: Formation of thermochemical plume via interaction of subducting plate with LLSVPs. Modified from Hassan et. al., (2015) and Koppers et. al., (2021).

Recent studies using 3D, time-dependent numerical models incorporating plate motion history shows that as a subducting plate reaches the CMB in the vicinity of LLSVPs, two processes are onset. The slab pushes the pile laterally that tends thicken the LLSVP edge; secondly, the TBL height between the LLSVP and the slab increases, and as the local Rayleigh number (Ra) of the TBL surpasses the critical Rayleigh number, a thermal instability forms. This thermal instability is then further pushed to the LLSVP edge where it incorporates chemically distinct pile material to increase its volume and height. Although the LLSVP material is thought to be denser than the ambience, the overall height and volume of the instability gives rise to a mature thermochemical plume. Due to time-dependence and variability of the entrainment, the overall dynamics of such plumes is very complex and different from the classical thermal plume dynamics (Dannberg and

Gassmöller, 2018) (Figure 1.1). This explains the much thicker plume tail as observed in recent tomographic studies (Tsekhmistrenko et al., 2021). Due to the lower buoyancy these plumes upwell slowly and the plume head gets progressively deflected away from the source in the upper mantle due to plate velocity. The plume head ultimately reach LAB to form hotspot by partial melting that produces massive volcanism over a short geological time (< 1 million year). The entrainment of pile materials also explains the observed dynamic topography (due to lowering of buoyancy) and chemical zonation (Material coming from both LLSVP and ambient lowermost mantle) reported from various hotspots.

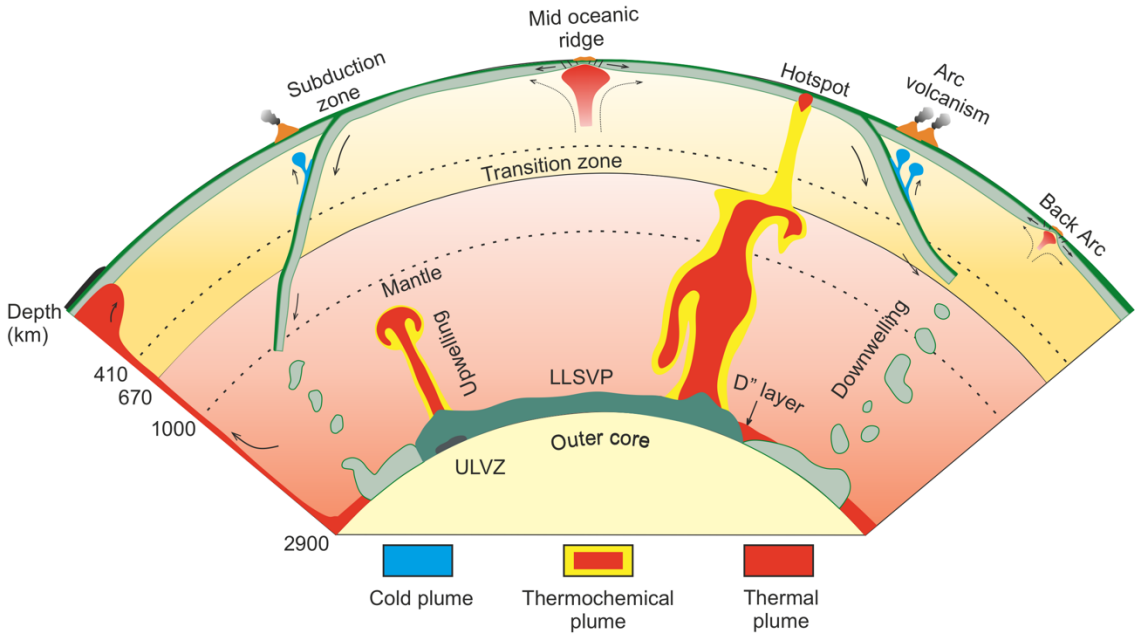

Figure 1.15: Different location of plume generation with Earth's mantle. Modified from Koppers, (2021).

Subduction zones, on the other hand, develop a specific geodynamic setting for Rayleigh Taylor instability to produce plumes in a relatively cold environment (Davies and Stevenson, 1992; Hall and Kincaid, 2001; Tamura et al., 2002). These 'cold plumes' are thought to originate at a depth of 100-200 km, driven by compositional buoyancy attributed to partial melting due to fluids released by serpentinization of the underthrusting slab (Gerya and Yuen, 2003a; Poli and Schmidt, 2002), and lubrication by viscous dissipation (Hansen and Yuen, 1996, 1995). Estimates suggest these cold plumes can ascend with high velocities, in the order of 10 cm/yr (Gerya and Yuen, 2003a). Geophysical studies (Flück et al., 2003; Tamura et al., 2002; Zhao et al., 2009, 2002) indicate that the plume-driven magmatism in subduction zones is a three-dimensional (3-D) phenomenon, where both

along and across trench melt dynamics need to be accounted to comprehensively model the melt generation and migration phenomena. Zhu et al. (2009) have shown from 3-D petrological-thermomechanical numerical simulations that slab dehydration sets in small-scale convection and cold plumes in the mantle wedge. Their simulations produce three types of plume patterns: (1) finger-like plumes, forming sheet-like structure parallel to the trench, (2) across-trench ridge-like structures, and (3) flattened wave-like instabilities, forming trench-parallel zigzag patterns. According to their model, the viscosity of melt zones is the principal factor to control the plume type. Lowering in viscosity results in Rayleigh-Taylor like instabilities with smaller wavelengths. Their low-viscosity models (10^{18}–10^{19} Pa s) develop finger-like plumes with a spacing of 30–45 km, which increases to 70-100 km for higher viscosity (10^{20}–10^{21}Pa s), and finally these plumes attain sheet-like structures.

The various possible locations of plume generation within earth mantle along with their predicted dynamics and geometry are shown in Figure 1.15.

1.7 The thesis structure

The thesis is presented in eight main chapters. The next chapter (**Chapter 2**) provides the various modelling approaches used in this study. These include a general introduction to Finite Element method (FEM) and description of the computational geodynamic codes used to perform computational fluid dynamic (CFD) simulations, followed by a detailed account of the laboratory model scaling, with an emphasis on mantle plume. **Chapter 3** deals with the problem of *cold plumes* formed in subduction zones. Scaled analogue experiments are presented to show how their dynamics is affected by different parameters, such as the slab dip angle and partially molten layer thickness. The results are then verified using CFD simulations. **Chapter 4** describes basic premises of thin-layer approximation used to develop a theory for the evaluation of thin layer stability under the influence of steady Couette flow. The theory is then used for the linear stability analysis to investigate the control of the aforesaid factor in gravitational instabilities in inclined source layers. **Chapter 5** extends this theory to third dimensions, where Navier-Stokes equation is solved to derive linear and non-linear equations for the evolution of the interface by considering interaction of various wavevectors. Then the various modes of gravity instability for different substrate inclination is demonstrated using various Fourier modes. **Chapter 6** builds a thermochemical model to determine the stability of thermochemical pile at the

CMB under different model parameters on a sub-1000 Ma scale. Then the model is applied to find a connection between Deccan volcanism, Réunion hotspot and African LLSVP. In **Chapter 7**, Scaled laboratory experiments are conducted using three phases to investigate relative importance of gravity and interfacial instability. The entire work is then summarized in **Chapter 8,** highlighting the major discussions and conclusions. This includes discussions on the validity of the cold plume model in the Andean, Central American and Java-Sumatra subduction systems, and determination and validation of time periodicity of Réunion hotspot eruption and Deccan volcanism to the natural data.

Chapter 2

Numerical and Laboratory Methods

2.1 Introduction

Most of the geological processes take millions, even billions of years to attain their steady states on complicated paths with various thermo-mechanical parameters affecting the course of its history. It is thus a great challenge to render a complete understanding or a theory for such problems. Field studies do help but they provide only a snapshot in time and few clues to reconstruct the whole evolutionary process. One can therefore infer the evolutions of geological processes and the resulting structures, but cannot directly show their evolution from field studies. One way to overcome these limitations is to conduct experimental studies to investigate geological processes whose length and time-scales extend far beyond the range of any direct experimentations and field observations. In the field of geodynamics, experimental studies are carried out primarily in two ways: real scale numerical models and laboratory scale analogue models. Both the approaches help geoscientists quantitatively investigate the influence of various geometrical and rheological parameters as well as initial and boundary conditions on the geological process in question. These experiments are not only useful to support or disprove an existing or a new hypothesis, but they are excellent standalone tools to discover new physical processes responsible for a particular natural phenomenon. Like any other branch of sciences, these problems can be investigated with the following approaches.

- **Laboratory modelling**. This approach uses scaling laws to choose appropriate geometry and materials for the experimental set-up. The experiments are then conducted in highly controlled environment in a laboratory that can take accurate measurements for various quantitative analysis. The main difficulty in laboratory experiment is concerned with the accuracy of model scaling and availability to the corresponding analogue materials to conduct the experiments. To test the scaling accuracy, we often upscale the parametric values obtained from our experiments and compare them with numerical simulations and natural data/observations.

- **Theoretical modelling.** This approach represents the given phenomena in a physical domain as an *Initial Boundary Value problem* (IBVP) where the system behavior is tackled with a set of *Partial Differential Equations* (PDEs) and appropriate *Initial Conditions* (ICs) and *Boundary Conditions* (BCs). The mathematical operations then employ reasonable approximations and solve the IBVP to obtain an exact analytical solution as a function of system variables. Generally speaking, geological systems are very complicated with complex geometry, and analytical solutions are often difficult to obtain. Under these circumstances it is necessary to deal with their linear or weakly nonlinear analysis with reasonable approximation or use some numerical techniques available.

- **Numerical modelling**. These are useful and efficient in solving problems with complex geometry and where the parameters affecting the problem is large and analytical solutions are not readily available. In numerical methods, the system domain is first discretized into small domains and the governing equations with some approximation are used to solve them within each domain, considering the initial and boundary conditions. The various numerical methods differ in the way they discretize the domain and how they approximate the differential equations. The solving procedure is iterative in nature i.e., the computation makes a guess for the solution and test how good the solution is by calculating the error. The solution is then fed into the loop to get a better solution. The iteration process is allowed to continue until the error magnitude turns lower than a predefined error. Although, this is an approximate solution, it is generally good enough to represent the system under consideration (e.g., it can be shown that the weak form solution for a finite element problem belongs to the space of all possible solution the strong form of the differential equation may have). Compared to laboratory experiments, which require various sophisticated equipment and a proper lab facility, numerical experiments only expect high computational power.

This thesis adopts both numerical and analogue experiments as well as theoretical modelling to study gravity instabilities under different geodynamic conditions. Analogue experiments are performed using various scaled fluid dynamics set-up in the laboratory and numerical modelling is conducted primarily using various *Computational Fluid Dynamics* (CFD) tools that employ *Finite Element Method* (FEM). The details of techniques used are provided in the respective chapters. This chapter is dedicated to the basics of numerical and analogue modelling. § 2.2 provides a brief introduction to the fundamentals of finite

element method. § 2.3 then describes how the FEM is implemented in a CFD code. Finally § 2.4 offers an introduction to analogue model scaling.

2.2 Introduction to Finite Element Method (FEM)

2.2.1 Vector space and Norms

Consider the most fundamental mathematical environments and tools that are necessary to understand FEM. We start by introducing the main function spaces with corresponding norms and state the basic inequalities of vital importance.

- Let $\mathbf{x} = (x_1, x_1, \dots, x_n) \in \mathbb{R}^n$ be a vector in $\mathbb{R}^n$. The *norm* of $\mathbf{x}$ is defined as its Euclidean length:

$$\|\mathbf{x}\| = |\mathbf{x}| = (x_1^2 + x_2^2 + \cdots + x_n^2)^{1/2} \tag{2.1}$$

- The space of all square integrable functions over a given domain Ω in $\mathbb{R}^n$ is known as the $L_2(\Omega)$-space. If $u \in L_2(\Omega)$, then the L_2-norm of u associated with the above scalar product is defined by

$$\|u\|_{L_2(\Omega)} \coloneqq \sqrt{(u,u)} = \left(\int_\Omega |u(x)|^2 dx\right)^{1/2}$$
$$L_2(\Omega) \coloneqq \{u: \Omega \to \mathbb{R};\ \ \|u\|_{L_2(\Omega)} < \infty\} \tag{2.2}$$

  Any constant, polynomial or Heaviside function (Figure 2.1a) are $L_2(\Omega)$ function. Direc delta function (Figure 2.1b), on the other hand $\notin L_2(0, L)$.

- A set of vectors $S = \{\mathbf{x_1}, \mathbf{x_2}, \dots, \mathbf{x_n}\}$ in V is said to be a *basis* of V if S spans V(i.e., every element in V can be written as a linear combination of S) and S in linearly independent.
- A linear space V is said to have dimension n, we write $\dim V = n$, if n is the maximum number of linear independent vectors in V. For example, $\mathbb{R}^n$ has dimension n, since the set $\{\mathbf{e}_i\}_1^n$ is linearly independent and spans $\mathbb{R}^n$ but the set of polynomials $\mathcal{P}^{(q)}$ has dimension $q + 1$, as the monomials $p_1(x) = 1, p_2(x) = x, \dots, p_n(x) = x^q$ are linearly independent and span $\mathcal{P}^{(q)}$.
- A function f of one real variable is said to be of class $\mathcal{C}^{(k)}$ on an open interval I if its derivatives $f', \dots, f^{(k)}$ exist and are continuous on I. A function f of n real variables is said to be of class $\mathcal{C}^{(k)}$ on a set $S \subset \mathbb{R}^n$ if all of its partial derivatives

of order $\leq k$, i.e., $\partial^{|\alpha|} f/(\partial x_1^{\alpha_1} \dots \partial x_n^{\alpha_n})$ with the multi-index $\alpha = (\alpha_1, \alpha_2, \dots, \alpha_n)$ and $|\alpha| \leq k$, exist and are continuous on S.

- **Space of differentiable functions**: Let $\Omega \subset \mathbb{R}^n$ be a bounded open set, then $\mathcal{C}^{(k)}(\overline{\Omega})$ is the set of all functions $u \in \mathcal{C}^{(k)}(\Omega)$ such that $D^\alpha u$ can be extended from Ω to its closure $\overline{\Omega}$, for all multi-index $\alpha = (\alpha_1, \alpha_2, \dots, \alpha_n)$, $|\alpha| \leq k$. The space $\mathcal{C}^{(k)}(\Omega)$ is equipped with supremum norm defined by

$$\|u\|_{\mathcal{C}^{(k)}(\overline{\Omega})} \coloneqq \sum_{|\alpha| \leq k} \sup_{x \in \Omega} |D^\alpha u|$$

e,g., for $k = 1$, we write

$$\|u\|_{\mathcal{C}^{(1)}(\overline{\Omega})} \coloneqq \sum_{|\alpha| \leq 1} \sup_{x \in \Omega} |D^\alpha u| = \sup_{x \in \Omega} |u(x)| + \sum_{i=1}^{n} \sup_{x \in \Omega} \left| \frac{\partial u}{\partial x_i}(x) \right| \tag{2.3}$$

For simplicity, we can write

$$\mathcal{C}(\overline{\Omega}) \coloneqq \mathcal{C}^0(\overline{\Omega}) = \left\{ u : \|u\|_{\mathcal{C}(\overline{\Omega})} = \|u\|_{\mathcal{C}^0(\overline{\Omega})} < \infty \right\}$$

where

$$\|u\|_{\mathcal{C}(\overline{\Omega})} \coloneqq \|u\|_{\mathcal{C}^0(\overline{\Omega})} = \sup_{x \in \Omega} |u(x)| = \max_{x \in \Omega} |u(x)|$$

- **Space of *Lebesgue* integrable functions**: For a real number $p \geq 1$, we define the space $L_p(\Omega)$ by

$$L_p(\Omega) \coloneqq \left\{ u : \int_\Omega |u(x)|^p \quad dx < \infty \right\}, \quad 1 \leq p < \infty$$

$$L_\infty(\Omega) \coloneqq \left\{ u : \operatorname{ess.sup}_{x \in \Omega} |u(x)| < \infty \right\},$$

The $L_p(\Omega)$ is associated with the norm

$$\|u\|_{L_p(\Omega)} \coloneqq \left(\int_\Omega |u(x)|^p dx \right)^{\frac{1}{p}}, \qquad 1 \leq p < \infty \tag{2.4}$$

$$\|u\|_{L_p(\Omega)} \coloneqq \operatorname{ess.sup}_{x \in \Omega} |u(x)|$$

Where the latter is called the *L-infinity norm*. Of particular interest is the $L_2(\Omega)$-norm (which can be related to measuring the energy) defined by Eq. (2.2).

- **Weak Derivative**: Let $\omega \subset \Omega$ be a bounded and open subset of Ω with $\omega \subset \Omega$. Suppose that $u \in L_1(\omega)$, $\forall \omega$ (i.e. u is locally integrable on Ω). Suppose, further, that there exists a locally integrable function χ_α on Ω such that

$$\int_\Omega \chi_\alpha v(x)dx = (-1)^{|\alpha|} \int_\Omega u(x) D^\alpha v(x)dx, \quad \forall v \in C_0^\infty(\Omega) \tag{2.5}$$

  Then χ_α is called a *weak derivative* of u of order $|\alpha|$, and we write $D^\alpha u = \chi_\alpha$.

- **Sobolev spaces:** Let Ω be an open subset of $\mathbb{R}^n$. For a nonnegative integer k and $p \in [1, \infty]$, we define the *Sobolev space* of order k by

$$W_p^k(\Omega) := \{u \in L_p(\Omega) : D^\alpha u \in L_p(\Omega), \quad |\alpha| \le k\} \tag{2.6}$$

  The corresponding *Sobolev norms* are given by

$$\|u\|_{W_p^k(\Omega)} := \left(\sum_{|\alpha| \le k} \|D^\alpha u\|_{L_p(\Omega)}^p \right)^{\frac{1}{p}}, \quad 1 \le p < \infty$$

  and (2.7)

$$\|u\|_{W_\infty^k(\Omega)} := \sum_{|\alpha| \le k} \|D^\alpha u\|_{L_\infty(\Omega)}.$$

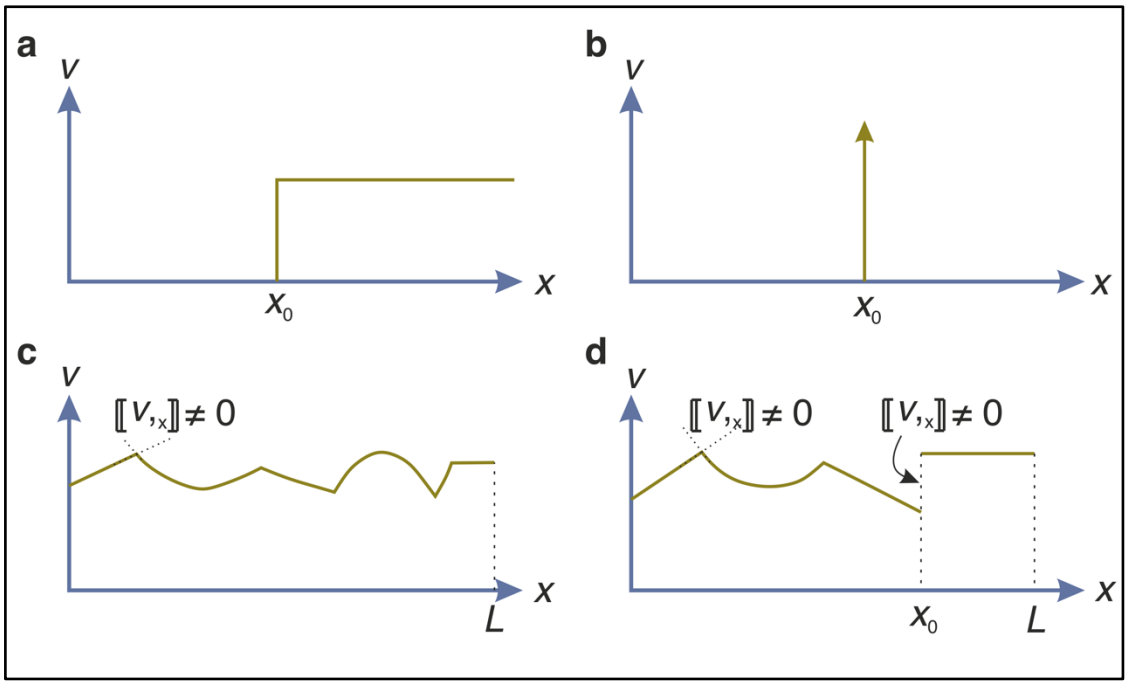

Figure 2.1: (a) Heaviside function as an example of $L_2(\Omega)$ function, (b) Direc delta function is not a $L_2(\Omega)$ function; (c) Continuous function with jump in first derivative and thus it belongs to H^1 space, (d) Discontinuous function with jump in function at x_0 and thus it does not belong to H^1space.

- **Hilbert Spaces:** The special cases $p = 1, 2, \infty$, and $k = 1, 2$ are the most frequently used function spaces, where in particular $p = 2$ and $k = 1, 2$ called the *Hilbert spaces* and denoted by $H^k(\Omega)$, $\Omega \subset \mathbb{R}^n$, viz.

$$H^1(\Omega) \coloneqq \left\{ u \in L_2(\Omega) | \frac{\partial u}{\partial x_j} \in L_2(\Omega), \quad j = 1, \dots, n \right\}$$

$$\|u\|_{H^1(\Omega)} \coloneqq \left(\|u\|^2_{L_2(\Omega)} + \sum_{j=1}^{n} \left\| \frac{\partial u}{\partial x_j} \right\|^2_{L_2(\Omega)} \right)^{\frac{1}{2}}, \tag{2.8}$$

$$|u|_{H^1(\Omega)} \coloneqq \left(\sum_{j=1}^{n} \left\| \frac{\partial u}{\partial x_j} \right\|^2_{L_2(\Omega)} \right)^{\frac{1}{2}}$$

And

$$H^2(\Omega) \coloneqq \{ u \in L_2(\Omega) : \frac{\partial u}{\partial x_j} \in L_2(\Omega), \quad j = 1, \dots, n, \quad \text{and}$$

$$\frac{\partial^2 u}{\partial x_i \partial x_j} \in L_2(\Omega), \quad i, j = 1, \dots, n \}$$

$$\|u\|_{H^2(\Omega)} \coloneqq \left(\|u\|^2_{L_2(\Omega)} + \sum_{j=1}^{n} \left\| \frac{\partial u}{\partial x_j} \right\|^2_{L_2(\Omega)} + \sum_{i,j=1}^{n} \left\| \frac{\partial^2 u}{\partial x_i \partial x_j} \right\|^2_{L_2(\Omega)} \right)^{\frac{1}{2}}, \tag{2.9}$$

$$|u|_{H^2(\Omega)} \coloneqq \left(\sum_{j=1}^{n} \left\| \frac{\partial^2 u}{\partial x_i \partial x_j} \right\|^2_{L_2(\Omega)} \right)^{\frac{1}{2}}$$

- For solving *homogeneous problems*, we specifically use the particular Sobolev space: $H_0^1(\Omega)$. The closer of $\mathcal{C}_0^\infty(\Omega)$ in the norm $\|u\|_{H^1(\Omega)}$ is the set of all $u \in H^1(\Omega)$ such that u is the $H^1(\Omega)$ limit of a sequence $\{u_m\}_{m=1}^{\infty} \subset \mathcal{C}_0^\infty(\Omega)$. This closer defines a special space denoted by $H_0^1(\Omega)$, which for sufficiently smooth $\partial\Omega$, can be identified as

$$H_0^1(\Omega) \coloneqq \{ u \in H^1(\Omega) | u = 0 \text{ on } \partial\Omega \} \tag{2.10}$$

  It has the same norm as $H^1(\Omega)$.

- In simple terms we can rewrite the first equation of Eq. (2.10) as

$$u \in H^1(0, L) \; if \int_0^L (u^2 + (m(0, L))^2 u_{,x}^2) dx < \infty \tag{2.11}$$

where $m(0, L)$ is the measure of the domain (length in 1D). H^1 indicates we are controlling both the function and it's first derivative. To control higher order derivatives, the mathematical operation uses higher order Hilbert spaces. Any constant and polynomial functions $\in H^1$. Figure 2.1c shows a function with a jump in the first derivative. But the function is still continuous and $\in H^1$. Figure 2.1d, on the other hand, shows a jump in the function itself and therefore $\notin H^1(0, L)$.

2.2.2 Finite Element Method in 1D

Consider a one-dimensional elasticity problem where a 1D bar is fixed at the left and there is an displacement u_g or traction t on the other end (Figure 2.2). Let us also consider a body force at the top marked as f. The strong form The strong form of the problem can thus be written as

$$\begin{aligned} & u(x): (0, L) \to \mathbb{R} && \text{s.t.} \\ & \frac{d\sigma}{dx} + f = 0 && \text{in } \Omega \\ & u(0) = u_0, \text{and } u(L) = u_g \text{ or } \sigma(L) = t && \text{on } \partial\Omega \end{aligned} \tag{2.12}$$

where σ relates to the velocity via the constitutive equation

$$\sigma = E u_{,x} \tag{2.13}$$

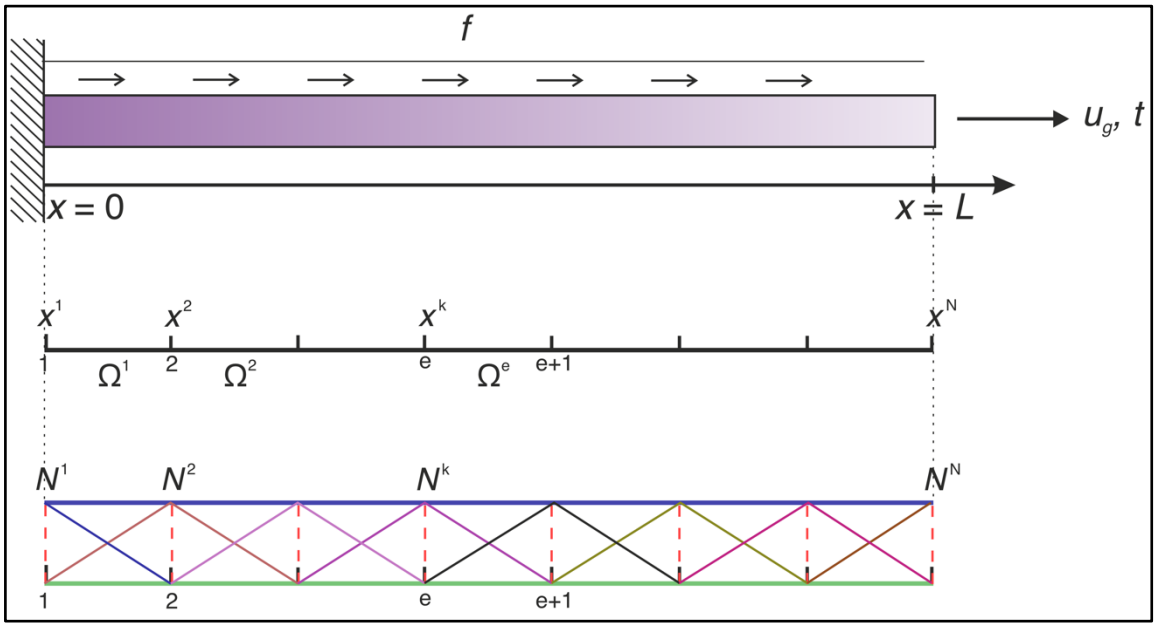

Figure 2.2: 1D elasticity problem and its finite element discretization.

Here u is treated as a mapping from an open interval $(0, L)$ into a range of 1D scalar field $\mathbb{R}$. This is called the strong formulation as the ODE is specified at each point within the interval $(0, L)$ and since we need to differentiate twice, it makes the formulation strong as if u is not iteratively smooth, it is difficult to obtain two derivatives. For example, it is difficult to obtain a solution near a crack. The corresponding weak form of the problem would be

$$\begin{aligned} &\text{Find} && u(x) \in \mathcal{S} = \{u | u(0) = u_0\} \\ &\text{s.t.} && \forall\, w \in \mathcal{V} = \{w | w(0) = 0\} \\ & && \int_0^L w_{,x}\, \sigma A dx = \int_0^L w f dx A + w(L) t A \end{aligned} \tag{2.14}$$

Or in terms of inner product, it follows

$$\langle \nabla w, \nabla u \rangle = \langle w, f \rangle \tag{2.15}$$

$\mathcal{S}$ and $\mathcal{V}$ are infinite dimensional function spaces and w is the test function. The weak form states that we are looking for a function u in such a way that Eq. (2.15) holds true for all values of the test function w. The solution of this is a function $u(x)$ from an infinite-dimensional function space. But as computers cannot handle objects with infinite number of coefficients, it is necessary to approximate this weak form to make the PDE solvable. Now by definition

$$\mathcal{S}, \mathcal{V} \in P^n(x), \qquad n = 0, 1, 2, ... \tag{2.16}$$

where $P^n(x)$ denotes polynomial of order n. Here we consider a finite dimensional function space that is a subset of the original space. So, for linear polynomials (1st order) we have

$$\begin{aligned} & && P^n(x), \qquad n = 0{,}1 \\ &\text{s.t.} && \mathcal{S}^h \subset \mathcal{S}, \text{ and } \mathcal{V}^h \subset \mathcal{V} \in P^n(x), \ n = 0{,}1 \end{aligned} \tag{2.17}$$

So we restrict our solution space and weighting function space. Since this is an approximate solution, we want to find $u^h(x)$ instead of $u(x)$. This can be written as

$$\begin{aligned} & && u^h(x) = \mathcal{S}^h = \{u^h \in H^1(0, L) | u^h(0) = u_0\} \\ &\text{s.t.} && \forall w^h(x) = \mathcal{V}^h = \{w^h \in H^1(0, L) | w^h(0) = 0\} \end{aligned} \tag{2.18}$$

The following holds

$$\int_0^L w_{,x}^h \sigma A dx = \int_0^L w^h f dx A + w^h(L) t A$$

This is our finite dimensional weak form or the *Galerkin* weak form. $u^h(x)$ is known as the trial function. To obtain u^h and w^h, we can partition the domain into *finite elements* which are disjoint subdomain of $(0, L)$ with each element is given by Ω^e. The elements are separated by *nodes* given by $x^1, x^2, \ldots, x^N$. This can be written as

$$\Omega = \bigcup_{e=1}^{n_{el}} \Omega^e \tag{2.19}$$

and

$$\Omega^e = (x^e, x^{e+1})$$

We also need to define the closure of the open interval denoted by $\overline{\Omega}$ which is given by

$$\overline{\Omega} = \Omega \cup \partial\Omega$$
$$\overline{\Omega} = \bigcup_{e=1}^{n_{el}} \overline{\Omega^e} \tag{2.20}$$

We now write the integral of weak form as a sum over the finite elements

$$\sum_{e=1}^{n_{el}} \int_{\Omega^e} w_{,x}^h \sigma^h A dx = \sum_{e=1}^{n_{el}} \int_{\Omega^e} w^h f dx A + w^h(L) t A \tag{2.21}$$

Linear Basis function

We now need to represent $\mathcal{S}^h$ and $\mathcal{V}^h$ over each Ω^e. To do that consider u^h and w^h in terms of local *basis function* of Ω^e. For the simplest case we need to find two basis functions over Ω^e and they will be linear polynomial on Ω^e.

$$u_e^h(x) = \sum_{A=1}^{N_{ne}} N^A(x) d_e^A$$
$$u_e^h(x) = N^1(x) d_e^1 + N^2(x) d_e^2 \tag{2.22}$$

where $N^A(x)$ is the basis function, d_e^A is the nodal degrees of freedom, and N_{ne} is number of nodes in each element. Similarly, for w_e^h

$$w_e^h(x) = \sum_{A=1}^{N_{ne}} N^A(x) C_e^A$$
$$w_e^h(x) = N^1(x) C_e^1 + N^2(x) C_e^2 \tag{2.23}$$

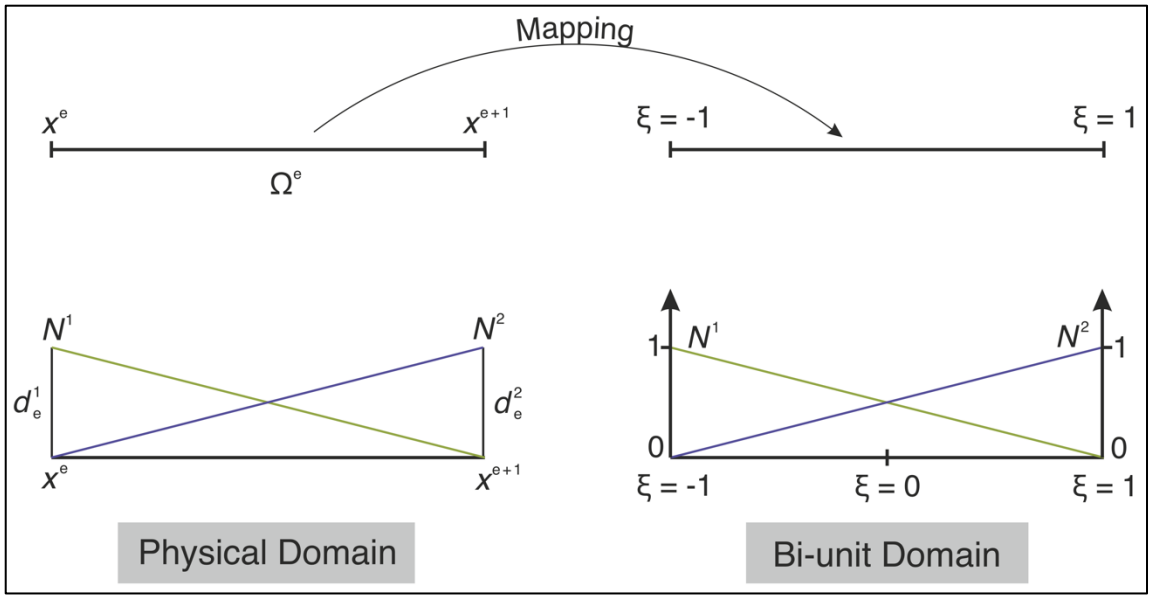

Figure 2.3: Mapping of physical domain from a bi-unit domain for linear basis function.

where C_e^A is the degrees of freedom for the weighing function. Our unit has two nodes with co-ordinate x^e and x^{e+1} in physical domain. In order to formulate the basis functions, we think of arbitrary elements constructed via a mapping from a bi-unit domain (Figure 2.3) as it is easier to define and integrate in this domain.

$$N^1(x) = N^1(x(\xi)) = N^1(\xi)$$
$$N^2(x) = N^2(x(\xi)) = N^2(\xi)$$
$$N^1(\xi) = \frac{1-\xi}{2}, N^2(\xi) = \frac{1+\xi}{2} \tag{2.24}$$
$$N^1(-1) = 1, N^1(1) = 0$$
$$N^2(-1) = 0, N^2(1) = 1$$

Some properties of bi-unit domain are as follows:

- At any point of the bi-unit domain the sum of the basis function is always unity

$$N^1(\xi) + N^2(\xi) = 1 \tag{2.25}$$

- Another characteristics is the Kronecker delta property:

$$N^A(\xi^B) = \delta_{AB} = \begin{cases} 1 & A = B \\ 0 & A \neq B \end{cases} \tag{2.26}$$

- Finally, they can be generalized to *Legendre polynomials*.
- All elements (e.g., Ω^e or Ω^{e+1}) are constructed using the same domain Ω^ξ in the bi-unit space to get the basis functions in the physical domain.
- The global node x^{e+1} with the global node number $e+1$ will have a local node number 2 for Ω^e and local node number 1 for Ω^{e+1} (Figure 2.4). The basis function is non-zero only in elements Ω^e or Ω^{e+1}. This property is called the *compact support* of the basis function. In higher dimension, there will be neighbors in other direction as well.
- For the given problem, the boundary nodes can be fully defined by a single basis function N^2 (Figure 2.4) as this confirms that w^h would vanish at x^1.

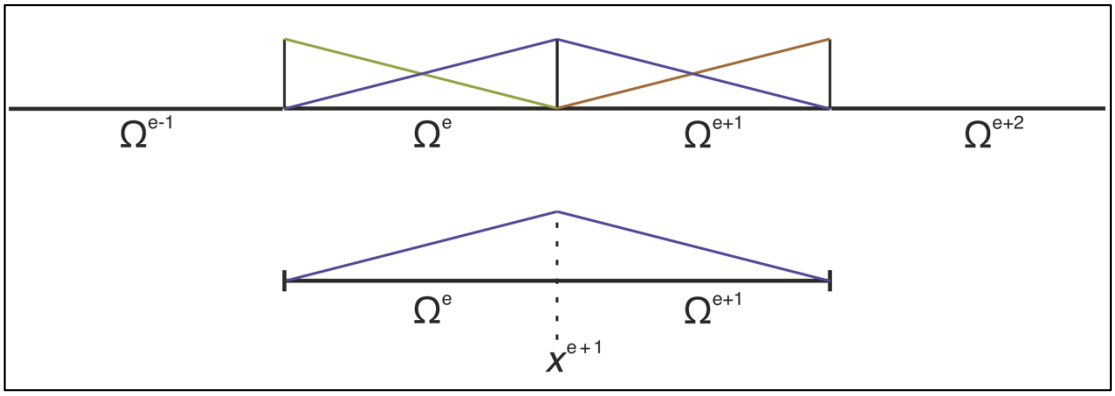

Figure 2.4: Finite elements with linear basis functions.

Next we need to write our solution variables in terms of the new domain as

$$u_e^h(\xi) = \sum_{A=1}^{N_{ne}} N_{,\xi}^A \, \xi_{,x} \, d_e^A$$
$$w_e^h(\xi) = \sum_{A=1}^{N_{ne}} N_{,\xi}^A \, \xi_{,x} \, C_e^A \tag{2.27}$$

And the mapping from the one domain to the other is done by

$$x_e(\xi) = \sum_{A=1}^{N_{ne}} \left(N^A(\xi)\right) x_e^A \tag{2.28}$$

where the first part in the RHS is any basis function for representing u^h and w^h and x_e^A represents the nodal value. This mapping is *isoparametric* in nature, such that

$$x_{,\xi}\big|_e = \sum_{A=1}^{N_{ne}} N_{,\xi}^A\, x_e^A = N_{,\xi}^1\, x_e^1 + N_{,\xi}^2\, x_e^2 = \frac{h^e}{2} \tag{2.29}$$

where Eq. (2.24) is used. h^e is the length of the element and thus, can be non-uniform. Since this isoparametric map is invertible (i.e., it is one-one and onto map), it leads to

$$\xi_{,x} = {}^1\!/_{x,\xi} = \frac{2}{h^e} \tag{2.30}$$

So the variables finite-dimensional weak form becomes

$$\begin{aligned} u_e^h(\xi) &= \sum_{A=1}^{N_{ne}} N_{,\xi}^A \frac{2}{h^e} d_e^A \\ w_e^h(\xi) &= \sum_{A=1}^{N_{ne}} N_{,\xi}^A \frac{2}{h^e} C_e^A \end{aligned} \tag{2.31}$$

Using these the terms in Eq. (2.21) becomes

$$\begin{aligned} \int_{\Omega^e} w_{,x}^h\, \sigma^h A dx &= \sum_{A,B} C_e^A \left(\int_{\Omega^\xi} N_{,\xi}^h \frac{2EA}{h^e} N_{,\xi}^h\, d\xi \right) d_e^A \\ \int_{\Omega^e} w^h f dx A &= \sum_{A} C_e^A \int_{\Omega^\xi} N^A \frac{fAh^e}{2} d\xi \end{aligned} \tag{2.32}$$

For the boundary node for this specific problem, we only need $A = 2$ instead of the sum over A. To eliminate the summations in Eq. (2.32) the *Matrix-Vector formulation* is employed. Since the present operation uses linear basis function, the number of nodes in each element would be two. It then follows

$$\begin{aligned} &\langle C_e^1 \;\; C_e^2 \rangle \frac{2EA}{h^e} \int_{\Omega^\xi} \begin{bmatrix} N_{,\xi}^1 N_{,\xi}^1 & N_{,\xi}^1 N_{,\xi}^2 \\ N_{,\xi}^2 N_{,\xi}^1 & N_{,\xi}^2 N_{,\xi}^2 \end{bmatrix} d\xi \begin{Bmatrix} d_e^1 \\ d_e^2 \end{Bmatrix} \\ &\qquad = \langle C_e^1 \;\; C_e^2 \rangle \frac{EA}{h^e} \begin{bmatrix} 1 & -1 \\ -1 & 1 \end{bmatrix} \begin{Bmatrix} d_e^1 \\ d_e^2 \end{Bmatrix} \times \\ &\langle C_e^1 \;\; C_e^2 \rangle \frac{fAh^e}{2} \int_{\Omega^\xi} \begin{Bmatrix} N^1 \\ N^2 \end{Bmatrix} d\xi = \langle C_e^1 \;\; C_e^2 \rangle \frac{fAh^e}{2} \begin{Bmatrix} 1 \\ 1 \end{Bmatrix} \end{aligned} \tag{2.33}$$

And for the left boundary element, they become

$$C_e^2 \frac{EA}{h^e} \langle 1 \;\; 1 \rangle \begin{Bmatrix} d_e^1 \\ d_e^2 \end{Bmatrix} \tag{2.34}$$

and $$C_e^2 \frac{fAh^e}{2}$$

Thus Eq. (2.21) as a whole becomes

$$\begin{aligned} C_1^2 \frac{EA}{h^1} \langle -1 \;\; 1 \rangle \begin{Bmatrix} d_1^1 \\ d_1^2 \end{Bmatrix} + \sum_{e=2} \langle C_e^1 \;\; C_e^2 \rangle \frac{EA}{h^e} \begin{bmatrix} 1 & -1 \\ -1 & 1 \end{bmatrix} \begin{Bmatrix} d_e^1 \\ d_e^2 \end{Bmatrix} \\ = C_1^2 \frac{fAh^1}{2} + \sum_{e=2} \langle C_e^1 \;\; C_e^2 \rangle \begin{Bmatrix} \frac{fAh^e}{2} \\ \frac{fAh^e}{2} \end{Bmatrix} + C_{n.el}^2 . t . A \end{aligned} \tag{2.35}$$

where last term in the RHS corresponds to the last element. Some important point to note are

- At the node the degree of freedom = trial solution, i.e., $u^h(x_e) = d_e^1$. This comes from the Kronecker-delta property (Eq. (2.26)).
- The local and global DoFs are related by

$$\begin{aligned} d_e^A &= d_{e+A-1} \\ C_e^A &= C_{e+A-1} \end{aligned} \tag{2.36}$$

- The term $\frac{EA}{h^e} \begin{bmatrix} 1 & -1 \\ -1 & 1 \end{bmatrix} = K_e$ is called the element stiffness matrix.
- The term $\begin{Bmatrix} \frac{fAh^e}{2} \\ \frac{fAh^e}{2} \end{Bmatrix} = \tau_e$ is called the element force vector.

Finally we assemble local DoFs into the global DoFs, to get

$$\langle C_2 \; C_3 \cdots C_{n_{el}} \; C_{n_{el+1}} \rangle EA \begin{bmatrix} -\frac{1}{h^1} & \frac{1}{h^1} + \frac{1}{h^2} & -\frac{1}{h^2} & & \\ & -\frac{1}{h^2} & \frac{1}{h^2} + \frac{1}{h^3} & -\frac{1}{h^3} & \\ & & \ddots & & \\ & & & \frac{1}{h^{n_{el-1}}} + \frac{1}{h^{n_{el}}} & -\frac{1}{h^{n_{el}}} \\ & & & -\frac{1}{h^{n_{el}}} & \frac{1}{h^{n_{el}}} \end{bmatrix} \tag{2.37}$$

$$\times \begin{Bmatrix} d_1 \\ d_2 \\ \vdots \\ d_{n_{el}} \\ d_{n_{el+1}} \end{Bmatrix} = \langle C_2\ C_3 \cdots C_{n_{el}}\ C_{n_{el+1}} \rangle \frac{fA}{2} \begin{Bmatrix} h^1 + h^2 \\ h^2 + h^3 \\ \vdots \\ h^{n_{el-1}} + h^{n_{el}} \\ h^{n_{el}} \end{Bmatrix}$$

$$+ \langle C_2\ C_3 \cdots C_{n_{el}}\ C_{n_{el+1}} \rangle \begin{Bmatrix} 0 \\ 0 \\ \vdots \\ 0 \\ tA \end{Bmatrix}$$

We can simplify it by considering a uniform grid, which gives

$$\begin{aligned} &\langle C_2\ C_3 \cdots C_{n_{el}}\ C_{n_{el+1}} \rangle \frac{EA}{h^e} \begin{bmatrix} 2 & -1 & & & 0 \\ -1 & 2 & -1 & & \\ & \ddots & \ddots & \ddots & \\ & & -1 & 2 & -1 \\ 0 & & & -1 & 1 \end{bmatrix} \begin{Bmatrix} d_1 \\ d_2 \\ \vdots \\ d_{n_{el}} \\ d_{n_{el+1}} \end{Bmatrix} \\ &= \langle C_2\ C_3 \cdots C_{n_{el}}\ C_{n_{el+1}} \rangle \left[\frac{fAh^e}{2} \begin{Bmatrix} 2 \\ 2 \\ \vdots \\ 2 \\ 1 \end{Bmatrix} + \begin{Bmatrix} 0 \\ 0 \\ \vdots \\ 0 \\ tA \end{Bmatrix} + \frac{EA}{h^e} \begin{Bmatrix} u_0 \\ 0 \\ \vdots \\ 0 \\ 0 \end{Bmatrix} \right] \end{aligned} \tag{2.38}$$

This can be written as

$$C^T K d = C^T F \qquad \forall C \in \mathbb{R}^{n_{el}}$$

Or

$$K d = F \tag{2.39}$$

The matrix K is a $n_{el} \times n_{el}$ stiffness matrix, d is a $1 \times n_{el}$ column vector representing the global DoFs and F is the force vector representing the RHS. The tensor K is *symmetric*, *positive-definite*, and has a *banded*, *tridiagonal* structure.

In the same manner, the pure Dirichlet-Dirichlet problem can be written as

$$\langle C_2\ C_3 \cdots C_{n_{el}}\ C_{n_{el+1}} \rangle \frac{EA}{h^e} \begin{bmatrix} 2 & -1 & & & 0 \\ -1 & 2 & -1 & & \\ & \ddots & \ddots & \ddots & \\ & & -1 & 2 & -1 \\ 0 & & & -1 & 1 \end{bmatrix} \begin{Bmatrix} d_1 \\ d_2 \\ \vdots \\ d_{n_{el}} \\ d_{n_{el+1}} \end{Bmatrix} \tag{2.40}$$

$$= \langle C_2\ C_3 \cdots C_{n_{el}}\ C_{n_{el+1}} \rangle \left[\frac{fAh^e}{2} \begin{Bmatrix} 2 \\ 2 \\ \vdots \\ 2 \\ 1 \end{Bmatrix} + \begin{Bmatrix} u_0 \\ 0 \\ \vdots \\ 0 \\ 0 \end{Bmatrix} + \frac{EA}{h^e} \begin{Bmatrix} 0 \\ 0 \\ \vdots \\ 0 \\ u_g \end{Bmatrix} \right]$$

Quadratic basis function

In two dimensions, each quadratic element has three nodes as shown in Figure 2.5. They are given by

$$N^1(\xi) = \frac{\xi(1-\xi)}{2}, N^2(\xi) = (1-\xi)^2\ , N^3(\xi) = \frac{\xi(1+\xi)}{2} \qquad (2.41)$$

In fact, one can generate any basis function from the Legendre polynomial using the following formula

$$N^A(\xi) = \frac{\prod_{\substack{B=1 \\ B \neq A}}^{N_{ne}} (\xi - \xi^B)}{\prod_{\substack{B=1 \\ B \neq A}}^{N_{ne}} (\xi^A - \xi^B)} \qquad A = 1, \dots, N_{ne} \qquad (2.42)$$

They all satisfy Kronecker delta property.

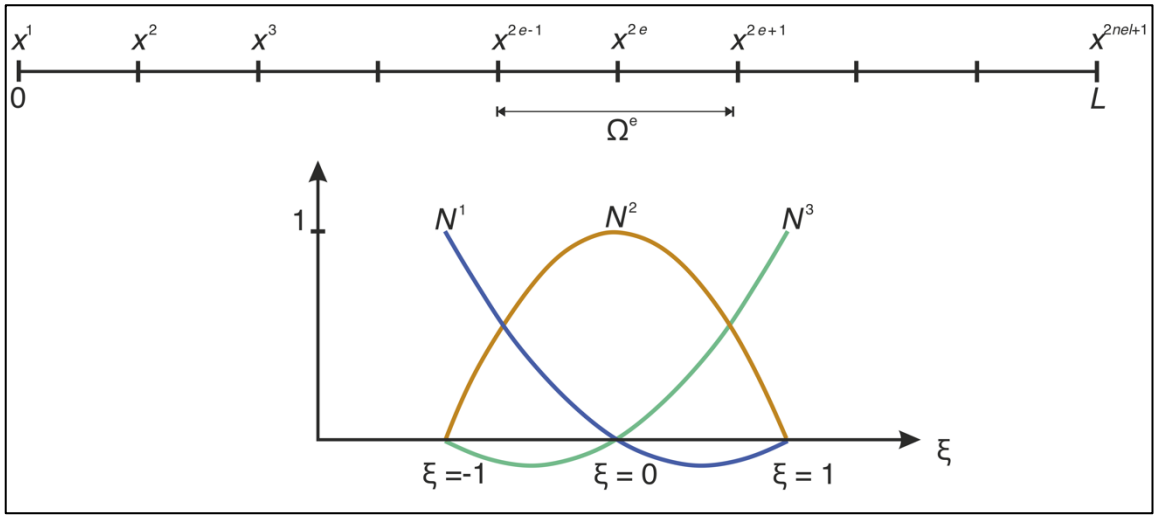

Figure 2.5: Quadratic basis function in 2D for a 1D problem.

If we use quadratic basis function to develop the FE formulation of the given problem, the variables and the elements will be given by

$$N,_{\xi}^{1} = \frac{1}{2}(-1+2\xi), \qquad N,_{\xi}^{1} = -2\xi, \qquad N,_{\xi}^{1} = \frac{1}{2}(1+2\xi) \qquad (2.43)$$

$$x_e(\xi) = \sum_{A=1}^{3} \left(N^A(\xi)\right) x_e^A$$

$$x_{,\xi} = \sum_{A=1}^{3} N_{,\xi}^{A}\, x_e^A = \frac{x_e^3 - x_e^1}{2} + \xi(x_e^1 - 2x_e^2 + x_e^3) = \frac{h^e}{2}$$

$$\xi_{,x} = \frac{2}{h^e}$$

In this case, instead of (2.33), we can write

$$\langle C_e^1 \;\; C_e^2 \;\; C_e^3 \rangle \frac{2EA}{h^e} \begin{bmatrix} \int_{-1}^{1} N_{,\xi}^{1} N_{,\xi}^{1}\, d\xi & \int_{-1}^{1} N_{,\xi}^{1} N_{,\xi}^{2}\, d\xi & \int_{-1}^{1} N_{,\xi}^{1} N_{,\xi}^{3}\, d\xi \\ & \int_{-1}^{1} N_{,\xi}^{2} N_{,\xi}^{2}\, d\xi & \int_{-1}^{1} N_{,\xi}^{2} N_{,\xi}^{3}\, d\xi \\ SYM & & \int_{-1}^{1} N_{,\xi}^{3} N_{,\xi}^{3}\, d\xi \end{bmatrix} \begin{Bmatrix} d_e^1 \\ d_e^2 \\ d_e^3 \end{Bmatrix} \tag{2.44}$$

$$\text{and} \qquad \langle C_e^1 \;\; C_e^2 \;\; C_e^3 \rangle \frac{fAh^e}{2} \begin{Bmatrix} \int_{-1}^{1} N^1 d\xi \\ \int_{-1}^{1} N^2 d\xi \\ \int_{-1}^{1} N^3 d\xi \end{Bmatrix}$$

Solving the integrals and putting everything together including the Dirichlet-Neumann boundary condition leads to

$$\begin{aligned} &\langle C^1 \;\; C^2 \rangle \frac{EA}{h^1} \begin{bmatrix} -\frac{4}{3} & \frac{8}{3} & -\frac{4}{3} \\ \frac{1}{6} & -\frac{4}{3} & \frac{7}{6} \end{bmatrix} \begin{Bmatrix} d^1 \\ d^2 \\ d^3 \end{Bmatrix} \\ &+ \sum_{e=2} \langle C^{2e-1} \;\; C^{2e} \;\; C^{2e+1} \rangle \frac{2EA}{h^e} \begin{bmatrix} \frac{7}{6} & -\frac{4}{3} & \frac{1}{6} \\ & \frac{8}{3} & -\frac{4}{3} \\ SYM & & \frac{7}{6} \end{bmatrix} \begin{Bmatrix} d^{2e-1} \\ d^{2e} \\ d^{2e+1} \end{Bmatrix} \\ &= \langle C^2 \;\; C^3 \rangle \frac{fAh^1}{2} \begin{Bmatrix} \frac{4}{3} \\ \frac{1}{3} \end{Bmatrix} + \sum_{e=2} \langle C^{2e-1} \;\; C^{2e} \;\; C^{2e+1} \rangle \frac{fAh^e}{2} \begin{Bmatrix} \frac{1}{3} \\ \frac{4}{3} \\ \frac{1}{3} \end{Bmatrix} \\ &+ C^{2n_{el}+1}.t.A \end{aligned} \tag{2.45}$$

Finally, assembling local DOFs into global DoFs, we get

$$if\ h^e = h \quad \forall e$$

$$\langle C_2\ C_3 \cdots C_{2n_{el}}\ C_{2n_{el+1}} \rangle \frac{2EA}{h} \begin{bmatrix} \frac{8}{3} & -\frac{4}{3} & 0 & \cdots & & & \\ -\frac{4}{3} & \frac{7}{3} & -\frac{4}{3} & \frac{1}{6} & & & \\ 0 & -\frac{4}{3} & \frac{8}{3} & -\frac{4}{3} & & & \\ \vdots & & \ddots & \ddots & & & \vdots \\ & & & \frac{7}{3} & -\frac{4}{3} & -\frac{1}{6} & 0 \\ & & & & -\frac{4}{3} & \frac{8}{3} & -\frac{4}{3} \\ & & \cdots & 0 & \frac{1}{6} & -\frac{4}{3} & \frac{7}{3} \end{bmatrix} \times$$

$$\begin{Bmatrix} d_1 \\ d_2 \\ \vdots \\ d_{2n_{el}} \\ d_{2n_{el+1}} \end{Bmatrix} = \langle C_2\ C_3 \cdots C_{2n_{el}}\ C_{2n_{el+1}} \rangle \left(\frac{fAh}{2} \begin{Bmatrix} \frac{4}{3} \\ \frac{2}{3} \\ \vdots \\ \frac{1}{3} \end{Bmatrix} + \begin{Bmatrix} 0 \\ 0 \\ \vdots \\ 0 \\ tA \end{Bmatrix} - \frac{2EA}{h^e} u_0 \begin{Bmatrix} -\frac{4}{3} \\ \frac{1}{6} \\ \vdots \\ 0 \\ 0 \end{Bmatrix} \right) \tag{2.46}$$

Thus, the bandwidth of the matrix K has increased compared to the linear basis function formulation. Moreover, now the mid-side nodes have greater contribution to forcing vector F.

FEM in 2- and 3-Dimensions

In two dimensions, the mapping from Ω^{ξ} to Ω^e is done using the following:

$$N^A = N^A(\xi, \eta) = \frac{1}{4}(1 + \xi\xi^A)(1 + \eta\eta^A) \tag{2.47}$$

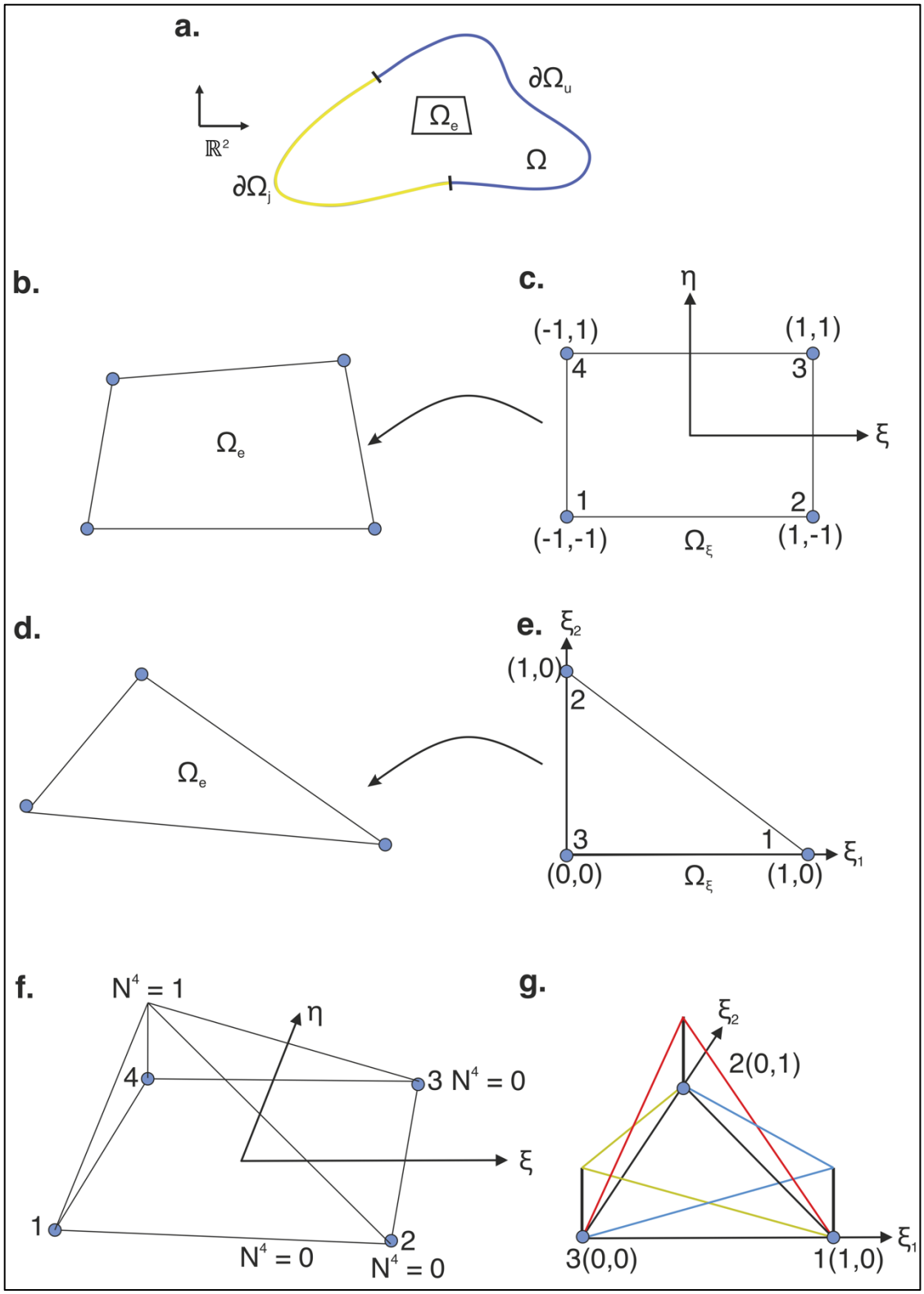

Figure 2.6: (a) Definition of a domain in 2D along with its boundaries. (b)-(c) Rectangular element and its corresponding bi-unit domain. (d)-(e) Triangular element and its corresponding bi-unit domain. (f)-(g) 3D representation of the 2D basis function.

$N^A(\xi,\eta)$ is called the tensor product function. The basis functions for a rectangular element (Figure 2.6c) are as follows

$$\begin{aligned} N^1(\xi,\eta) &= \frac{1}{4}(1-\xi)(1-\eta) \\ N^2(\xi,\eta) &= \frac{1}{4}(1+\xi)(1-\eta) \\ N^3(\xi,\eta) &= \frac{1}{4}(1+\xi)(1+\eta) \\ N^4(\xi,\eta) &= \frac{1}{4}(1-\xi)(1+\eta) \end{aligned} \tag{2.48}$$

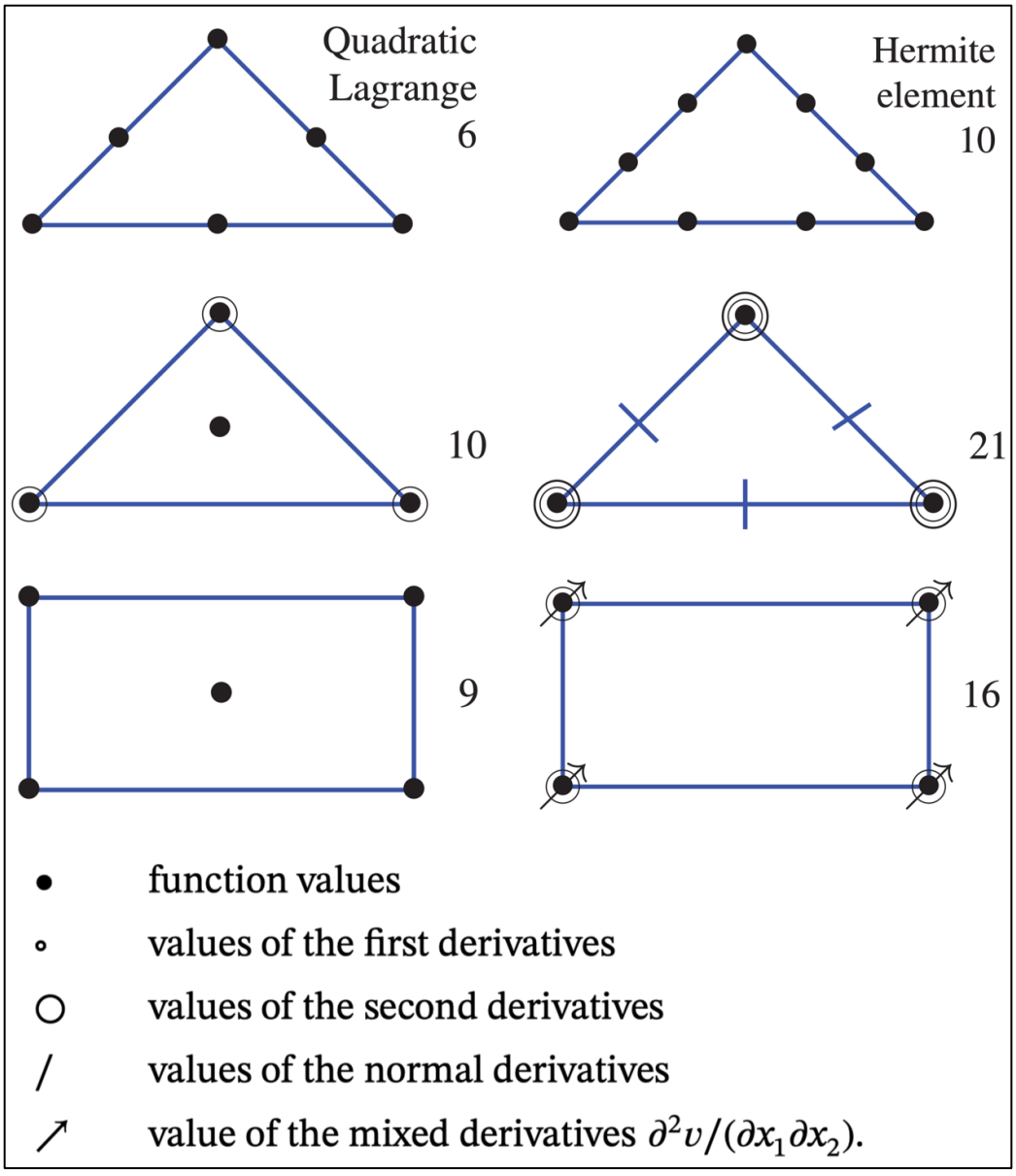

Figure 2.7: Commonly used elements in 2D

The function looks link a tent-like structure (Figure 2.6f) and follows the following properties

$$N^A(\xi^B, \eta^B) = \delta_{AB}$$

and

$$\sum_{A=1}^{N_{ne}} N^A(\xi, \eta) = 1 \tag{2.49}$$

We also often use simplex element so that space can be filled easily. In a 2D domain, the most common simplex element is the *triangular elements*. But here we use a *unit-domain* instead of a *bi-unit* domain (Figure 2.6e) and we intentionally chose a third dimension such that $\xi_3 = 1 - \xi_1 + \xi_2$ for the convenience of defining the elements as

$$\begin{aligned} N^1(\xi_1, \xi_2, \xi_3) &= \xi_1 \\ N^2(\xi_1, \xi_2, \xi_3) &= \xi_2 \\ N^3(\xi_1, \xi_2, \xi_3) &= \xi_3 \end{aligned} \tag{2.50}$$

Similarly we can define higher order linear element ($P_1, P_2, ...$) or quadratic elements ($Q_1, Q_2, ...$) as shown in Figure 2.7.

In a similar way, in 3D the mapping is done by

$$N^A = N^A(\xi, \eta, \zeta) = \frac{1}{4}(1 + \xi\xi^A)(1 + \eta\eta^A)(1 + \zeta\zeta^A) \tag{2.51}$$

The basis functions for a rectangular element (Figure 2.8c) are as follows

$$\begin{aligned} N^1(\xi, \eta, \zeta) &= \frac{1}{8}(1 - \xi)(1 - \eta)(1 - \zeta) \\ N^2(\xi, \eta, \zeta) &= \frac{1}{8}(1 + \xi)(1 - \eta)(1 - \zeta) \\ N^3(\xi, \eta, \zeta) &= \frac{1}{8}(1 + \xi)(1 + \eta)(1 - \zeta) \\ N^4(\xi, \eta, \zeta) &= \frac{1}{8}(1 - \xi)(1 + \eta)(1 - \zeta) \\ N^5(\xi, \eta, \zeta) &= \frac{1}{8}(1 - \xi)(1 - \eta)(1 + \zeta) \\ N^6(\xi, \eta, \zeta) &= \frac{1}{8}(1 + \xi)(1 - \eta)(1 + \zeta) \\ N^7(\xi, \eta, \zeta) &= \frac{1}{8}(1 + \xi)(1 + \eta)(1 + \zeta) \end{aligned} \tag{2.52}$$

$$N^8(\xi,\eta,\zeta) = \frac{1}{8}(1-\xi)(1+\eta)(1+\zeta)$$

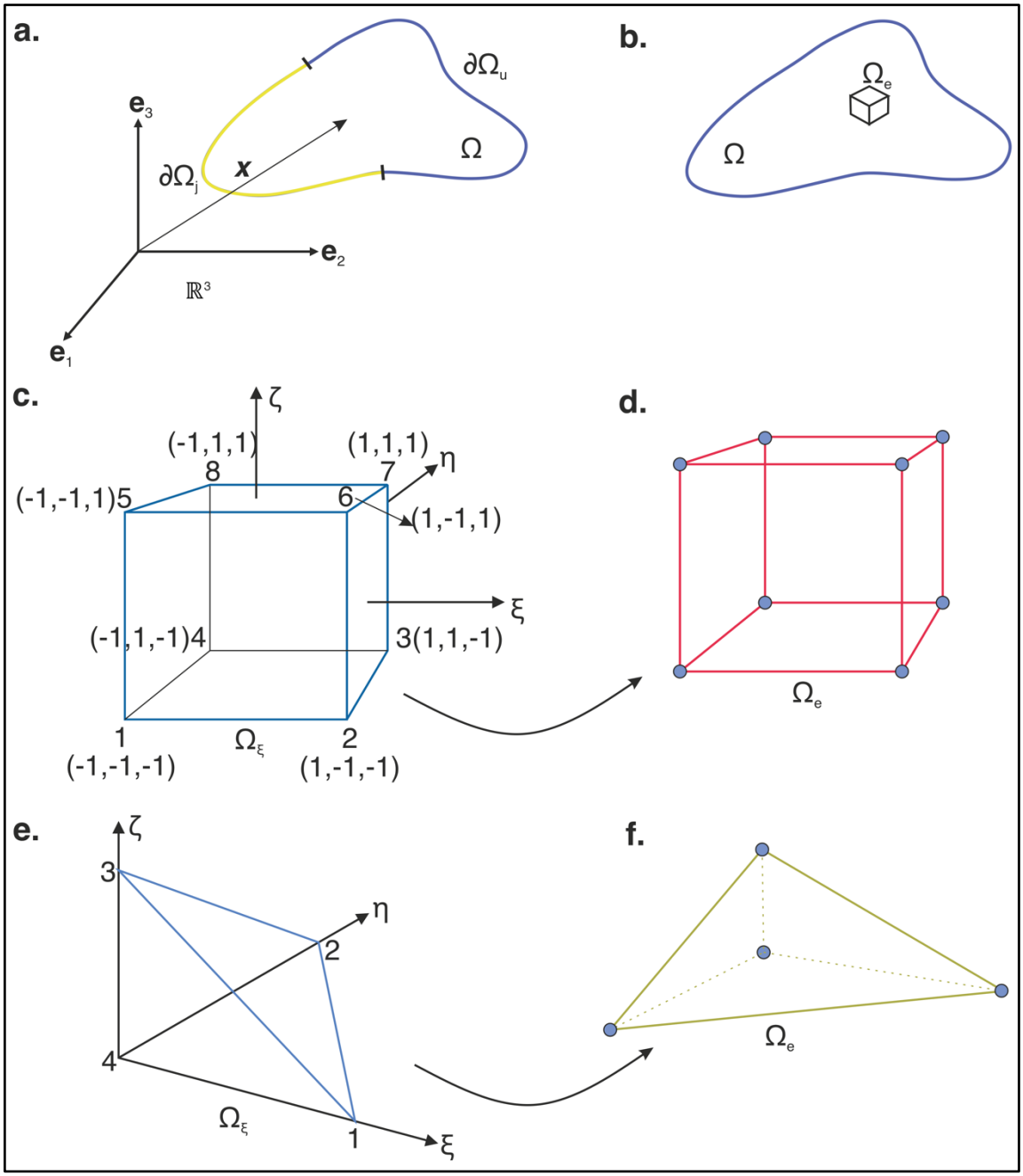

Figure 2.8: (a)-(b) Definition of a domain along with its boundaries in 3D space. (b)-(c) Rectangular element and its corresponding bi-unit domain. (d)-(e) Triangular element and its corresponding bi-unit domain. (f)-(g) 3D representation of the 2D basis function.

For filling space more efficiently in 3D we use tetrahedral elements (Figure 2.8d). Similar to the triangular elements in 2D, they are a mapping from a unit-domain and we define a fourth dimension such that $\xi_4 = 1 - \xi_1 + \xi_2 + \xi_3$ so that the elements are defined as

$$
\begin{aligned}
N^1(\xi_1, \xi_2, \xi_3, \xi_4) &= \xi_1 \\
N^2(\xi_1, \xi_2, \xi_3, \xi_4) &= \xi_2 \\
N^3(\xi_1, \xi_2, \xi_3, \xi_4) &= \xi_3 \\
N^3(\xi_1, \xi_2, \xi_3, \xi_4) &= \xi_4
\end{aligned}
\tag{2.53}
$$

Similarly we can define higher order linear element $(P_1, P_2, ...)$ or quadratic elements $(Q_1, Q_2, ...)$ as shown in Figure 2.9.

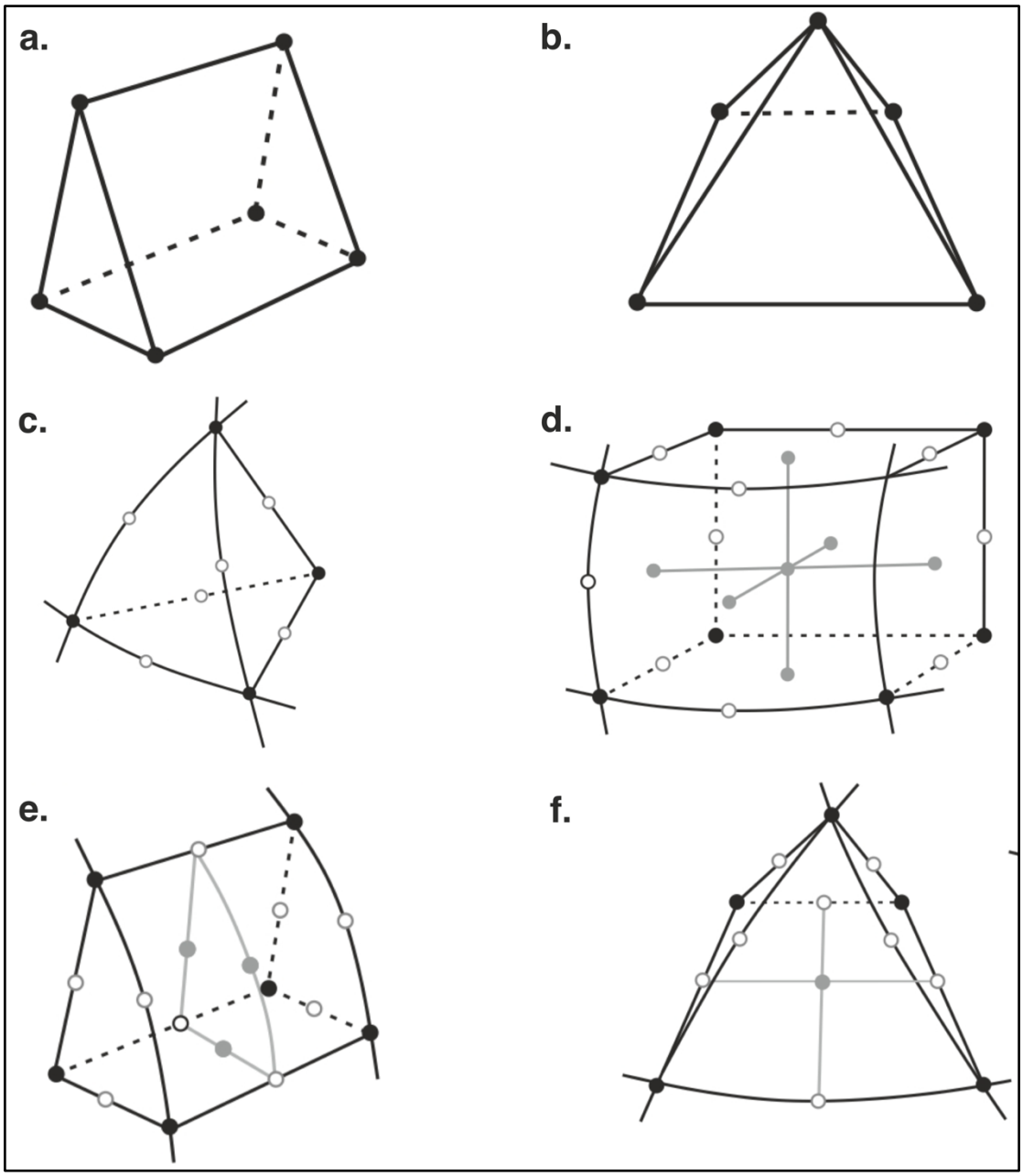

Figure 2.9: Commonly used elements in 3D

2.2.3 Norms and error estimation in FEM

Consider finite dimensional trial solution u^h along with quadratic basis function. By definition our finite element solution u_e^h is continuous over the domain Ω ($\mathcal{C}^0(\Omega)$) but, its derivatives $u_{,x}^h$, on the other hand, are only continuous within the elements but discontinuous at the boundary ($u_{,x}^h \in \mathcal{C}^0(\Omega)$ but $u_{,x}^h \notin \mathcal{C}^1(\Omega)$). It does however, belongs to H^1 space whose norm is given by

$$\|u\|_{H^1} := \left[\frac{1}{m(\Omega)^{1/n_{sd}}} \int_\Omega \left(u^2 + m(\Omega)^{2/n_{sd}} (u_{,x})^2\right) dx\right]^{1/2} \tag{2.54}$$

Where $m(\Omega)$ is the measure of Ω and n_{sd} is the number of special dimensions.
Similarly, we define the H^0 norm as

$$\|u\|_{H^0} := \left[\frac{1}{m(\Omega)^{1/n_{sd}}} \int_\Omega u^2 dx\right]^{1/2} \equiv \|u\|_{L^2} \tag{2.55}$$

From this we define the *energy norm* of u given by

$$\left[\int_\Omega u_{,x}\, E u_{,x}\, dx\right]^{1/2} \tag{2.56}$$

This gives the total strain energy of u in case of the elasticity problem. This is often denoted via the bilinear form notation, given by

$$a(u,u) = \int_\Omega u_{,x}\, E u_{,x}\, dx \tag{2.57}$$

The energy norm and the H^1 norms are equivalent, s.t.,

$$c_1 \|u\|_{H^1} \leq \left[\int_\Omega u_{,x}\, E u_{,x}\, dx\right]^{1/2} \leq c_2 \|u\|_{H^1} \tag{2.58}$$

with c_1 and c_2 being any arbitrary constants.
Using the bilinear form notation and inner product notation, the infinite and the finite dimensional weak form Eq. (2.14) and (2.18) can be written as

$$a(w,u) = (w,f) + (w,t)_L \qquad \forall\, w \in \mathcal{V} \tag{2.59}$$

and

$$a(w^h, u^h) = (w^h, f) + (w^h, t)_L \ldots\ldots \forall\, w^h(x) \in \mathcal{V}^h \subset \mathcal{V} \tag{2.60}$$

This implies that Eq. (2.77) also hold for $w^h(x) \in \mathcal{V}$. Thus, we have

$$a(w^h, u) = (w^h, f) + (w^h, t)_L \tag{2.61}$$

From Eq. (2.78) and Eq. (2.79) we get

$$a(w^h, u^h) - a(w^h, u) = 0 \tag{2.62}$$

Since a is bilinear, we have

$$a(w^h, u^h - u) = a(w^h, e) = 0 \tag{2.63}$$

where e is the error of the numerical method as u represents the exact solution. The above equation states that the projection of the error on the space $\mathcal{V}^h$ is zero, i.e., the error is orthogonal to $\mathcal{V}^h$.

The best approximation property

Let $u^h(x) \in \mathcal{S}^h$ be the finite element solution

$w^h(x) \in \mathcal{V}^h$ be a weighting function

$U^h(x) \in \mathcal{S}^h = \{U^h \in H^1(\Omega) | U^h(0) = u_0\}$

where $U^h = u^h + w^h$. Since w^h is zero at Dirichlet BC, U^h also satisfies that BC condition.

The theorem states that *the energy norm of the error is such that the energy will be minimum for* $U^h = u^h \in \mathcal{S}^h$ *than any other value of* $U^h(x) \in \mathcal{S}^h$. This is given by

$$a(e, e) \leq a(U^h - u, U^h - u) \tag{2.64}$$

Thus, FE solution minimizes the energy norm of $U^h - u^h$ over all the members of $U^h(x) \in \mathcal{S}^h$.

Sobolev estimates and Convergence of FEM

Following the previous section, consider U^h s.t. $U^h(x_A) = u^h(x_A) = d_A$; where A is the global degrees of freedom, x_A is the globally numbered node and d_A is the globally numbered trial solution. Also consider $\widetilde{U}^h$ s.t. $\widetilde{U}^h(x_A) = u(x_A) - \widetilde{U}^h(x)$ is nodally exact. Thus, we have $\widetilde{U}^h(x_A) = u(x_A)$ at the nodes, otherwise $\widetilde{U}^h$ is linear over an element (if we consider linear basis function). $\widetilde{U}^h$ is the *interpolate* of the exact solution. The *interpolate error estimate* in Sobolev space is given by

$$\left\|\tilde{U}^h - u\right\|_m \leq c(h^e)^\alpha \|u\|_r \tag{2.65}$$

where the left hand term represents the interpolation norm, c is any constant, h^e is the step size and the last term represents the H_r norm of u that is measure of the smoothness of u. α is an exponent that satisfies

$$\alpha = \min(k + 1 - m, r - m) \tag{2.66}$$

where k is the order of the polynomial of our basis. Eq. (2.84) states that if our solution is smooth such that we can take derivatives up to an high order r. Under these circumstances the exponent will be given by $\alpha = k + 1 - m$ and interpolation norm is thus given by

$$\left\|\tilde{U}^h - u\right\|_m \leq c(h^e)^{k+1-m} \|u\|_r \tag{2.67}$$

Hence the exponent is now primarily controlled by the order of the polynomial. Eq. (2.85) states that as $h^e \to 0$, we will also have $\left\|\tilde{U}^h - u\right\|_m \to 0$ at the rate $(k + 1 - m)$ provided $(k + 1 - m) > 0$. This implies that mesh refinement will cause interpolation error to become zero as long as $(k + 1 - m) > 0$ and the easiest way to achieve this is to increase the order of polynomial of the basis function. This is an inherent property of the Sobolev space.

Extending the equivalence of H^1 and energy norm Eq. (2.58) up to n −norm, we can write

$$\|e\|_n \leq \bar{c}(h^e)^\alpha \|u\|_r \tag{2.68}$$

and for smooth solution, we can write

$$\|e\|_n \leq \bar{c}(h^e)^{k+1-n} \|u\|_r \tag{2.69}$$

Considering $n = 1$, that corresponds to the H^1-norm of the error (where we look at the square integrated error and square integrated first derivative of the error), we have

$$\|e\|_1 \leq \bar{c}(h^e)^k \|u\|_r \tag{2.70}$$

Thus it converges at a rate of k. Hence, for higher order polynomial, the same norm of the the error will converge at a higher rate.

One special case is the H^1-norm (here we consider only the error) which is equivalent to the L_2-norm, and is thus given by

$$\|e\|_{L_2} \leq \bar{c}(h^e)^{k+1} \|u\|_r \tag{2.71}$$

The equation indicates that the error converges more rapidly.

2.3 Implementation of FEM in CFD code

The code used for the numerical simulations is primarily ASPECT, a massively parallel finite element code designed to model thermal convection in mantle. It consists of a small core which solves the basic fluid dynamics equations and for other tasks it relies on external libraries and plug-ins. The code is based on the DEAL.II software library, and assumes that, at a regional length scale and geological time scale, earth materials may be treated as highly viscous fluid with infinite Prandtl number and hence Stokes equations can be solved neglecting inertial forces. The code is based on state-of-the-art numerical method such as adaptive mesh refinement (AMR), accurate discretizations, efficient linear and iterative solvers and parallelization. The various components of ASPECT is shown in Figure 2.10.

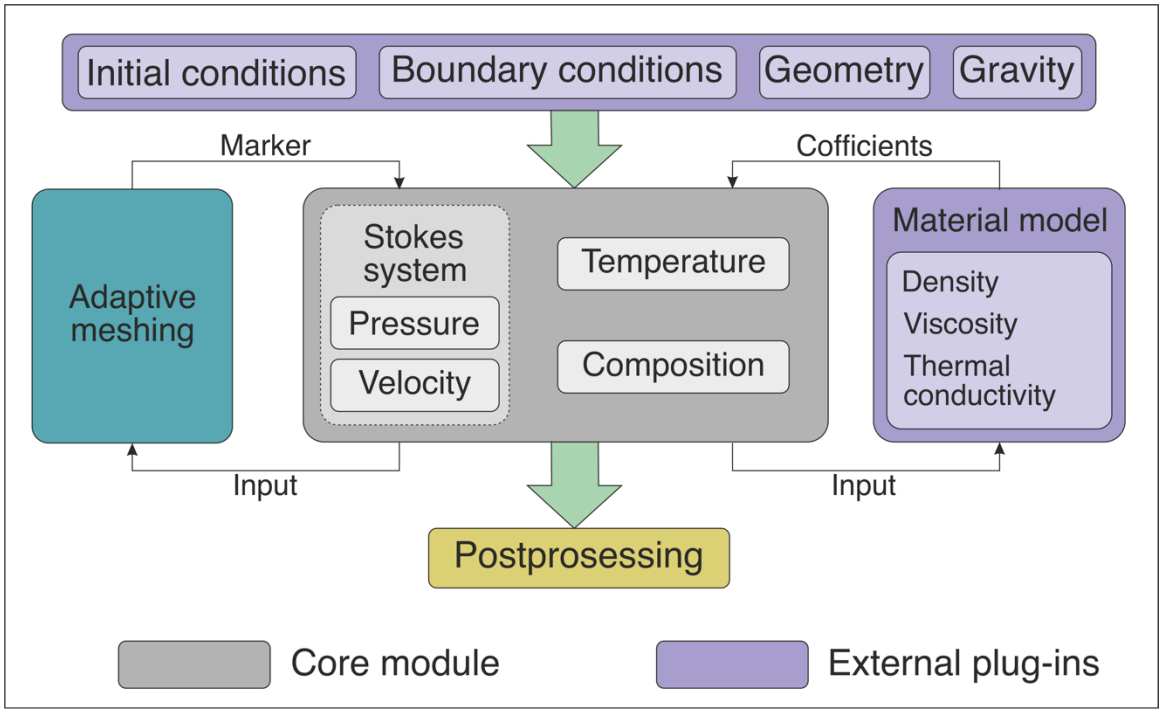

Figure 2.10: Various component of FEM code ASPECT.

2.3.1 Basic equations

Like other geodynamics codes ASPECT assumes that the solid Earth materials can be treated as a highly viscous fluid and solves a system of equations driven by differences in the gravitational force due to a density that depends on the temperature. Specifically, it considers the conservation of momentum, mass and energy

$$-\nabla.\left(2\mu_{eff}\dot{\epsilon}(\boldsymbol{u})\right)+\nabla P=\rho\boldsymbol{g} \tag{2.72}$$

$$\nabla.\boldsymbol{u}=0 \tag{2.73}$$

$$\begin{aligned}\rho C_P\left(\frac{\partial T}{\partial t}+\boldsymbol{u}.\nabla T\right)-\nabla.(k+\upsilon_h(T))\nabla T\\ =\rho H_r+2\mu_{eff}\left(\dot{\epsilon}(\boldsymbol{u}):\dot{\epsilon}(\boldsymbol{u})\right)+\alpha T(\boldsymbol{u}.\nabla P)\\ +\rho T\Delta S\left(\frac{\partial X}{\partial t}+\boldsymbol{u}.\nabla X\right)\end{aligned} \tag{2.74}$$

where μ_{eff} is the effective viscosity, $\dot{\epsilon}$ is the strain rate tensor, $\boldsymbol{u}$ is the velocity vector, ρ is the density and $\boldsymbol{g}$ is the gravity vector. Materials the assumed incompressible leading to zero divergence of the velocity vector $\boldsymbol{u}$. C_P is the heat capacity, T is temperature, k is thermal conductivity and H_r is the internal radiogenic heat production. υ_h is the artificial diffusivity that prevents the oscillations due to advection of the temperature field calculated following entropy viscosity method. The right-hand side terms of this equation correspond to internal heat production for example due to radioactive decay, friction heating, adiabatic compression of material and latent heat due to phase change. To account for the advection of material properties, ASPECT relies on compositional fields that are advected with the flow. Hence the system of equation is closed by solving for a conservation equation for each compositional field as:

$$\frac{\partial c_i}{\partial t}+\boldsymbol{u}.\nabla c_i-\nabla.\left(\upsilon_h(c_i)\right)\nabla c_i=0 \tag{2.75}$$

where c_i is the i^{th} compositional field. Artificial viscosity is again introduced to stabilize advection.

2.3.2 Time discretization

The size of the chosen timestep is important in numerical geodynamics as when the timesteps are large, the solver may not be able to find a good solution, whereas if the timesteps are too small, a lot of computational time will be needed to obtain the desired result. To solve this problem the Courant-Friedrich-Lewy (CFL) condition is introduced. The time step k is chosen according to

$$k = c \min_K \frac{h_K}{\|u\|_{\infty,KpT}} \tag{2.76}$$

where h_K is the diameter of cell K, and the denominator is the maximal magnitude of the velocity on cell K times the polynomial degree pT of the temperature discretization. The dimensionless constant c is called the CFL number in this program.

2.3.3 Solving the equations

In FEM the discretized basis equations are written in a matrix-vector form. The set of linear equations in its simplest form looks like

$$\boldsymbol{Ax} = \boldsymbol{b} \tag{2.77}$$

Where $\boldsymbol{A}$ is a $n \times n$ matrix, and $\boldsymbol{x}$ and $\boldsymbol{b}$ are vectors of length n, where n is the number of unknowns. Vector $\boldsymbol{b}$ contains the boundary conditions and buoyancy forces. Vector $\boldsymbol{x}$ contains the unknowns of the system to be solved, such as velocity, pressure temperature. Here we used an iterative solver to solve our basic matrix-vector equation. Although it doesn't solve the equation immediately, it requires much less memory than a direct solver and hence computationally much less expensive. Iterative solvers use the previous solution of vector $\boldsymbol{x}$ as a starting condition to solve the system of equations again. ASPECT calculates the linear residual vector $\boldsymbol{r}$ of the system (the *inner iteration*) defined by

$$\boldsymbol{r} = \boldsymbol{Ax} - \boldsymbol{b} \tag{2.78}$$

for each iteration and when the L_2 norm of vector $\boldsymbol{r}$ is smaller than a user defined tolerance, the system is seen as solved. Then it moves from *inner iteration* to the *outer iteration*. Within *outer iteration*, first the strain-rate is recomputed and based on the strain-rate, the viscosity is recomputed. If the relative residual is not smaller than a user defined value, given by

$$\frac{\|R_n\|_2}{\|R_0\|_2} < \Theta \tag{2.79}$$

matrix A is updated as it is dependent on strain-rate and viscosity. With this new $\boldsymbol{A}$, the system is solved again. When the nonlinear iterations have converged, the velocity field is used for advection of the material. The complete algorithm is shown in Figure 2.11.

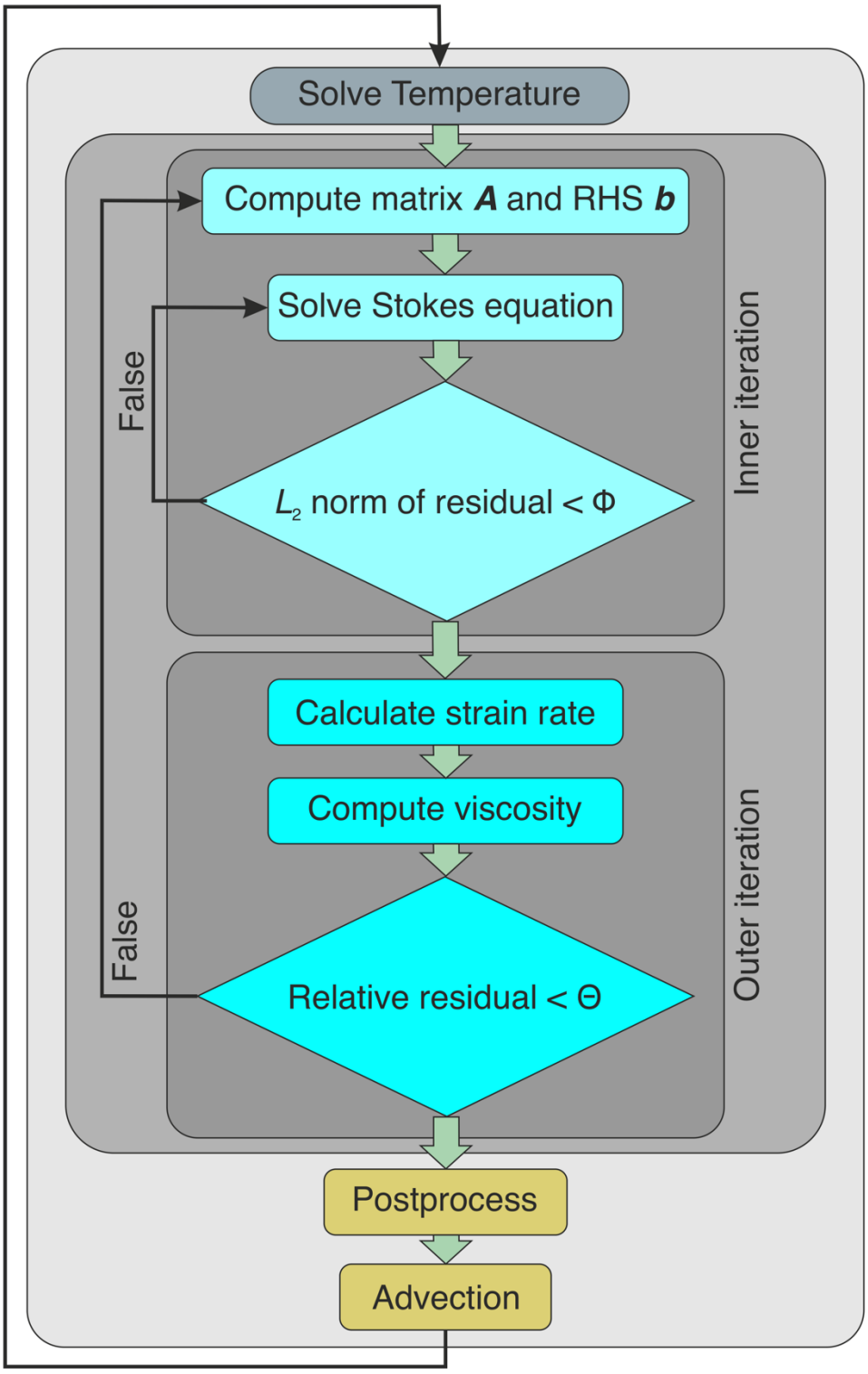

Figure 2.11: A simplified algorithm for each time step in ASPECT.

2.3.4 Rheology

In ASPECT, the material properties are implemented within the *Material model* module which adapts a visco-plastic rheology. The model threats the material as incompressible, which primarily follow the diffusion-dislocation and Drucker-Prager criterion often combined into more complex rheologies.

At higher temperature, materials experience nonlinear viscous deformation either via power-law *dislocation creep* or grain boundary (or bulk) *diffusion creep*. These two rheologies can be expressed by strain rate and temperature dependent viscosity as

$$\mu_{eff}^{vis} = \frac{1}{2} A^{-1/n} d^{m/n} \dot{\epsilon}_{ii}^{(1-n)/n} \exp\left(\frac{E + PV}{nRT}\right) \tag{2.80}$$

where A is the prefactor, n is the stress exponent, $\dot{\epsilon}_{ii} = \sqrt{\frac{1}{2}\dot{\epsilon}'_{ij}\dot{\epsilon}'_{ij}}$ is the effective deviatoric strain rate, which is the square root of second invariant of deviatoric strain rate tensor, d is the grain size, m is the grain size exponent, E is the activation energy, V is the activation volume and R is the gas constant. In case diffusion creep (μ_{eff}^{df}), $n = 1$ and $m > 0$, while for dislocation creep (μ_{eff}^{dl}) $n > 1$ and $m = 0$.

At relatively low temperature the material behavior is modelled using plastic rheology. The effective viscosity is locally adapted in such a way that the stress generated during deformation does not exceed the yield stress (viscosity rescaling method). The effective plastic viscosity is given by

$$\mu_{eff}^{pl} = \frac{\sigma_y}{2\dot{\epsilon}_{ii}} \tag{2.81}$$

where σ_y is the yield stress. Here plasticity limits viscous stress via Drucker-Prager yield criterion given by:

$$\sigma_y = Ccos(\varphi) + Psin(\varphi) \tag{2.82}$$

where C is the cohesion and φ is the friction angle. This 2D form of the equation is equivalent to Mohr Coulomb yield surface and for $\varphi = 0$, the yield stress is fixed and equal to cohesion (Von Mises yield criterion).

In nature, under same deviatoric stress, both viscous creeps act simultaneously. Hence, we consider composite viscous rheology by harmonically averaging μ_{eff}^{dl} and μ_{eff}^{df}

$$\mu_{eff}^{cp} = \frac{\mu_{eff}^{df}\mu_{eff}^{dl}}{\mu_{eff}^{df} + \mu_{eff}^{dl}} \tag{2.83}$$

Moreover, the model assumes that the viscous creep and plastic yielding are independent process that can occur simultaneously and the mechanism resulting in the lowest effective viscoplastic stress is favoured

$$\mu_{eff}^{vp} = \min\left(\mu_{eff}^{pl}, \mu_{eff}^{cp}\right) \tag{2.84}$$

Strain weakening is included in the system by calculating the finite strain invariant through compositional fields within the material model and linearly reducing the cohesion and internal friction angle as a function of the finite strain magnitude. While calculating finite strain invariant (e_{ii}), a single composition field tracks the value of finite strain invariant via

$$e_{ii}^{t} = e_{ii}^{(t-1)} + \dot{e}_{ii}dt \tag{2.85}$$

where t and $t-1$ are current and prior time steps, $\dot{e}_{ii}$ is the second invariant of strain rate tensor and *dt* is the time step size. When the accumulated strain is less than a given value, C and φ are constant. For accumulated strain values greater than this threshold, C and φ decrease linearly until the system attains a certain maxima of accumulated strain, after which they are kept constant again.

2.3.5 Free surface calculations

The upper surface is considered as free surface in order to observe the change in elevation with time. For this we require zero stress on this surface. Since there will be flow across the surface we also need to have a dynamically deformable mesh. To handle the motion of the mesh with a free surface ASPECT incorporates the arbitrary Lagrangian-Eulerian (ALE) implementation. The ALE approach allows the mesh motion $\boldsymbol{u_m}$ to be largely independent of the fluid. The mass conservation condition requires that $\boldsymbol{u_m} \cdot \boldsymbol{n} = \boldsymbol{u} \cdot \boldsymbol{n}$ on the free surface, but otherwise the mesh motion is unconstrained, and should be chosen to keep the mesh as well behaved as possible. The mesh velocity is calculated by using a Laplacian scheme given by

$$\begin{aligned} -\Delta \boldsymbol{u}_m &= 0 && \text{in } \Omega, \\ -\Delta \boldsymbol{u}_m &= (\boldsymbol{u}.\mathbf{n})\mathbf{n} && \text{on } \partial\Omega_{\text{free surface}}, \end{aligned} \tag{2.86}$$

$$\boldsymbol{u}_m . \mathbf{n} = 0 \qquad \text{on } \partial\Omega_{\text{free slip}},$$

$$\boldsymbol{u}_m = 0 \qquad \text{on } \partial\Omega_{\text{Dirichlet}}.$$

After calculating mesh velocity, mesh vertices are time-stepped explicitly for minimally distorting perturbation to the mesh. To further stabilize the free surface, a quasi-implicit free surface integration scheme is incorporated.

2.4 Scaled laboratory experiments

Using this experimental approach, the present thesis investigates geodynamic processes using simplified geometries, rheologies and boundary conditions. This is adopted mainly to overcome the inherent observational limitation of geologic processes where spatial and temporal scales are enormously large. This experimental approach allows one to systematically investigate and quantify the influence of a particular physical parameter on a particular geodynamic process on short time (seconds to hours) and length scales (millimetres to metres). In contrast to field studies that mostly deal with the final products, analogue models allow us to visualize the progressive development of a specific geological process, giving us a complete evolutionary picture of the process. Furthermore, when an analogue model is properly scaled to nature the experimental results can be directly applied to the natural prototype, providing useful insights into the natural processes/system.

Analogue models have a long history and it first started in studying geological process some 200 years ago with James Hall's experiments (Hall, 1815), who developed models to investigate folding in sedimentary rock layers. During 1900s analogue modelling properly flourished with advanced laboratory facilities. Some pioneering work on the subject of analogue modelling on various geodynamic processes are as follows:

- Salt dome formation (Escher and Kuenen, 1929; Link, 1930; Parker and McDowel, 1955),
- Folding (Kuenen and Sitter, 1938; Mead, 1920),
- Faulting (Hubbert, 1951),
- Fracturing (Cloos, 1955),
- Mantle flow (Griggs, 1939),
- Orogeny (Griggs, 1939; Kuenen, 1936),
- Boudinage (Ramberg, 1955),
- Plume formation (Whitehead and Luther, 1975),

- Subduction (Jacoby, 1976),
- Lithospheric rifting (Benes and Davy, 1996; Shemenda and Grocholsky, 1994),
- Collision-indenter tectonics (Tapponnier et al., 1982).

Another major change that came during the 1900s is the approach of the experiments. With the introduction of model scaling, analogue experiments became more quantitative . The scaling theory requires geometric, kinematic and dynamic similarity between analogue model and natural prototype. It allows the experimenter to scale quantitative model results such as lengths, geometries, velocities, forces, stresses and strains to values in nature, allowing for a quantitative and deeper understanding of the geological phenomenon or geodynamic process under investigation. This theory is primarily developed by Hubbert, (1937) and later advanced by various authors on varies geoscience disciplines:

- Hubbert, (1951) developed scaling for normal and reverse faulting;
- Ramberg, (1981, 1968) advanced it to properly scale the effect of gravity for varies geologic phenomena such as salt tectonics, plume formation, folding and boudinage;
- Weijermars and Schmeling, (1986) advanced it for rock flow due to gravity;
- Ribe and Davaille, (2013) advanced it for mantle convection.

2.4.1 Approach for scale modelling

Depending on the imposed deformation, scale modelling can be of two types:

- Closed scale model: where the deformation is driven *internally* and
- Open scale model: where the deformation is driven either *externally* or both internally and externally.

i) **Closed scale model:** These models are governed by the internal buoyancy present within the experimental set-up itself and the deformations are thus internally driven. Here, the experimenter only imposes the initial conditions at $t = 0$ and the model evolution is driven by internal forces rather than the boundary conditions. They are also referred to as self-consistent model, fully dynamic model or buoyancy-driven model. Since, no materials are externally introduced and no external forces such as velocity or temperature are imposed into the setup, the system is fully closed and mass and energy are always conserved in these experiments. Examples are plume and salt dome modelling through mechanical buoyancy

driven Rayleigh-Taylor instabilities, plume-lithosphere interaction modelling, buoyancy-driven subduction modelling, gravitational collapse/spreading models etc.

ii) **Open scale model:** In these models the deformation is either externally applied forces or a combination of external and internal forces. For purely external models, we need to impose the initial condition at $t = 0$ as well as the boundary conditions for $t \geq 0$. Since energy is continuously added to the system, we consider it as open. Commonly used external approaches are:

1. **kinematic external approach.** the main imposed condition is the velocity boundary condition with negligible influence of the buoyancy forces. Common example are the sand-box experiments for thrust wedging, externally driven subduction experiments, lithosphere extension experiments and shear zone experiments and boudinage formation.
2. **external thermal approach.** Thermal boundary conditions (generally vertical) are imposed in one of the boundaries to create a density and/ or viscosity gradient in the system which eventually drives the experiment. Examples include mantle convection experiments and thermal plume experiments.
3. **mass influx approach.** Materials are externally applied to the experimental domain which eventually drives the deformation. Examples are magma intrusion and dike formation experiments.

Different combination of the aforementioned three approaches also exists.

In case of combined approach both buoyancy force and externally driven boundary condition are important. These are thus commonly referred to as externally + internally-driven model. The most common external boundary condition is the combination of applied velocity and mass influx. Examples include salt dome experiments with external loading, externally controlled plume injection experiments and experiments on thermochemical plumes and convection.

2.4.2 General principle of model scaling

Model scaling provides an objective criterion that enables one to determine the correct properties of a model, provided the properties of the natural system are known. The main focus for performing such scaling is not to mimic the nature rather to explore specific

aspects a problem in a systematic manner under controlled environment and then compare it to nature

It is quite obvious that when the size of a body decreases, various of physical properties change accordingly. But these physical properties does not, in general, change proportionally with size. We need scaling to investigate how various physical properties of the body change as its size is changed. The first well-posed theory of scaling was derived by Hubbert (1937) that we can apply to various geologic and geodynamic scenario. He showed that for a model to be properly scaled, there are three similarity criterion that needs to be fulfilled: geometric similarity, kinematic similarity and dynamic similarity.

Geometrical Similarity states that the model and the natural prototype are said to be geometrically similar when all corresponding lengths are proportional and all corresponding angles of the two bodies are equal. This is given by

$$\frac{l_x^p}{l_x^m} = \frac{l_y^p}{l_y^m} = \frac{l_z^p}{l_z^m} = \lambda_g \tag{2.87}$$

$$\frac{\alpha_x^p}{\alpha_x^m} = \frac{\alpha_y^p}{\alpha_y^m} = \frac{\alpha_z^p}{\alpha_z^m} = 1 \tag{2.88}$$

where l is the length dimension, α is the angle, the subscripts x, y, z represents various directions, the superscripts p and m represents natural prototype and model, respectively, and lastly λ_g is the constant of proportionality known as *geometric scaling factor*. Similarly, two geometrically similar objects should have the following relationship in terms of their area

$$\frac{A^p}{A^m} = \left(\frac{l^p}{l^m}\right)^2 = \lambda_g^2 \tag{2.89}$$

and volume

$$\frac{V^p}{V^m} = \left(\frac{l^p}{l^m}\right)^3 = \lambda_g^3 \tag{2.90}$$

For kinematic similarity, the required time for a geometrically similar model to undergo any change in shape or position should be proportional to that required for the corresponding change in the natural prototype. This is given by

$$\frac{t^p}{t^m} = \tau_k \tag{2.91}$$

where t is time and τ_k is the *kinematic scaling factor*. Kinematic similarity also demands that the velocities and accelerations of the model and the prototype must also be proportional.

$$\frac{v^p}{v^m} = \frac{\frac{l^p}{t^p}}{\frac{l^m}{t^m}} = \lambda_g \tau_k^{-1} \tag{2.92}$$

and

$$\frac{a^p}{a^m} = \frac{\frac{l^p}{(t^p)^2}}{\frac{l^m}{(t^m)^2}} = \lambda_g \tau_k^{-2} \tag{2.93}$$

Dynamic similarity states that the masses of the model and the forces acting upon the model must be, point by point, proportional to the corresponding masses and the forces acting on the natural prototype. Moreover, the direction of the forces must be the same. The first portion of the statement demands

$$\frac{dm^p}{dm^m} = \mu_d \tag{2.94}$$

where dm is the mass of a small volume dV and μ_d being the scaling ratio of mass. The ratio of density can thus be obtained as

$$\frac{\rho^p}{\rho^m} = \delta = \mu_d \lambda_g^{-3} \tag{2.95}$$

The last part of the can be expressed as

$$\frac{F^p}{F^m} = \phi \tag{2.96}$$

where F is the force acting on the body and ϕ is the scaling ratio for force. Now to properly scale the model, we need to consider both the body forces and the surface forces acting on the system. This can be done by either scaling the density or the density contrast. Dynamic similarity also requires scaling of rheology to properly scale the resistive forces. To scale forces using density, we use Cauchy's equation of motion, which states

$$\rho \frac{Dx_i}{Dt^2} = \frac{\partial \sigma_{ij}}{\partial x_j} + \rho g_i \tag{2.97}$$

where ρ is the density, x is the position vector, t is the time, σ_{ij} is Cauchy's stress tensor. Neglecting inertial terms and integrating leads to

$$\sigma_{ij} = -\rho g_i x_j \tag{2.98}$$

Representing it as ratio of prototype and model will lead to

$$\frac{\sigma_{ij}^p}{\sigma_{ij}^m} = \frac{\rho^p l^p}{\rho^m l^m} = \sigma_d = \mu_d \lambda_g^{-2} \tag{2.99}$$

where σ_d is the scaling ratio for stress. Here we have considered normal field of gravity i.e., it is same for both the natural prototype and the model. Writing Eq. (2.99) in terms of force, we have

$$\frac{F^p}{F^m} = \frac{\rho^p (l^p)^3}{\rho^m (l^m)^3} = \phi = \mu_d \tag{2.100}$$

Thus, when scaling experiments for densities, forces scale with the product of density and the cube of length.

Similarly, it can be shown that scaling with density contrast will lead to

$$\frac{\Delta\rho^p (l^p)^2 g^p}{\eta^p v^p} = \frac{\Delta\rho^m (l^m)^2 g^m}{\eta^m v^m} \tag{2.101}$$

Here, we can use Stokes' settling law at low Reynolds number. Again considering normal field of gravity, we can scale viscosity using the following relationship

$$\frac{\eta^p}{\eta^m} = \frac{\Delta\rho^p l^p t^p}{\Delta\rho^m l^m t^m} = \mu_d \lambda_g^{-2} \tau_k \tag{2.102}$$

where velocity appears as length over time. From Eq. (2.102), the scaling of stress follows

$$\frac{\sigma_{ij}^p}{\sigma_{ij}^m} = \frac{\Delta\rho^p l^p}{\Delta\rho^m l^m} = \mu_d \lambda_g^{-2} \tag{2.103}$$

Similarly, Force can then be scaled as

$$\frac{F^p}{F^m} = \frac{\Delta\rho^p (l^p)^3}{\Delta\rho^m (l^m)^3} = \phi = \mu_d \tag{2.104}$$

Thus, in case one scales experiments for density contrasts, forces scale with the product of density contrast and the cube of length.

Finally, using Eq. (2.101) we can also scale velocity as

$$\frac{v^p}{v^m} = \frac{\Delta\rho^p (l^p)^2 \eta^m}{\Delta\rho^m (l^m)^2 \eta^p} = \lambda_g \tau_k^{-1} \tag{2.105}$$

The methods for model scaling described here are used extensively throughout this thesis. Details of each application is provided in the respective chapters.

Chapter 3

Dynamics of cold plumes in subduction zones

3.1 Introduction

Understanding the underlying mechanisms of subduction-driven arc volcanism has recently set a new milestone in geodynamic modeling with a multidisciplinary approach (Ito and Stern, 1986; Grove et al., 2012; Perrin et al., 2018). Natural subduction zones show broadly two types of volcano distributions. One is characterized by approximately regularly spaced volcanoes along a trench parallel linear zone (called *linear distribution* pattern hereafter), such as the Sumatra and the Caribbean subduction zones. The other is characterized by sporadic distribution of arc volcanoes both parallel and perpendicular to the trench (called *areal distribution* pattern), such as the Mexican and the South American subduction zones. The linear distribution pattern forms a laterally persistent narrow belt (~10 km wide; Marsh, 1979), also referred to as volcanic front, located at a specific horizontal distance perpendicular to the trench line, corresponding to a vertical depth of ~ 110 km to the dipping slab boundary (Syracuse and Abers, 2006). A volcanic front displays a regular spacing (30 to 70 km) of the volcanic centers arranged parallel to the trench (Andikagumi et al., 2020; Drake, 1976; Marsh and Carmichael, 1974; Tamura et al., 2002; Vogt, 1974). Despite remarkable progress in subduction zone modeling in recent years (Horiuchi and Iwamori, 2016; Wang et al., 2019; Wilson et al., 2014), the variables that control the locations of arc volcanoes and their spatio-temporal distributions in the overriding plate remain a challenging topic of research in the subduction geodynamics community (Grove et al., 2009; 2012).

It is now widely accepted that dehydration slab melting is the key process to drive arc volcanisms in subduction zones. Subducting slabs undergo dehydration reactions, releasing fluids into the hot mantle wedge (Figure 3.1), which in turn causes partial melting by lowering the solidus temperature of rocks in the overlying mantle wedge (Arcay et al., 2005; Davies and Stevenson, 1992; Fumagalli and Poli, 2005; Grove and Till, 2019; Tatsumi, 1989). Stability field of chlorite, which can accommodate as much as ~13 wt% H_2O in its structure, has been used to predict the depth of such dehydration melting in the peridotitic mantle wedge (Till et al., 2012; Zheng et al., 2016). Fertile peridotite with high

Al_2O_3 content can host 6 to 7 wt% chlorite that equates to 2 wt% bulk H_2O at the *P-T* condition of the vapor-saturated peridotite solidus. Petrological calculations suggest chlorite breaks down at depths, corresponding to pressures and temperatures of 2 to 3.6 GPa and 800 to 860°C, respectively, implying that dehydration melting occurs on the upper slab surface beginning at a depth of 70 km and extending to a depth of 200 km (Bose and Ganguly, 1995; Grove et al., 2009; Grove and Till, 2019; Iwamori, 1998). A number of previous studies have shown that partially molten zones formed by dehydration melting can be 2 to 20 km thick, depending upon the thermal structure of the subduction zone, and the depth and the degree of dehydration melting above the dipping slab (Marsh 1979, Gerya and Yuen 2003, Grove et al., 2006, 2009). In some cases, they may incorporate materials derived from serpentinized subduction channel and subducted crustal sediments, as reported from the recycled sediment signatures in arc volcanoes (Marschall and Schumacher, 2012; Zhang et al., 2020).

The extent and minimum depth of dehydration melting in the wedge above the subducting slabs, the mantle wedge temperature, and the presence of some preexisting regional flaws in the overriding plate have been proposed as the crucial factors to ultimately determine the spatio-temporal distributions of arc volcanoes in the overriding plate. For example, England and Katz (2010) showed the location of volcanic front above the slab at the point where the anhydrous peridotite solidus is closest to the trench. Alternatively, Grove et al. (2009) estimated volcano locations as a function of the depth of aqueous fluids released from the subducting plate, the mantle wedge temperature above the region of fluid release, and plate tectonic variables, such as subduction velocity and slab dip. Furthermore, the regular distribution of volcanic centers along the volcanic front line is attributed to various factors, such as regional fracture distribution (Pacey et al., 2013), depth of the magma source (Lingenfelter and Schubert, 1974; Perrin et al., 2018), slab thickness (Marsh, 1975), and heterogeneous melting of the mantle wedge (Yoo and Lee, 2020). Although regional fractures can cause segmentation of the volcanic-arc front, there is no spatial correlation between the fracture zones and volcano distribution within an arc segment (Marsh, 1979; Pacey et al., 2013). Several studies, on the other hand, indicate that such regular spacing can be more readily conceived as a result of Rayleigh-Taylor instability (RTI), where the characteristic wavelength of instabilities determines the spacing (Marsh and Carmichael, 1974; Fedotov, 1975; Morishige, 2015).

A line of studies has focused on the transport mechanism of partially molten materials in the mantle wedge to investigate the processes of arc-volcanisms, including their spatio-

temporal patterns (Aharonov et al., 1995; Pec et al., 2017; Spiegelman et al., 2001; Weatherley and Katz, 2012). However, a number of key questions, especially on the melt transport mechanisms are yet to be resolved. For example, there is still debate on whether partial melts ascend by forming porosity channels, as observed beneath mid-ocean ridges (Liang et al., 2010; Mandal et al., 2018), and if so, what can be their pathways patterns, or are channels formed by fracturing of the mantle rocks? Several recent studies suggest cold plume formation as a potential mechanism for the upward advection of partially molten materials in the mantle wedge (Gerya and Yuen, 2003; Zhu et al., 2009; Codillo et al., 2018). These materials are less dense than the overburden, and resulting density inversion triggers RTIs, leading to the formation of cold plumes (Figure 3.1).

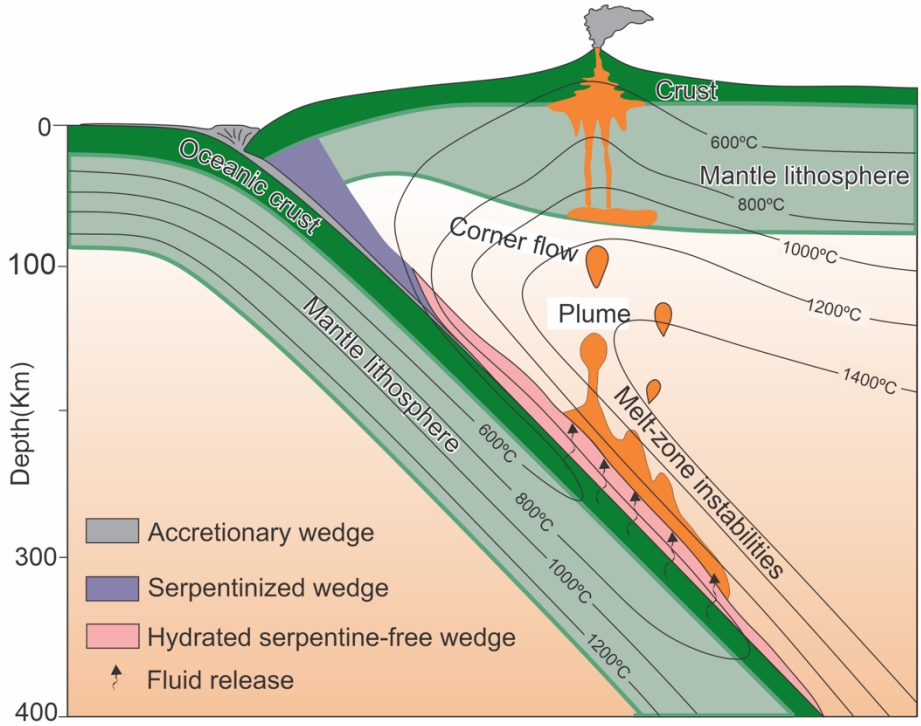

Figure 3.1: 2-D cartoon presentation of cold plume formation from a partially molten layer above the dipping slab in a subduction setting.

Geophysical studies of subduction zone magmatism (Tamura et al., 2002; Zhao et al., 2009) point to the fact that the cold-plume driven magmatism in subduction zones is essentially a three-dimensional (3-D) phenomenon, where both trench parallel and trench perpendicular plume dynamics need to be accounted for to comprehensively model the partial melt generation and migration. Zhu et al., (2009) have shown from petrological-thermomechanical modeling that slab dehydration initiates small-scale convection to produce numerous cold plumes in the mantle wedge. Based on their simulations, they

recognized three types of plumes: 1) closely spaced finger-like plumes, arranged parallel to the trench, 2) ridge-like plumes perpendicular to the trench, and 3) flattened wave-like instabilities parallel to the trench. The viscosity of partially molten zones is found to be the principal factor that controls the type of plume in Zhu et al's models. The low-viscosity models (10^{18}–10^{19} Pa s) develop finger-like plumes with a spacing of 30–45 km. The spacing jumps to 70-100 km, and the cold plumes attain sheet-like structures as the viscosity increases by two orders of magnitude (10^{20}–10^{21} Pa s).

Despite significant progress in modeling subduction related cold plumes, there is a lack of systematic investigation to address how far the slab dip might control the flow dynamics in partially molten zones to regulate volcano distribution in the overriding plate. Our present study aims to meet this gap. We investigate the evolution of cold plumes in the framework of 3D RTIs to explore the origin of the two principal types: linear and areal distributions of arc volcanoes described above. We address the following questions: 1) how does slab dip (α) influence the development of RTIs and thereby determine the modes of plume growth, and 2) what is the consequence in the spatial and temporal distributions of arc volcanoes? We use scaled laboratory experiments to demonstrate the effects of α, and support the experimental findings with 2D and 3D computational fluid dynamics (CFD) simulations. Volcano distributions from the South American (the Andes) (Ramos and Folguera, 2009), the Central American (Mexico) (Stubailo et al., 2012), and the Sumatra-Java subduction system are used to discuss the relevance of our model results. Several studies have reported kiloyear scale frequency in the arc volcanisms, irrespective of their spatial distribution (Kutterolf et al., 2013; Schindlbeck et al., 2018). This study such episodic eruptions are a consequence of the pulsating ascent behaviour of cold plumes.

3.2 Laboratory modeling

3.2.1 Experimental setup

Scaled laboratory models were developed using two immiscible fluids of contrasting densities ($\rho = \rho_o/\rho_s$) and viscosities ($R = \mu_o/\mu_s$), subscripts o and s refer to the overburden and source layer which represent mantle wedge and partially molten zone, respectively. The density and viscosity ratios are limited in our laboratory experiments by the availability of suitable materials. Two series of laboratory experiments were performed with $R < 1$ and $R > 1$, where the first series had $\rho = 1.03$ and $R = 10^{-5}$ while the second series had $\rho = 1.13$ and $R = 25$. All the parameters used in the experiments are summarized in

Table 3.1. For models with $R = 10^{-5}$ (called $R < 1$ type model), I used Polydimethylsiloxane (PDMS) (ρ_s = 965 kg/m^3, $\mu_s = 10^2$ Pa s), which agrees with the scaled down viscosity (in the order of 10^2 Pa s) of natural partially molten zones (~10^{18} Pa s). Water (ρ_o = 998 kg/m^3, $\mu_o = 10^{-3}$ Pa s) was chosen as the overburden material because it is denser, which is the key mechanical factor for triggering gravitational instabilities, and also it is transparent, allowing us to continuously monitor the three-dimensional evolution of RTIs in the model. Surface tension had an insignificant effect on the RTIs because of the high source layer viscosity.

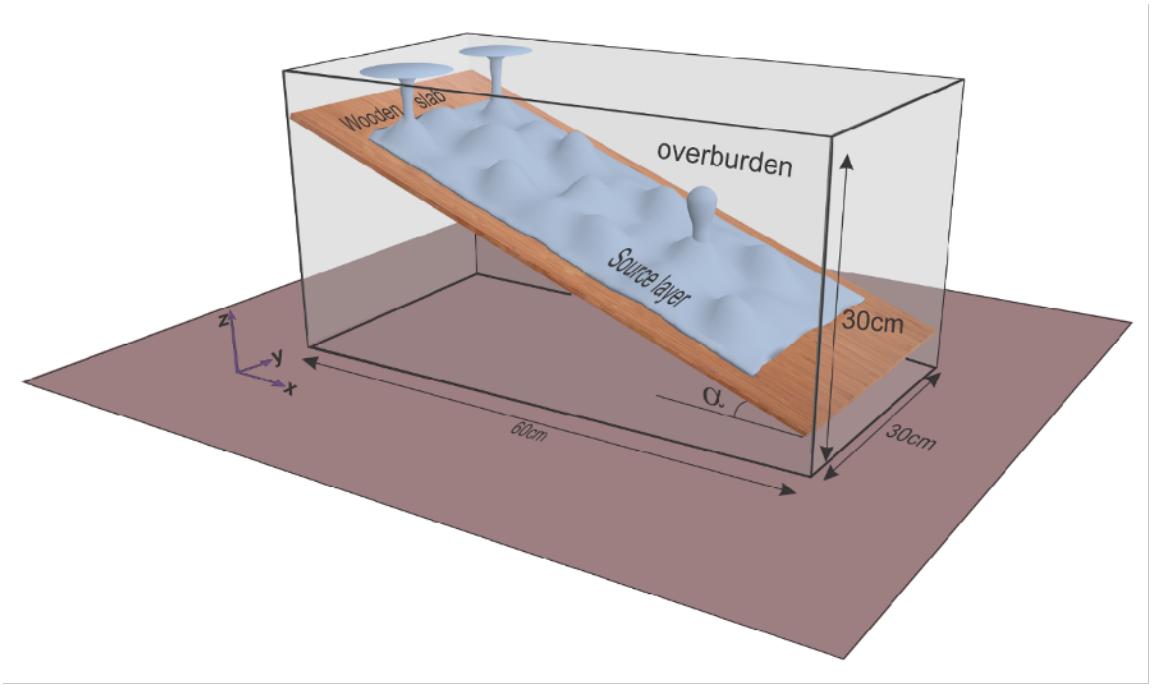

Figure 3.2: Perspective of the experimental set-up used for scaled RTI experiments. The setup had thin buoyant layers, resting upon a dipping slab beneath a denser fluid. α: slab dip.

The experimental setup consisted of a rectangular (60 cm × 30 cm × 30 cm) glass box (Figure 3.2) filled with water to form the overburden above the source layer. Within the glass box, a wooden rectangular plate (60 cm × 30 cm × 5 cm) was placed in a tilted position to represent slab dip (α) in the model. The overburden above the dipping slab had sufficient space for plume growth. Before placing the plate in the box, a volume of PDMS was spread over its top surface in a dry condition to produce a mechanically coherent layer with uniform thickness. The layer was left undisturbed for 2 to 3 hours to remove air bubbles trapped in the source layer.

Table 3.1: Model dimensions and material properties used in the laboratory experiments

	Model Parameters	Symbol	Units	Value
	Model length	L	cm	60
	Model width	W	cm	30
	Model height	H	cm	30
$R < 1$	Overburden density	ρ_o	kg/m^3	998
	Overburden viscosity	μ_o	Pa s	10^{-3}
	Source density	ρ_s	kg/m^3	965
	Source viscosity	μ_s	Pa s	100
	Viscosity ratio	R	-	10^{-5}
$R > 1$	Overburden density	ρ_o	kg/m^3	1100
	Overburden viscosity	μ_o	Pa s	250
	Source density	ρ_s	kg/m^3	970
	Source viscosity	μ_s	Pa s	10
	Viscosity ratio	R	-	25

The $R < 1$ type of models does not completely replicate the mechanical settings of natural subduction zones, where the mantle wedge has viscosity higher than the partially molten layer, i.e., $R > 1$. To reproduce such a mechanical setting, we used the second series of models with $R = 25$ (referred to as $R > 1$ type hereafter). These models consisted of source layers of hydraulic oil (ρ_s = 970 kg/m^3, μ_s = 10 Pa s), and an overburden of translucent glue (ρ_o = 1100 kg/m^3, μ_o = 250 Pa s); both the source-layer and overburden materials satisfy the viscosity scaling, as shown in the next section. The major disadvantage of using glue as the overburden is that it is translucent, giving a limited scope to capture the third dimension of the RTIs. However, this type of model provides us good scaling to the natural prototype.

3.2.2 Model scaling

The present laboratory experiments were designed by fulfilling the requirements of geometric, kinematic, as well as dynamic similarity with the natural prototype (Hubbert,1937). For geometric similarity, the model length of source layers is scaled to their corresponding length in natural settings and it yields a length scale factor (Λ) of 3×10^{-6} (Marques and Mandal, 2016). For kinematic similarity, the time required for any

change in the model needs to be proportional to the time involved in the natural prototype, which in our case is the plume growth time. This is used to estimate the time ratio (Hubbert, 1937). It can be deduced from the equivalent strain rates, as enumerated by Marques and Mandal (2016). The ascent rates of plumes are in the order of 10 cm/year (Gerya et al., 2006; Hasenclever et al., 2011). Accounting the model dimension ratio, this yields the strain rates ratio, $\varepsilon* = 10^{10}$. Taking time as reciprocal to strain rate, we obtain the time ratio in our model: $\tau = 10^{-10}$. As the inertial forces in the present case are negligibly small, the main controlling factor for dynamic similarity is the body force due to gravity and leads to the ratio of the acceleration due to gravity being unity. We can choose model dimension, mass and time ratios: Λ, M, and τ independently, without violating the dynamic similarity. For our model, the dynamic scaling must satisfy a specific viscosity ratio, given by

$$\mu^* = \rho^* \Lambda \tau \qquad (3.1)$$

where ρ^* is the density ratio (0.37) (Table 3.2). Equation (1) yields the viscosity ratio (μ^*) in the order of 10^{-16}. Considering the viscosity as ~10^{18} Pa s (Zhu et al., 2009), the scaling factor yields the model material viscosity as ~10^2 Pa s, which is the viscosity of PDMS used for the layer in our model.

Table 3.2: Model parameters and the scaling ratios used in the experiments with $R < 1$.

Quantities	Model material parameters	Natural Parameters	Ratio (Model/Nature)
Acceleration due to gravity	9.81 m/s^2	9.81 m/s^2	1
Length (L)	30 cm	100 km	$\Lambda = 3 \times 10^{-6}$
Density (ρ)	965 kg/m^3	2600 kg/m^3	$\rho^* \sim 0.3$
Time of plume growth (t)	30000 s	3×10^{14} s	$\tau = 10^{-10}$
Velocity (v)	9.5×10^{-3} cm/s	10 cm/year	$v^* = 3 \times 10^4$
Viscosity (μ)	10^2 Pa s	10^{18} Pa s	$\mu^* = 10^{-16}$

For experiments with R = 25, we use the same length scale ratio (Λ) and similar density ratio (ρ^*) factor, but have the time scale lower by one order (i.e., $\tau = 10^{-11}$) (Table 3.3). This leads to a viscosity ratio of 10^{-17} (Eq. (3.1)). The scaling factor gives a source

layer viscosity of 10 Pa s (*cf.* viscosity of hydraulic oil). Considering $R = 10^2$, the overburden viscosity should be 10^3. I chose translucent glue (μ_o =250 Pa s) as the overburden to obtain the scaling factor closest to our desired value (~10^3).

Table 3.3: Model parameters and the scaling ratios used in the experiments with R >1.

Quantities	Model material parameters	Natural Parameters	Ratio (Model/Nature)
Acceleration due to gravity	9.81 m/s^2	9.81 m/s^2	1
Length (L)	30 cm	100 km	$\Lambda = 3 \times 10^{-6}$
Density (ρ)	970 kg/m^3	2600 kg/m^3	$\rho^* \sim 0.3$
Time of plume growth (t)	3000 s	3×10^{14} s	$\tau = 10^{-11}$
Velocity (v)	9.5×10^{-2} cm/s	10 cm/year	$v^* = 3 \times 10^5$
Viscosity (μ)	10 Pa s	10^{18} Pa s	$\mu^* = 10^{-17}$

3.2.3 Experimental runs and quantitative analysis.

In conducting the laboratory experiments, two main parameters were considered: source-layer dip (α) and source-layer thickness (T_s). In the first series of experiments with $R = 10^5$, α was systematically varied between 10° and 60° at an interval of 10°. For a given α, we chose T_s = 0.5 cm, 1 cm, and 1.5 cm, which scale to ~1.7 km, ~3.3 km, and ~5.2 km thick partially molten zones respectively in natural settings. In the second series of experiments with R =25, α was varied in the range 10° to 40° at an interval of 10° with T_s = 0.5 cm, 1 cm.

For post-processing of the model observations we used a set of four parameters to quantitatively present our experimental results. 1) *Normalized wavenumbers of instabilities*: a time series analysis of this parameter from the experimental runs was performed to show how 3D instabilities grow in size with ongoing process. This analysis also allows us to assess the degree of wave coalescence in their geometrical evolution. 2) *Wavelength ratio of RTI waves along and across the slab strike*: This ratio is used to quantitatively express the 3D shape of RTIs in the source layer as a function of slab dip and consequently to characterize the contrasting modes of RTIs. 3) *Updrift and plume*

growth velocities: These kinematic parameters were estimated from the mean velocities of domes and plumes, respectively. They are used as a measure of the relative transport rates in the source layer under varying slab dips (α). I present this kinematic analysis specifically for the $R > 1$ type of models as they provide a better approximation to natural subduction system. 4) *Plume distance*: This parameter is used to quantitatively compare volcano separation in model and in natural settings.

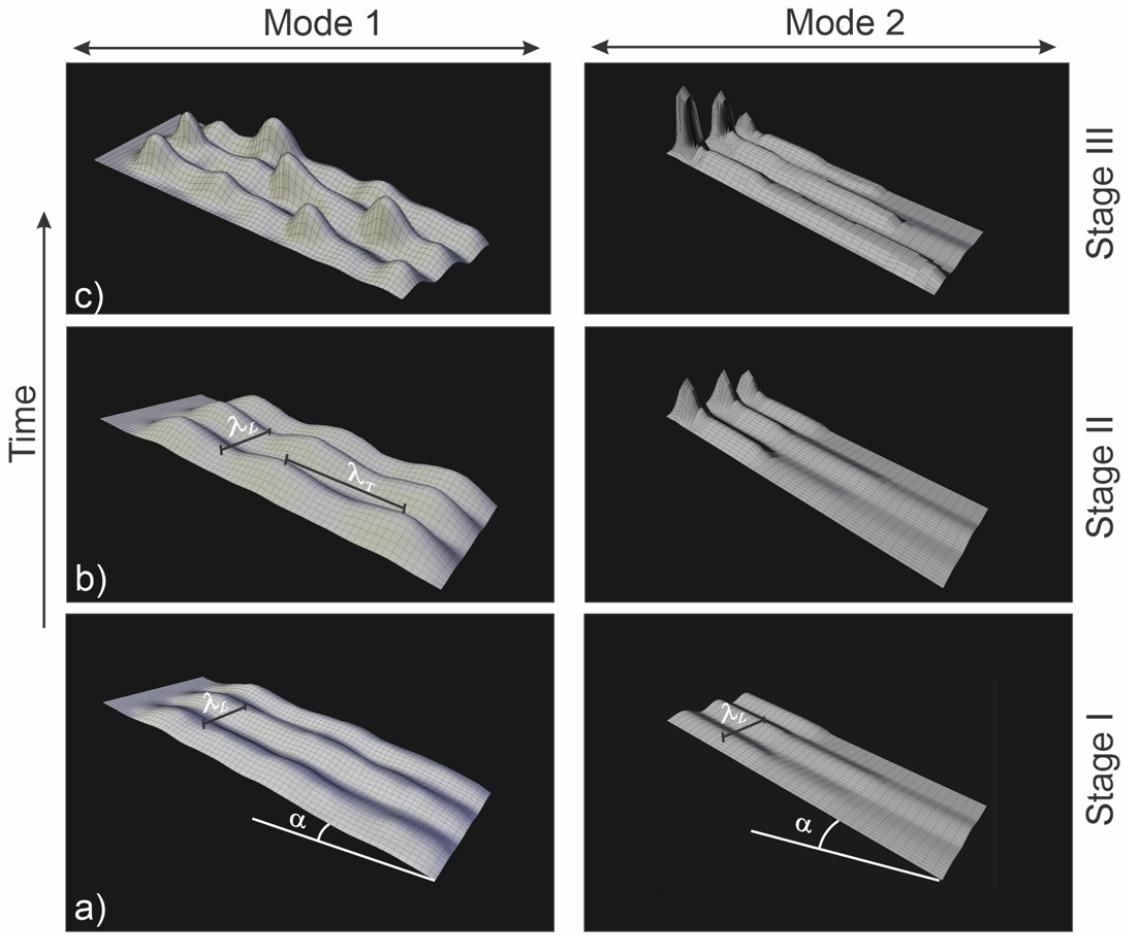

Figure 3.3: Two principal modes of evolution of 3D RTI structures (sketches derived from experiments). Mode 1: spatially distributed dome formation by the interference of longitudinal (λ_L) and transverse (λ_T) instability waves; Mode 2: Instability dominated by λ_L waves, which focus updip material advection to localize an array of plumes at the upper edge of the source layer. (α : slab dip). The three stages are classified based on normalized experimental runtime $t^* = t/t_T$, (t_T is the total runtime; new instabilities almost ceased to occur in the source layer after t_T), Stage I: $t^* = 0$-0.2, Stage II: $t^* = 0.2$-0.6, Stage III: $t^* > 0.6$.

3.2.4 Modes of plume growth

In the laboratory models, plumes evolved in three stages (Figure 3.3), which are described using a normalized experimental runtime ($t^* = t / t_T$, where t_T is the total runtime and it is

noted that instabilities almost ceased to occur in the source layer after t_T). Stage I (t^* = 0-0.2): RTIs developed a train of waves along the slab dip direction with a characteristic wavelength λ_L (called *longitudinal waves* hereafter), followed by another set of RTI waves orthogonal to λ_L-waves (called *transverse waves*) with a characteristic wavelength λ_T. Stage II (t^* = 0.2-0.6): λ_T and λ_L waves progressively interfered to form 3D instability structures, characterized by a series of domes. Stage III ($t^* > 0.6$): the domes grew vertically to form spatially scattered plumes (areal distribution). This mode of plume formed by λ_T and λ_L interference is described as *Mode 1*. The other mode (called *Mode 2*) reflects RTIs dominated by λ_L waves, with little or no growth of λ_T-waves, produced an array of plumes (linear distribution) preferentially at the upper edge of the source layer.

3.2.5 Reference model-Mode 1

The reference model (α = 20°, T_s = 0.5 cm and $R = 10^{-5}$) for Mode 1 plumes is shown in Figure 3.4a. In Stage I, the RTIs produced sequentially longitudinal and transverse waves with $\lambda_T > \lambda_L$ (e.g., $\lambda_L \sim 6$ km and $\lambda_T \sim 11$ km), where λ_T/λ_L ratios lie between 1.8 and 2.5. In Stage II their interference gave rise to approximately regular 3D wave structures in the source layer, which underwent geometrical transformation in time with progressively reducing wavenumbers in both longitudinal and transverse directions; e.g., k_T^* from 0.73 to 0.42, whereas k_L^* from 0.86 to 0.64 (Figure 3.5a-b, blue lines). These transformations resulted mostly from lateral coalescence of the domes. λ_T was always larger than λ_L forming an overall linear trend of the RTI waves along the slab dip direction (Figure 3.5c). The waves progressively amplified to produce nearly periodic arrays of elongate domes (Figure 3.4a), each dome covering an area of ~13 km × 7 km (in transverse and longitudinal direction, respectively). The RTI structures ultimately preserved a smaller number of large elongate domes (15 km × 11 km) with transverse and longitudinal spacing around 11 km and 6 km. These large domes subsequently transformed into asymmetrical shapes, verging to the updip direction. In a given time interval (0.5 Ma), some of them (1 to 2 out of 10 domes) selectively grew vertically at faster rates (15 cm/year) to form typical plumes, leaving the rest in a dormant state. A plume remained active for a finite time period (0.1 Ma) and then pinched out, facilitating nucleation of another plume elsewhere in the source layer. This is how plumes developed randomly in space and time to form a spatially distributed (Mode 1) pattern.

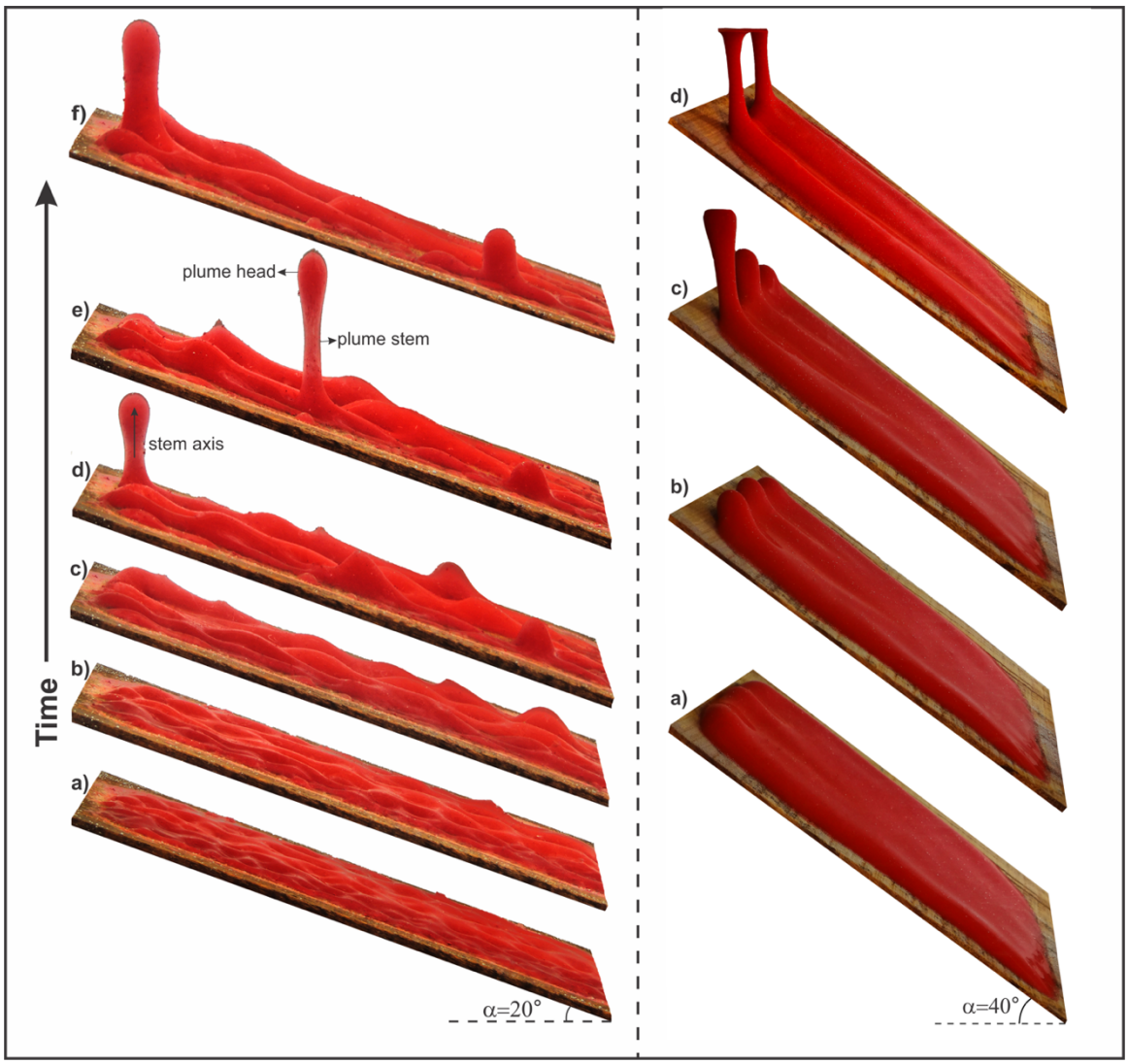

Figure 3.4: Laboratory reference models with $R = 10^{-5}$ and $T_s = 0.5$ cm showing the evolution of a) Mode 1 plumes for $\alpha = 20°$. b) Mode 2 plumes for $\alpha = 40°$.

3.2.6 Reference model-Mode 2

Another reference model ($\alpha = 20°$, $T_s = 0.5$ cm and $R = 10^{-5}$) is presented to show the evolution of Mode 2 plumes (Figure 3.4b). During Stage I, RTIs were dominated by λ_L waves, showing insignificant growth of λ_T waves. They eventually gave rise to linear ridge structures in Stage II, where each ridge acted as a conduit to channelize flows in the source layer. This process initiated trench perpendicular updip advection of the buoyant fluid. Updip advection reduced the wave coalescence, reflecting much smaller variations of the longitudinal wavenumber (k_L^* from 0.94 to 0.8) (Figure 3.5b, magenta line), but prompted RTIs to localize domes preferentially at the upper terminal edge of each λ_L wave. In Stage III, the domes grew vertically to form *Mode 2* plumes with a characteristic spacing (50-

55km), controlled by λ_L. Each plume in the linear distribution trailed into down-dipping ridges, which acted as feeders to supply the buoyant fluids into the growing plumes (Figure 3.4).

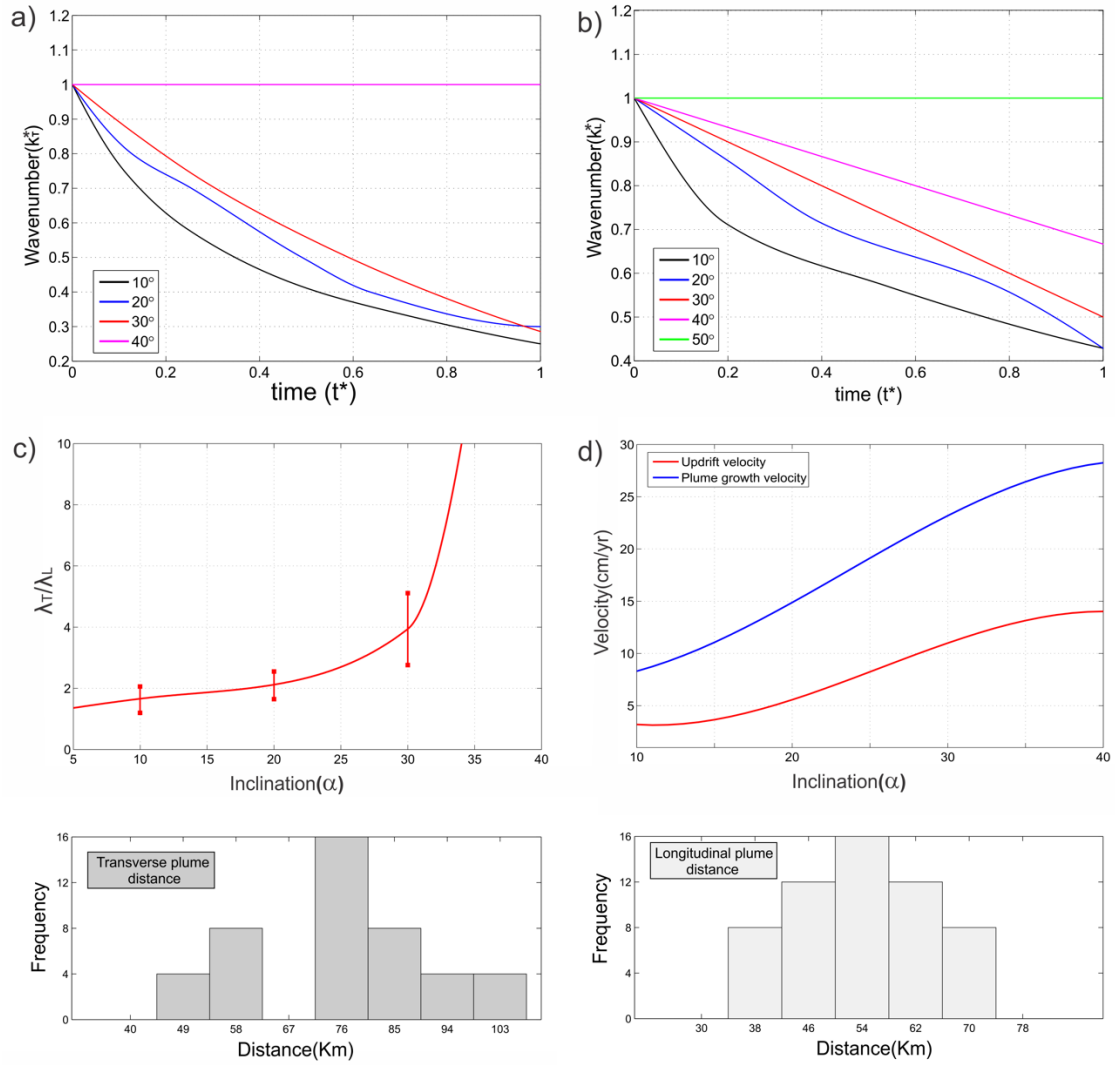

Figure 3.5: Experimental models showing a) variations of normalized transverse wavenumbers (k_T^*) with normalized experimental run time (t*) for varying slab dips (α). b) Variation of normalized longitudinal wavenumbers (k_L^*) with t* for different values of α, where wavenumber $k = 2\pi/\lambda$. c) Estimated plots of λ_T/λ_L with α. d) Variations of the updrift velocity and plume growth velocity with α. e) Histograms of trench-perpendicular and trench-parallel distances of plumes obtained for both $R < 1$ and $R > 1$.

3.2.7 Transition from Mode 1 to Mode 2

I describe here a set of laboratory experimental models (R = 10^{-5}) for α = 10° to 40° to show how and at what threshold α values (i.e., α*) the Mode 1 to Mode 2 transition occurs. At α = 10°, RTIs developed plumes in Mode 1 (Figure 3.6a) (Stage I, II), where $\lambda_T > \lambda_L$ (λ_T/λ_L = 1.2-2) (Figure 3.5c), and the λ_T - λ_L interference formed domes globally in the source

layer (Stage II). During their growth, they drifted at low rates (3-3.4 cm/year) towards the up dip region of the slab (Figure 3.5d). In places, the process of dome coalescence reduced their spatial density in the source layer as revealed by significant decrease in the wavenumbers k_T^* (0.62 to 0.37) and k_L^* (0.71 to 0.54), respectively (Figure 3.5a, b, black lines). In stage III the model produced typical Mode 1 plumes that grew vertically at relatively slow rates (8.1-8.6 cm/year) (Figure 3.5d) and had average transverse and longitudinal distances of 80-100 km and 35-45 km (Figure 3.5e), respectively.

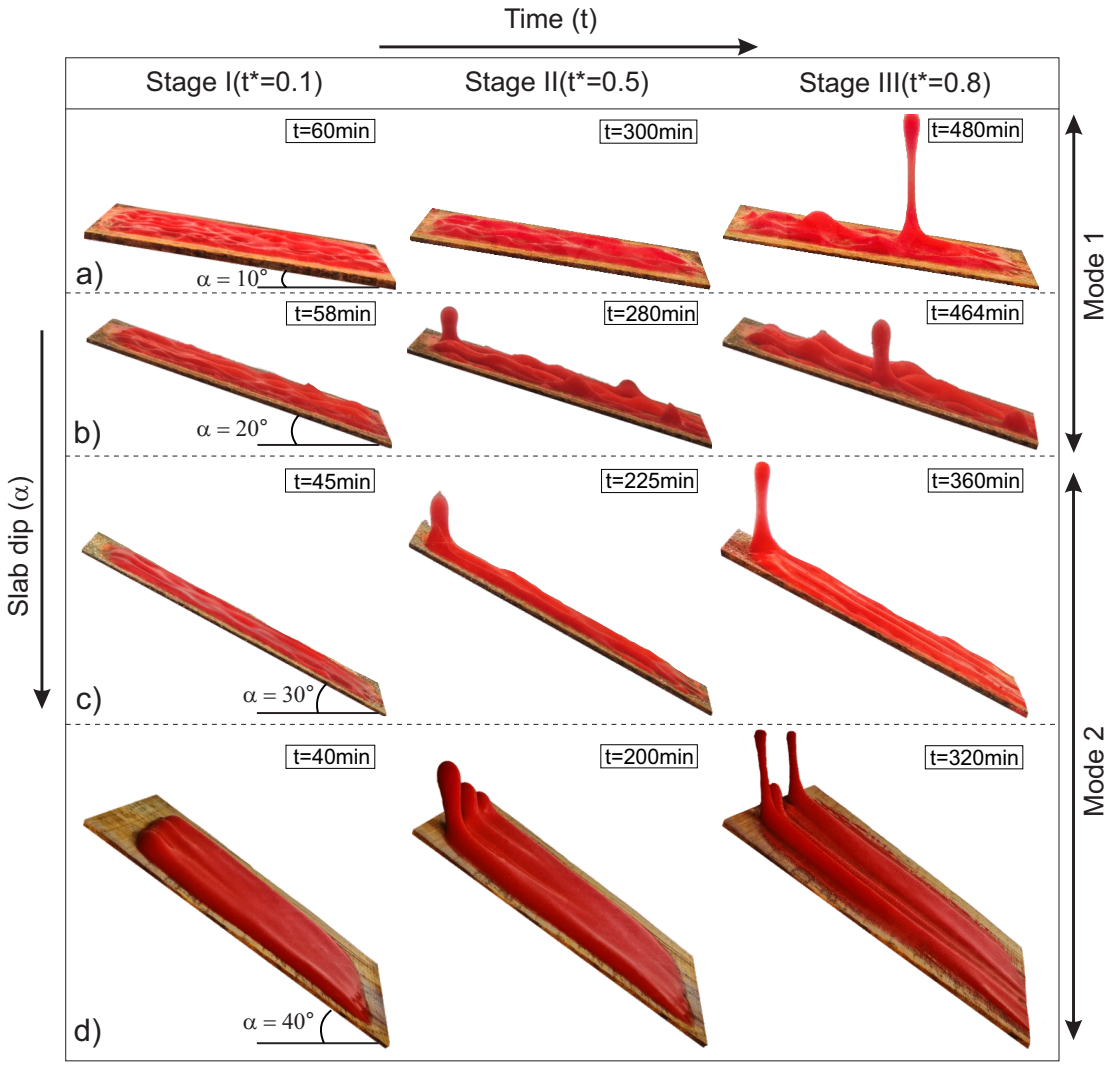

Figure 3.6: Development of RTIs in analogue experiments with R =10^{-5} for varying slab dips (α = 10-40°), and a constant source layer thickness (T_s = 0.5cm). a) λ_T/λ_L wave interference in the initial stage (Stage I), leading to extensive dome formation in the source layer in the intermediate stage (Stage II), and their selective vertical growth into plumes (Mode 1) in the advanced stage (Stage III). b) λ_T/λ_L wave interference, dominated by λ_L instability to form down-dipping RTIs in Stage I, followed by formation of trains of asymmetric elongate domes in Stage II, and subsequent growth of Mode 1 plumes in Stage III. c) Formation of elongate λ_L instability in Stage I, prompting updip material advection to nucleate plumes at the upper edge of the source layer in Stage II, and their subsequent growth in Stage III. d) Growth of strongly elongated λ_L-wave instability in Stage I, focusing the updip advection to localize periodic domes at the upper edge in Stage II, and their rapid growth into matured plumes in Stage III.

Increasing α resulted in quantitative changes in the RTI structure (Figure 3.6b). For α = 20°, λ_T/λ_L ratios became 1.8 to 2.5 (Figure 3.5c), and the interference of longer λ_T waves with λ_L waves gave rise to persistent ridges with their long axis parallel to the slab dip direction. In addition, the coalescence process became significantly weaker; the wavenumbers thus underwent relatively less changes (k_T^*: 0.73 to 0.42, and k_L^* : 0.86 to 0.64) in Stage II, as compared to the α = 10° model (Figure 3.5a-b, blue lines). However, the λ_T instability was active enough to form the 3D wave geometry, characterized by regularly spaced elongate domes. Each dome drifted in the updip direction tracking the λ_L crest lines at faster rates (5-6.8 cm/year) (Figure 3.5d). In Stage III, these drifting domes grow vertically to produce Mode 1 plumes at average transverse and longitudinal distances of 60-95 km and 40-50 km, respectively (Figure 3.5e). Compared to plumes in the α = 10° model, they ascended at much higher rates, (13-16 cm/year) (Figure 3.5d).

Further increase in α to 30° showed a transition from Mode 1 to Mode 2 RTI evolution (Figure 3.6c). The model produced λ_L waves in Stage I, which amplified rapidly to form a train of down dipping ridges with regular spacing. The transverse waves appeared with $\lambda_T >> \lambda_L$ ($\lambda_T/\lambda_L > 3$) (Figure 3.5c), but they had a weak interference with λ_L to form gentle asymmetric domes. In Stage II, the domes had little tendency to grow vertically as the λ_T waves ceased to amplify with time; they rather updrifted at high velocities (10-12 cm/year) (Figure 3.5d). The wavenumbers, in longitudinal and transverse directions went through small changes; k_T^*: 0.79 to 0.49 and k_L^*:0.9 to 0.7 (Figure 3.5a-b, red lines). The λ_L waves acted as effective conduits to channelize the buoyant materials to localize the domes preferentially at their upper ends (Figure 3.6c-II-III). These domes were arranged along a trench parallel linear trend at a spacing of 30-40 km, in consistent with λ_L (~30 km), and they produced Mode 2 plumes with an average longitudinal distance of 40-45 km (Figure 3.5e), leaving the source layer almost free from any instabilities down the slab dip in Stage III. The plumes had characteristically high ascent rates (21–25 cm/year) (Figure 3.5d). The λ_T wave instability practically disappeared when $\alpha \geq 40°$ (Figure 3.6d). k_T^* remained almost constant throughout the experiments (Figure 3.5a, magenta line). The growth of λ_L in such a condition greatly facilitated the rapid development of Mode 2 plumes (26-28 cm/year) (Figure 3.5d), trailing into a series of parallel linear ridges with spacing ~40 km, plunging down the slab dip direction (Figure 3.6d).

3.2.8 Effect of source layer thickness on modes of plume growth

I also varied initial thickness (T_s) of the source layers, keeping the slab dip constant (e.g., $\alpha = 20^o$). For a small thickness ($T_s = 0.5$ cm), the model developed globally both λ_L and λ_T-wave instabilities, which interfered with one another to produce elongate domal structures (Figure 3.7a). The domes drifted up dip, albeit at slow rates, and some of them grew vertically to form Mode 1 plumes. However, most had limited vertical growth rates owing to sluggish updip material supply into their roots. Instead they produced isolated elongate ridges, plunging down the slab dip. Increase in T_s (T_s = 1.5cm) facilitated the updrift of domes produced by λ_L-λ_T interference (Figure 3.7b). Some of them rapidly amplified into plumes while migrating upward and formed a cluster of matured plumes in the upper region of the dipping slab. Unlike Mode 2 plumes, they are scattered across the trench. Large T_s enhanced updip material advection, and continuously supplied materials to sustain an uninterrupted growth of the plumes.

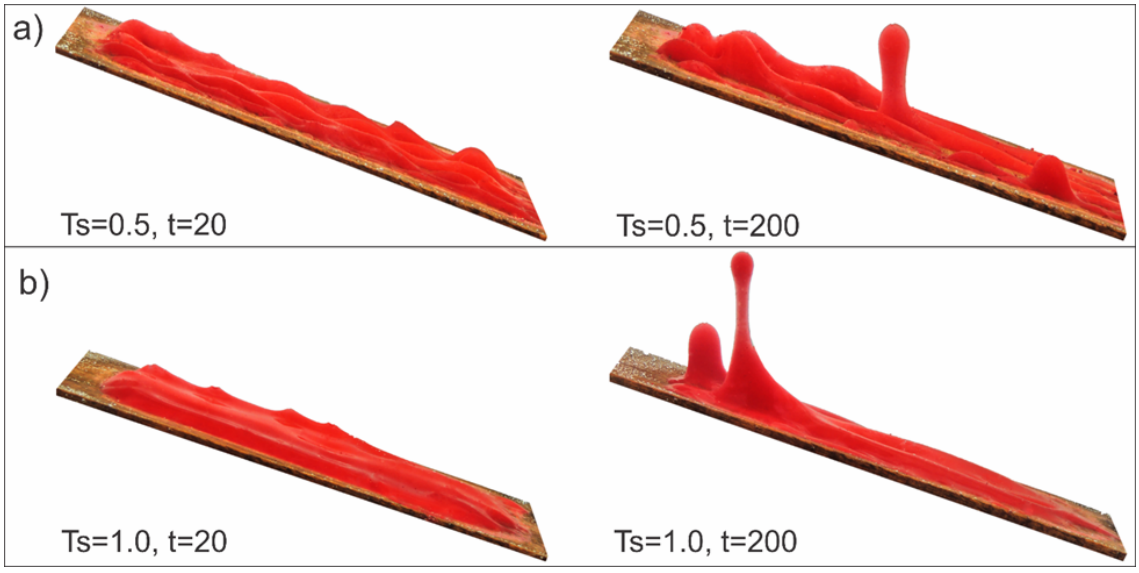

Figure 3.7: Effects of T_s on the RTIs and the plume distributions in analogue experiments for $\alpha = 20°$. a) T_s = 0.5cm. Notice development of distributed plume in the source layer (Mode 1). b) For T_s = 1.0, the plumes underwent updip drift, and formed a plumes cluster at the upper edge of the source layer (t is in minute).

3.2.9 Unsteady dynamics of cold plumes

In some of my experiments the plume evolution occurred in unsteady states, mainly due to interference with transient secondary processes, e.g., coalescence and pinching out of plume stems. Such unsteady dynamics often resulted in pulsating behaviour of plume growth (Dutta et al., 2016; Hasenclever et al., 2011). For significant slab dips ($\alpha > 10^o$),

domes drifted up the slab dip, but at different rates. Trailing domes drifted faster than a leading plume, and eventually coalesced with the latter, rejuvenating the plume growth by supplying fresh pulse of material (Figure 3.8). Similarly, two matured plumes migrated in the upslope direction to form a cluster of plumes, which subsequently coalesced with one another to produce a single plume of larger dimension.

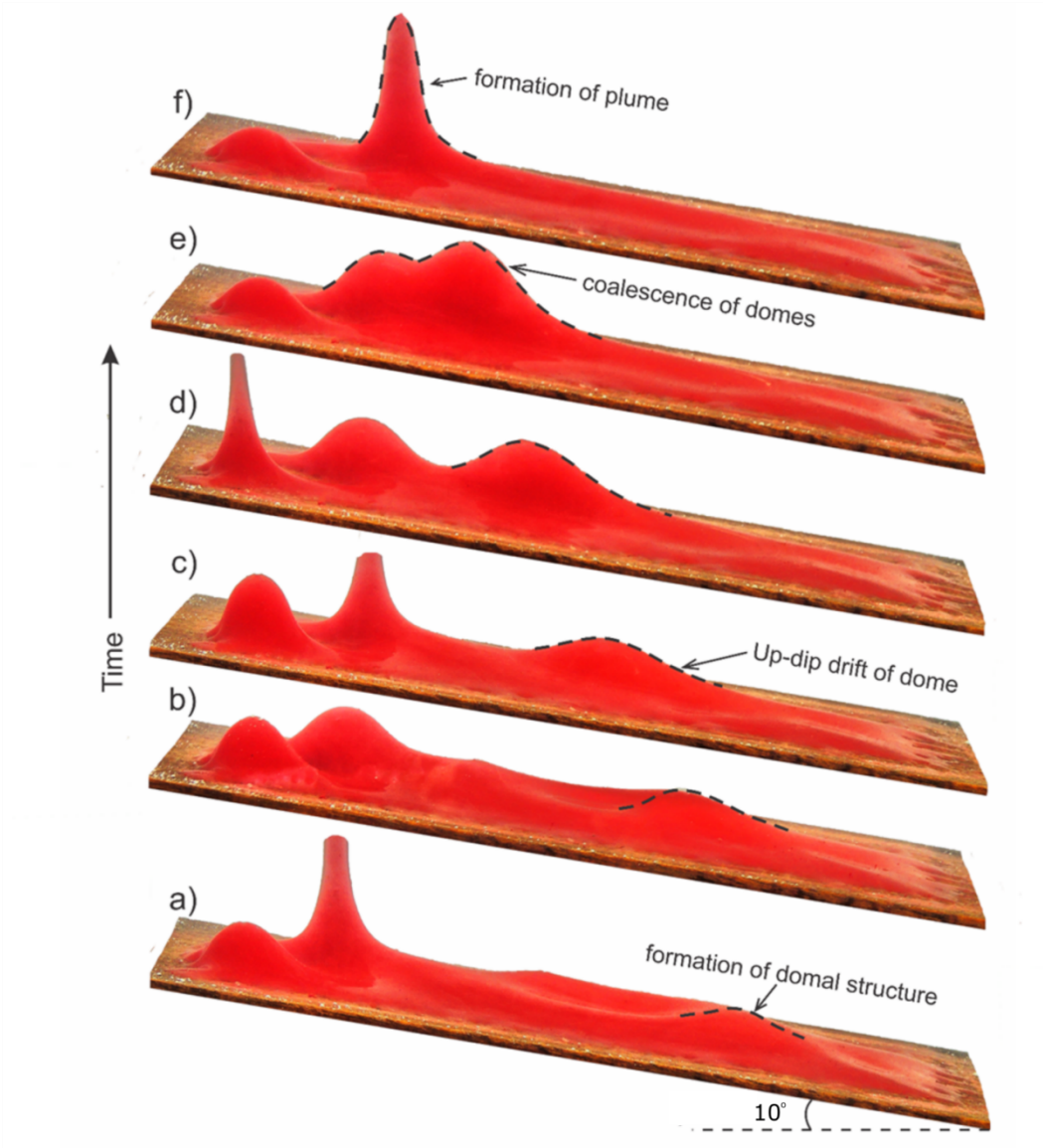

Figure 3.8: (a) – (f) Successive stages of RTIs in experimental model with large source layer thickness (T_s = 1.0 cm). Domes formed by the interference of λ_L and λ_T waves underwent updip migration, and subsequently coalesced with one another to form large plumes in the upper region of the source layer.

Both Mode 1 and 2 plumes showed pulsating dynamics as a consequence of difference between material flow through the plume stem and the material influx to their roots. I have discussed previously that λ_L waves largely control material advection, a key

process in controlling the plume kinematics in the up-slab region. The advection process was interrupted due to λ_T/λ_L interference, and thus failed to support material supply required for the steady ascent of plume head. This eventually caused the plume stem to pinch out during the period of low material influx (Figure 3.9a-b). The stem formed a secondary head following a new pulse of material influx to the stem root (Figure 3.9c-d). A periodic arrangement of domes along λ_L-ridges also resulted in more or less periodic pulsating growth of plumes.

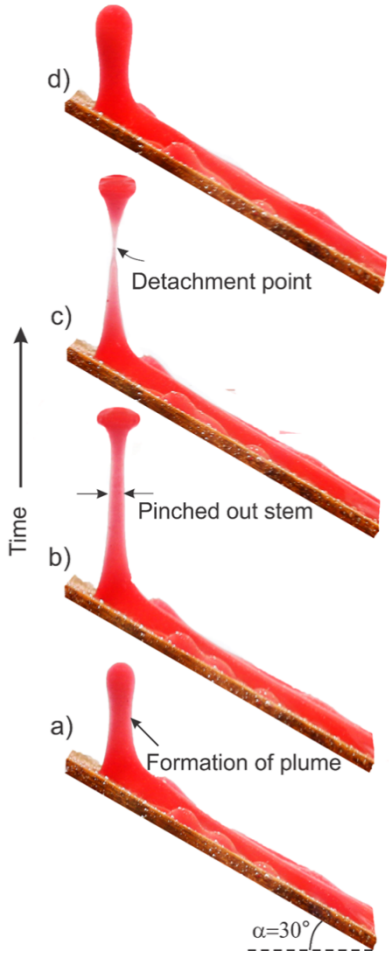

Figure 3.9: Pulsating behaviour of plume growth: formation of plume (a); pinching out of plume stems during their ascent (b); detachment of the plume head, leaving pointed stems (c) and formation of a new plume head with the next pulse of material flux into the plume root (d).

3.2.10 Applicability of the model results for $R > 1$

To test how far the experimental results obtained from the $R < 1$ type of models apply to an actual subduction setting, I used the $R > 1$ type of model and found qualitatively similar results. To demonstrate this, I present here two specific models with $R = 25$ for low ($\alpha =$

20°) and high ($\alpha = 30°$) angle slab dips. For $\alpha = 20°$, the RTI produced 3D wave structures, forming several regularly arranged domes in the source layer. They subsequently grew vertically to produce distributed plumes (Mode 1) (Figure 3.10a), as in the $R < 1$ models. However, the growth rate of plumes in case of $R > 1$ was relatively low (15 cm/year, as compared to 20 cm/year for $R < 1$). The estimated average longitudinal and transverse plume spacing was found to be 45 km and 60 km, respectively, which are in agreement with the $R < 1$ model results. For $\alpha = 30°$, the RTI produced a dominant set of λ_L waves, as in $R < 1$ models. These waves evolved into linear ridges along the slab dip direction, which subsequently gave rise to a linear distribution of Mode 2 plumes (Figure 3.10b). Their spacing varied from 40 to 50 km , broadly matching the value obtained from the $R < 1$ models. Models with $R > 1$ produced flattened plume heads, in contrast to rounded plume heads in case of $R < 1$. However, the threshold value for Mode 1 to 2 transition (α*) remains unchanged.

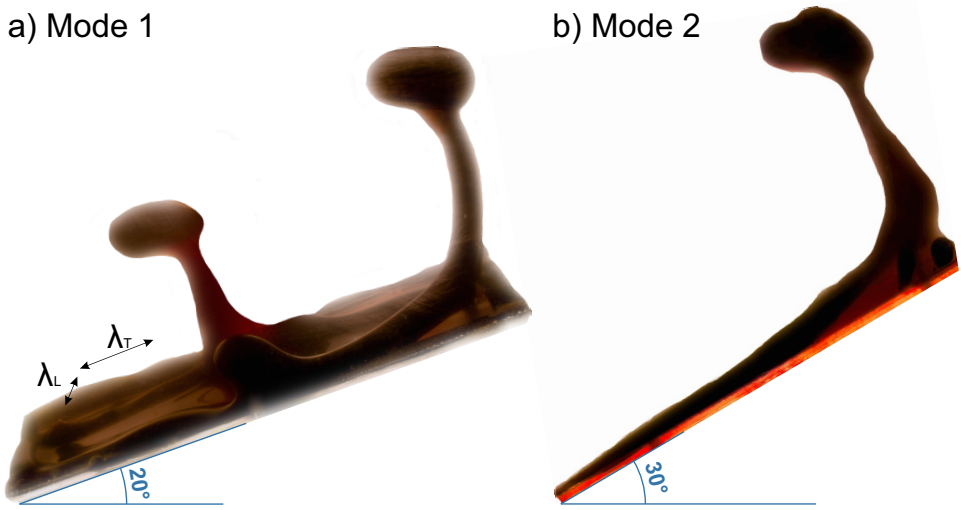

Figure 3.10: Development of Mode 1 and Mode 2 plumes for low-angle and high-angle slab dips analogue experiments with $R = 25$ and $T_s = 0.5$ cm. λ_T typically varies from 10-60 km

3.3 Computational fluid dynamics (CFD) simulations

3.3.1 Model design

I performed 2D computational fluid dynamics (CFD) simulations considering two-phase fluid models, consisting of a source layer (phase 1) and mantle wedge (phase 2). The conservative level set (CLS) method was used to track the evolving phase-interface between the two immiscible fluids. Our CFD modeling used two governing equations: the

Navier-Stokes equation and the continuity equation. These equations were solved using commercial finite element code (COMSOL Multiphysics, 2015) (details given in the following section). Several earlier workers used this code for large scale modeling in geodynamics (Dutta et al., 2016; He, 2014; Ryu and Lee, 2017). I ran two types of CFD simulations: 1) models with dimensions and material parameters, corresponding to the laboratory setup and 2) models approximated to the natural prototype. The first type was used mainly to validate our laboratory findings. The models had a horizontal dimension of 60 cm and a vertical dimension of 30 cm, chosen to reproduce the laboratory model dimensions. I performed laboratory scale model simulations for both $R < 1$ and $R > 1$ with $\alpha = 20°$ and 30° and $T_s = 1$ cm (model parameters given in Table 3.4).

Table 3.4: Description of the values of different model parameters used in CFD simulations.

Parameter	Units	Melt layer	Overburden mantle
Density	kg/m^3	2800-3100	3300
Viscosity	Pa s	10^{17}	10^{19}-10^{22}
Thickness	km	2-6	50-300
Subduction Angle (α)	(deg.)	10-40	-

The second type of CFD models covered a trench perpendicular section with a horizontal (x) dimension of ~ 350 km and vertical (y) dimensions of 110 to 330 km, depending upon the slab dip (10° to 40°) (Figure 3.11). For 3D simulations, we extended the 2D geometry in a z dimension (~ 200 km) parallel to the trench. These models contained a low-viscosity (10^{17} Pa s) and low-density (3000 kg/m^3) source-layer at the interface between the dipping slab and the overlying mantle wedge. Based on the available data in published literature (Marsh, 1979; Gerya and Yuen, 2003), I chose the source-layer thickness to vary in the range 2 to 6 km. We introduced initial geometrical perturbations at the interface between the source layer and the overburden (small seed and sinusoidal type perturbations) with a very small amplitude (~ 40 m) and varying wavelengths (10 to 60 km) (Evans and Fischer, 2012; Mancktelow, 1999; Schmalholz and Schmid, 2012). The bottom and top model walls were assigned a no-slip condition, keeping the sidewalls under a free-slip condition. The estimated Reynolds number (Re) in our model was found to be in the

order of $Re \sim 10^{-19}$, which ensures the choice of model boundary conditions and parameters with a good approximation to the natural prototype (Hasenclever et al., 2011; Zhu et al., 2009).

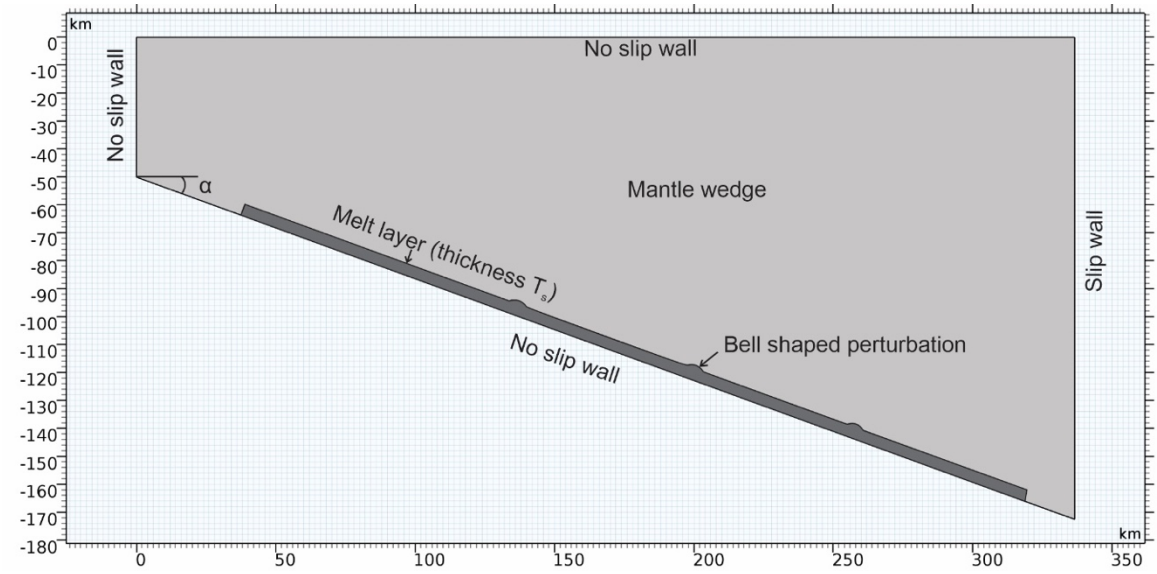

Figure 3.11: Initial condition of the 2-D numerical set-up used for scaled RTI experiments.

3.3.2 Computational method

To study the RTI as a function of α, we performed natural scale computational fluid dynamic (CFD) simulations using the level set (LS) method (Osher and Sethian, 1988). The LS method employs an Eulerian technique to track the moving interface between two immiscible fluid phases with the help of a globally defined smooth continuous function known as *level set function* ($ø$). The function $ø$ varies smoothly from 0 to 1, where the functional values 0 and 1 denote fluid phases 1 and 2, respectively, whereas *0.5* delineates the interface. The region assigned with $ø>0.5$ is filled with fluid phase 1 and that with $ø<0.5$ is occupied by fluid phase 2.

The $ø$ is also advected in the flow field; its time dependent expression for the moving interface is given by the advection equation:

$$\frac{\partial \emptyset}{\partial t} + v.\nabla \emptyset = 0 \qquad (3.2)$$

The most critical challenge of two-phase flow simulations concerns an abrupt jump of physical parameters across the moving interface, which often causes mass conservation problems and constant interface thickness. To overcome these, a conservative level-set

(CLS) method (Olsson and Kreiss, 2005) is used to express the advection in the following form,

$$\frac{\partial \emptyset}{\partial t} + v.\nabla\emptyset = \gamma\nabla.\left(\varepsilon\nabla\emptyset - \emptyset(1-\emptyset)\frac{\nabla\emptyset}{|\nabla\emptyset|}\right) \quad (3.3)$$

The left-hand side of the Eq. ((3.3) defines motion of the interface; the right side stands for reinitialization and numerical stabilization. Parameter ε is responsible for controlling the interface thickness and γ defines intensity of reinitialization. Density (ρ) and dynamic viscosity (μ) in the model can be expressed in terms of the LS function as,

$$\rho = \rho_1 + (\rho_2 - \rho_1)\emptyset \quad (3.4)$$

$$\mu = \mu_1 + (\mu_2 - \mu_1)\emptyset \quad (3.5)$$

where ρ_i and μ_i are the density and viscosity of the two end-member fluid phases, i = 1, 2. The simulations consider incompressible flow conditions and momentum conservation, which are expressed by continuity equation and Navier-stokes equations, respectively:

$$\nabla.\boldsymbol{u} = 0 \quad (3.6)$$

$$\rho\frac{\partial \boldsymbol{u}}{\partial t} + \rho(\boldsymbol{u}.\nabla)\boldsymbol{u} = \nabla.[-pI + \mu(\nabla\boldsymbol{u} + \nabla\boldsymbol{u}^T] + \boldsymbol{F} + \rho\boldsymbol{g} \quad (3.7)$$

where $\boldsymbol{u}$ and p are the velocity vector and hydrostatic pressure. I represent the identity matrix and $\boldsymbol{g}$ is the gravity. The geological setting under consideration lacks any significant inertial force. Thus, $\frac{\partial \boldsymbol{u}}{\partial t} = 0$ in Eq. ((3.7).

3.3.3 Laboratory scale simulations

The laboratory-scale CFD models for $R < 1$ ($R = 10^{-5}$) produced Mode 1 plumes for low-angle slab dips ($\alpha < 30°$), and Mode 2 when the slab dip angles became large ($\alpha \geq 30°$) (Figure 3.12). This Mode 1 to 2 transition at $\alpha^* = 30°$ is in excellent agreement with the experimental value of threshold slab dip ~30°. The plumes drifted up dip and the rate increased with increasing α, e.g., it was 0.8 cm/minute (up-scaled 13 cm/year) for $\alpha = 20°$, which increased to 1.2 cm/minute (20 cm/year) when $\alpha = 30°$. These estimates match our experimental values (8.5-23 cm/year). The CFD models for $R > 1$ ($R = 25$) also showed Mode 1 to 2 transition at a similar angle with increasing α (Figure 3.12). To summarize, the Mode 1 to 2 transition occurs as a function of slab dip angle, irrespective of $R > 1$ or < 1.

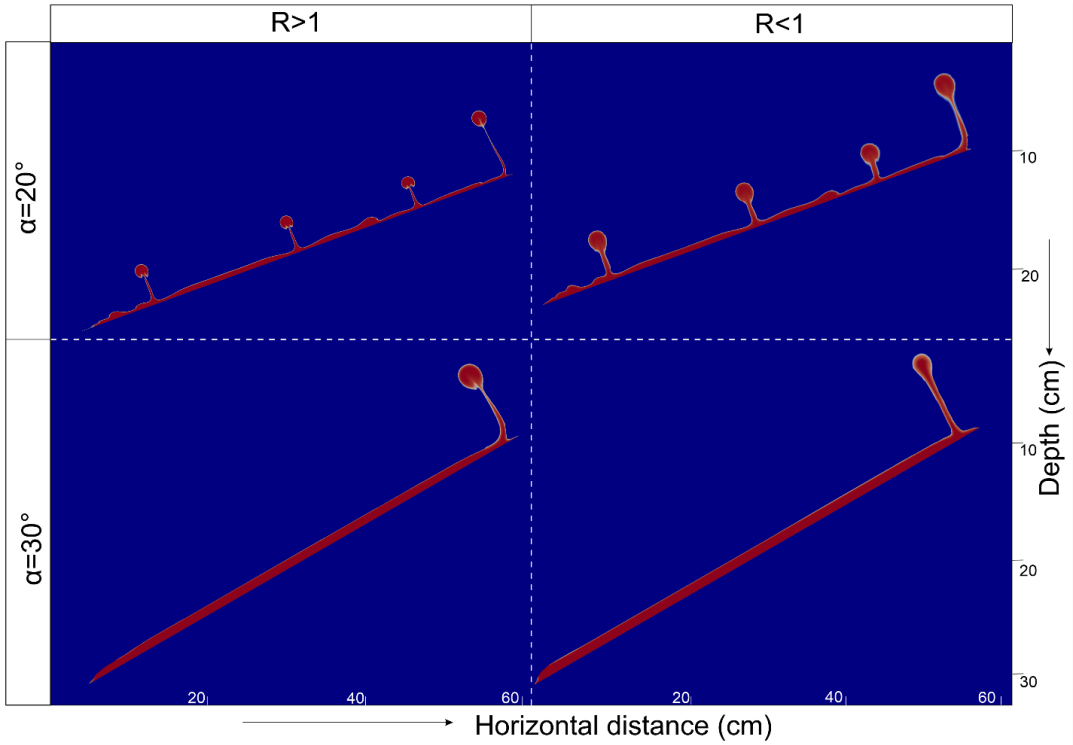

Figure 3.12: Laboratory scale numerical model for R < 1 and R > 1 to validate the experimental results.

3.3.4 Large scale simulations

To extrapolate the laboratory experiments and their equivalent CFD model results to natural subduction zones, I used the second type of CFD simulations. Here I present a set of simulations run with α = 10° to 40° keeping T_s = 4 km, R = 10^2 and $\Delta\rho$ = 300 kg/m^3. For α = 10°, the RTI develops globally in the form of a series of regularly spaced domes down the slab dip direction (Figure 3.13a). The domes grow more or less simultaneously in the vertical direction, albeit at varying rates (12 to 14 cm/year) (Figure 3.15c, red line) to produce an array of Mode 1 plumes. Low-angle slab dips promote RTIs to occur in multiple generations, forming several secondary plume pulses, which are discussed later. The pulsating plumes show little or no updrift as they attain a mature stage. Models with α = 20° produce similar Mode 1 plumes (Figure 3.13b). However, steepening of α results in some quantitative changes both in their geometry and kinematics. First, the RTIs do not occur in multiple generations, and the plume frequency in the source layer is reduced.

Secondly, Mode 1 plumes show a strong spatial variation in their growth rates; plumes located in the updip region grow faster (16 cm/year) than those further down the slab (10 cm/year). Tall, mature plumes concentrate mostly in the shallow part of the source layer, as observed in our physical experiments. At α^* = 30°, the RTI undergoes a transition

from Mode 1 to Mode 2 (Figure 3.13c). The instabilities in the source layer form a series of domes in the down-dip direction; but they hardly grow vertically, rather they drift up dip to coalesce sequentially with the growing plume at the upper edge. This process results in pulsating ascent behavior of Mode 2 plumes. Due to this active material transport, Mode 2 plumes grow at higher rates (~29 cm/year) (Figure 3.15c, green line). For $\alpha = 40°$, the RTIs localize exclusively at the upper edge of the source layer to form a row of Mode 2 plumes (Figure 3.13d). The undisturbed part of the layer acts as a passage for updip material advection to sustain the plume growth at high rates (35 cm/year) (Figure 3.15c, black line).

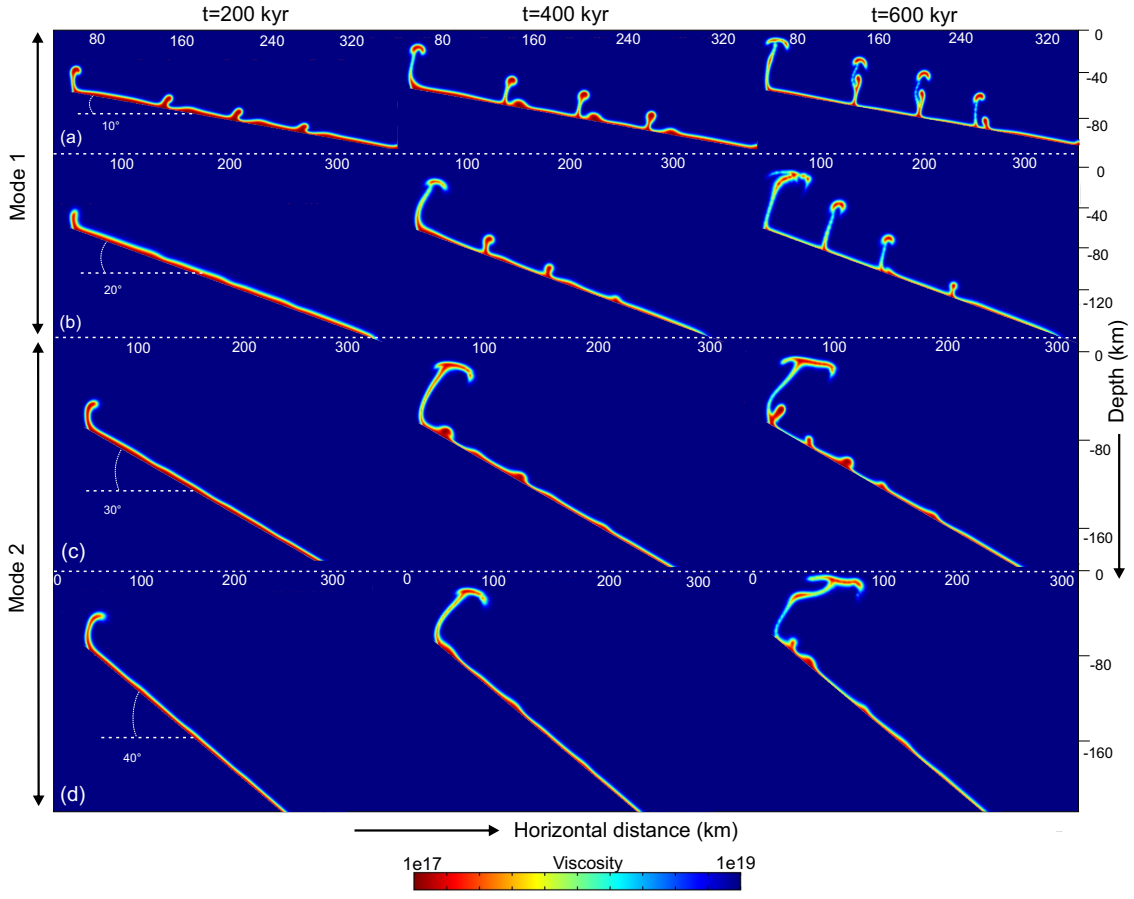

Figure 3.13: CFD simulations showing the growth patterns of large scale RTIs from dipping source layers (T_s = 4 km) in subduction zones. a) – d) α = 10-40°. It is noteworthy that the transition from Mode 1 to 2 as α reaches 30°, as observed in physical experiments.

3.3.5 λ_L instability

A set of 3D simulations was run to test the growth of λ_L instability in a natural scale setting. These simulations were computationally expensive, and there was a limitation with our computational facility to run these simulations on a long time (tens of million years). I

present here preliminary 3D simulation results to support our experimental findings (Figure 3.14). The buoyant layer develops a train of periodic instability waves along the slab dip that resemble λ_L instability in our laboratory experiments and earlier numerical models (Hasenclever et al., 2011; Zhu et al., 2009). These waves show a wavelength of ~33-50 km, with their persistent crest lines down the slab dip, but terminate against a dominant trench-parallel instability in the up-dip region, as observed in physical experiments. Experimental models produced multiple isolated plumes at the terminal points of λ_L waves. However, their coalescence produces single, large plumes, as obtained from numerical simulation.

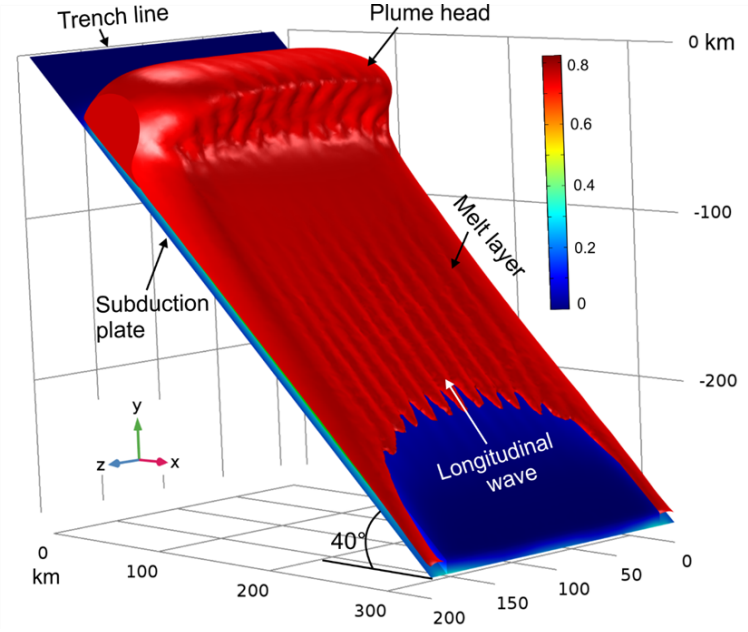

Figure 3.14: Real scale 3D simulation showing growth of λ_L instability on a melt layer with $\alpha = 40°$.

3.3.6 Parametric analysis

I varied the density contrast ($\Delta\rho$) between the overburden and the source layers from 200 to 500 kg/m^3 to investigate the buoyancy effects on the mode of plume growth. The overall plume dynamics remains unaffected by $\Delta\rho$, and the Mode 1 to 2 transition occurs at the same threshold slab dip ($\alpha^* = 30°$). However, their ascent rates significantly increase with increasing $\Delta\rho$, e.g., 12.5 cm/year to 21.5 cm/year from 200 to 500 kg/m^3 at $\alpha = 20°$ (Figure 3.15a).

This study investigated the role of viscosity ratio R in controlling the evolution of plumes. Increasing R lowers their ascent velocity, e.g., ~ 18 cm/year for $R = 10^3$, which decreases to 8.5 cm/year when $R = 10^5$, when $\alpha = 20°$ (Figure 3.15b, blue line). The effect

of viscosity ratio can be attributed to a higher viscous resistance to the ascending plume head by the overburden. However, the threshold slab dip for Mode 1 to 2 transition remains unaffected by R. Decreasing R below 10^2 again reduces the ascent velocity, possibly due to higher viscous resistance within the source layer. The plume ascent rate becomes maximum for $R = 10^3$ (Figure 3.15b).

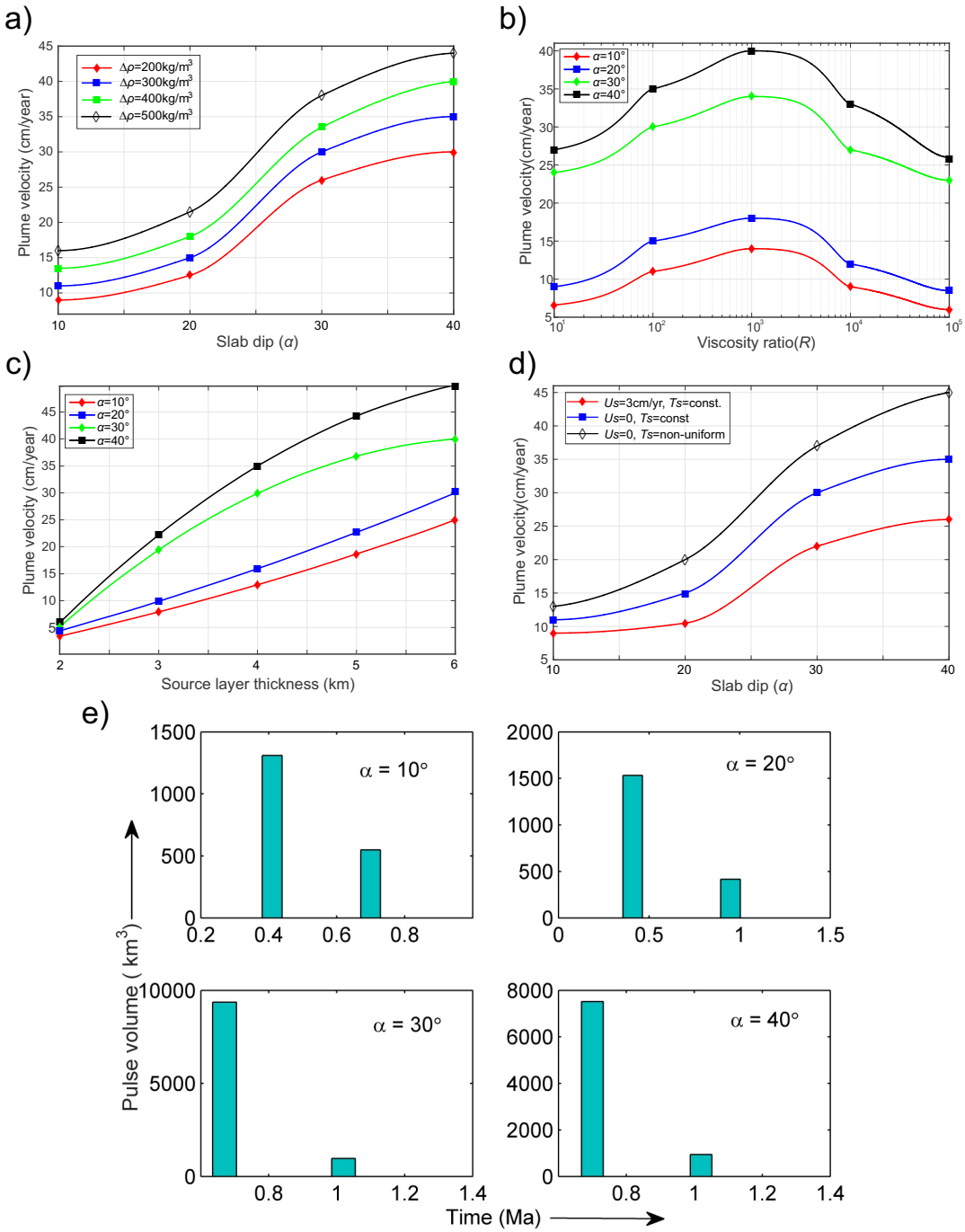

Figure 3.15: Calculated plots from numerical models to show plume growth rate as a function of the following parameters: a) slab dip (α) for different density contrast ($\Delta\rho$), b) viscosity ratio (R) for different values of α c) uniform source layer thickness (T_s) for different α values, d) slab dip for given plate velocity and non-uniform source layer thickness; and e) volume of partially molten material pulses as a function of α and run time.

A series of simulations were run to study the effects of source layer thickness (T_s) keeping slab dip (α) fixed (Figure 3.15c). For $\alpha = 10^o$, the ascent rate of plumes is nearly 4 cm/year for T_s = 2 km; the rate increases to 25 cm/year when T_s = 6 km. Most of the models in our present study dealt with a source layer of uniform thickness. Earlier studies suggested that partially molten zones in natural subduction settings can progressively thicken with depth (England and Katz, 2010; Grove et al., 2012). To investigate the possible effects of non-uniform thickness, we ran simulations with T_s varying down the slab dip (4 km at 70 km to 10 km at 150 km), for different α. For α =20°, the simulations showed a higher ascent velocity of plumes (20 cm/year) than for uniform T_s (15 cm/year) (Figure 3.15d, black line as compared to the blue line). Increase in α to 30° widens their difference, 30 cm/year (uniform T_s) to 37 cm/year (non-uniform T_s) (Figure 3.15d, black line). However, the overall Mode 1 to Mode 2 transition with α occurs in the same fashion.

In a set of simulations, I introduced a slab motion (3 cm/year), as applicable to natural subduction settings. The slab motion influenced mostly the overall plume geometry to attain an updip convex curvature. However, it hardly affected the threshold slab dip for Mode 1 to Mode 2 transition. The plume growth velocity also remained unaffected, but their updrift velocity dropped from 15 cm/year to ~10 cm/year when α = 20° (Figure 3.15d, red line). The estimates suggest increasing slab dip promotes the material volume (V_H) transport in pulses on a time scale of ~ 0.3 Ma (Figure 3.15e). For α = 10°, the maximum V_H in a single pulse is 1310 km^3, increasing to 7518 km^3 when α = 40°. However, V_H does not significantly change with other parameters such as density contrast and viscosity ratio. Considering 5% of the plume volume as eruptible partial melts, a plume pulse is expected to produce volcanic magmas in the order of 67-376 km^3, which is in agreement with the dense rock equivalent (DRE) reported from several modern subduction zones (Kimura et al., 2015; Umeda et al., 2013). Steepening of slab dip angle from 10° to 40° can thus increase the magma volume by ~6 times.

3.3.7 Simulations with subducting plate velocity

To replicate natural subduction kinematics, I performed numerical simulations introducing slab motion at a rate of 3 cm/year. The slab motion influenced mostly the plume geometry to form an overall up-dip curvature of the plume structures. However, these models showed exactly the same Mode 1 to 2 transitions of RTIs with increasing α. The updrift velocity of

plumes decreased as a result of slab parallel downdip drag by subducting slab motion (Figure 3.16).

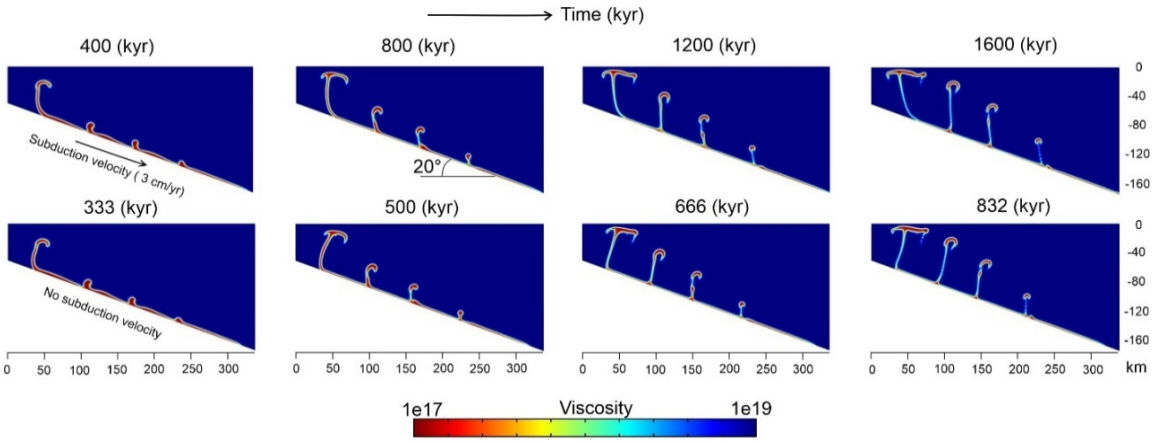

Figure 3.16: Large scale 2D simulations showing effect of subduction velocity on plume growth.

3.3.8 Simulations with non-uniform source layer thickness

Several studies suggested that the thickness of partially molten zones in natural subduction zones increases with depth due to an interplay between the rate of hydration, the thermal structure of the wedge and increasing pressure (Grove et al., 2012; Till et al., 2012). To test the possible effects of non-uniform source-layer thickness (T_s), I ran simulations on models with a downdip variation of source layer thickness, 4 km at 70 km to 10 km at 150 km. This kind of non-uniform T_s gave rise to a higher up-drift velocity (20 cm/year), as compared to that (15 cm/year) for uniform T_s (Figure 3.17). However, increasing the slab dip leads to Mode 1 to 2 transitions at the same threshold α.

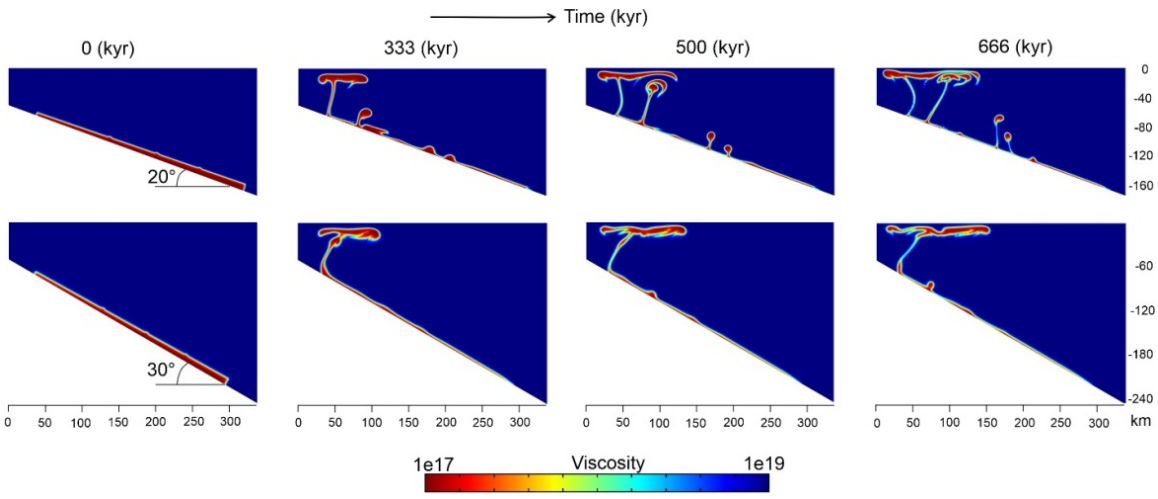

Figure 3.17: Large scale 2D simulations showing effect of non-uniform T_s on plume growth.

3.4 Discussion

3.4.1 Comparison of laboratory, numerical model and natural observations

The experimental and numerical model results for $R = 25$ were compared with the available data from natural subduction zones. The initial values of plume growth rate in the range 8 to 15 cm/year (Figure 3.18a, red line), predicted from numerical models for $\alpha = 20°$ agree well with the laboratory results (9-12 cm/year) (Figure 3.18a, blue line). The model estimates are consistent with the ascent rates (6 to 14 cm/year) provided by Gerya et al. (2006) and Hasenclaver (2011).

I also chose the spatial density of distributed (Mode 1) plumes produced in our laboratory experiments with low-angle slab dips to compare them with natural data. From Google Earth Pro I calculated the spatial density of volcanic spots, measured as the number of volcanic spots per 1000 km^2 in important subduction zones. For example, in the Mexican subduction system densities range from 0.4 to 0.49, whereas from 0.53 (West Java) to 0.6 (East Java) in the Java trench. The Andean subduction zone displays scattered volcanic spots with their spatial density varying from 0.58 (Paro) to 0.8 (Punakha) (Figure 3.18b). Similarly, the plume density (number of plumes per unit area of the source layer) was calculated from our laboratory models with $R = 25$ and $T_s = 0.5$-1.0 cm using their plan view images. Up-scaling of the laboratory estimates yield a spatial density of 0.35-0.7 per 1000 km^2 (Figure 3.18b), which is in agreement with the data for natural subduction settings discussed above.

The volcanic arc distributions in natural subduction zones broadly fall into two distinct categories: 1) regularly spaced volcanic centres, forming a distinct, trench-parallel arc, similar to Mode 2 plume distribution obtained from our laboratory models with steep slab dips ($\alpha \geq 30°$), and 2) scattered distribution with volcanoes spread both parallel and perpendicular to trench similar to Mode 1 plume distributions produced in our models with gentle dips ($\alpha < 30°$). I consider volcano spacing as a parameter to compare with the plume spacing obtained from the experimental (for $R = 25$, $T_s = 0.5$-1.0 cm) and numerical (for $R = 10^2$, $T_s = 2$-6 km, $\Delta\rho = 300$ kg/m^3) results. The longitudinal and transverse plume spacing in laboratory experiments (up-scaled) is found to be 35-75 km and 44-105 km, respectively (Figure 3.18c). On the other hand, the numerical simulations show a longitudinal plume spacing of 33 to 50 km in 3D models and transverse plume distance of 70-90 km in 2D models. A compilation of the estimates from $\alpha < 30°$ natural subduction zones suggests that

the spacing of volcanic centres ranges from 32 to 60 km and 48 to 100 km in the longitudinal and transverse direction, respectively (Figure 3.18c). This marked similarity in the estimates validates our models.

I have also compared time scales of periodicity of pulsating events recorded in natural subduction zones with those predicted from our experimental and numerical models. The frequency of natural volcanic events (300–500 kiloyear) closely matches with the experimental (270–520 kiloyear, upscaled) and numerical (270–510 kiloyear) model estimates (Figure 3.18d).

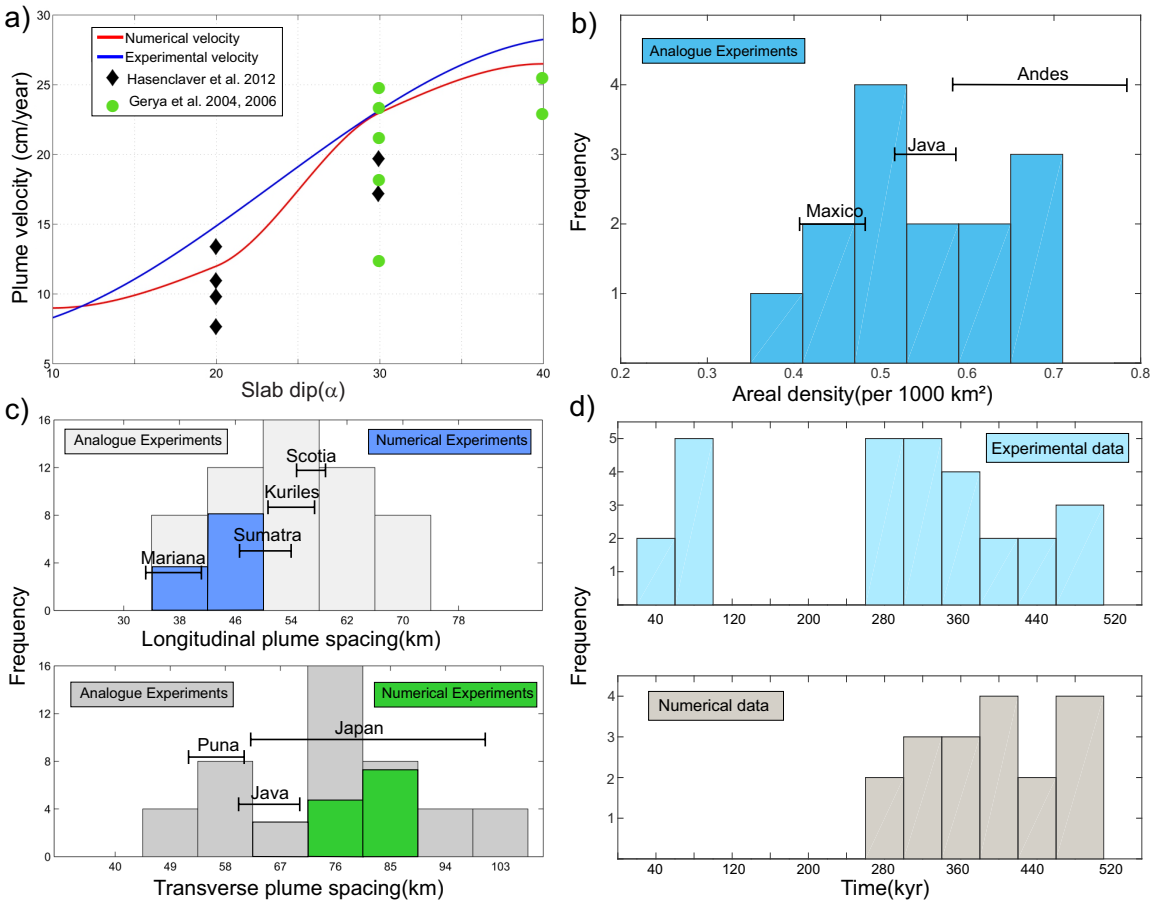

Figure 3.18: a) Validation of the numerical ($R = 10^2$, $\Delta\rho$ = 300 kg/m^3) and experimental ($R = 25$) plume growth velocities with published data. b) Comparison of the areal density of plumes from analogue experiments (R = 25, T_s = 0.5-1.0 cm) with that of volcanoes from different subduction zones. c) Comparison of longitudinal and transverse plume spacing from our analogue ($R = 25$, T_s = 0.5-1.0 cm) and numerical experiments ($R = 10^2$, T_s = 2-6 km, $\Delta\rho$ = 300 kg/m^3) with natural volcano spacing from different subduction zones; d) Analysis of the time scale of frequency of plume ascent from numerical and experimental results (Model properties same as that of c).

3.4.2 Geological relevance of the model parameters

Slab dip variability is a common feature of natural subduction zones throughout the globe. Such variability can even occur within a single subduction zone along the trench line (Lallemand et al., 2005). Several convergent plate boundaries, such as the Mexico subduction system (Currie et al., 2002), the southern Ecuador subduction (Gailler et al., 2007), and the Pampean flat subduction (Ramos et al., 2002) show low slab dip angles (10° to 25°). In contrast, there are many boundaries, such as the Western Sunda and the Kamchatka plates, which display high-angle slab dips ($\alpha \geq 30°$) (Chiu et al., 1991; Hall and Spakman, 2015). The present modelling thus considers α as the principal model parameter to explore how low- versus high-angle subduction dynamics can influence the RTIs in the partially molten zones produced by dehydration melting. Experiments with α < 30° suggest that low-angle subduction would produce an areal distribution of the RTIs, involving relatively small updip advection of the partially molten materials. Steepening of α ($\geq 30°$) weakens the global RTIs to facilitate the advection process that eventually leads to RTIs localization at a shallow depth along the upper fringe of the partially molten zone, as observed in our experimental models and CFD simulations, as well as earlier numerical models (e.g. Zhu et al. 2009). One of the major implications of this finding is that high-angle subduction cannot readily produce plumes from the partially molten materials in deeper sources. Under these circumstances, materials advect to accumulate in the updip region, and form Mode 2 plumes at a shallower depth.

It is worth discussing that the trench normal width of volcanic belts in a subduction zone should depend on the steepness of slab dip from a geometrical point of view; this width represents the horizontal projection of plume distances on the source layer as a cosine function of α (Marsh, 1979). Steepening of the slab dip would reduce the transverse plume distance measured on the horizontal upper surface. But in this study, we have shown that the Mode 1 to 2 transition in RTIs at $\alpha \geq 30°$ leads to a drastic transformation of the distributed plume pattern into a focused one. If the focusing would occur solely due to the geometrical relation, α must be 70° or more. Both our model and natural observations suggest focused arc volcanism can occur at much lower values of α due to the transition in RTI mode.

Many natural subduction zones, e.g. the Mariana, the East Caribbean, and some parts of the Java-Sumatra subduction zones (Chiu et al., 1991; Deville et al., 2015; Hall and Spakman, 2015), steepen their dips to nearly vertical orientations at greater depths. Both

analogue and CFD model results suggest the RTI patterns would remain qualitatively unchanged when $\alpha > 30°$, and always give rise to a linear distribution of plumes at the upper edges of source layers, leaving the down slab region completely undisturbed. Further steepening of slab dip angle (i.e., $\alpha > 40°$) does not cause any qualitative change in the RTIs. We therefore restricted our experimental runs within $\alpha < 60°$.

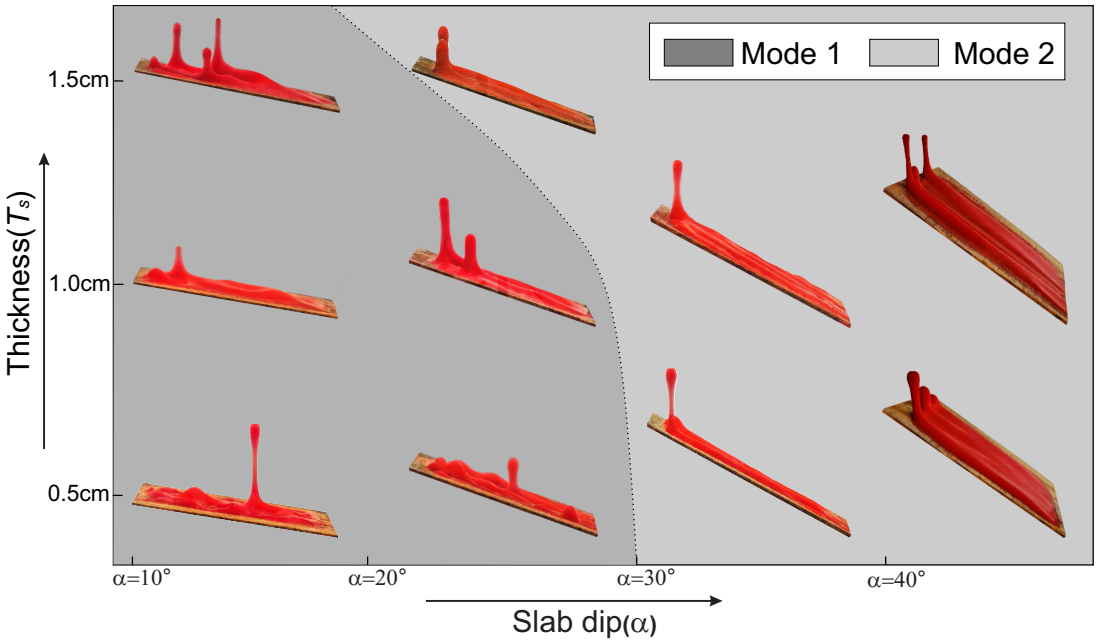

Figure 3.19: A regime diagram of the two modes of plumes as a function of source layer thickness (T_s) and slab dip (α) for $R < 1$.

Petrological calculations have predicted dehydration reactions in the subducting slabs, resulting in partial melting within a narrow zone at the interface of slab and mantle wedge (Grove and Till, 2019; Till et al., 2012). Such partially molten zones generally begin at a depth of 70 to 160 km, and cover a distance of 70 to 200 km along slab dip, giving rise to a mechanically distinct layer atop the dipping slab (Grove et al., 2012; Schmidt and Poli, 1998; Ulmer and Trommsdorff, 1995). For the natural scale CFD modelling, I thus fixed the upper extremity of partially molten regions at a depth of 70 km (Gerya et al., 2006). The maximum stability-depth of different water-bearing phases varies depending upon the subduction angle (α) and subduction velocity as they can modify the thermal structure in the mantle wedge, and thereby the downward extent of partially molten zones. However, the RTI mode is found to be sensitive not to the areal coverage of the partially molten zone,

but its thickness. I varied the partially molten zone thickness (T_s) from 2 to 6 km in CFD simulations and their scaled equivalence in our laboratory experiments. Earlier studies modeled the partially molten zones as 1 to 10 km thick layers (Marsh, 1979; Gerya and Yuen, 2003). The two most important petrological factors in controlling T_s are: 1) the volume of H_2O-rich fluids released from the subducting slab, and 2) the thermal structure in the mantle wedge. For a given thermal structure, increasing fluid volumes would result in higher degrees of dehydration melting to produce thicker partially molten zones. According to the experiments, increasing T_s facilitates domes to drift up the slab, ultimately forming a cluster of plumes at shallow depths. This kind of plume clustering occurs in a particular region of the Mode 1 field defined by T_s and α (Figure 3.19), causing a decrease in transverse plume separation. This ultimately leads to Mode 1 to Mode 2 transition at a lower value of α (~ 20°) for large T_s (~1.5 cm in our experiments) (Figure 3.19).

3.4.3 Time scale of episodic magmatic events

Geological evidence suggests that most of the subduction zones witness episodic arc volcanism, with the time scale of periodicity ranging from tens of years to millions of years. Short time scales periodicity is interpreted as a proxy to fluctuations in the magma chamber dynamics (Gerya et al., 2004). Understanding the mechanisms of long-timescale periodicity poses a major challenge in geodynamic studies. Recent measurements have also predicted 20-100 kiloyear to 0.3-1 Ma cycles of the eruption from tephra deposits in Pacific volcanic arcs (Gudmundsson, 1986; Kutterolf et al., 2013; Schindlbeck et al., 2018). The present investigation suggests the pulsating plume dynamics as a possible mechanism of such kiloyear frequency in arc volcanisms, reported from various subduction zones (Conder et al., 2002; Marsh, 1979; Tamura et al., 2002). In the present experiments, the unsteady growth of plumes involved episodic partial melt supply into the overriding plate. For low slab dips ($\alpha < 30°$), the melt-rich domes produced thereby do not grow simultaneously to form plumes, rather they are episodically activated. I have calculated the time intervals of volcanic events from a single volcanic spot and compared them with the up-scaled values obtained from our experimental and numerical model results. It is worth mentioning that the frequency found from the experimental findings is bimodal with one peak at 20-30 kiloyear owing to small fluctuations in material influx within a single plume, and another peak at 300 kiloyear (Figure 3.18d), which can be attributed to a deficit of source material at the plume base. The numerical model produces a similar 270-500 kiloyear frequency

(Figure 3.18d) but not the 20 kiloyear frequency due to the model resolution, that likely failed to capture small-scale fluctuations within a single plume. Overall, the model results match with the time scales (200 to 400 kiloyear) of the frequency of natural volcanism (Figure 3.18d).

For high-angle slab dips ($\alpha > 30°$), Mode 2 plumes evolve in a pulsating manner as the trailing domes sequentially meet their roots, and accelerate the material supply through the plume tails. The estimates for time-dependent supply of partially molten materials indicate an episodic material flux on a time scale of 300–500 kiloyear, which may help explain the timescale of frequency in arc volcanism. For example, Prueher and Rea (2001) have reported from the Kamchatka–Kurile arcs episodic explosive volcanism at an average time interval of ~0.5 Ma (Prueher and Rea, 2001). Based on this match, it is suggested pulsating plume dynamics plays a crucial role in dictating the episodic behavior of arc volcanism in subduction settings.

3.4.4 Limitations

The present study adopted a mechanical modeling approach to develop the laboratory experiments and numerical simulations, excluding the possible effects of depth-dependent thermal and rheological changes. Thermo-mechanical modeling of subduction zones suggests that the complex thermal structures due to dehydration melting, coupled with strong temperature-dependent rheologies give rise to heterogeneity in the system. Such heterogeneities might eventually act as an additional factor in triggering subsidiary plume generations in the mantle wedge. The models are, however, simplified to show the effect of slab dip on the growth of cold plumes in the partially molten layer initiated by RTIs. Secondly, recent subduction models took into account compaction pressure to show partial melt focusing in the mantle wedge through porous media flows (Wilson et al., 2014). According to these models, varying bulk viscosity and permeability can largely control the direction of partial melt migration and thereby determine the location for partial melt focusing. The models exclude the role of such porosity driven partial melt advection, which is expected to play an important role in plume-driven upward advection of partially molten materials. Moreover, the mantle wedge flow is not considered in this experimental study, assuming that plumes ascend through a vigorously stirred wedge. In our numerical simulations the corner flow initiated by subducting plate motion (3 cm/year) was too slow to affect the updrift or plume growth velocity. There is a need to fully explore how the wedge flow can influence the mode of plume generation on a wide spectrum of

subduction kinematics. Mechanical mixing of partial melts originated at different depths during their updip advection is another potential factor to introduce complexity in plume dynamics. The present model has been simplified considering the partially molten zone as a single mechanical layer. The 3D models presented in this study were run for a limited time span (< 10 Ma), and they depict only the initiation of three-dimensional wave instabilities in the source layer. However, Zhu et al., (2009) ran 3D simulations on a long-timescale (~ 35 Ma) to demonstrate the evolution of complex 3D instability geometry as a function of the viscosity of partially molten zone, which was varied between 10^{18} to 10^{20} Pa s. Their models produced no finger-like plumes when the viscosity of the source layer was high (10^{20} Pa s). I performed numerical simulations mostly with 2D models because of our computational limitations.

The present laboratory models do not account for the probable effects of the lithospheric upper plate on plume distributions. Thermal variations at the lithosphere-asthenosphere boundary (LAB) can generate heterogeneities in the upper plate, which can influence the melt pathways at shallow depths, leading to higher-order variations in the plume distribution. However, the overall first-order distribution of plumes would be controlled mainly by the slab dip, as demonstrated from our CFD models.

Despite all these limitations, our simple analogue experiments and numerical models provide an insight into the role of slab dip in determining the distributions of volcanic centres in the overriding plates observed in the major subduction zones.

Chapter 4

Rayleigh-Taylor instabilities in thin geological strata: A theoretical approach

4.1 Introduction

Rayleigh-Taylor instability (RTI) plays a critical role in driving planetary processes on a wide spectrum, ranging from the core-mantle segregation and thermal plume generation to salt dome formation in sedimentary basins. RTI studies in the geological perspective focused mainly upon the mechanics of gravity instabilities in horizontally layered settings (Fernandez and Kaus, 2015; Houseman and Molnar, 1997; Miller and Behn, 2012; Ramberg, 1972, 1968; Schmalholz and Schmid, 2012; Turcotte and Schubert, 2014; Whitehead, 1986; Wilcock and Whitehead, 1991). However, in non-horizontal layered systems, the inherent inclinations of the layers become an added factor to influence the RTIs (El Jaouahiry and Aniss, 2020; Lister et al., 2011; Rohlfs et al., 2017). Some experimental findings suggest that updip advection of the buoyant materials can greatly influence the growth of gravitational instabilities in a dipping buoyant layer (Dutta et al., 2016; Lin et al., 2012; Lin and Kondic, 2010). Understanding the role of such layer-parallel advection in the RTI growth has many implications in interpreting gravity-driven structures in various geological settings, such as the development of salt domes on dipping source layers. Recent studies have shown the origin of cold plumes in subduction zones as a consequence of the RTIs in melt-rich zones resting above the inclined subducting slabs (Codillo et al., 2018; Gerya and Yuen, 2003b). In such dipping slabs, the layer parallel advection makes the material transport dynamics quite complex, and it cannot be fully explored within a framework of the RTI mechanics for horizontal density stratification. Previous studies suggest that the RTI patterns on inclined buoyant layers are markedly different from those reported for horizontal systems (Brun et al., 2015; Dutta et al., 2016; Gallaire and Brun, 2017; Lin et al., 2012). Unlike axisymmetric gravity structures in horizontal settings, the RTIs patterns show their directional growth in melt-rich layers on dipping slabs. These patterns have been investigated primarily as a function of viscosity

ratio of the melt-rich layer and the overlying mantle wedge (Zhu et al., 2009). However, the effects of varying slab-dips on the growth of cold plumes are yet to be fully explored. The slab-dip is expected to largely increase the buoyancy-driven advection of melt-rich materials in the updip direction. This phenomenon is accounted for various hydrodynamic problems, e.g., dripping of water drops down a sloping glass plate (Brun et al., 2015).

This study is organized in the following manner: In § 4.2 I briefly discuss the basics of lubrication approximation. In § 4.3 I discuss the effect of Couette flow on the saturation of the RTIs. In § 4.4 I treat the RTI and slab-parallel advection are treated as two competing mechanisms to control the gravity-driven flow in the melt-rich layer above a subducting slab. Using lubrication approximations, a theory is developed to find a dispersion relation for the wave instability in a buoyant layer, and perform a criticality analysis for the RTI/advection transition.

4.2 Lubrication approximation

Let H be the characteristic depth and L the characteristic length in the direction of the flow, and assume a shallow layer, such that

$$H/L \ll 1 \tag{4.1}$$

Let U be the scale of u, then by continuity, the scale of v must be UH/L in order not to violate mass conservation. Leaving the velocity and pressure scales U, P undermined for the time being, we introduce the following scales and normalized variables, denoted by primes,

$$t = Tt', x = Lx', y = Hy', u = Uu', v = U\left(\frac{H}{L}\right)v', p = Pp' \tag{4.2}$$

The continuity equation thus becomes

$$\frac{\partial u'}{\partial x'} + \frac{\partial v'}{\partial y'} = 0 \tag{4.3}$$

The momentum conservation equation is subdivided into longitudinal and transverse components. The longitudinal momentum equation is normalized to

$$\begin{aligned} &\frac{U}{T}\frac{\partial u'}{\partial t'} + \frac{U^2}{L}\left(u'\frac{\partial u'}{\partial x'} + v'\frac{\partial u'}{\partial y'}\right) \\ &\qquad = g\sin\alpha - \frac{P}{\rho L}\frac{\partial p'}{\partial x'} + \frac{\nu U}{H^2}\left(\frac{H^2}{L^2}\frac{\partial^2 u'}{\partial x'^2} + \frac{\partial^2 u'}{\partial y'^2}\right) \end{aligned} \tag{4.4}$$

Multiplying by $H^2/\nu U$, we get

$$\frac{H^2}{\nu T}\frac{\partial u'}{\partial t'} + \frac{UH^2}{\nu L}\left(u'\frac{\partial u'}{\partial x'} + v'\frac{\partial u'}{\partial y'}\right) = g\sin\alpha\frac{H^2}{\nu U} - \frac{PH^2}{\rho L\nu U}\frac{\partial p'}{\partial x'} + \left(\frac{H^2}{L^2}\frac{\partial^2 u'}{\partial x'^2} + \frac{\partial^2 u'}{\partial y'^2}\right) \tag{4.5}$$

From Eq. (4.1) we can write

$$\frac{UH}{\nu} = \mathcal{O}(1) \tag{4.6}$$

and

$$\frac{H^2}{\nu T} \ll 1 \tag{4.7}$$

Omitting these terms, the leading order equation becomes

$$\frac{\partial^2 u'}{\partial y'^2} - \frac{PH^2}{\rho L\nu U}\frac{\partial p'}{\partial x'} + g\sin\alpha\frac{H^2}{\nu U} = 0 \tag{4.8}$$

or in dimensional form

$$\frac{\partial^2 u}{\partial y^2} - \frac{1}{\rho}\frac{\partial p}{\partial x} + g\sin\alpha = 0 \tag{4.9}$$

Similarly, the transverse component of momentum equation becomes

$$\frac{H}{L}\left[\frac{U}{T}\frac{\partial v'}{\partial t'} + \frac{U^2}{L}\left(u'\frac{\partial v'}{\partial x'} + v'\frac{\partial v'}{\partial y'}\right)\right] = -g\cos\alpha - \frac{P}{\rho H}\frac{\partial p'}{\partial y'} + \frac{\nu U}{LH}\left(\frac{\partial^2 v'}{\partial x'^2} + \frac{\partial^2 v'}{\partial y'^2}\right) \tag{4.10}$$

or

$$\frac{H^2}{L^2}\left[\frac{H^2}{\nu T}\frac{\partial v'}{\partial t'} + \frac{UH^2}{\nu L}\left(u'\frac{\partial v'}{\partial x'} + v'\frac{\partial v'}{\partial y'}\right)\right] = -g\sin\alpha\frac{H^2}{\nu U}\frac{H}{L\tan\alpha} - \frac{PH^2}{\rho L\nu U}\frac{\partial p'}{\partial y'} + \frac{H^2}{L^2}\left(\frac{H^2}{L^2}\frac{\partial^2 v'}{\partial x'^2} + \frac{\partial^2 v'}{\partial y'^2}\right) \tag{4.11}$$

In dimensional variables, this becomes

$$\frac{1}{\rho}\frac{\partial p}{\partial y} + g\sin\alpha = 0 \tag{4.12}$$

Eq. (4.9) and (4.12) are the final result of lubrication approximation. They imply that the pressure scale can be given by

$$P = \frac{\rho L\nu U}{H^2}, or\ P = \rho gH\cos\alpha \tag{4.13}$$

This gives the velocity scale as

$$U = \frac{gH^2 \cos\alpha}{\nu L} \tag{4.14}$$

4.3 Gravity instability at the interface between two viscous fluids in a two-phase Couette flow

Consider a two-layer system (Figure 4.1) with a lower thin layer of thickness h and upper layer of height H sandwiched between two rigid plates. The upper and lower fluids have density ρ_2 and ρ_1 and viscosity μ_2 and μ_1 respectively with $\rho_2 > \rho_1$. A Cartesian coordinate system is chosen, with xz centered at the interface and the z axis in the vertical direction (positive upward). The interface is at $z = 0$ and the upper and bottom rigid layers are located at $z = H$ and $z = -h$, respectively. The upper plate is given a horizontal velocity of U_0 in the positive x-direction such that

$$U_0 = WH = \frac{U_2(z)H}{z} = \frac{U_1(z)h}{z} \tag{4.15}$$

In the following, we formulate an evolution equation for the interface and compare it will the work of Babchin (1983).

This theory is developed in the framework of mass and momentum conservation conditions. Considering incompressible fluid within the thin-layer, the mass conservation condition can be expressed by Eq (4.3) as

$$\frac{\partial v_1}{\partial z} + \frac{\partial u_1}{\partial x} = 0 \tag{4.16}$$

where the notations are changed to align them with the present problem. The subscript represents velocity component of fluid 1 (bottom fluid). The momentum conservation follows from Eq. (4.9) and (4.12) as

$$\frac{\partial p_1}{\partial z} = 0 \tag{4.17}$$

and

$$\mu_1 \frac{\partial^2 u_1}{\partial z^2} - \frac{\partial p_1}{\partial x} = 0 \tag{4.18}$$

where the trigonometric function is omitted as the bottom surface is horizontal. At the interface, we have the following BCs

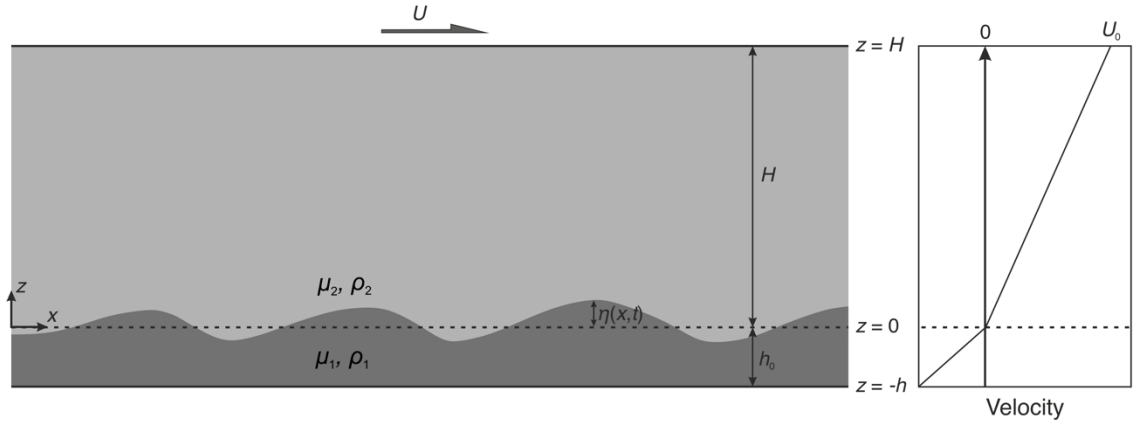

Figure 4.1: Schematic diagram of the two-layer fluid system subject to deformation by Couette flow.

The tangential stress BC

$$\left.\frac{\partial u_1}{\partial z}\right|_{z=0} = \mu \left.\frac{\partial u_2}{\partial z}\right|_{z=0} \tag{4.19}$$

where μ is the viscosity ratio given by μ_2/μ_1. We also have the normal stress BC, given by

$$p_1 = -\Delta\rho g\eta - \sigma\frac{\partial^2\eta}{\partial x^2} + \mu_2\frac{\partial v_1}{\partial z} \tag{4.20}$$

where the first term in the RHS is related to gravity, the second term is related to the surface tension and the last term is the viscous force exerted by the upper layer at the interface. Lastly, we have the kinematic BC at the interface which states

$$\frac{\partial\eta}{\partial t} = v_1|_{z=0} - \frac{U_0}{H}\eta\frac{\partial\eta}{\partial x} \tag{4.21}$$

At the lower boundary, we have

$$v_1|_{z=-h} = 0 \quad \text{and} \quad u_1|_{z=-h} = 0 \tag{4.22}$$

Using continuity equation (Eq. (4.16)) and Eq. (4.22), we get

$$v_1|_{z=0} = -\int_{-h}^{0}\frac{\partial u_1}{\partial x}dz \tag{4.23}$$

Next, we find an expression of u_1 by integrating Eq. (4.18) twice and using the BCs (4.19) and (4.22)

$$u_1 = \frac{1}{2\mu_1}\frac{\partial p_1}{\partial x}(z^2 - h^2) + \mu\left.\frac{\partial u_2}{\partial z}\right|_{z=0}(z + h) \tag{4.24}$$

Using Eq. (4.24) into (4.23), and then putting the result in Eq. (4.21) we get

$$\frac{\partial \eta}{\partial t} + \frac{U_0}{H}\eta\frac{\partial \eta}{\partial x} - \frac{h^3}{3\mu_1}\frac{\partial^2 p_1}{\partial x^2} + \mu\, h\frac{\partial u_2}{\partial z}\Big|_{z=0} = 0 \tag{4.25}$$

Finally, we express p_1 in terms of the normal stress condition (Eq. (4.20)) to get our final expression

$$\frac{\partial \eta}{\partial t} + \frac{U_0}{H}\eta\frac{\partial \eta}{\partial x} - \frac{h^3}{3\mu_1}\frac{\partial^2}{\partial x^2}\left[-\Delta\rho g\eta - \sigma\frac{\partial^2 \eta}{\partial x^2} + \mu_2\frac{\partial v_1}{\partial z}\Big|_{z=0}\right] + \mu\, h\frac{\partial u_2}{\partial z}\Big|_{z=0} = 0 \tag{4.26}$$

This expression is analogous to Kuramoto–Sivashinsky equation. It is known to produce solutions that can generate irregularly fluctuating quasi-periodic waves (Babchin et al., 1983). More importantly, it provides a mechanism for the saturation of an instability: the longwave modes transfer their energy to the shortwave modes, which are then damped by surface tension or viscosity.

4.4 Slab-parallel advection versus Rayleigh-Taylor instabilities in melt-rich layers in subduction zones: a criticality analysis

This study adopts a linear stability approach to develop a theory in predicting the critical slab-dip angle (α*) for the RTI/slab-parallel advection transition. Consider a buoyant layer (density: ρ_1) of uniform thickness (h_o) on a rigid slab with an inclination of α, placed beneath a denser fluid layer of height h_2 (density: ρ_2) (Figure 4.2). A Cartesian space (xz) is chosen with the x-axis at the base of the buoyant layer. The system is subject to the acceleration to gravity $\boldsymbol{g}$ in the vertical direction. In the theoretical formulation, the viscosity of fluids determines the dynamics of RTI, assuming negligible surface tension in the large-scale mechanical system considered here. The buoyant and the overburden fluids are assigned to viscosities, μ_1 and μ_2, where $\mu_1 < \mu_2$. The starting point of our theoretical derivation stands upon the lubrication approximation of the Navier-Stokes equation:

$$\begin{aligned} \frac{\partial p_1}{\partial x} &= \mu_1\frac{\partial^2 u_1}{\partial z^2} + \rho_1 g\sin\alpha\,, \qquad \frac{\partial p_1}{\partial z} = -\rho_1 g\cos\alpha, \\ \frac{\partial p_2}{\partial x} &= \mu_2\frac{\partial^2 u_2}{\partial z^2} + \rho_2 g\sin\alpha\,, \qquad \frac{\partial p_2}{\partial z} = -\rho_2 g\cos\alpha, \end{aligned} \tag{4.27}$$

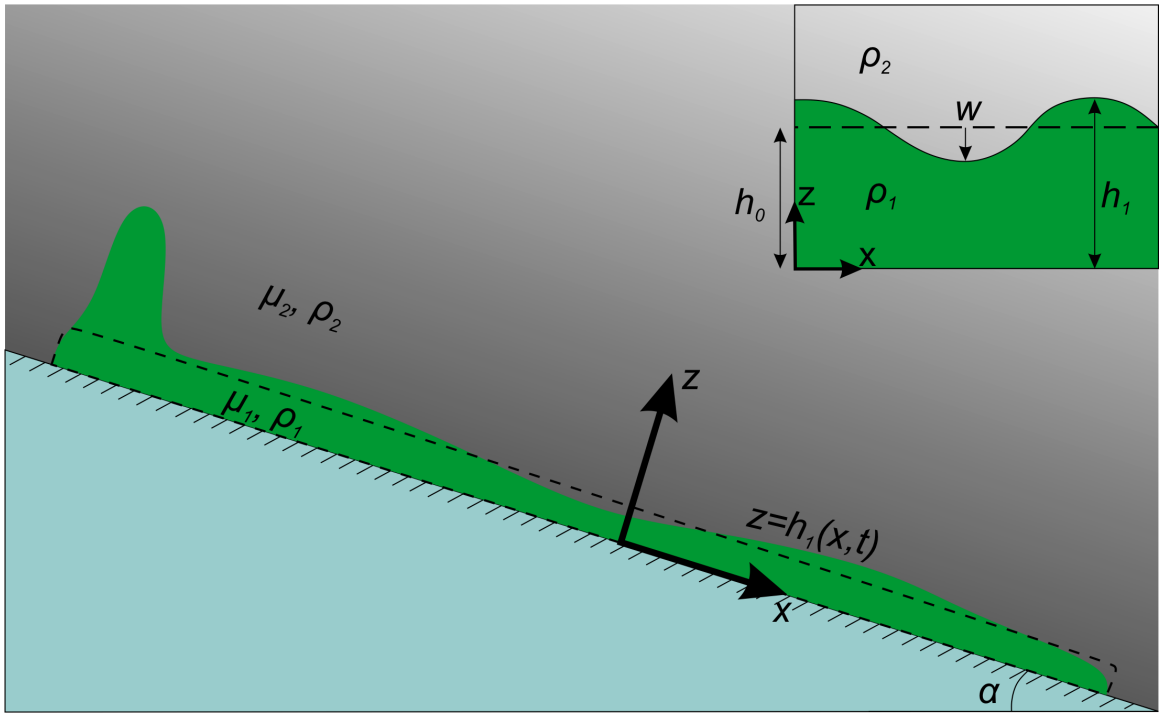

Figure 4.2: Consideration of a thin buoyant layer (density: ρ_1 and viscosity μ_1) on an inclined substrate with a denser overburden layer (density: ρ_2 and viscosity: μ_2). α denotes the inclination of the substrate to a horizontal plane. The initial condition is shown in dashed line. Inset shows deformed geometry of the interface due to RTI, where w and h_o represent the deflection and the initial layer thickness, respectively and h_1 is the height of the deformed interface at a point.

The two sets of equations are to be solved with boundary conditions appropriate to the physical setting: 1) mechanical coherence between the buoyant layer and the substrate, 2) velocity continuity across the fluid interface, 3) shear stress continuity across the same interface, and 4) pressure balance at the deformed interface, which follow

$$u_1|_{z=0} = 0, \tag{4.28}$$

$$u_1|_{z=h_1} = u_2|_{z=h_1}, \tag{4.29}$$

$$\left.\frac{\partial u_1}{\partial z}\right|_{z=h_1} = R\left.\frac{\partial u_2}{\partial z}\right|_{z=h_1}, \tag{4.30}$$

$$p_2|_{z=h_1} = p_1|_{z=h_1} + (\rho_2 - \rho_1)gw, \tag{4.31}$$

where u_1 and u_2 represents the slab parallel flow velocity in the source layer and overburden, respectively; $h_1$is the height of the deformed interface normal to the substrate. In Eq. (4.31) w is the layer-normal deflection of the interface, which is related to the characteristic length scale of the problem (H) and interfacial curvature (κ). We can express

w as a function of the interface curvature following the standard mathematical form: $w = H^2\kappa = H^2\frac{\partial^2 h_1}{\partial x^2}$. Theoretical problems of mechanical instability, driven by surface tension have used a capillary length scale to deal with the same relation between w and κ (e.g., Brun et al., 2015). For the mechanical setting of our present concern, the characteristic length scale H can be obtained from Re in the following expression, $H = \frac{Re\mu_1}{\rho_1 U}$.

We then integrate the momentum equation in the z-dimension Eq. (4.27), apply the boundary condition for pressure at the deformed interface Eq. (4.31), and differentiate the resultant equation with respect to x, which yields,

$$\frac{\partial p_1}{\partial x} = \frac{\partial p_2}{\partial x} - (\rho_2 - \rho_1)g\cos\alpha\frac{\partial h_1}{\partial x} - (\rho_2 - \rho_1)g\frac{\partial w}{\partial x}, \tag{4.32}$$

Similarly, for the overburden layer, we get,

$$\frac{\partial p_2}{\partial x} = \rho_2 g\cos\alpha, \tag{4.33}$$

Integrating the momentum equation in x-dimension, Eq. (4.27) yields the slab-parallel flow velocity,

$$u_1 = A_1 + B_1 z - \chi_1(x)z^2, \text{and } u_2 = A_2 + B_2 z - \chi_2(x)z^2, \tag{4.34}$$

for the source and the overburden layers, respectively, where

$$\chi_1(x) = \frac{1}{2\mu_1}\left(-\frac{\partial p_1}{\partial x} + \rho_1 g\sin\alpha\right),$$

and (4.35)

$$\chi_2(x) = \frac{1}{2\mu_2}\left(-\frac{\partial p_2}{\partial x} + \rho_2 g\sin\alpha\right)$$

Utilizing the other boundary conditions Eq. (4.28)-(4.30),

$$A_1 = 0;\ B_1 = 2\chi_1(x)h_1 + 2R\chi_2(x)[h_2 - h_1];\ \ B_2 = 2\chi_2(x)h_2 \tag{4.36}$$

On integration of u_1, the slab-parallel flow rate in the buoyant layer follows,

$$Q_1 = \int_0^{h_1} u_1 dz = \frac{2}{3}\chi_1(x)h_1^3 + R\chi_2(x)(h_2 - h_1)h_1^2, \tag{4.37}$$

Using the expressions of $\chi_1(x)$ and $\chi_2(x)$,

$$Q_1 = \frac{\rho_2 g}{\mu_1}\left[\frac{h_1^3}{3}\left(\left(\frac{\rho_2-\rho_1}{\rho_2}\right)\cos\alpha\frac{\partial h_1}{\partial x}+\left(\frac{\rho_2-\rho_1}{\rho_2}\right)\frac{\partial w}{\partial x}+\frac{\rho_1\sin\alpha}{\rho_2}\right)+\frac{h_1^2}{2}(h_2-h_1)\sin\alpha\right], \tag{4.38}$$

The gradient in flow rate, Q_1 determines the evolution of the interface in the condition of mass conservation, given by

$$\frac{\partial h_1}{\partial t} = -\frac{\partial Q_1}{\partial x}$$

$$= -\frac{\partial}{\partial x}\left[\frac{\rho_2 g}{\mu_1}\left\{\frac{h_1^3}{3}\left(\left(\frac{\rho_2-\rho_1}{\rho_2}\right)\left(\cos\alpha\frac{\partial h_1}{\partial x}+H^2\frac{\partial^3 h_1}{\partial x^3}\right)+\frac{\rho_1\sin\alpha}{\rho_2}\right)+\frac{h_1^2}{2}(h_2-h_1)\sin\alpha\right\}\right]. \tag{4.39}$$

Derivation of Eq. (4.39) follows Pozrikidis (2004). We will now evaluate the stability of the interface, subject to small perturbations in the following form,

$$h_1(x,t) = h_0 + \epsilon h_d(x,t), \tag{4.40}$$

assuming $\epsilon \ll 1$, (i.e., for infinitesimal displacement at the interface) and h_d is of $\mathcal{O}(1)$. Introducing this perturbation to Eq. (4.39), and keeping only the $\mathcal{O}(\epsilon)$ order terms, it follows

$$\frac{\partial h_d}{\partial t} = -\frac{\partial}{\partial x}\left[\frac{\rho_2 g}{3\mu_1}\left\{\left(\left(\frac{\rho_2-\rho_1}{\rho_2}\right)\left(h_0^3\frac{\partial h_d}{\partial x}\cos\alpha+H^2h_0^3\frac{\partial^3 h_d}{\partial x^3}\right)+\frac{\rho_1 3h_0^2 h_d\sin\alpha}{\rho_2}\right)\right\}+\frac{\rho_2 g}{2\mu_1}\{(h_2-h_0)2h_d h_0 - h_d h_0^2\}\sin\alpha\right] \tag{4.41}$$

Next, we now choose the spatio-temporal perturbation term in the form:$h_d(x,t) = Aexp(i(kx-\omega t))$ and obtain the following dispersion relation,

$$\omega = \left(\frac{\rho_2 g h_0^3}{3\mu_1}\left(\frac{\rho_2 - \rho_1}{\rho_2}\right)(k^2 \cos\alpha - H^2 k^4)\right) i + \frac{\rho_2 g h_0 \sin\alpha}{\mu_1}\left\{(h_2 - h_0) - \frac{\rho_1 h_0}{\rho_2} + \frac{h_0}{2}\right\} k. \quad (4.42)$$

Eq. (4.42) combines the advection and the amplification of perturbations at the interface between the two fluid layers. H is the characteristic length scale of the system. The imaginary part of this dispersion relation stands for the temporal growth rate of instability,

$$\sigma = \frac{\rho_2 g h_0^3}{3\mu_1}\left(\frac{\rho_2 - \rho_1}{\rho_2}\right)(k^2 \cos\alpha - H^2 k^4). \quad (4.43)$$

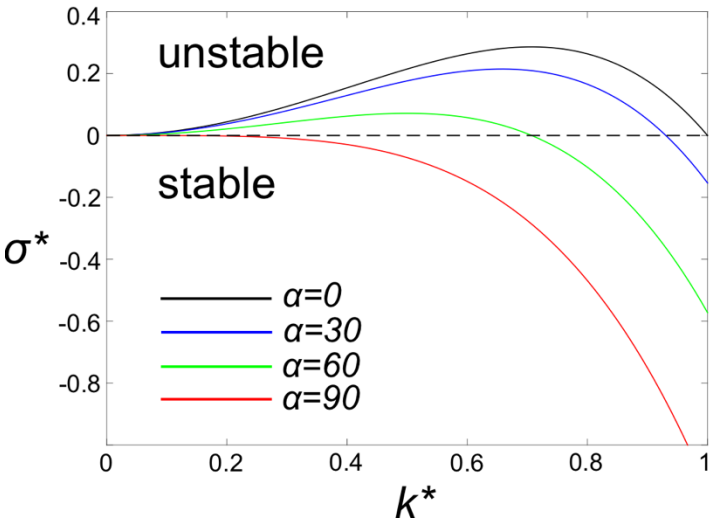

Figure 4.3: Normalized growth rates ($\sigma^* = \sigma.\mu_1 H^2/(\rho_2 - \rho_1)gh_0^3$) corresponding to normalized wavenumber ($k^* = k.H$) for α values varying from 0 to 90˚.

This equation evaluates the condition favouring the growth of instability for a specific wavenumber (k). The perturbed interface remains stable when $\sigma < 0$, or marginally stable when $\sigma = 0$. It turns to be unstable only when $\sigma > 0$ (Figure 4.3). Eq. (4.43) shows such an unstable condition demands $\rho_2 > \rho_1$ for the RTI growth; otherwise, the initial perturbations in the flow would dampen over time. Imposing $d\sigma/dk = 0$ in Eq. (4.43), one can find the dominant wavelength of fastest-growing instabilities,

$$\lambda_d = \frac{2\sqrt{2}\pi H}{\sqrt{\cos\alpha}} \quad (4.44)$$

It is obvious from Eq. (4.44) that, for $\alpha = \pi/2$, λ_d becomes indefinite, implying a stable state in the flow (Figure 4.4). The interface is generally potential to develop instability with a characteristic wavelength, which would be a minimum at $\alpha = 0$, i.e., in case of horizontal layers. The graphical plots of σ with k also reveal reducing growth rates of the instability with an increase in α (Figure 4.3). Now, we need to account for the slab-parallel advection process to show the existence of a threshold α for instability.

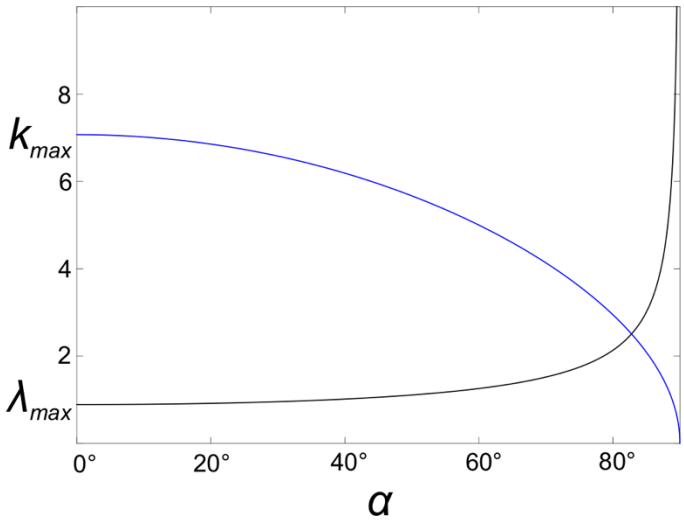

Figure 4.4: Variations of the most unstable wavenumber and wavelength with α

The real part of ω represents the advection velocity (V_0) of the wave for a uniform source layer thickness h_0, where,

$$V_0 = \frac{\rho_2 g h_0 \sin\alpha}{\mu_1}\left((h_2 - h_0) - \frac{\rho_1 h_0}{\rho_2} + \frac{h_0}{2}\right) \tag{4.45}$$

In Eq. (4.45) V_0 is proportional to α, and h_0. An increase in α would thus promote the advection process in the buoyant layer (Figure 4.5), and facilitate the material to accumulate at the upper edge of the layer, suppressing RTIs at the interface. The two processes: advection and RTI counter to each other, setting a critical condition in which one takes over the other.

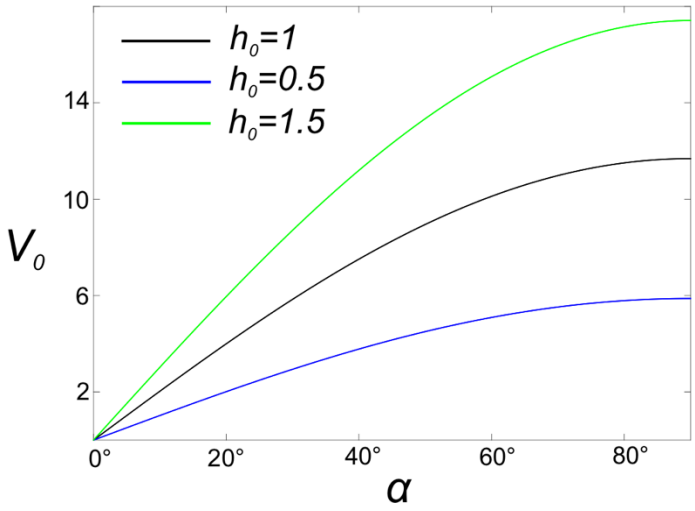

Figure 4.5: Increase of the advection velocity (V_0) with α for different h_o values

For the criticality analysis, we nondimensionalize the dispersion relation:

$$\frac{\omega^*}{\omega} = \frac{3\mu_1 H^2}{g(\rho_2 - \rho_1)h_0^3 \cos^2\alpha}, \qquad \frac{k^*}{k} = \frac{H}{\sqrt{\cos\alpha}}. \tag{4.46}$$

Using these non-dimensional terms in Eq. (4.46), it follows

$$\omega^* = U^* k^* + i(k^{*2} - k^{*4}), \tag{4.47}$$

where,

$$U^* = \frac{3H\rho_2}{h_0^2(\rho_2 - \rho_1)\cot\alpha\sqrt{\cos\alpha}}\left((h_2 - h_0) - \frac{\rho_1 h_0}{\rho_2} + \frac{h_0}{2}\right) \tag{4.48}$$

Eq. (4.48) represents the non-dimensional up-drift velocity (U^*). U^*increases with α (Figure 4.6) and a switch over from the interfacial instability to advection mode of flow in the buoyant layer occurs at a critical $U^*(U_c^*)$. To evaluate it, the Briggs-Bergs zero-group velocity criterion is adapted that takes into account the dispersion relation in a complex expression of both wavenumber (k) and frequency (ω) (Gallaire and Brun, 2017; Huerre and Monkewitz, 1990). So, considering the wave frequency in a complex form, we have

$$\omega^* = \omega_r^* + i\omega_i^* \tag{4.49}$$

Our non-dimensional velocity equation gives us,

$$\omega_i^* = -k_i^{*4} + k_i^{*2}(6k_r^{*2} - 1) + k_i^* U^* - k_r^{*4} + k_r^{*2} \tag{4.50}$$

which leads to:

$$\frac{\partial \omega_i^*}{\partial k_r^*} = -4k_r^{*3} + 2k_r^* + 12k_r^* k_i^{*2},$$
$$\frac{\partial \omega_i^*}{\partial k_i^*} = -4k_i^{*3} + 2k_i^*(6k_r^{*2} - 1) + U^* \tag{4.51}$$

According to this criterion, this transition can be determined from the saddle point $k_0 \in \mathbb{C}$ in the wave characteristics of instabilities, where a complex value of the wavenumber k_o exist to satisfy,

$$\frac{\partial \omega_i}{\partial k_i}(k_0) = \frac{\partial \omega_i}{\partial k_r}(k_0) = 0. \tag{4.52}$$

k_i and k_r are the imaginary and the real parts of the complex wavenumber, and ω_i is the imaginary wave frequency. An excellent description of this mathematical treatment is available in Brun et al. (2015). After taking Eq. (4.47) in a complex form, and applying the conditions in Eq. (4.53), we find that at the saddle point, the following holds

$$k_{0r}^{*2} = \frac{(1 + k_{0i}^{*2})}{2}, \quad \text{and} \quad -16k_{0i}^{*3} - 2k_{0i}^* = \frac{U^*}{2} \tag{4.53}$$

This leads to the normalized advection velocity at the transition to be given by,

$$U_T^* \approx 1.6. \tag{4.54}$$

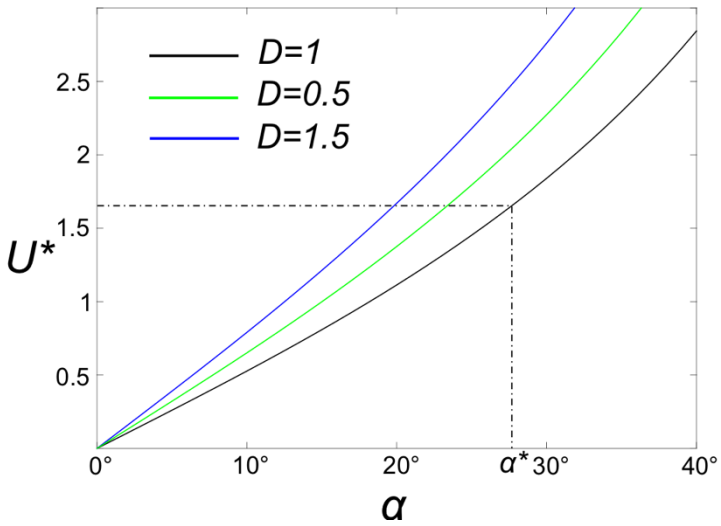

Figure 4.6: Nondimensional critical updrift velocity (U^*) versus α plots for different values of the non-dimensional characteristic length ($D = h_2 H / h_0^2$).

In a $U^* < U_T^*$ kinematic state, the RTI waves will amplify without any significant updip migration. On the other hand, the slab-parallel upward advection would dominate to

suppress the global instability when $U^* > U_T^*$. The critical slab-dip angle ($\alpha*$) corresponding to the $U^* = U_T^*$ condition can be obtained from Eq. (4.53). For the physical setting under consideration, we choose the parametric values: $\frac{\rho_2}{(\rho_2-\rho_1)} \sim 5$, h_2 = 200 km, h_0 = 10 km and H ~ 0.1 km, and find critical value of α (Figure 4.6),

$$\alpha^* \sim 28°, \tag{4.55}$$

The critical slab-dip angle (α^*) in Eq. (4.55) is consistent with the analogue and numerical model results as well as natural data . Considering different possible parametric values for natural subduction systems, α^* can however range from 20° to 28° (Figure 4.6).

Chapter 5

Three-dimensional patterns of Rayleigh-Taylor instability patterns in viscous layers: the effect of substrate inclination

5.1 Introduction

The interface of a fluid layer with another denser overlying fluid develops a hydrodynamic instability, called Rayleigh-Taylor instability (RTI), in the form of periodic waves, which grow vertically against the gravity direction. Such an instability sets in a horizontal pressure gradient, forcing the buoyant fluid to flow upward through the overlying denser fluid (Rayleigh, 1882). Using a linear stability analysis, the classical RTI theory (Taylor, 1950) predicts the unstable state of the interface between two inviscid incompressible fluids in a normal acceleration field, directed from the denser to the lighter fluid in the absence of surface tension. Bellman & Pennington, (1954) later advanced the theory to include the effect of surface tension at the interface and predicted the critical wavenumber (k_{max}) that preferentially favours the initial perturbations at the fluid interface to amplify at the fastest rate. A complete RTI theory for two semi-infinite fluid domains can be found in Chandrasekhar, (1961). In late 60s the role of inherent nonlinear growth of RTI was recognized as a factor to describe the evolution of instability structures**.** Rajappa, (1970) and Nayfeh, (1969) addressed this nonlinear problem by using a method of strained coordinate and asymptotic expansion, respectively. They showed that the nonlinear effects strengthen with progressive amplification of the interface instabilities and eventually captures the growth dynamics, forming specific patterns. For example, the growth of RTIs in a horizontally stratified setting can give rise to a hexagonal upwelling pattern in the underlying lighter fluid layer (Whitehead and Luther, 1975). The first major work on the 3D RTI structure was carried out by Jacobs & Catton, (1988a, 1988b), who presented a nonlinear analysis of the wavy interface with large amplitudes. They claimed from their theoretical and experimental analysis that weakly nonlinear analysis can predict RTI behaviour beyond the linear stability limit. They also showed that the eigenfunctions

corresponding to different patterns are amplified at different rates in the nonlinear domain. A line of theoretical studies dealt with the growth of instabilities in thin fluid films, treating the hydrodynamic setting with lubrication approximation. To show their dispersive behvaviour, some workers (Babchin et al., 1983; Fermigier et al., 1992) extended the theory with Fourier mode expansion to explain the surface patterns of RTIs. They used equations for thin films in predicting the transition between two different patterns. They also utilized the nonlinear analysis to derive the preferential selectivity of various 3D patterns.

The RTI theory subsequently gained remarkable momentum, owing to its applications in a wide spectrum of physical systems, ranging from millimetre-scale microfluidics to cosmic scale supernova as well as various technological operations, such as the nuclear weaponry during World War II. Earth scientists also extensively used this theory to model a number of planetary scale hydrodynamic processes, e.g., solar wind induced instabilities in ionosphere (Figure 5.1a) (Panda et al., 2019), plume generation in subduction zones (Figure 5.1b) and mantle (Kelly and Bercovici, 1997), and salt dome formation in sedimentary basins (Figure 5.1c) (Biot and Ode, 1965). Understanding the RTI phenomena is often quite demanding in many engineering applications, such as surface coating of solid bodies, where irregularities or detachment of droplets from the paint film become a major issue (Figure 5.1d). This kind of engineering problem has motivated a direction of RTI studies, primarily aimed at developing specific mechanisms to suppress the growth of such pendant drops (Cimpeanu et al., 2013; Sterman-Cohen et al., 2017). For example, in toroidal fusion reactors, the liquid metal coatings of inside reactor walls must be retained intact, allowing no droplets to form and fall into the plasma materials and quench the whole system (Katia et al., 2010). These studies eventually opened up a new theoretical paradigm of instability dynamics, governed by competing effects of surface tension on the process of gravity or acceleration driven drop formation.

A parallel line of studies investigates various hydrodynamic processes that suppress RTI in stratified fluids with density inversion. The pioneering work of Babchin et al., (1983) showed a layer-parallel convective flow can greatly impede gravitational instabilities in horizontal layers, allowing the stratified system to retain its hydrodynamic stability. Understanding the stabilization mechanisms later became a major focus of RTI studies, primarily to meet the increasing demand of industrial applications. This new attempt gave rise to a number of potential mechanisms, e.g., thermally induced surface tension gradient (Burgess et al., 2001), high-frequency vibration of the substrate (Lapuerta

et al., 2001; Sterman-Cohen et al., 2017) and induction of electric fields (Cimpeanu et al., 2013). Some workers demonstrated the stabilization as a function of the inclination of tilted stratification in the gravity field (Oron and Rosenau, 1989; Rohlfs et al., 2017). Experiments and linear stability analyses later showed that instability-driven dripping from fluid undercoating of an inclined plate completely ceases to occur when the inclination exceeds a critical value ($\sim 22°$) (Brun et al., 2015). The convective flow down the plate inclination has been recognized as the key factor to inhibit RTIs growth in the gravity direction. These studies predict the transition from absolute to convective instability for varying fluid film thickness, capillary length (Scheid et al., 2016), and other factors, such as the kinematic viscosity and density of participating fluids (Gallaire and Brun, 2017). This theory is further extended to show the effects of substrate curvature on the instability growth (Balestra et al., 2018). In a recent study, Lerisson et al., (2020) investigated the instability in a thin viscous film under an inclined substrate, considering the hydrodynamic steadiness in the experimental film to compute a time-dependent linear response of the instability growth. Their analysis enumerates the group velocity of the unstable wave packet to predict the growth of a front from a stationary localized perturbation imposed at the film boundary. Their prediction suggests that surface tension dampens the growth of short waves linearly in films, but the effects turn to be strongly nonlinear as the film thickness is reduced to a critical value. The most non-stationary structures, on the other hand, are span-wise invariant in response to an oscillating phase that prevails during the advection of fluid down the substrate dip. However, the nonlinear effect can dampen them, allowing the streamwise stationary rivulets to grow preferentially in the thin film. The authors conclude that a thin film would not immediately attain a dripping state for its initial flat configuration, but the process operates via an intermediate dynamic state.

Earlier theoretical and experimental studies have shown the most unstable wavenumbers of RTI and their corresponding growth rates in inclined fluid layers (Whitehead, 1982), cylinders (Lister et al., 2011) and films (Gallaire and Brun, 2017) as a function of the inclination for varying physical variables, such as viscosity ratio and surface tension. For a given condition, an increase in inclination facilitates advection-driven migration along the inclination direction. Despite all these advances, it is still unexplored, at least from a theoretical point of view, how the 3D RTI structures evolve in a flat buoyant viscous layer on a tilted substrate. This is in part due to difficulty with the nonlinear issues of this problem. Most of the earlier studies focused upon the 2D analysis of wave instabilities on a vertical section along the inclination direction of stratified settings. In this

thesis the study shows from physical experiments that the instabilities in inclined layers grow with characteristic 3D geometry, which cannot be theorized by a single set of waves. A new linear stability analysis is presented in the framework of Stokes equation for viscous flows to explain the 3D structures of instability as a product of two sets of interfering waves oriented along and across the inclination direction. The theoretical analysis is extended with a nonlinear treatment of the problem to show the 3D evolution of RTIs and their transition into a 2D form (cylindrical waves) with increasing substrate inclinations.

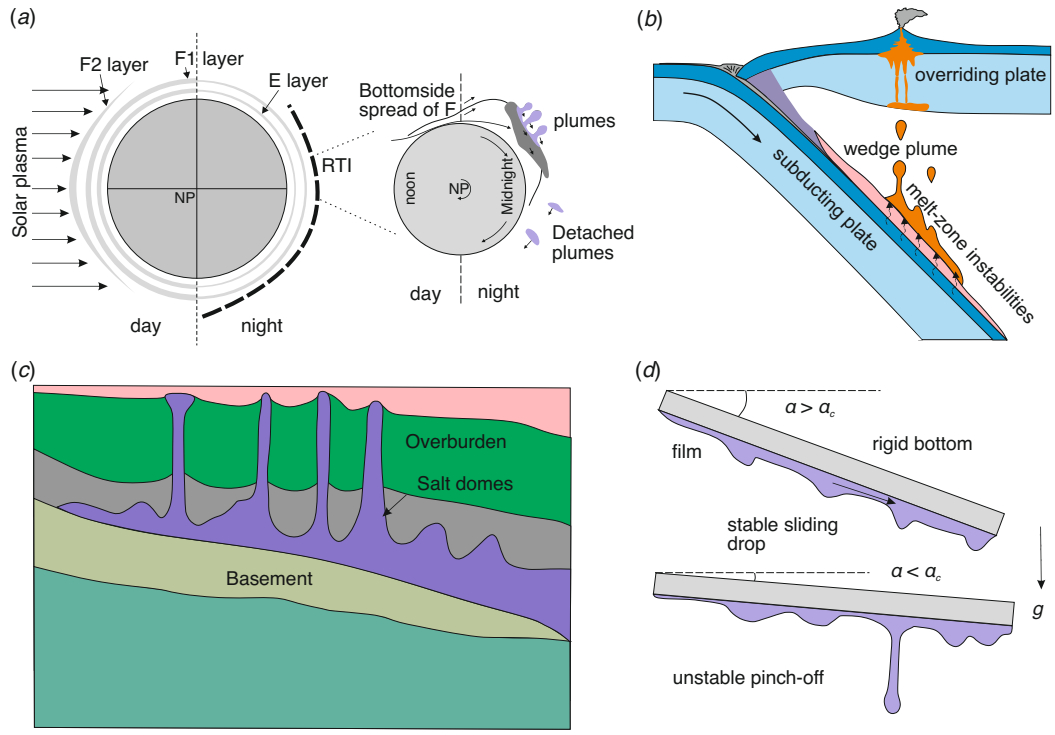

Figure 5.1: Rayleigh-Taylor instabilities (RTIs) in various natural settings with inclined orientations of the density stratification to the gravity direction. (*a*) (Left panel) Diurnal structure of ionospheric layers, showing the location of RTIs and (Right panel) formation of equatorial RTI-driven plasma bubbles (modified after Panda et al., (2019)). (*b*) Development of plumes initiated by RTI in the partially molten layer upon a subducting lithospheric plate (modified after Ghosh et al., (2020)). (*c*) Generation of RTI-driven salt domes in a dipping sedimentary rock sequence. (*d*) Dripping mechanisms of a fluid film during undercoating of an inclined rigid plate: (Top panel) temporal growth of instabilities, accompanied by convection down the plate slope and (Bottom panel) absolute instability; α: inclination angle of the substrate.

The chapter is organized in the following order: In § 5.2 I present my experimental findings of Rayleigh-Taylor instabilities in a thin viscous layer atop an inclined rigid substrate, below a denser fluid. The instabilities manifested at the inclined interface between the two fluids produce 3D geometrical patterns with varied symmetry, which

ultimately attain a 2D form with increasing substrate inclination. § 5.3 develops a theory to show contrasting wavenumbers of RTI instabilities and their corresponding growth rates along and across the inclination direction. In § 5.4 I extend the theoretical study with nonlinear analysis, up to third order to enumerate the finite geometry of instabilities for increasing substrate inclination.

5.2 Laboratory experiments

5.2.1 Method

Laboratory experiments were performed to produce Rayleigh-Taylor instabilities in a thin viscous-fluid layer of lower density, placed on an inclined rigid substrate, beneath an overburden fluid of higher density. PDMS fluid (ρ_s = 980 kg/m^3, μ_s = 100 Pa s) was used for the low-density layer, whereas water ((ρ_o = 965 kg/m^3, μ_0 ~ 10^{-3} Pa s) for the denser overburden fluid (Table 5.1). The two fluids are immiscible. We chose a transparent overburden (water) to capture the three-dimensional topography of instability at the interface between the two fluids.

Table 5.1: Material properties used in the laboratory experiments

Model Parameters	Symbol	Units	Value
Overburden density	ρ_o	kg/m^3	998
Overburden viscosity	μ_o	Pa s	10^{-3}
Source density	ρ_s	kg/m^3	965
Source viscosity	μ_s	Pa s	100
Viscosity ratio	R	-	10^{-5}

The experimental apparatus consisted of a rectangular (60 cm × 30 cm × 30 cm) glass box with dimensions (Figure 5.2). The box was first filled with water to form the overburden above the source layer. Within it, we placed a rectangular (60 cm × 30 cm × 5 cm) wooden plate in a slanted position, used as the rigid substrate to rest the buoyant fluid (PDMS) layer at the desired inclination (α). During an experimental run, the substrate was held in a fixed α orientation with the help of weight bars. Before placing the wooden plate inside the box, a volume of PDMS was spread over its top surface in a dry condition to

form a mechanically coherent, uniformly thick layer. It was 40 cm long, 25 cm wide and 10 mm thick buoyant layer beneath the denser overburden. The PDMS layer on the wooden plate was then left undisturbed for 2 to 3 hours to remove air bubbles trapped in it. I chose the dimensions of this layer less than those of the substrate to minimize the boundary effect. During an experimental run, the Rayleigh-Taylor instabilities developed at the interface between the PDMS layer and the overlying denser fluid.

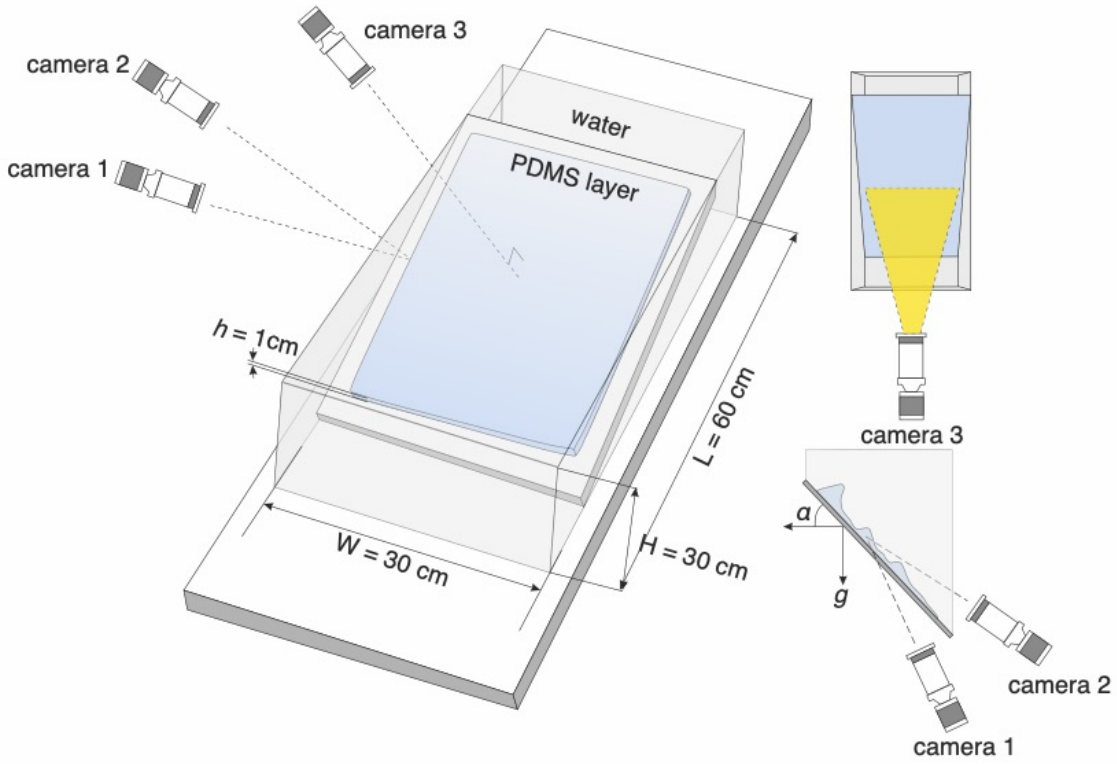

Figure 5.2: Schematics of the laboratory setup used for RTI experiments.

I ran a series of RTI experiments by systematically varying α. For $\alpha < 10°$, the inclination was chosen to vary between 4° and 8° at an interval of 2°, whereas for $\alpha \geq 10°$ (10° to 40°) at an interval of 10°. The progressive stages of instability growth were photographed at regular time intervals through lateral glass plates, maintaining a fixed focal length (18 mm). A stereo arrangement of the cameras was employed in the experiments to reproduce the 3D instability structures produced in the experimental setup (Figure 5.2). A total of three cameras were placed, with two of them on two sides of the box and the third one on the top. To describe the experimental setting, a Cartesian frame (*xyz*) is chosen with the *xy* plane parallel to the inclined substrate and the *x*-axis along the downslope direction

of the substrate (Figure 5.2). One of the side cameras was placed perpendicular to the long side wall to capture the 2D features on the *xz*- plane of the system, while the other camera was placed at an angle to the *xz*-plane to capture the details of the 3D features through the side wall. The top camera (Camera 3) was placed perpendicular to the inclined plane to capture the 3D structure of the interface between the PDMS and the overlying water.

Table 5.2: Parametric values measured form laboratory experiments

Exp.	α	h, cm	Runtime, s	d'	λ_x, cm	λ_y, cm
E3D01	4°	0.5	48500	0.06	1.2-1.5	1.2-1.4
E3D02	6°	0.5	46300	0.09	1.2-1.5	1.2-1.5
E3D03	8°	0.5	42800	0.12	1.3-1.7	1.2-1.5
E3D04	10°	0.5	36000	0.27	1.5-1.9	1.2-1.6
E3D05	10°	1.0	35200	0.55	2.1-2.8	1.7-1.9
E3D06	20°	0.5	35600	0.5	2.3- 2.5	1.3-1.8
E3D07	20°	1.0	32500	0.75	3.4-3.6	1.8-2.1
E3D08	30°	0.5	29800	0.9	11-13	1.5-1.9
E3D09	30°	1.0	25200	1.12	12.5-13	1.9-2.1
E3D10	40°	0.5	24000	1.08	-	1.4-1.9
E3D11	40°	1.0	23000	1.40	-	2-2.3

Using the data captured via these three cameras, we performed the following quantitative analysis. 1. The horizontal wavenumbers (k_x, k_y) were calculated using the camera perpendicular to the substrate (Camera 3). 2. The transverse and longitudinal

wavelengths (λ_x, λ_y) were measured using camera 1 and camera 3, respectively. 3. I evaluated the normalized transverse drift of the low-density material as a function of inclination for various dome-shaped structures. 4. The normalized amplification of low-density material was quantified using Camera 1 for various instabilities. A statistical mean was then calculated to obtain the amplification rate for a specific value of α.

Each experiment was run for about 5 to 10 hours. The growth time of instability varied depending upon the substrate inclination, α and buoyant layer thickness, h. In general, increasing α and h facilitated the growth rates of instability and thereby reduced the time duration of an experimental run (Table 5.2). All experiments were carried out under a static condition, considering no global flow in the overburden fluid.

5.2.2 Results

Reference experiments

I first present a reference experiment to demonstrate the mode of RTI evolution in a buoyant viscous layer inclined to the gravity direction (Figure 5.3). The instability develops 3D wave geometry at the interface between the buoyant layer and the denser overburden, forming well-defined directionality down the substrate slope. The structure progressively grows into series of elongate domes, periodically arranged in *x* and *y* directions, i.e., the downslope direction of the inclined substrate and the substrate-strike, respectively. Their geometrical analysis suggests that the 3D instability structure represents two distinct orthogonal sets of periodic waves with contrasting wavelengths, one set of waves down the substrate inclination with a characteristic wavelength λ_x , and the other set of waves with a wavelength λ_y (Figure 5.3). The instabilities at the inclined interface are thus initiated in the form of doubly periodic Fourier modes, where λ_x is found to be always greater than λ_y. Their wavenumber ratio, $k_y/k_x \approx 1.6 - 2.5$, implying that the 3D instability develops at a lower wave frequency down the slope direction than in the strike direction. However, the two wave trains were initiated simultaneously and grew, although at varying rates, to interfere with each other to form 3D waves at the interface. In the initial stage, the 3D structure amplified dominantly normal to the inclined substrate, giving rise to symmetrical elongate domes with their long axes aligned in the substrate's slope direction. At a given instant, their amplitudes (A to λ_y ratio) varied in a narrow range 0.1 to 0.4. I analyzed the spatial distribution of domes to study the 2D patterns of instability growth on the inclined

layer (Figure 5.3a). Unlike the hexagonal symmetry shown in earlier studies for horizontal layers (Whitehead and Luther, 1975), they form typically a rectangular symmetry typically with the long dimension aligned along the slope direction.

Another reference experiment run with a steeper substrate inclination is presented (Figure 5.3b). In this experiment $\lambda_x >> \lambda_y$, and the amplification rate of λ_x waves are far dominated by that of λ_y waves. The instability eventually transforms into a single Fourier mode, giving rise to a train of cylindrical waves at the interface, plunging down the substrate slope. These cylindrical structures strongly polarize the upward substrate-parallel advection to localize a row of plumes at their upper extremities.

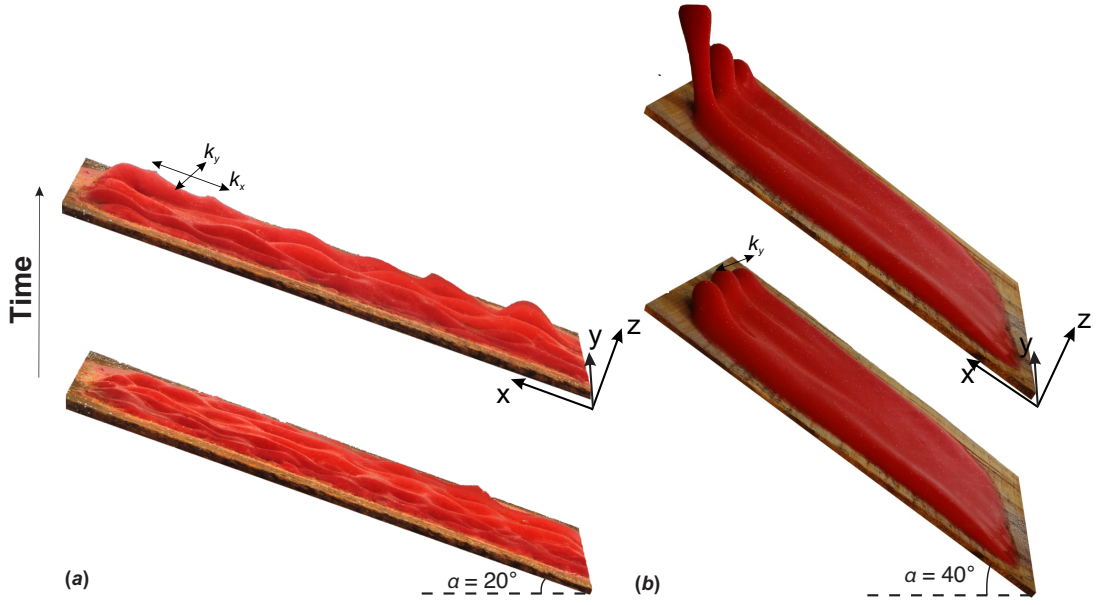

Figure 5.3: Contrasting modes of Rayleigh-Taylor instabilities in reference laboratory experiments: (*a*) gentle ($\alpha = 20°$) and (*b*) steep ($\alpha = 40°$) substrate inclinations. In (a), instabilities are initiated as a double mode of waves with unequal wavelengths ($\lambda_x > \lambda_y$), and their interference gives rise to periodic elongate domes, oriented along the inclination direction. In (b) the instability occurs in a single-mode, forming a train of cylindrical waves in the inclination direction. k_x and k_y are the wave vectors in the x and y directions.

Models with α < 10°

I ran a set of laboratory experiments to study the evolution of RTI on a gently dipping (α = 4°- 8°) substrate (Figure 5.4a). The experiments produced instabilities with nearly equal λ_x and λ_y ($\lambda_x/\lambda_y \sim 1 - 1.2$). The two trains of waves interfered to form nearly axisymmetric 3D domal structures in a hexagonal pattern with their wavelength

components, λ_x^* = 2.4-3 and λ_y^*= 2.4-2.8, normalized to the initial source-layer thickness (h). At an early stage, the instability pattern closely resembles those typically observed in horizontal stratification (α = 0°), extensively reported in the literature (e.g., Whitehead & Luther, 1975). The domes amplified preferentially in the vertical direction, but at varying rates (6-8 cm/hr) (Figure 5.5a), and they eventually transformed into asymmetric shape due to the substrate parallel up-dip advection of buoyant materials ($d^*{\sim}0.06-0.1$) (Figure 5.6a). In the advanced stages of the experimental run, some of the domes amplified nonlinearly with time to form vertical plume structures (*cf*. Jacobs & Catton, 1988).

Models with α ≥ 10°

Steepening of the substrate inclination ($\alpha \geq 10°$) resulted in a spectacular transition of the hexagonal symmetry of 3D instability into a rectangular pattern, with the long dimension oriented along the inclination direction (Figure 5.4b). The instability characteristically had unequal wavelengths in *x*- and *y*- direction ($\lambda_x^* = 3-3.8$ and $\lambda_y^* = 2.4-3.2$), forming periodic arrays of elongate domes with their long dimensions oriented down the substrate dip. The λ_y wave train dominated over λ_x waves to control the three-dimensional geometrical evolution of the instability structures. Increase in α facilitated the up-dip advection process during the instability growth, which in turn forced λ_x waves to migrate in the upslope direction at higher rates ($d^* = 0.27$), as depicted in Figure 5.6b. Consequently, the instability growth involved stronger upward phase advection (Figure 5.6b), as compared to that in $\alpha = 4°$ model. In this model, the double Fourier mode characteristically had larger wavelength ratios (λ_x/λ_y ~ 1.25-1.59).

Further increase in substrate inclination (α = 20°) resulted in a further change in the 3D instability geometry, primarily due to a large difference in the growth rates between the two wave trains, λ_x and λ_y (Figure 5.4c). The λ_x waves reduced their growth rates, allowing the λ_y waves to dominate in the instability process. Secondly, steepening of the substrate dip increased their wavelength ratios (λ_x/λ_y ~ 1.3-2), and the λ_x / λ_y wave interference gave rise to a 3D structure with rectangular symmetry, characterized by a set of long parallel ridges down the substrate dip. These ridges had wavy crest lines with a series of periodic culminations, which advected upward along the λ_x wave crest lines at a much higher rate ($d^*{\sim}0.5$) (Figure 5.6c). The vertical amplification rates of $\lambda_x$instability

were significantly lower than that for α = 10°, as shown from the calculated plots in Figure 5.6c.

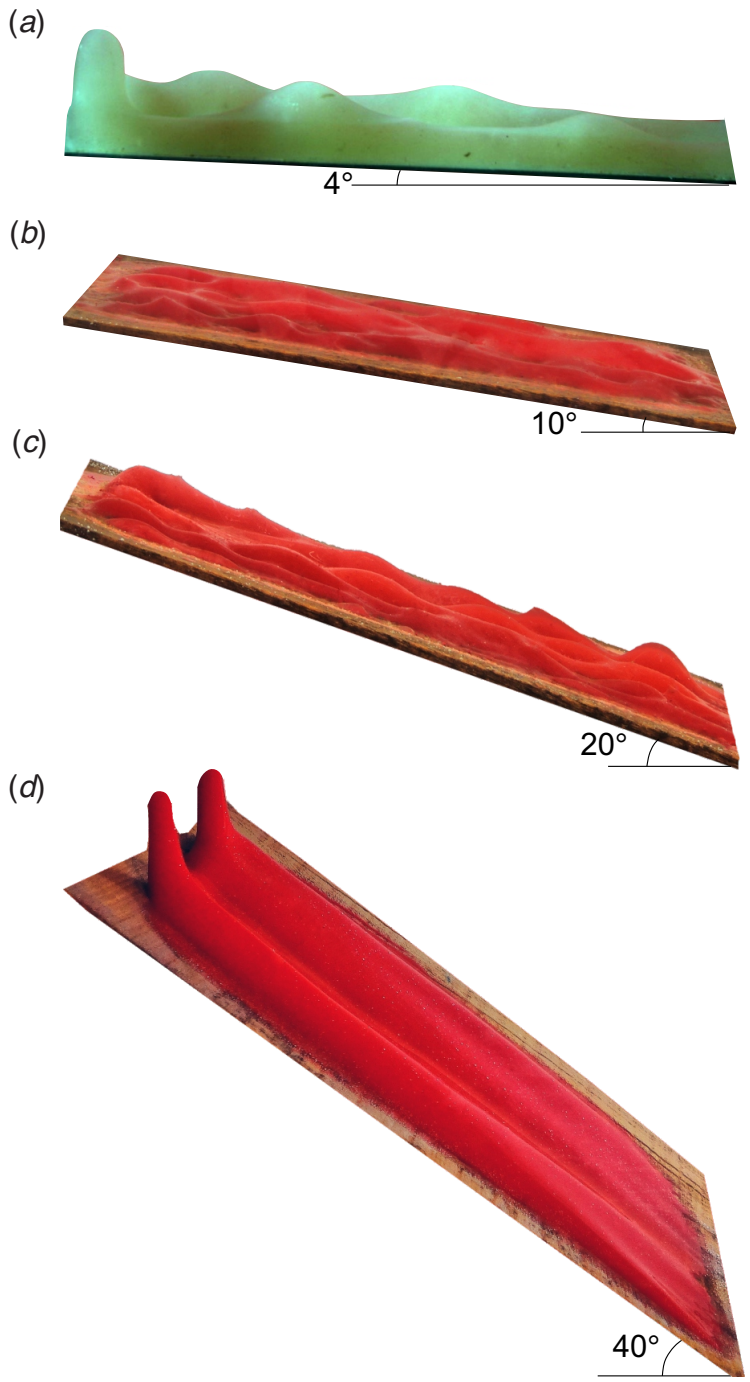

Figure 5.4: RTIs in laboratory models with increasing substrate inclination, $\alpha = 4$ to 40°. (*a*) Instabilities in a double-Fourier mode with $\lambda_x \approx \lambda_y$, forming plumes in a hexagonal pattern. (*b*) Double Fourier mode of instability with $\lambda_x > \lambda_y$, giving rise to a structure with rectangular symmetry, (*c*) Formation of elongate domes ($\lambda_x \gg \lambda_y$), and their upward advection. (*d*) Growth of a single set of cylindrical waves (λ_y) , which facilitate the upward advection process and eventually forms a row of plumes at their upper extremities.

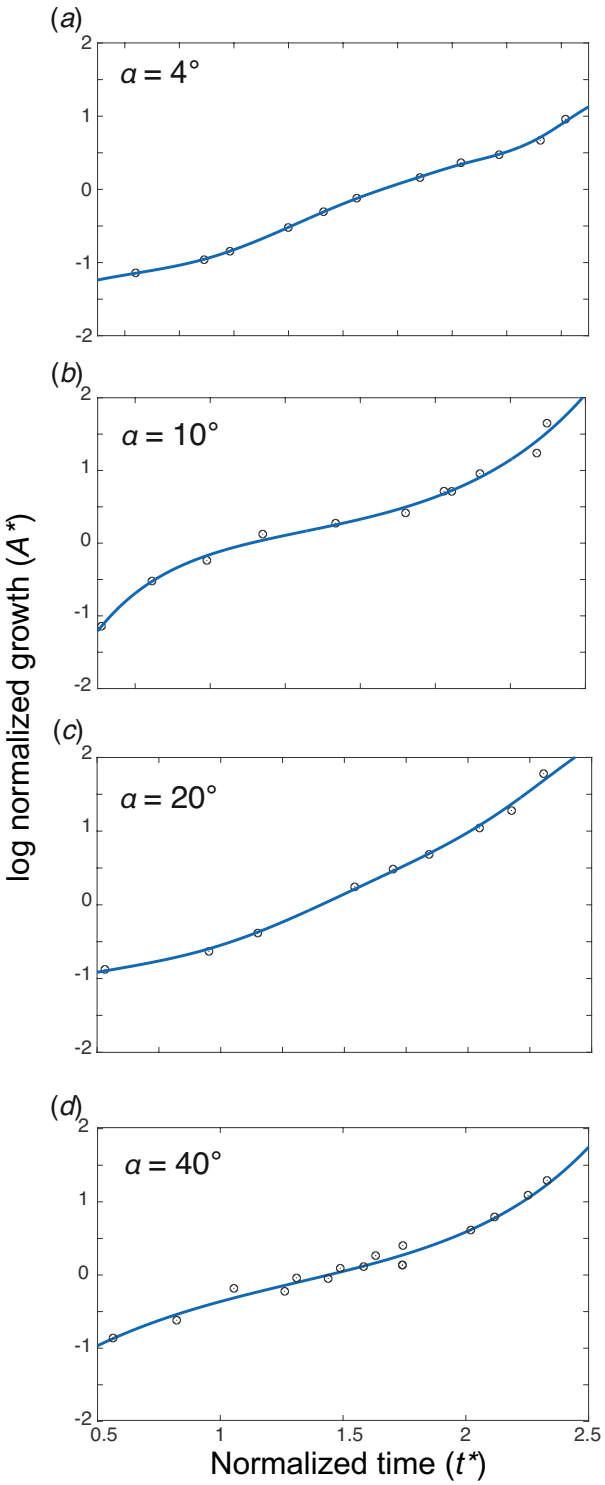

Figure 5.5: Measured plots of the normalized growth (A^*) of instabilities (logarithmic scale) in experiments as a function of normalized time (t^*) for increasing values of substrate inclinations.

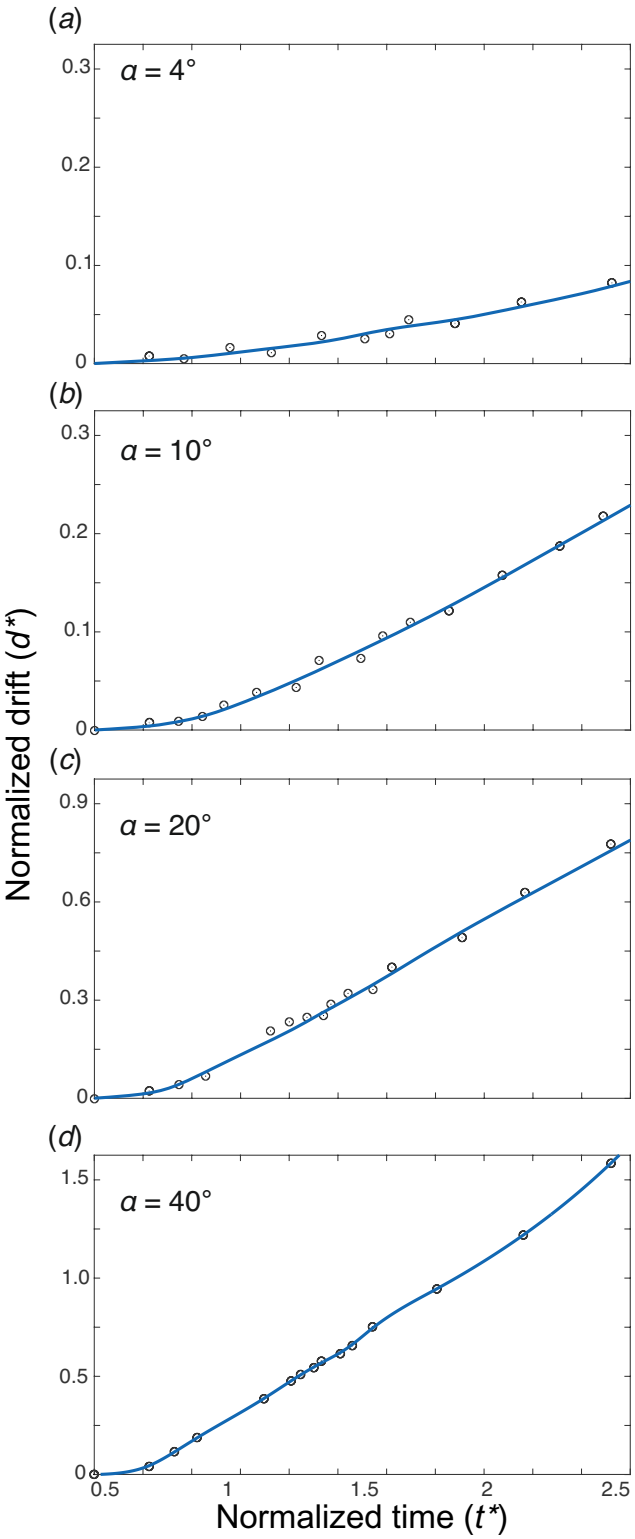

Figure 5.6: Temporal variations of normalized drift (d^*) of RTI domes, measured from the experiments run with different α values.

At $\alpha = 40°$, λ_x became much larger than λ_y ($\lambda_x/\lambda_y > 3$) and its frequency assumed a negligibly small value (i.e., $k_x \sim 0$). The λ_y waves eventually overshadowed the λ_x waves,

resulting in a 3D to 2D transition of the instability at the fluid interface (Figure 5.4d). Interestingly, the cylindrical structures acted as effective conduits to facilitate the upward advection of buoyant materials at high rates (d^*~1.08) (Figure 5.6d). Such λ_y-wave controlled substrate-parallel directional advection dampened the amplification of λ_x/λ_y interference (Figure 5.5d), and the RTIs transformed into a single Fourier mode of instability.

5.3 Linear stability analysis

5.3.1 Mathematical derivations

Consider a thin viscous layer (viscosity μ_1) of density ρ_1 and thickness h_1 upon an inclined rigid substrate with inclination α beneath another denser viscous fluid (viscosity μ_2) of density ρ_2, and thickness $h_2(x)$ ($\rho_2 > \rho_1$ and $h_2 \gg h_1$) (Figure 5.7). This mechanical system is subjected to a destabilizing gravity field with a vertical component $g_z = -g\cos\alpha$ and a downslope component, $g_x = -g\sin\alpha$, setting RTI at the interface between the two fluids. The local deflection at the interface is a function of the surface coordinates. $\boldsymbol{r} = (x, y)$, and its deformed geometry is expressed as, $h(r,t) = h_1 + \eta(\boldsymbol{r}, t)$, where $\eta(\boldsymbol{r}, t)$ is the deflection of the interface from its original position. In this subsection, I seek a general solution of the linear stability analysis for inclined viscous layers and find a dispersion relation for the wave instability using boundary conditions applicable to our problem. I consider two different coordinate frames, xy and $\hat{x}\hat{y}$ at the top surface of the inclined substrate for the buoyant fluid (source) layer and the denser overburden fluid with the z and $\hat{z}$ axes normal to the inclined substrate, as shown in Figure 5.7. For fluid 1, $z = 0$ is set at the base of the source layer on the inclined rigid substrate. Its interface with the overburden fluid at $t = 0$ is then given by $z = h_1$, and the top surface of the overburden can be expressed by $z = h_1 + h_2(x)$. The coordinate frame for fluid 2 is chosen with $\hat{z} = z - \big(h_1 + h_2(x)\big)$.

Assuming the fluids incompressible, we can write Navier-Stokes equation for the inclined system as

$$\rho\frac{\partial u_i}{\partial t} = -\nabla p + \mu\nabla^2 u_i + \left(\frac{\partial u_k}{\partial x_i} + \frac{\partial u_i}{\partial x_k}\right)\frac{d\mu}{dx_k} + \rho F_i \qquad (5.1)$$

$$F_i = \begin{bmatrix} -gsin\alpha \\ 0 \\ -gcos\alpha \end{bmatrix}$$

where u_i is the velocity of the fluid phases, ρ is the density, μ is the dynamic shear viscosity and p is the total pressure. The pressure in excess of hydrostatic pressure is given by

$$P(x, y, z, t) = p - \rho_2 g \cos\alpha \, z, \tag{5.2}$$

Equation (5.1) excludes the effects of surface tension, considering that this present theory applies to large scale systems where viscous forces play the dominant role in the instability dynamics.

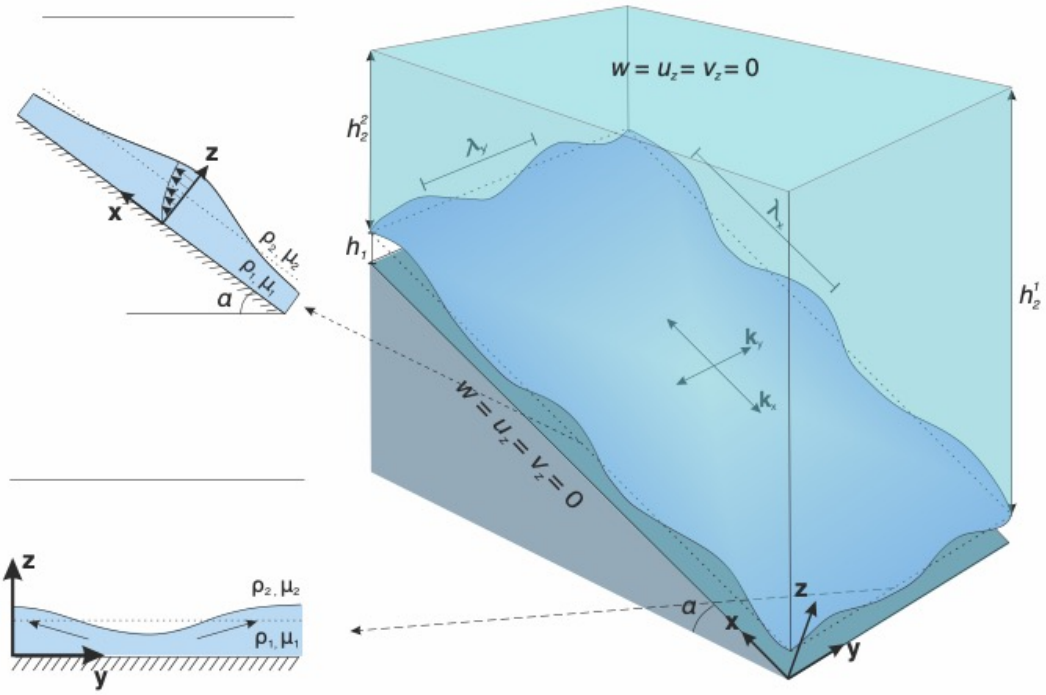

Figure 5.7: Sketch of the physical setting, showing the boundary conditions and the two Cartesian coordinate frames chosen for the linear stability analysis. A low-density (ρ_1) layer of uniform initial thickness, h_1 and viscosity, $\mu_1$and a high-density layer of viscosity μ_2 are confined by a traction free, horizontal surface at the top and an inclined substrate with a non-slip interface at the bottom. α is the substrate inclination. The sketch also illustrates the wavenumbers (k_x and k_y) and the corresponding wavelengths (λ_x and λ_y) of the double Fourier mode of instability at the interface between two fluids. Two cross-sections of the diagram are shown to represent the instabilities on the xz and yz planes.

The equation is expanded to express the corresponding velocity components,

$$\rho\frac{\partial u}{\partial t} = -\nabla p + \mu\nabla^2 u + \left(\frac{\partial w}{\partial x} + \frac{\partial u}{\partial z}\right)\frac{d\mu}{dz} + g\sin\alpha,$$

$$\rho\frac{\partial v}{\partial t} = -\nabla p + \mu\nabla^2 v + \left(\frac{\partial w}{\partial y} + \frac{\partial v}{\partial z}\right)\frac{d\mu}{dz}, \tag{5.3}$$

$$\rho\frac{\partial w}{\partial t} = -\nabla p + \mu\nabla^2 w + 2\frac{\partial w}{\partial z}\frac{d\mu}{dz} - g\cos\alpha,$$

where (u, v, w) are the velocity components along $x, y,$ and z coordinate axes.

The experimental models show that instabilities at the fluid interface develop a 3D wave structure, which, in its canonical form, can be conceived as a superposition of two orthogonal sets of waves, oriented parallel and perpendicular to the inclination direction (Figure 5.8). I thus considered two wave vectors, $k_x$and k_y corresponding to the x and y coordinate axis to deal with the 3D wave structure, and express the initial deflection at the interface in the following normal mode, exp $(ik_x x + ik_y y + \omega t)$. Using this expression in Eq. (5.3), I obtain

$$\begin{aligned} ik_x p &= -\omega\rho u + \mu\left(D^2 - (k_x^2 + k_y^2)\right)u + (D\mu)(ik_x w + Du) \\ &\quad - g\sin\alpha\,\delta\rho \\ ik_y p &= -\omega\rho v + \mu\left(D^2 - (k_x^2 + k_y^2)\right)v + (D\mu)\left(ik_y w + Dv\right) \\ Dp &= -\omega\rho w + \mu\left(D^2 - (k_x^2 + k_y^2)\right)w + 2(D\mu)(Dw) - g\cos\alpha\,\delta\rho \end{aligned} \tag{5.4}$$

And the condition of incompressibility gives rise to continuity equation as,

$$ik_x u + ik_y v = -Dw \tag{5.5}$$

where $D = d/dz$ is the derivative in the vertical direction. Simplifying Eq. (5.4), a generalized equation is obtained to find the condition of RTI initiation in the buoyant layer upon the inclined substrate as,

$$\begin{aligned} D\left\{[\omega\rho + \mu(D^2 - k^2)]Dw + (D\mu)(D^2 + k^2)w + ik_x\frac{g}{\omega}(D\rho)w\sin\alpha\right\} \\ = k^2\{[\omega\rho - \mu(D^2 - k^2)]w + 2(D\mu)Dw \\ - \frac{g}{\omega}(D\rho)w\cos\alpha\} \end{aligned} \tag{5.6}$$

In the foregoing analysis, the viscosity of the upper and lower layer is held constant but unequal to each other. Hence, the terms with $D\mu$ in Eq. (5.6) will be neglected from now on.

I now consider the following boundary conditions (BCs) to solve Eq. (5.6):

- $w_1 = Dw_1 = 0$ at the bottom bounding surface [$z = 0$; $\hat{z} = -(h_1 + h_2)$].
- $w_2 = Dw_2 = 0$ at the top bounding surface [$z = h_1 + h_2(x)$; $\hat{z} = 0$]
- $w_1 = w_2$ at the interface [$z = h_1; \hat{z} = -h_2$]
- $Dw_1 = Dw_2$ at the interface [$z = h_1; \hat{z} = -h_2$]
- $\mu_1(D^2 + k^2)w_1 = \mu_2(D^2 + k^2)w_2$ at the interface [$z = h_1; \hat{z} = -h_2$]
- The kinematic boundary condition for deflection at the interface requires,

$$\eta_t + u\eta_x + v\eta_y = w, \tag{5.7}$$

the subscripts in Eq. (5.7) indicate the derivatives of the term on the left side of the equation. The normal stress BC at the interface is given by

$$\left\{\left[\rho_2 - \frac{\mu_2}{\omega}(D^2 - k^2)\right]Dw_2\right\}\Big|_{\hat{z}=-h_2} - \left\{\left[\rho_1 - \frac{\mu_1}{\omega}(D^2 - k^2)\right]Dw_1\right\}\Big|_{z=h_1}$$

$$= -\frac{2k^2}{\omega}(\mu_2 - \mu_1)Dw_0 + \frac{g}{\omega^2}(\rho_2 - \rho_1)[ik_x^2 \sin\alpha - k^2\cos\alpha]w_0 \tag{5.8}$$

$$-\frac{\mu_2 k^3}{\omega^2}w_{to}$$

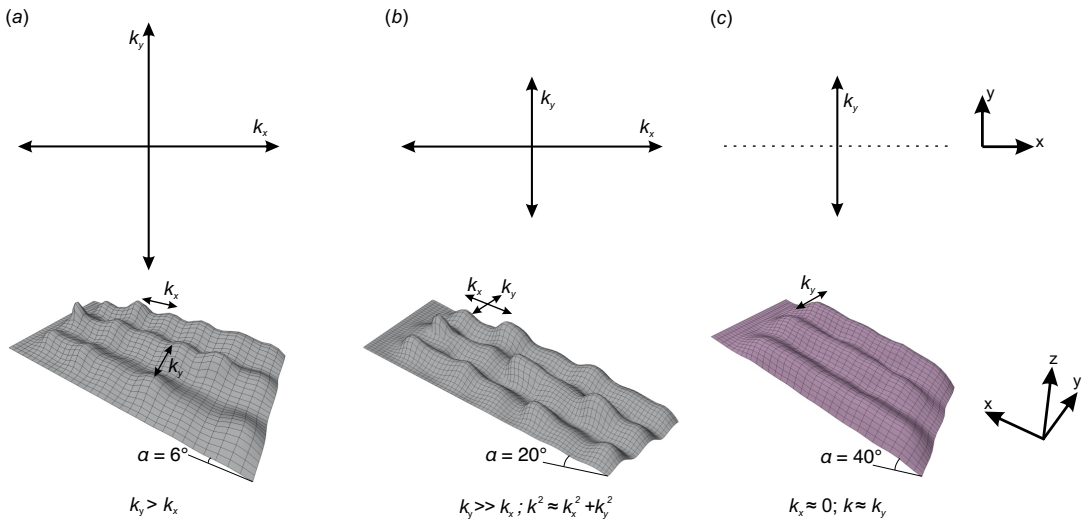

Figure 5.8: Different 3D instability structures generated by the interference of two orthogonal sets of waves in a double Fourier mode: (*a*) hexagonal pattern with $k_x \geq k_y$, (*b*) rectangular pattern with $k_y \gg k_x$ and (*c*) roll pattern with $k_x \approx 0$.

Now, for the lowest order of $\eta(\boldsymbol{r}, t)$, the flow is purely poloidal (Ribe, 1998), and it can be described by a poloidal potential function, Φ_n for each fluid, satisfying the following biharmonic equation,

$$\nabla^4 \Phi_n = 0 \tag{5.9}$$

$\eta(\boldsymbol{r}, t)$ and Φ_n are expressed in the form,

$$\begin{aligned} \eta(\boldsymbol{r}, t) &= \eta_0 f(r) e^{\omega t} \\ \Phi(\boldsymbol{r}, t) &= \phi_n(z) f(r) e^{\omega t} \end{aligned} \tag{5.10}$$

To satisfy the boundary conditions in Eq. (5.8) to Eq. (5.9), I take the potential in the following form (Canright and Morris, 1993),

$$\begin{aligned} \phi_1 &= A_1 \sinh(kz) + B_1 kz \cosh(kz) \\ \phi_2 &= A_2 \sinh(k\hat{z}) + B_2 k\hat{z} \cosh(k\hat{z}) \end{aligned} \tag{5.11}$$

Using these two equations in the boundary conditions, I obtain eight linear equations and solve them to find the dispersion equation:

$$\sigma(k) = \frac{g(\rho_2 - \rho_1) h_1 K^2 \cos\alpha - \mu_2 K'^3}{K \mu_1} \Omega \tag{5.12}$$

$$V_0 = \frac{\rho_2 g h_1^2 \sin\alpha}{K \mu_1} \Omega \tag{5.13}$$

where $\Omega = \left[\frac{(\sinh K - K)(\cosh K' - 1) + R(\sinh K' - K')(\cosh K - 1)}{(\sinh K' - K')(\sinh K + K) + 2R(\cosh K \cosh K' - 1 + KK') + R^2(\sinh K' + K')(\sinh K - K)} \right]$ (5.14)

and

$$\omega = V_0 + i\sigma$$

and R represents the viscosity ratio, μ_2/μ_1 , $K = 2kh_1$ and $K' = 2kh_2$.

Equation (5.12) and (5.13) combines the advection and the amplification of perturbations at the interface between the two fluid layers. The imaginary part of this dispersion relation stands for the temporal growth rate of instability, whereas the real part of ω represents the advection velocity (V_0) of wave instabilities in the source layer of uniform thickness h_1.

5.3.2 Results

As shown in earlier theoretical studies (Yiantsios and Higgins, 1989), the perturbed interface remains stable when $Im(\omega) < 0$, or marginally stable in the critical state, $Im(\omega) = 0$. It becomes unstable as $Im(\omega) > 0$. Eq. (5.12) shows such an unstable

condition demands $\rho_2 > \rho_1$ and $\alpha < \pi/2$ for the growth of RTIs; otherwise, the initial perturbations at the interface would decay over time. I utilize Eq. (5.12) to perform a dispersion analysis of the instability growth, which reveals the most unstable state of the interface corresponding to a specific wavenumber, denoted as k_{max} (Figure 5.9a). The mode of maximum instability can be calculated by applying $\frac{d\omega}{dk} = 0$ in Eq. (5.13),

$$K_{max} \sim \frac{(\rho_2 - \rho_1) g \cos\alpha}{\mu_2} \tag{5.15}$$

According to Eq. (5.15), the preferred mode k_{max} depends on the viscosities (μ_2/μ_1) of the source and overburden fluids and the rigid substrate inclination (α). It is also evident from Eq. (5.15) that, for $\alpha = \pi/2$, λ_d becomes indefinite, implying a stable state in the flow. For any value of $\alpha < \pi/2$, the interface is potential to develop instability with a characteristic wavelength, which would be a minimum at $\alpha = 0$, i.e., in the case of horizontal layers (Figure 5.9b).

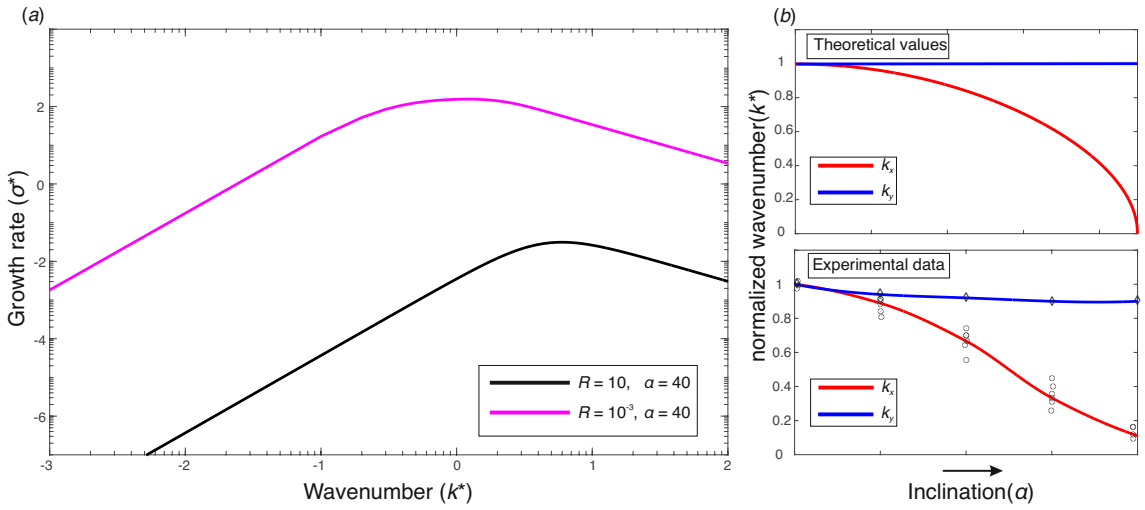

Figure 5.9: (*a*) Linearized growth rate (σ^*) of instability as a function of normalized wavenumber (k^*), for two different values of viscosity ratio (R). (*b*) Variation of k^* with the substrate inclination (α), extrapolated from theory and experimental observations.

Equation (5.12) can yield a number of dispersion relations for instability depending on the viscosity ratio $R = \mu_2/\mu_1)$ of the two-fluid layers. However, there can be two extreme situations (Ribe, 1998). The 'hard film' limit suggests a low-viscosity layer of semi-infinite thickness, resting on top of a relatively high viscosity layer develops instabilities with their corresponding growth rate curve characterized by a broad flat top.

The other limit corresponds to a thin, low-viscosity layer below an infinite fluid of higher viscosity, termed as "soft film", in contrast, favours the growth of instability for a specific value of k, i.e., the dispersion curve characterized by a distinct peak and a preferred mode of wavenumber (k_{max}). k_{max} shows a proportional relation with the viscosity ratio R. RTIs thus develop at shorter wavelengths for higher values of R (Figure 5.9a). I analyzed both $(k_x)_{max}$and $(k_y)_{max}$in terms of α to find how the substrate inclination would independently influence the two sets of RTI waves along and across the inclination direction, observed in laboratory experiments. k_x decreases nonlinearly with increasing α (Figure 5.9b), whereas k_y remains almost constant with α (Figure 5.9b). This theoretical finding agrees well with the experimental result (Figure 5.9b).

The growth rate σ is also found to be sensitive to α, but not equally for the two sets of waves corresponding to k_x and k_y (Figure 5.10). The substrate-strike parallel waves [λ_x] with k_x show strongly decreasing σ with increase in α. On the other hand, the growth rate of the waves [λ_y] plunging down the substrate slope with k_y remains virtually constant. At large substrate inclinations ($\alpha > 30^{\circ}$) λ_x waves hardly grow in amplitudes, leaving the interface instability captured by λ_y waves (Figure 5.10). The absence of λ_x/λ_ywave interference eventually results in RTI instabilities to grow in a train of cylindrical waves along the inclination direction.

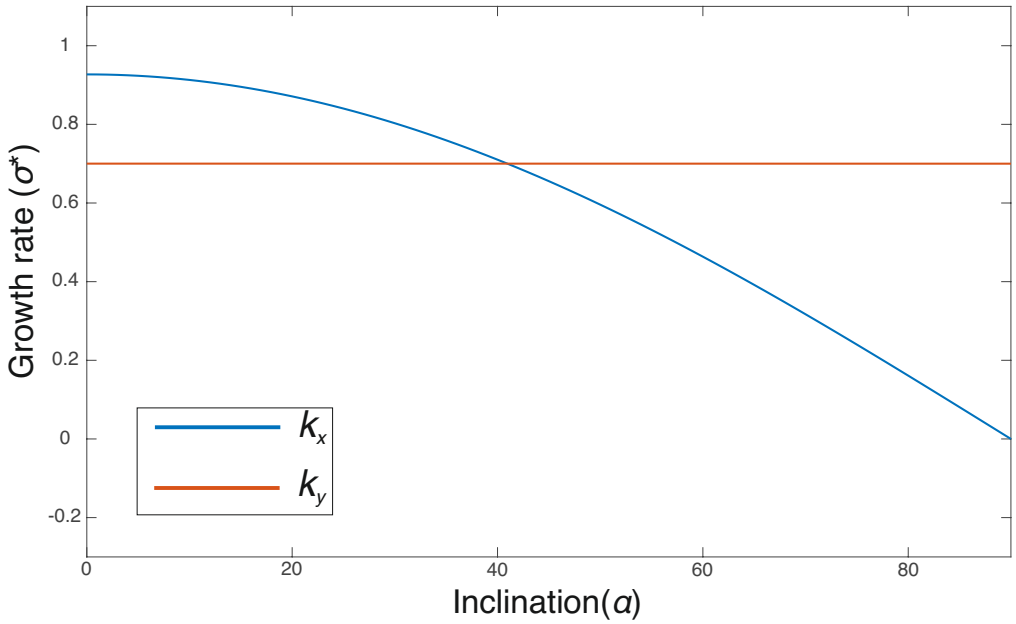

Figure 5.10: Normalized growth rate (σ^*) of instability as a function of inclination (α) both for k_x and k_y.

The theoretical analysis presented in this section allows us to explain the 3D to 2D transition of RTIs with increasing substrate inclination in our laboratory experiments. I evaluated the advection velocity (V_0), the real term of $\omega(k)$ in Eq. (5.13), as a function of substrate inclination (α) and initial layer thickness (h_1). An increase in α facilitates V_0 (Figure 5.11). It means that, for large α values λ_x waves grow slowly but advect up the substrate inclination at fast rates, as observed in experiments . These waves thus have little scope to grow and interfere with λ_y waves. Their fast advection forces them to localize at the upper edges of the source layer, forming a series of periodic plumes, as seen in the experiment with a large substrate inclination.

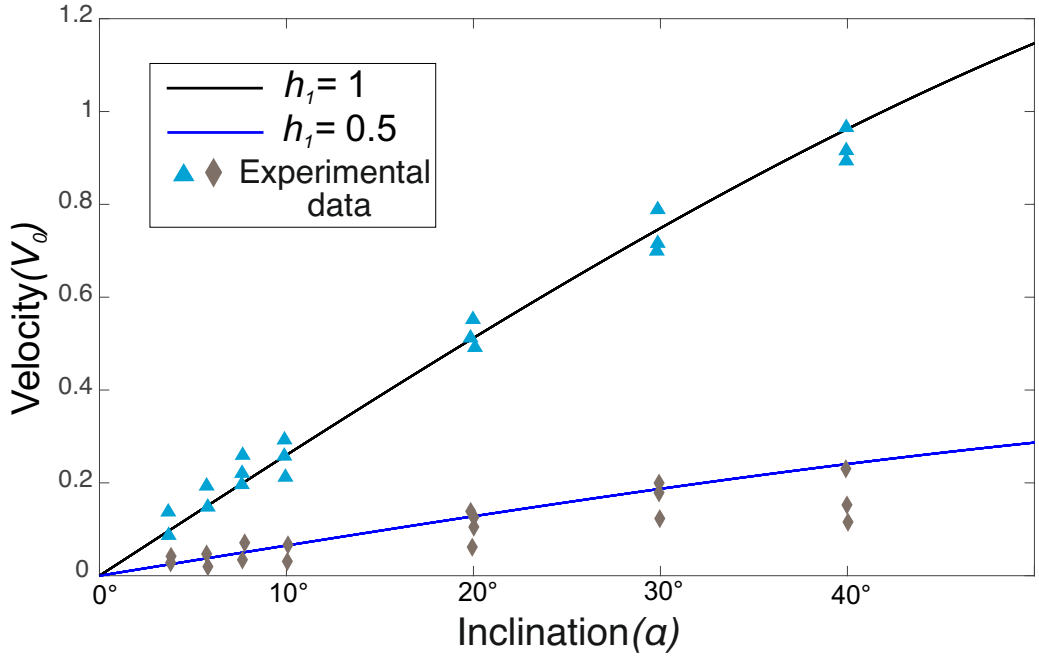

Figure 5.11: Variations of normalized advection velocity (V_o^*) with increasing substrate inclination (α) for different source-layer thicknesses (h_1).

5.4 Non-linear analysis of the instability patterns

5.4.1 Mathematical framework

I extend the linear stability analysis in § 5.3 with a weakly nonlinear theory to explain the finite growth pattern of instabilities at the interface observed in our laboratory experiments. The linear theory is no longer applicable as the interface instabilities progressively grow to large finite amplitudes with time. The problem thus demands nonlinear interactions within the system to predict the evolution of interface geometry and associated flow kinematics in the inclined source layer. To develop this nonlinear theory, I choose the same Cartesian

space with the *xy*-plane at the interface (Figure 5.8), and express the interface in terms of a function $F(x, y)$, which satisfies the following wave equation,

$$\nabla_r^2 F_n(r) = -k^2 F_n(r) \tag{5.16}$$

The first step would be to nondimensionalize the whole system of equations in terms of $1/k$ and $\sqrt{(g/k)}$, which represent length and velocity scales, respectively. The two main parameters we consider here are the interface deflection (η) and the velocity field, represented by poloidal potential ϕ. For small amplitudes of the instabilities, we can neglect the non-linear components of the solution in (5.16) and expand η and ϕ in the following way.

$$\begin{aligned} \eta(r,t) &= \sum_n \eta_n(t) F_n(r), \\ \phi(r,z,t) &= \sum_n \phi_n(t) G_n(r,z), \end{aligned} \tag{5.17}$$

where F_n and G_n are the Fourier modes (eigenfunctions) corresponding to the linear problem.

Adopting the multiple scales method (J. W. Jacobs and Catton, 1988; Nayfeh, 1969) used to solve weakly non-linear RTI problems, we expand the solutions of Eq. (5.17) in terms of a small parameter ϵ as,

$$\begin{aligned} \eta_1 &= \epsilon\eta_{11}(\tau) + \epsilon^2\eta_{21}(\tau) + \epsilon^3\eta_{31}(\tau) + \cdots, \\ \phi_1 &= \epsilon\phi_{11}(\tau) + \epsilon^2\phi_{21}(\tau) + \epsilon^3\phi_{31}(\tau) + \cdots, \end{aligned} \tag{5.18}$$

The above equations transform the time variable (t) to a different form (τ), where $\tau = t + \epsilon^2 t + \cdots$, is the *strained variable*. We are going to evaluate the inner solution with respect to this strained variable in time as well as the outer solution in terms of the original time variable. As we know, the outer solution of (5.18) for the travelling waves is not valid for $K^2 - 1 \sim \mathcal{O}(\epsilon^2)$ (Nayfeh, 1969),

$$\begin{aligned} \eta_1 &= \eta_{10}(t_1) + \epsilon^2\eta_{12}(t_1) \ldots, \\ \phi_1 &= \epsilon\phi_{10}(t_1) + \cdots, \\ t_1 &= \epsilon t, \end{aligned} \tag{5.19}$$

where $K = 2kh_1^c$ with h_1^c being the critical thickness of source layer below which no instability will form.

After substituting these expansions into our main equations, the *inner solution* leads to the following differential equation,

$$\frac{\partial \eta_{11}^2}{\partial t^2} + \beta \tanh h_1 \cos \alpha \, \eta_{11} = \frac{1}{2} F \cos \alpha \tanh h_1 \, \eta_{11}^3, \tag{5.20}$$

where F is a constant related to the geometry of the problem defined by Eq. (5.16). With the initial conditions,

$$\eta_{11}(0) = 1 \quad \text{and} \quad \frac{\partial \eta_{11}(0)}{\partial t} = 0, \tag{5.21}$$

the solution of Eq. (5.20) takes the form

$$\eta_{11} = \mathrm{cn}(\Lambda t_1 | m) \tag{5.22}$$

with

$$\Lambda^2 = \tanh h_1 \, (\beta - \frac{1}{2} F) \cos \alpha, \tag{5.23}$$

where m is a function related to the Fourier mode and cn is a Jacobian elliptic function. This equation gives us a first-hand idea that the instability occurs when $\beta < \frac{1}{2} F$. Considering β very large, Eq. (5.22) leads to the following solution

$$\eta_{11} = \cosh \sigma_1 t + \cdots, \tag{5.24}$$

where,

$$\sigma_1^2 = (1 - \cos \alpha \, K^2) \tanh h_1, \tag{5.25}$$

We also seek an *outer solution* of the nonlinear problem to define the other limits of K. This is achieved by utilizing Eq. (5.19) and our governing equations.

For $\mathcal{O}(\epsilon)$,

$$\frac{\partial \eta_{11}}{\partial \tau} - \tanh h_1 \, \phi_{11} = 0, \text{and } \frac{\partial \phi_{11}}{\partial \tau} - (1 - \cos \alpha \, K^2) \eta_{11} = 0 \tag{5.26}$$

The solution of this type of equation is,

$$\eta_{11} = \cosh \sigma_1 \tau, \qquad \phi_{11} = \frac{\sigma_1}{\tanh h_1} \sinh \sigma_1 \tau \tag{5.27}$$

where σ_1 again is given by Eq. (5.25).

For $\mathcal{O}(\epsilon^2)$, it follows from Eq. (5.24), after taking the quadratic combinations of $\mathcal{O}(\epsilon)$ solutions

$$\begin{aligned}\frac{\partial \eta_{21}}{\partial \tau} - \tanh h_1\, \phi_{21} &= \eta_{11}\phi_{11}(C_{111} - D_{111}) \\ \frac{\partial \phi_{21}}{\partial \tau} - (1 - \cos\alpha\, K^2)\eta_{21} &\\ = -\tanh h_1 \cos\alpha\, \eta_{11} \frac{\partial \phi_{11}}{\partial \tau} C_{111} &\\ - \frac{\phi_{11}^2}{2}\left(D_{111} + \tanh^2 h_1\, C_{111} \right) &\end{aligned} \tag{5.28}$$

The solution on the $\mathcal{O}(\epsilon^2)$ eventually yields,

$$\begin{aligned}\eta_{21} &= A'_{21} \cosh\sigma_1\tau + A''_{21}(1 - \cosh\sigma_1\tau) \\ \phi_{21} &= B'_{21} \sinh 2\sigma_1\tau + B''_{21} \sinh\sigma_1\tau\end{aligned} \tag{5.29}$$

Finally, considering $\mathcal{O}(\epsilon^3)$, which have the contributions from both $\mathcal{O}(\epsilon^2)$ and $\mathcal{O}(\epsilon)$ terms, we obtain

$$\begin{aligned}\frac{\partial^2 \eta_{31}}{\partial \tau^{\,2}} - \tanh h_1\, (1 - \cos\alpha\, K^2)\eta_{31} &\\ = (\sigma_1 P'_1 + \tanh h_1\, Q'_1 - 2\sigma_1^2 \xi)\cosh\sigma_1\tau &\\ + (3\sigma_1 P''_1 + \tanh h_1\, Q''_1)\cosh 3\sigma_1\tau \;+\; \tau \tanh h_1\, Q'''_{11} &\\ +\; (2\sigma_1 P''''_{11} + \tanh h_1\, Q''''_{11})\cosh 2\sigma_1\tau. &\end{aligned} \tag{5.30}$$

The solution of Eq. (4.13) is of the form,

$$\begin{aligned}\eta_{31} = A''_{31}(\cosh 3\sigma_1\tau + \cosh\sigma_1\tau) + A'''_{311}(1 - \cosh\sigma_1\tau) &\\ + A''''_{311}(\cosh 2\sigma_1\tau - \cosh\sigma_1\tau) &\end{aligned} \tag{5.31}$$

The coefficients A, B, C, D, P, Q are related to the interface geometry and are provided in Jacobs & Catton, (1988a).

By combining (5.27), (5.29) and (5.31), we obtain the final equation for the temporal part of the interface deflection,

$$\begin{aligned}\eta_1 = \epsilon\cosh\sigma_1\tau + \epsilon^2[A'_{21}\cosh\sigma_1\tau + A''_{21}(1 - \cosh\sigma_1\tau)] &\\ + \epsilon^3[A''_{31}(\cosh 3\sigma_1\tau + \cosh\sigma_1\tau) + A'''_{311}(1 - \cosh\sigma_1\tau) &\\ + A''''_{311}(\cosh 2\sigma_1\tau - \cosh\sigma_1\tau)] + \cdots &\end{aligned} \tag{5.32}$$

After some simplification, Eq. (5.30) becomes

$$\eta(r,t) = \epsilon \cosh \sigma_1 \tau + \left[\epsilon^2 \left(\frac{1 - 2\tanh^2 h_1}{8 \tanh h_1}\right)(2\cosh \sigma_1 \tau - 1)\right] + \epsilon^3 \left[\left(\frac{7\tanh^2 h_1}{8} + \frac{3}{32\tanh^2 h_1} - \frac{39}{38}\right)(\cosh 3\sigma_1 \tau - \cosh \sigma_1 \tau)\right] F_n(r) \quad (5.33)$$

The nonlinear growth of $\eta(r,t)$ with time for different modes are depicted in Figure 5.12. In general, we see a marked difference in the growth patterns, depending on the initial source-layer thickness (h_1) and different geometries corresponding to different substrate inclination (α).

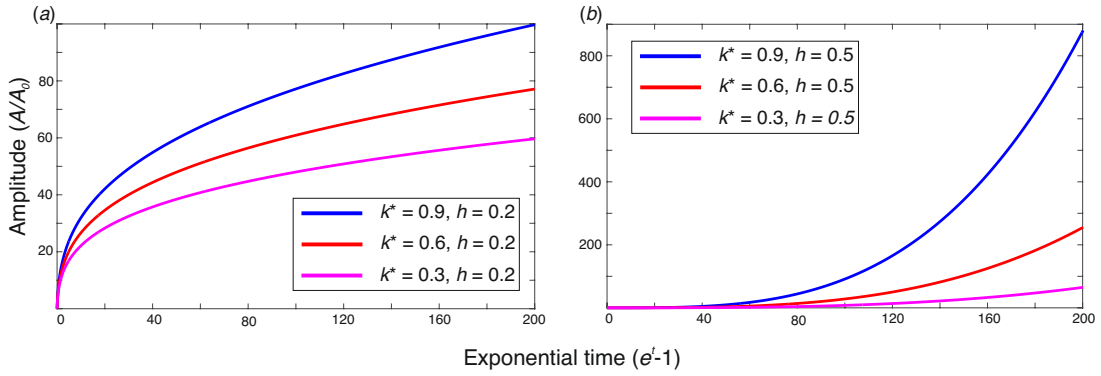

Figure 5.12: Non-linear solutions for the normalized amplitude (A/A_0) of the main modes of instabilities for varying normalized wavenumber (k^*) and source layer thickness (h_1).

5.4.2 Geometrical patterns of instabilities

I now proceed to analyse the spatial part in Eq. (5.33) or the Fourier modes. By specifying the geometrical patterns (from the symmetry point of view), this theoretical analysis allows us to show the evolution of the resulting instability structures at the fluid interface. Considering no preferred horizontal directions, the structures would be axisymmetric, forming a square or hexagonal pattern on the *xy* plane with vertical walls (*z*-direction). For a non-advecting system, the walls also act as flow-apophyses, with zero normal gradient of the vertical velocity component. Here, a mathematical description of the structures observed in our experiments is presented.

Consider an arbitrary perturbation as a set of normal modes and test the stability for each of these modes. The analysis is performed in terms of periodic waves with specified wave numbers. From the vertical component of velocity, it follows

$$\nabla_r^2 F = -K^2 F, \tag{5.34}$$

where K represents the normalized vertical dimension of the system and ∇_r is the horizontal operator on *xy*- plane.

The general solution of Eq. (5.34) can be given by

$$F = \sum_{\boldsymbol{k_i}} f_i e^{i\boldsymbol{k_i}.\boldsymbol{r}}, \tag{5.35}$$

where $|\boldsymbol{k_i}| = k$, $\boldsymbol{k_i}$ represents a set of *horizontal* wave vectors with wavenumber k. The wave vectors are differently oriented on the horizontal plane. The velocity components on the *xy* plane are (Chandrasekhar, 1961; Stuart, 1964),

$$\begin{aligned} u(x,t) &= \frac{1}{K^2}\frac{\partial^2 w}{\partial x \partial z}\eta_n(t) = \frac{1}{K^2}\frac{\partial F(x,y)}{\partial x} DW\eta_n(t), \\ v(x,t) &= \frac{1}{K^2}\frac{\partial^2 w}{\partial y \partial z}\eta_n(t) = \frac{1}{K^2}\frac{\partial F(x,y)}{\partial y} DW\eta_n(t), \end{aligned} \tag{5.36}$$

Equation (5.36) leads to

$$\begin{aligned} \nabla_r w &= W\nabla_r F \\ \boldsymbol{v} &= \frac{1}{K^2}\nabla_r w \frac{DW}{W} \end{aligned} \tag{5.37}$$

It has been previously stated that the boundary condition of each unit is that the normal component of the velocity vanishes at the wall. This condition is well established from our experiments in which the RTI produced periodic domes on the *xy* plane. We thus consider two vectors $\boldsymbol{a}$ and $\boldsymbol{b}$ to define their periodic structure as,

$$F(\boldsymbol{r} + m\boldsymbol{a} + n\boldsymbol{b}) = F(\boldsymbol{r}), \tag{5.38}$$

Where

$\boldsymbol{r} = x\boldsymbol{i} + y\boldsymbol{j};\ m, n = 0, \pm 1, ...$

Considering the periodic RTI structure on the *xy* plane, we express F in double Fourier series,

$$F = \sum_m \sum_n F_{mn} \tag{5.39}$$

From Bisshopp, (1960), the expression of F_{mn} in Eq. (5.39) follows,

$$\begin{aligned} 2F_{mn} = {} & (A_{mn} - D_{mn})\cos(m\boldsymbol{\alpha} + n\boldsymbol{\beta})\,.\boldsymbol{r} \\ & + (A_{mn} + D_{mn})\cos(m\boldsymbol{\alpha} - n\boldsymbol{\beta})\,.\boldsymbol{r} \\ & + (B_{mn} - C_{mn})\sin(m\boldsymbol{\alpha} - n\boldsymbol{\beta})\,.\boldsymbol{r} \\ & + (B_{mn} + C_{mn})\sin(m\boldsymbol{\alpha} + n\boldsymbol{\beta})\,.\boldsymbol{r} \end{aligned} \tag{5.40}$$

Since we can expand $F(r, z, t)$ in terms of Fourier series with modes proportional to $e^{i\alpha.r}$, both F and $e^{i\alpha.r}$must satisfy the same periodicity condition. This implies $e^{i\boldsymbol{\alpha}.\boldsymbol{a}}$ and $e^{i\boldsymbol{\alpha}.\boldsymbol{b}}$must be unity. We can then write,

$$\boldsymbol{\alpha}.\boldsymbol{a} = \boldsymbol{\beta}.\boldsymbol{b} = 2\pi;\ \boldsymbol{\alpha}.\boldsymbol{a} = \boldsymbol{\beta}.\boldsymbol{b} = 0 \tag{5.41}$$

For a solution of Eq. (5.40), the following relation must be satisfied,

$$m\boldsymbol{\alpha}.n\boldsymbol{\beta} = 0 \tag{5.42}$$

It follows from Eq. (5.41) and Eq. (5.42) that $\boldsymbol{a}$ and $\boldsymbol{b}$ must be perpendicular when $\boldsymbol{\alpha}$ and $\boldsymbol{\beta}$ are perpendicular.

Mode 2 instability growth

Experiments for $\alpha \geq 30°$ develop semi-cylindrical RTI structures with their axes down the substrate inclination. These structures indicate that one principal wave vector, oriented parallel to the *x* axis, far dominates over the other. The function *F* in Eq. (5.39) can be thus expressed as,

$$F_n = \sum_l A_l \cos\frac{l}{n}k_1.r + C_l \sin\frac{l}{n}k_1.r, \tag{5.43}$$

which on an appropriate choice of the co-ordinate axis, transforms into,

$$F = A\cos n\boldsymbol{\alpha}.\boldsymbol{r} = A\cos\frac{2\pi y}{L} + u_0 x \tag{5.44}$$

where the term is related to the inclination of the substrate.

This leads to,

$$w = W(z)\cos\frac{2\pi y}{L} + u_0 x \tag{5.45}$$

Using Eq. (5.45) in (5.34), and noting that one wavelength is much greater than the other, we find the velocity components on the *xy* plane,

$$v = -\frac{1}{K^2}\frac{2\pi}{L}DW\sin\frac{2\pi y}{L} \text{ and } u = u_0 \tag{5.46}$$

where $u_0$is the x component of velocity attributed to the upward advection along the inclined substrate.

According to Eq. (5.45) and (5.46),

$$v = 0 \text{ for } y = nL \text{ and } \left(n+\frac{1}{2}\right)L,$$
$$w_y = 0 \text{ for } y = (n/2 + 1/4)L, \tag{5.47}$$
$$w = W(z) \text{ for } y = (n/2)L$$

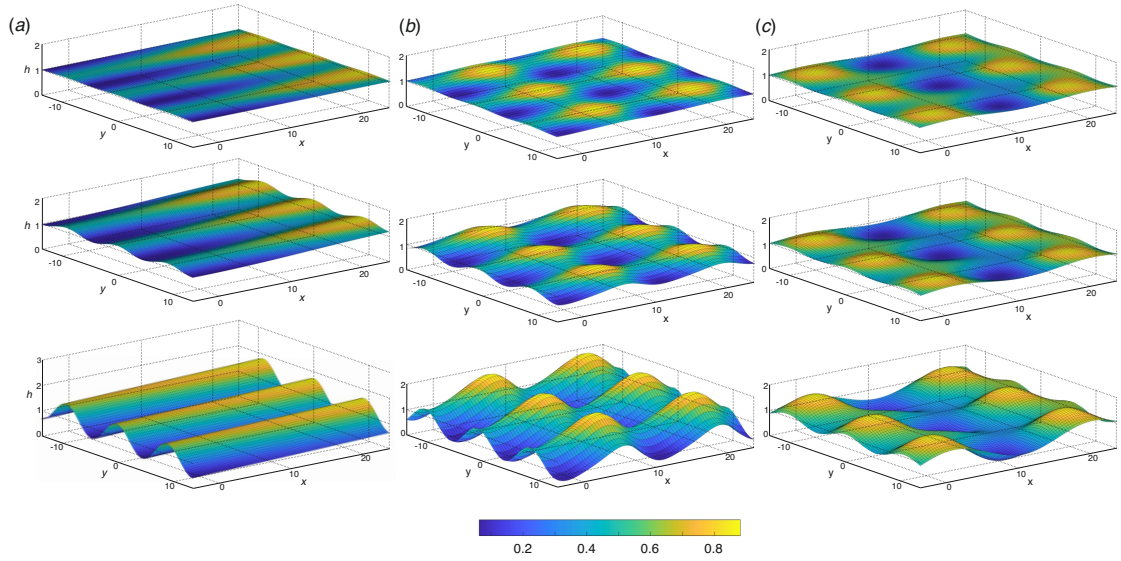

Figure 5.13: Temporal evolution of 3D instability structures at the fluid interface predicted from –the present non-linear theory. (*a*) Mode 2 instability with cylindrical structure, (*b*) Mode 1 instability with dome and depression structure and, (*c*) Mode 0 instability with hexagonal structure.

Using Eq. (5.33) and (5.44) the 3D geometry at the fluid interface was simulated (Figure 5.13a). The time-series simulation shows that λ_x waves hardly amplify with time to interfere with λ_y waves. Consequently, the latter solely determines the finite growth of instabilities as a single Fourier mode in the form of a nearly cylindrical wave train. The corresponding flow field shows the dominance of y-directional flow on the xy plane. However, the overall 2D flow pattern is influenced by the advection-driven velocity component in the x-direction, forming a periodic linear array of flow convergence oriented in the direction of substrate inclination, i.e., x-axis. The advection is found to be partitioned

in periodically arranged parallel linear zones of flow convergence. Such partitioning in the in-plane flow field results in cylindrical growth of RTIs along the lines of flow convergence, where the z-directional velocity components attain maximum values (Figure 5.14a).

Mode 1 instability growth

For $\alpha < 30°$, the linear stability analysis suggests that wave instabilities at the interface developed with two perpendicular wave vectors, k_x and k_y, of comparable magnitudes. Under such conditions, the surface function (F_{mn}) is expressed in terms of the wavenumbers along the x and y direction (Bisshopp, 1960),

$$F_{mn} = F_1 \cos(\mathbf{k_1}.\mathbf{r} + \vartheta_1) + F_2 \cos(\mathbf{k_2}.\mathbf{r} + \vartheta_2) + u_0 x \tag{5.48}$$

After manipulating the coordinate system and considering $F_1 = F_2$, we obtain the vertical velocity component

$$w = 2W(z)F \cos m\boldsymbol{\alpha} x \cos n\boldsymbol{\beta} y + u_0 x \tag{5.49}$$

Using

$\mathbf{k}_1 = m\boldsymbol{\alpha} + n\boldsymbol{\beta}, \quad \mathbf{k}_2 = m\boldsymbol{\alpha} - n\boldsymbol{\beta},$

where

$\boldsymbol{\alpha} = \frac{2\pi}{\lambda_x}\boldsymbol{i}, \quad \boldsymbol{\beta} = \frac{2\pi}{\lambda_y}\boldsymbol{j}.$

The corresponding velocity components are then,

$$u = -\frac{DW}{k^2}\frac{2\pi m}{\lambda_x}F \sin\frac{2\pi m x}{\lambda_x}\cos\frac{2\pi m y}{\lambda_y} + u_0$$
$$v = -\frac{DW}{k^2}\frac{2\pi n}{\lambda_y}F \cos\frac{2\pi m x}{\lambda_x}\sin\frac{2\pi m y}{\lambda_y} \tag{5.50}$$

The flow field obtained from Eq. (5.50) is partitioned by periodic nodes and saddles, as shown in Figure 5.14b. It is noteworthy that 1) the saddle points in the system are typically absent in the flow patterns for $\alpha > 30^o$ and 2) both stable (sink, i.e., flow convergence) and unstable nodes (source, i.e., flow divergence) occur as points instead of lines. One can easily find from Eq. (5.50),

$$u = \frac{\partial w}{\partial x} = u_0 \text{ along } x = p\lambda_x, \frac{2p+1}{2}\lambda_x \text{ and } y = \frac{2q+1}{4}\lambda_y \tag{5.51}$$

and

$$v = \frac{\partial w}{\partial y} = 0 \text{ along } y = q\lambda_y, \frac{2q+1}{2}\lambda_y \text{ and } x = \frac{2p+1}{4}\lambda_x$$

From Eq. (5.51), we find the locations of saddles: $x = p\lambda_x$ and $y = p\lambda_y$ and source/sink points: $x = \frac{2p+1}{2}$ and $y = \frac{2q+1}{2}$, recognized as zones of negative and positive *w*, respectively. By combining Eq. (5.33), (5.50) and (5.51), I ran a simulation to investigate the mode of temporal growth of instabilities at the fluid interface (Figure 5.13b). In the simulation λ_x and $\lambda_y$waves grow in a competitive way to produce a double Fourier mode of structure. The two wave trains interfere with each other, forming a 3D geometrical pattern characterized by a series of periodically arranged elongate domes aligned in the x-direction. These domes amplify with time in the vertical direction.

The flow pattern in the source layer for $0 < \alpha < 30^o$ typically develop rectangular cell structures showing periodicity both in *x* and *y* directions at wavelengths, λ_x and λ_y, respectively (Figure 5.14b). Each saddle point is coordinated by four nodes, two of them are sinks and the remaining are sources, forming a single rectangular cell bounded by $(x, y) = (\lambda_x/2\,, \lambda_y/2)$. The flow analysis provides an insight into the mode of layer-parallel advection in case of low substrate inclination ($\alpha < 10^o$). The skewed overall flow pattern indicates the influence of up-dip advection in the *x*-direction. However, the up-dip advection does not occur globally in the inclined layers because the sinks and saddles locally perturb the substrate parallel flow. However, when $\alpha << 30^o$, the advection velocity becomes weak and fails to break the RTI-driven symmetric flow on the *xy* plane.

Mode 0 instability growth

Experiments with $\alpha \sim 0°$ suggest that the layer-normal deflection and its corresponding wave vector are necessary to fully describe the instability patterns and their flow geometry. Considering, *m* = *n* = 1, the surface function can be expressed in the following form,

$$F(x, y) = \cos\frac{k}{2}\left(\sqrt{3}x + y\right) + \cos\frac{k}{2}\left(\sqrt{3}x - y\right) + \cos ky + u_0 x, \qquad (5.52)$$

which, by elementary means, leads to

$$w = \frac{1}{3}W(z)\left[2\cos\frac{2\pi x}{\sqrt{3}\lambda}\cos\frac{2\pi}{3\lambda}y + \cos\frac{4\pi}{3\lambda}y\right] + u_0 x, \qquad (5.53)$$

where $k = 4\pi/3\lambda$

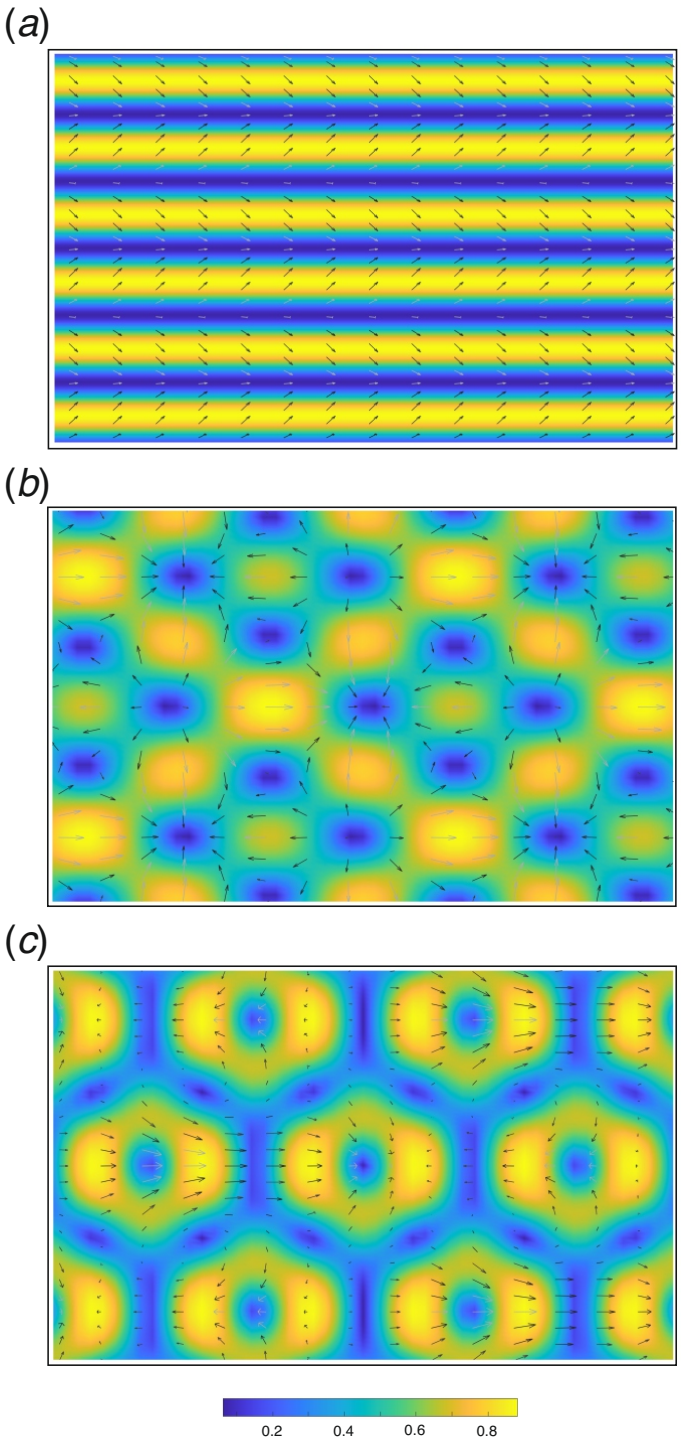

Figure 5.14: Characteristic flow fields on the *xy* plane (fluid interface), produced by the three modes of instability shown in Figure 5.13. (*a*) Mode 2: roll pattern (*b*) Mode 1: rectangular pattern, and (*c*) Mode 0: asymmetric hexagonal pattern.

It is noteworthy that Eq. (5.52) and (5.53) yield invariant property on 60° rotation. Three wave vectors $(\mathbf{k_1}, \mathbf{k_2}, \mathbf{k_3})$ thus constitute an equilateral triangle with sides λ (i.e., the wavelength). From Eq. (5.53), the velocity components in *x* and *y* directions follow,

$$u = -\frac{DW}{3k^2}\frac{4\pi}{\sqrt{3}\lambda}\sin\frac{2\pi x}{\sqrt{3}\lambda}\cos\frac{2\pi}{3\lambda}y + u_0$$
$$v = -\frac{DW}{3k^2}\frac{4\pi}{3\lambda}\left(\cos\frac{2\pi x}{\sqrt{3}\lambda} + 2\cos\frac{2\pi y}{3\lambda}\right)\sin\frac{2\pi y}{3\lambda} \quad (5.54)$$

Using Eq. (5.54) we calculated the in-plane flow field (Figure 5.14c), showing periodicity characterized by the vertical velocity component,

$$w(x, y) = w(x + \sqrt{3}\lambda p, y + 3q\lambda). \quad (5.55)$$

The saddle points and nodes are obtained from the following conditions.

$$u = u_0 \text{ for } x = 0, \frac{\sqrt{3}\lambda}{2} \text{ and } y = \frac{3\lambda}{4},$$
$$v = 0 \text{ for } y = 0 \text{ and } y = \frac{3\lambda}{2} \quad (5.56)$$

Based on the theoretical formulation discussed above, Figure 5.13c presents a simulation to demonstrate the mode of temporal growth of the instability structure for $\alpha \sim 0$. In this case, the two sets of waves: λ_x and λ_y grow equally to interfere with each other to produce periodic domes in a hexagonal pattern. In the corresponding flow field, obtained from Eq. (5.56), a source has two saddle points and two sink points on their either flank at a distance of $\pm\frac{\sqrt{3}\lambda}{2}$ along x = 0 along y = 0, respectively (Figure 5.14c). The saddle points lie at a distance of $\pm\frac{3\lambda}{4}$ along the straight lines: $y \pm x\sqrt{3} = 0$, oriented at an angle of 60° to the x-axis. On the other hand, the sinks are located a distance of $\pm\lambda$ along the straight lines, $y \pm \frac{1}{\sqrt{3}}x = 0$ at an angle of 30° to the x-axis. The flow pattern, overall, develops a network of hexagonal geometry with a source at the center and equally spaced six sinks around it.

Chapter 6

Origin of Réunion hotspot and its linkage to Deccan volcanism: an insight from numerical modelling.

6.1 Introduction

The presence of degree-2 pattern for Earth's lowermost mantle is now well established and is attributed to the presence of two LLSVPs beneath Africa and Pacific (Garnero et al., 2016; Lay and Garnero, 2011). The lowermost mantle dynamics thus exerts significant control on the formation of mantle plumes and LIPs as hotspots are now thought to be sourced by LLSVPs as the roots of the plume tails are tracked down to LLSVP margins (French and Romanowicz, 2015). But any such hypothesis must explain the pulsating nature that is often associated with the hotspot volcanisms, with the first pulse generating the LIP and the successive pulses creating the hotspot tract. Studies show that after reaching the lowermost lower mantle the subducted slabs flow laterally along the CMB to reach the piles, and periodic plumes is attributed to varying plate velocity or sinking rate (Li et al., 2018). But the timescale of the resultant periodicity is tens of hundreds of million year and thus it cannot be accounted for the pulsating nature of hotspots where the periodicity is only a few million years. Using numerical modeling, this study explores the cause of the pulses that lead to the periodicity in hotspot volcanism. I will first provide a stability analysis of the LLSVPs, which is the most crucial factor to the dynamics of the plumes originating at their margin. Specifically, the thesis looks at the Réunion hotspot which is thought to be responsible for the Deccan LIP and their connection with the eastern flank of African LLSVP.

Deccan Traps (DTs), the most spatially extensive continental flood basalt (CFB) province in peninsular India, witness a remarkable event of volcanism in the Phanerozoic history of the Earth (Chenet et al., 2009), which in recent time has received particular attention in connection with the mass extinction of biological species (Keller et al., 2012; Wilson, 2014). A school of thought relates this sudden biotic crisis to the enormous volume ($> 10^6$ km^3) of basaltic magma eruptions in the Deccan provinces (Schoene et al., 2015; Wignall, 2001) during late Mesozoic to early Cenozoic (Figure 6.1a). This massive

volcanism involved degassing on a global scale, resulting in two significant environmental changes: the first being global warming, carbon cycle disruption, and ocean acidification (Self et al., 2014) associated with volatile emissions, with the second a poisoning of the entire ecosystem (Schmidt et al., 2016) associated with SO_2 injection into the upper atmosphere. Another school of thought has proposed a Chicxulub bolide impact theory for the Cretaceous mass extinction (Alvarez et al., 1980; Schulte et al., 2010), but the issue is still debated. The DTs have also stimulated discussions on the long-standing critical question about the origins of large igneous provinces (Campbell and Griffiths, 1990; Dannberg and Sobolev, 2015; Farnetani and Richards, 1994) (LIPs). What is the potential source of enormous magma supply to LIPs and how are they connected to lower mantle dynamics (Glišović and Forte, 2017; White and McKenzie, 1995)? This Deccan volcanic province is excellent for studying LIPs as it is relatively young and geographically extensive thus, allowing geoscientists to reliably reconstruct the eruption events in space and time.

Based on volcanological and geochemical properties, the Deccan Volcanic Province (DVP) is divided into three principal stratigraphic successions: Kalsubai, Lonavala, and Wai subgroups (Figure 6.1b). The volcanic event that defines the Cretaceous-Paleogene boundary (KPB) at 66.043 ± 0.043 Ma (Sprain et al., 2018) occurred $\sim 165 \pm 68$ ka after the emplacement of Kalsubai falls within Khandala, Bushe, or Poladpur Formations (Richards et al., 2015). Using $^{40}K/^{40}Ar$ plagioclase geochronology of erupted basalts and U-Pb geochronology of zircon from intervening ash beds, several workers have constrained the timings of multiple eruption pulses (Keller et al., 2012; Richards et al., 2015; Schoene et al., 2019, 2015). All these studies agree that the main eruption phases started shortly before the C30n-C29r geomagnetic reversal and ended following the C29r-C29n reversal. Above the KPB, the Wai subgroup consists of geochemically and volcanologically distinct formations, which suggest more voluminous eruptions (Renne et al., 2015; Richards et al., 2015; Sprain et al., 2019).

The dynamics of pulsating eruption plays a critical role in determining the time-dependent variability of volcanic activities in LIPs and hotspot tracks. This article aims to explore the mechanism of such unsteady eruption in the evolution of DVP through multiple phases, punctuated by quiescent periods. Previous studies based on geochemical data (Chenet et al., 2007) suggested three phases of DT eruptions, with most of the volume erupted before the KPB, where the second phase is considered responsible for late

Cretaceous environmental changes (Chenet et al., 2009; Petersen et al., 2016) (Figure 6.1b, c). Alternative views emphasize the Chicxulub impact to propose that the DVP magma eruptions were mostly a post-KPB event (Renne et al., 2015; Richards et al., 2015). More recent investigations from high-precision U-Pb geochronology (Schoene et al., 2019) report three to four discrete pulses during the main eruption event at KPB, each lasting < 100 ka. The first eruption event that formed the lowermost seven formations lasted from ~ 66.3 to 66.15 Ma ago, followed by the second, third, and fourth pulses at ~ 66.1 to 66.0 Ma, ~ 65.9 to 65.8 Ma, and ~ 65.6 to 65.5 Ma to form the Poladpur Formation, the Ambenali Formation and the uppermost Mahabaleshwar Formation, respectively (Schoene et al., 2019).

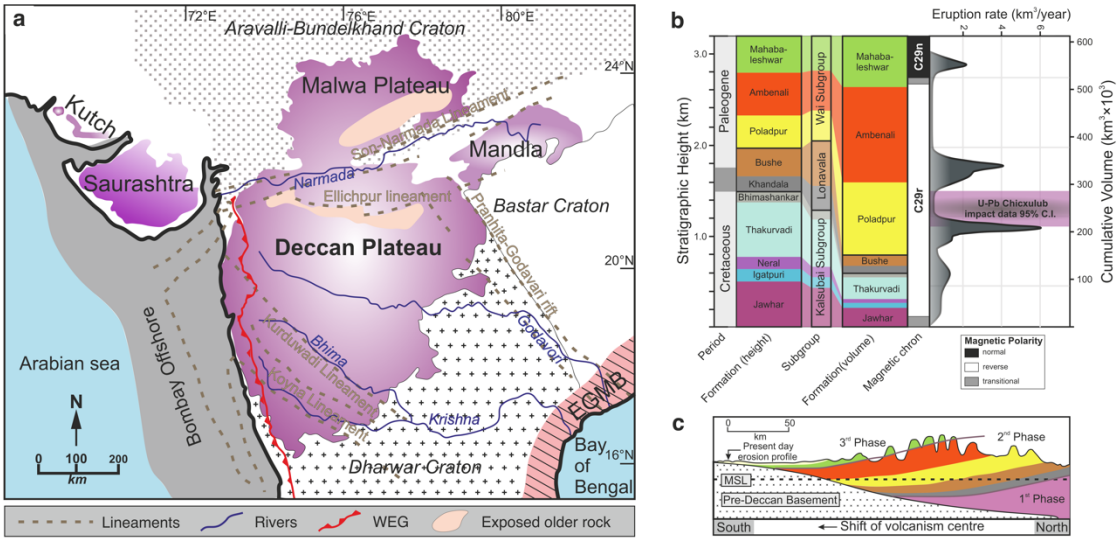

Figure 6.1: Geology of the Deccan volcanic province (DVP). (a) Map showing the four main sub-provinces of DVP. The Deccan traps (DTs) rest on Precambrian basement rocks (shown in various legend patterns). The terrain contains a number of structural zones, such as lineaments and escarpment (marked as green dashed lines). Blue lines depict the major rivers flowing across DVP. WGE = Western Ghat Escarpment, EGMB = Eastern Ghat Mobile Belt. Reconstructed from (Kale et al., 2020) (b) Stratigraphic succession of the DVP (Left column) and their corresponding cumulative eruption volumes (Right column) along with ages for the three main subgroups of DVP in the Western Ghats (Renne et al., 2015). The panel shows the following elements (from left to right): cumulative stratigraphic height, geological time scale with the KPB indicated by the gray area, timescale of geomagnetic polarity with various magnetic chrons, and cumulative volume of Deccan lava. It also includes the probabilistic volumetric eruption rate and the Chicxulub impact time from Schoene et al., 2019 (c) A thematic geological cross-section of the DTs to illustrate the three major phases and their corresponding formations (Chenet et al., 2009). Color legends correspond to those used in (b).

A spectrum of geophysical and geochemical studies finds a linkage of the DVP with the Réunion hotspot (Bredow et al., 2017; Fontaine et al., 2015; Ganerød et al., 2011). Geochemical proxies suggest a link of the source of Deccan basalts to ocean island basalts

(OIB), actively erupting on the island of La Réunion (Peters and Day, 2017). Glisovic *et al*., based on their geophysical model, predicted a deep mantle origin of DVPs and proposed a mantle plume hypothesis to show its connection with the Réunion hotspot. Interestingly, the temporal coincidence of the Deccan volcanic events with the plume-induced accelerated motion of the Indian plate further strengthens the mantle-plume hypothesis proposed for the origin of Deccan CFB (Cande and Stegman, 2011; Glišović and Forte, 2017). Moreover, like Iceland and Tristan da Cunha, the Réunion hotspot is thought to have originated from a laterally vast thermochemical pile above the
core-mantle boundary (CMB) beneath present-day Africa, referred to as the African large low shear-wave velocity province (LLSVP) (Tsekhmistrenko et al., 2021). This pile might have transported primordial material from CMB to the surface via Réunion and other plumes, as evident from geochemical studies on Sr-Nd-Os systematics (Peters and Day, 2017). Although geophysical and geochemical evidence suggests a connection between the Réunion hotspot and African LLSVP, the mechanism of episodic Deccan volcanism is still unknown.

This chapter explores the thermochemical scenario that favours the Réunion hotspot to operate in pulsating fashion with characteristic periodicity, producing a huge cumulative volume of Deccan basalt at the KPB. We also show how a single major pulse can give rise to a number of secondary pulses of smaller timescales, as reflected from volcanic episodes in the DVP on time scales less than a million years (Ma). This thermochamical model allows us to constrain a spectrum of the periodicity timescales (a few Ma to less than a Ma), depending on the thermomechanical properties of the source materials. I also present a budget for the volume flux from the mantle to the surface.

6.2 Methods

6.2.1 Model set-up

The developer version of finite element code ASPECT 2.4.0 (Dannberg and Heister, 2016; Heister et al., 2017) is used to develop our thermochanical model, treating the mantle as a system of stratified fluid layers with their density and viscosity varying as a function of pressure, temperature, composition, and phase transformations. The model domain covers the entire vertical depth (~ 2890 km) of the mantle with a horizontal width of 11560 km which is discretized into 5.5 × 5.5 km cells (Figure 6.2). Since the primary aim of this work is to study the dynamics and pulsating nature of the plumes, we assume a pre-existing

high-density basal layer of a specified thickness of 150-300 km (Citron et al., 2020) at the CMB given by a single compositional field representing the pile. The changes in the composition field are tracked using passive tracers that advect with the global flow. I have chosen the number of tracers within a cell to vary within a limit of maximum and minimum values, ensuring that each cell contains an average number of particles at each time step. For thermochemical calculations, we impose an initial sinusoidal temperature profile (Citron et al., 2020; Li et al., 2018) in the background mantle to initiate convection. I also added two thermal boundary layers using error functions at the top and the bottom of the domain to represent the bottom TBL and the lithosphere, respectively (Figure 6.3c). In addition, heat is introduced into the system by internal heating within the pile either in the form of constant heating or by varying the radioactive element concentration (Figure 6.3b) representing variation in chemical composition. In both constant and radioactive heating, the modelling considered heating rate up to 20 times the heating rate as compared to the background mantle.

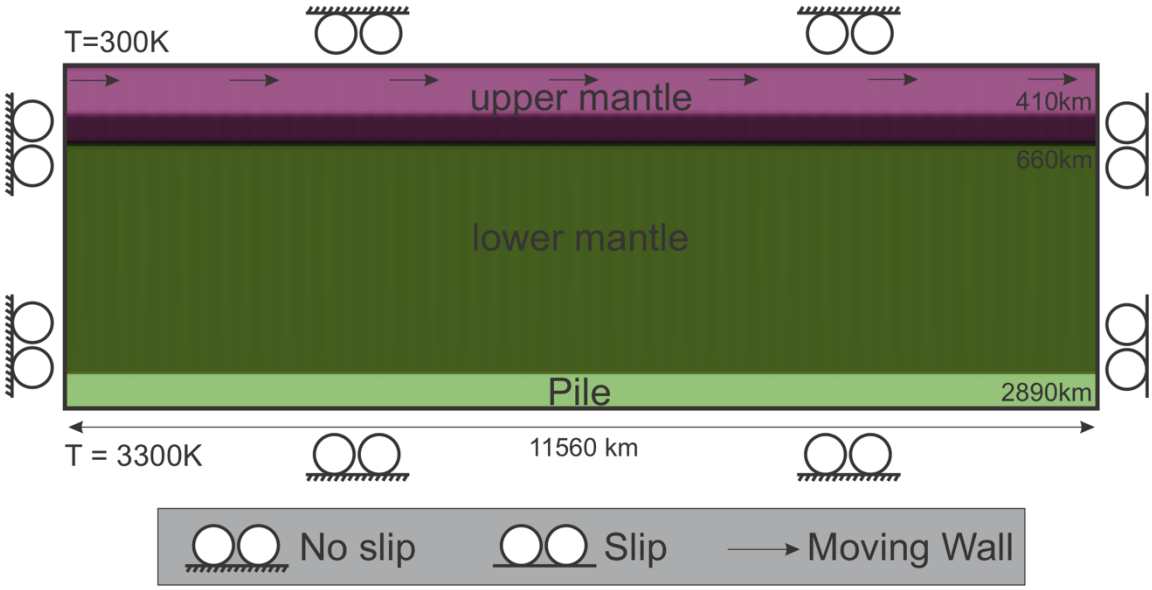

Figure 6.2: Model geometry with initial and boundary conditions for numerical modelling.

To calculate the physical parameters of different model components, I use a *depth-dependent* composite material model built in the ASPECT material library. All material properties are assigned from an incompressible *base model*; this model assumes constant parameter coefficients to represent the ambient mantle values, except for the density and viscosity. To incorporate viscosity, the depth-dependent material model is adopted to

describe the different viscosities for the lithosphere, upper and lower mantle. Additionally, I introduce the thermal and compositional pre-factors to express the viscosity as a function temperature and composition. Density varies due to both thermal expansion and composition in our model. The depth dependence of density is incorporated by introducing phase transition for both the ambiance mantle and the basal layer. I varied the excess basal layer (pile) density from 150 to 450 kg/m^3. The viscosity of the basal layer is 0.1 to 100 times that of the ambient mantle (Figure 6.3a, d).

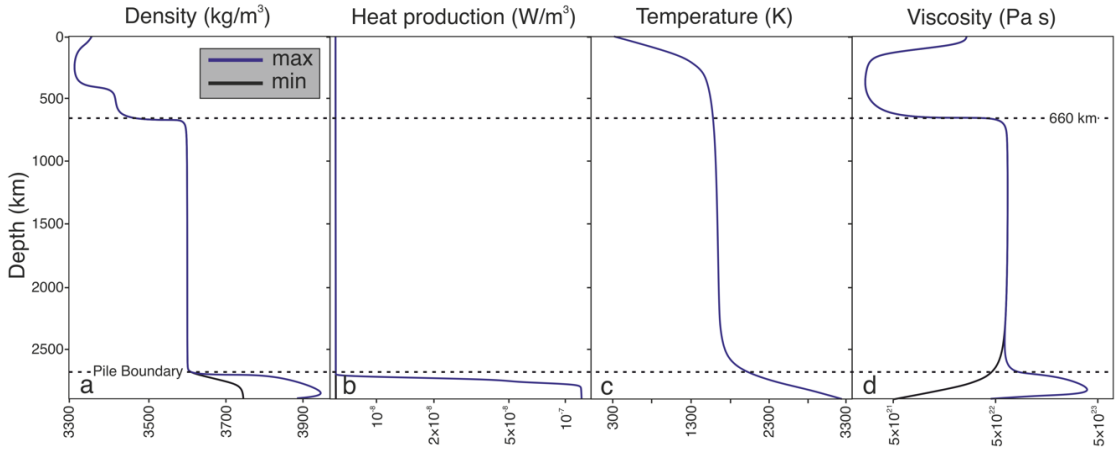

Figure 6.3: Initial conditions considered for plume model simulations. (a) Initial density profile showing jumps of density values at the phase transition at 410 km and 660 km boundaries, and steep density increase near CMB due to the presence of a thermochemical pile. Blue and black lines indicate the maximum and minimum pile density considered in the modelling. (b) Depth profiles of the initial internal heat-production rate for the ambient mantle and the pile. The pile at CMB is enriched in heat-producing element (HPE) by up to 20 times relative to the ambient mantle. (c) Initial thermal structure of the mantle at the onset of convection, characterized by strong thermal boundary layers (TBL) at the upper 200 km (lithosphere) and at 100 km above the CMB. (d) Initial viscosity profile considered in our models. It accounts for both temperature and depth effects. The pile material is up-to 100 times (blue) more viscous that the ambient mantle.

The top and bottom boundaries of our model are subjected to isothermal conditions with T = 298K and T = 3300K, respectively (Figure 6.3c). A uniform velocity condition is imposed at the top boundary for our initial model, keeping all other boundaries under a free-slip condition. The models were modified to accommodate the temporal variation of plate velocity and replicate the plate motion history using the plate motion model from previous studies (Seton et al., 2012). A comprehensive list of model parameters is provided in Table 6.1. To determine the physical properties of sequential plume surges, I consider a line segment across the model box length at a depth of 400 km, which is above the plume-pulses initiation depth. The treatment then finds excess or deficit of physical properties

from the peak amplitude from the curve with respect to the background value representing the ambient mantle.

Table 6.1: Physical parameters and their values used for thermochemical modelling

Model Parameters	Reference values
Mantle thickness z_0	2890 km
Reference density ρ_o	3340 kg/m^3
Reference viscosity μ_o	2×10^{20} Pa s
Thermal conductivity k	4.1 W K^{-1}m^{-1}
Specific heat C_P	1250 J K^{-1} kg^{-1}
Thermal expansivity α_0	3×10^{-5} K^{-1}
Thermal boundary layer thickness at the CMB (h_{TBL})	100 km
Initial basal layer thickness h_{pile}	150 km
Basal layer density ρ_b	3730-3950 kg/m^3
Basal layer viscosity μ_b	$5 \times 10^{21} - 5 \times 10^{23}$ Pa s
Viscosity ratio $\mu^{\dagger}$	$0.1 - 10^2$
Top temperature T_{top}	300 K
Bottom temperature T_{bot}	3300 K
Reference Temperature T_{ref}	1600 K
Buoyancy number B	0.6 to 1.4
Background Heating rate X	6×10^{-9} W/kg
Basal layer heat producing element concentration (c_{HPE})	1X − 20X
Initial basal layer volume‡	3×10^8 km^3
Clapeyron slope at 660 km phase transition (γ_{660})	-2×10^6 Pa/K
Clapeyron slope at 410 km phase transition (γ_{410})	3×10^6 Pa/K

† Ratio of viscosity of the basal layer and the ambience

‡ Initial basal layer volume is calculated from the total volume of African LLSVP considering that the eastern flank (corresponds to the initial basal layer) comprises only a fraction of the total volume.

6.2.2 Problem formulation

The 2D thermochemical convection simulations are developed in a theoretical framework of Boussinesq approximation, using mass, momentum, and energy conservation equations:

$$\nabla \cdot \mathbf{u} = 0, \tag{6.1}$$

$$\nabla P - \nabla \cdot [\mu_r \dot{\epsilon}] = \Delta\rho g \mathbf{e_z}, \tag{6.2}$$

$$\rho_0 C_P \left(\frac{\partial T}{\partial t} + \mathbf{u} \cdot \nabla T\right) - \nabla \cdot K \nabla T = \rho_0 H, \tag{6.3}$$

where $\mathbf{u}$, P, μ_r, $\dot{\epsilon}$ denote the following physical variables: velocity, dynamic pressure, viscosity, and strain rate, respectively. g is the gravitational acceleration, ρ_0 is the reference density of the ambient mantle, C_P is the specific heat at constant pressure, and T, K, and H are the absolute temperature, thermal conductivity, and the rate of internal heating, respectively.

To replicate Earth-like convective vigor, a set of parameters to appropriately is chosen to fix the reference Rayleigh number for the mantle:

$$Ra = \frac{\rho_0 g \alpha_0 \Delta T z^3}{\kappa_0 \mu_0}, \tag{6.4}$$

α_0, κ_0 and μ_0 represent the reference values of the coefficients of thermal expansion, the thermal diffusivity, and the viscosity of the ambient mantle, respectively. The basal layer has a density difference with the ambient mantle, which is introduced in our modelling as Buoyancy number:

$$B = \frac{\Delta\rho}{\rho_0 \alpha_0 \Delta T}, \tag{6.5}$$

B expresses the intrinsic density anomaly normalized to that caused by thermal expansion. Discontinuous Galerkin method is used in ASPECT to implement tracking of compositional fields. The advection of composition is given by

$$\frac{\partial \overline{c}}{\partial t} + (\mathbf{u}.\nabla \overline{c}) = 0, \tag{6.6}$$

where $\overline{c}$ is the compositional vector.

The density and viscosity in the material model vary according to the following equations.

$$\mu_b(p, T, \overline{c}) = \tau(T)\zeta(\overline{c})\mu_0, \tag{6.7}$$

$$\rho_b(p, T, \overline{c}) = \big(1 - \alpha(T - T_0)\big)\rho_0 + \Delta\rho c_0, \tag{6.8}$$

where μ_b and ρ_b are the viscosity and density calculated from the base model; μ_0 and ρ_0 denote their corresponding reference values. α is the coefficient of thermal expansion, $\Delta\rho$ is the density difference between the source layer and the ambient mantle, c_0 stands for the

first component of the compositional vector $\overline{c}$. The temperature pre-factor in Eq. (6.7) is expressed as

$$\tau(T) = H_T \exp\left(-\frac{A(T - T_0)}{T_0}\right), \tag{6.9}$$

where A is the thermal viscosity exponent, and

$$H_T = \begin{cases} \tau_{min} & \text{if } \varphi < \tau_{min}, \\ \varphi & \text{if } 10^{-2} < \varphi < 10^2, \\ \tau_{max} & \text{if } \varphi > \tau_{max}, \end{cases} \tag{6.10}$$

$\varphi = \exp(-A(T - T_0)/T_0)$. τ_{min} and τ_{max} represents the minimum and the maximum values of the thermal pre-factors, respectively. The compositional pre-factor in Eq. (6.7) is taken in the form:

$$\zeta(\overline{c}) = \xi^{c_0}, \tag{6.11}$$

ξ is the compositional viscosity pre-factor corresponding to composition c_0. From a depth-dependent model, we find model viscosity:

$$\mu(z, p, T, \overline{c}, \dots) = \frac{\mu(z)\mu_b(p, T, \overline{c}, \dots)}{\mu_0}, \tag{6.12}$$

where $\mu(z)$ is the depth-dependent viscosity calculated from a depth-dependent model. Depth dependent phase transition is defined in ASPECT, the expression of which follows,

$$\Gamma = 0.5\left(1 + \tanh\left(\frac{\Delta p}{w}\right)\right), \tag{6.13}$$

w denotes the phase-transition zone width. Δp is the pressure difference across the width of phase transition zones, given by

$$\Delta p = z - z_{transition} - \gamma(T - T_{transition}), \tag{6.14}$$

where γ is the Clapeyron slope.

ASPECT calculates the dynamic topography from the stress at the surface in the following way. First, it evaluates the stress component that acts in the direction of gravity at the centres of the cells along the top model surface. The dynamic topography is then calculated using,

$$h_{dt} = \frac{\sigma_{rr}}{(\mathbf{g}.\mathbf{n})\rho}, \tag{6.15}$$

where h_{dt} is the dynamic topography, σ_{rr} is the stress calculated in the previous step, ρ is the density of the corresponding cell center, and g. n is the component of gravity.

Initially, each simulation was run for 3.5×10^8 years to initiate strong convection from the provided initial conditions. Then we applied our boundary velocity condition to impose plate velocity at the top boundary Figure 6.2. This creates a cold, high viscous downwelling that pushes the dense material to from the thermochemical pile above the CMB. To classify the pile morphological variations, I used the following parameters:

- The max height of the pile,
- Rate of change of areal fraction of the pile defined by the proportion of unexposed CMB,
- Change in pile volume,
- Maximum slope of the pile topography, and
- CMB dynamic topography generated by each type of piles.

First, we describe a reference model, and then we do parametric analysis to show how that changes the results. Our primary focus is on the changes that occur after the initiation of the downwelling on the right boundary.

6.3 Results

6.3.1 Reference experiment

The reference case uses a Buoyancy number of $B = 1$, a viscosity ratio of $\mu = 100$, a pile thickness of $h_p = 150$ km, heat producing element concentration of $c_{HPE} = 6.034 \times 10^{-9}$, and a plate velocity of $v_p = 5\text{cm/yr}$. Figure shows the time evolution of the thermochemical pile along with the dynamic topography at the CMB. Before imposing the plate velocity, the dynamic topography is negative throughout the CMB due to the higher density of pile material (Figure 6.4). As subduction starts along the right boundary, the pile starts to move leftwards and the CMB topography beneath the subduction depresses further (Figure 6.5). This progressively increases the exposed CMB area (Figure 6.6d) and the height of the pile (Figure 6.6b). As the height of TBL (h_{TBL}) grows and moves towards the pile, the zone between the pile and the downwelling shows positive topography (Figure 6.5) which gradually grows with time as the TBL reaches its critical thickness primarily due to rising flow and reduced density of the TBL. Upon reaching the pile, both pile height and the h_{TBL} experience an increase in growth rate. On a shorter scale, however, we see

that there is a depression adjacent to the pile edge with the peak being the edge itself (Figure 6.4b).

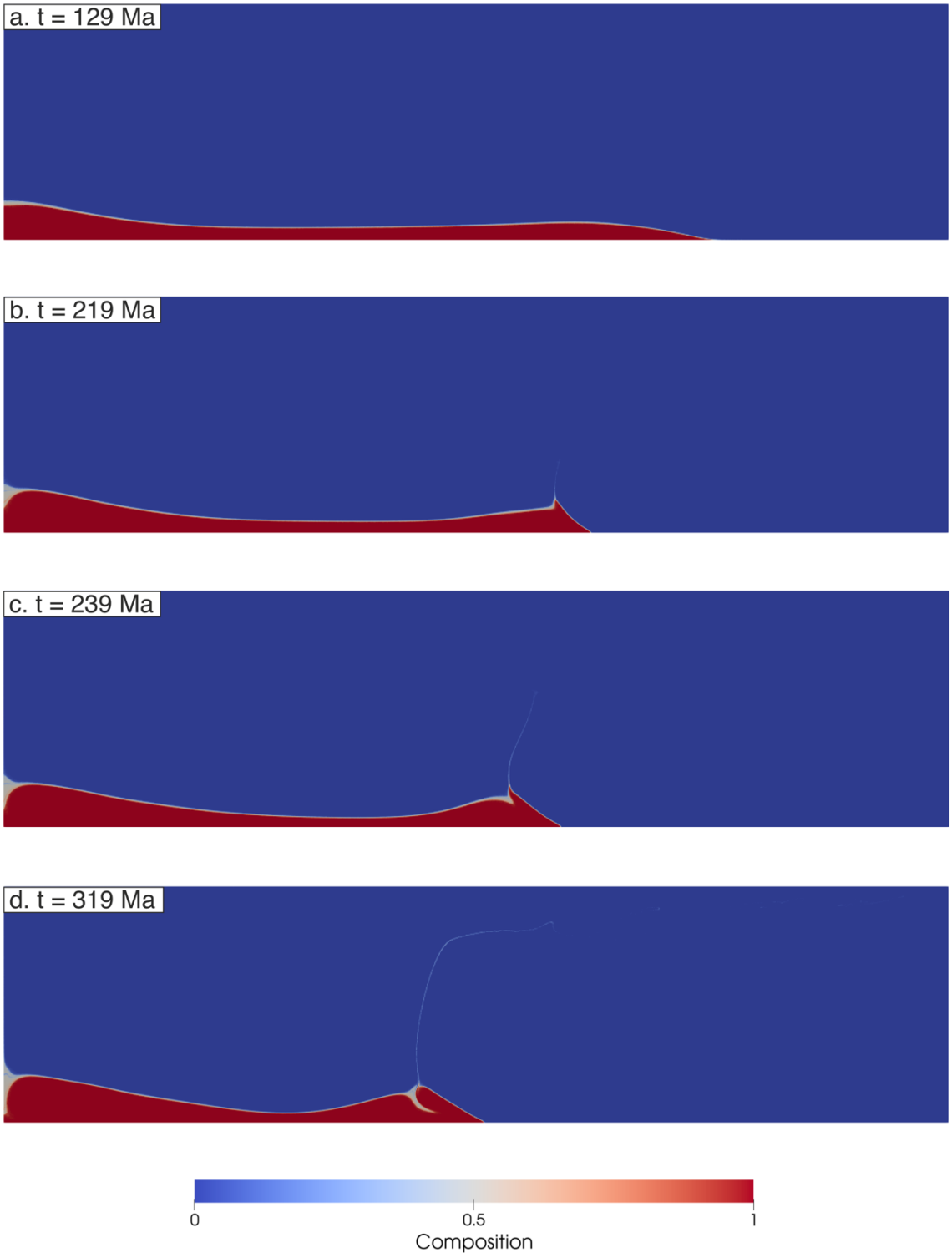

Figure 6.4: Reference simulation shows formation of thermochemical pile at CMB. The model parameters are $h_{pile} = 150$ km, $\mu = 100$, $c_{HPE} = 6.034 \times 10^{-9}$, and $B = 1.0$,

The peak forms due to increased coupling between the mantle and the CMB, but the depression on the other hand is due to stiffer nature of the pile ($\mu = 100$) which causes the velocity gradient (and stress) to focus over a much smaller area outside pile margin, causing radial stress towards the CMB, manifesting the depression (Heyn et al., 2020a). Initially the amplitude of the depression is comparable with the long-wavelength elevation associated with rising flow at the pile margin. But with time, the elevation increases due to formation of plume (Figure 6.4c).

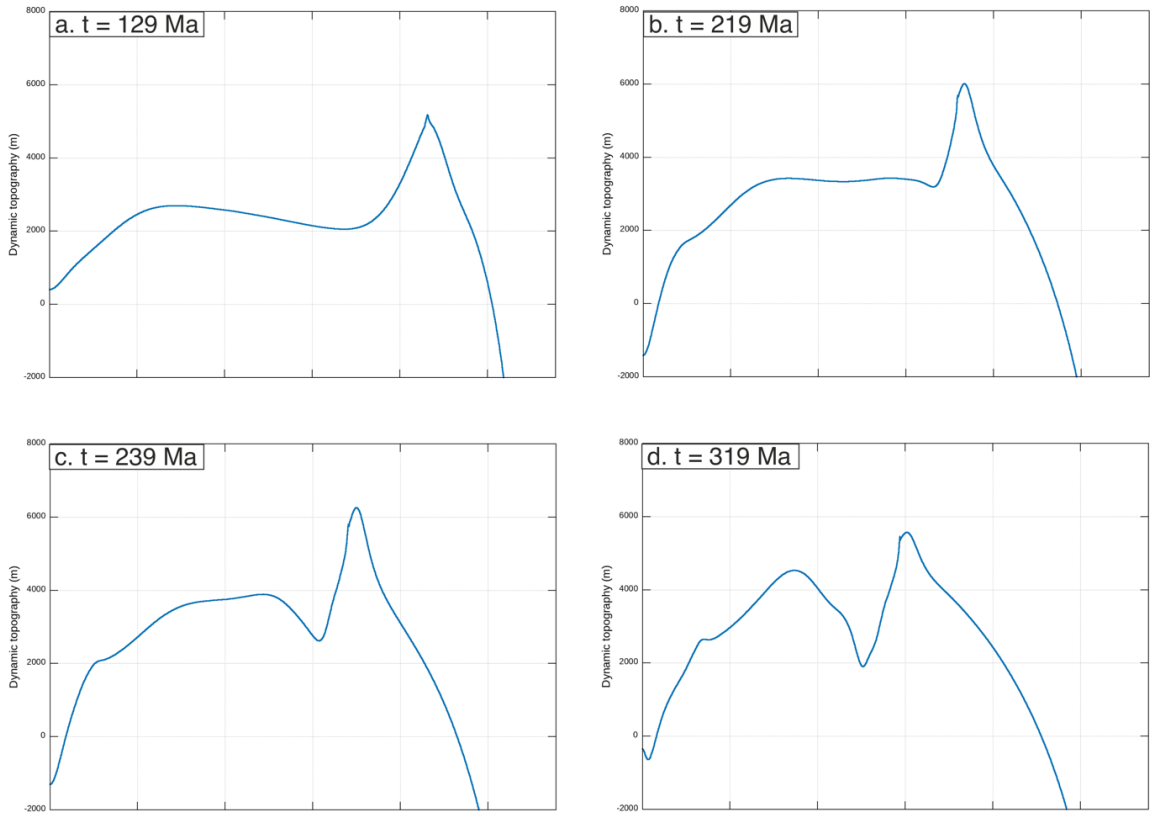

Figure 6.5: CMB dynamic topography for our reference experiment at different times.

With time, a mature plume starts to generate when the Ra_{TBL} is greater than local critical Rayleigh number Ra^{c}_{TBL} due to increase in h_{TBL}. This causes a gradual increase in maximum pile height to > 500 km. Plume growth, on the other hand, decreases the rate of CMB exposure by increasing the vertical growth of the pile in contrast to horizontal shortening. This is reflected by a drastic decrease in the rate of CMB exposure after the formation of the mature plume (Figure 6.6c). As the plume upwells, it also brings a certain portion of pile material to upper mantle which slowly mixes with the background mantle

via entrainment, effectively reducing the volume of the pile (Figure 6.6a). An increase in the vertical heat flux is also noticed as the plume tail is formed connecting the pile with the upper mantle. During this time, the evolution of pile height correlates well with the rate of change of exposed CMB fraction.

As the plume reaches the upper mantle, it creates successive pulses as seen by the periodicity of the plume heat flux within the upper mantle (e.g., at 410 km). The heat flux within the CMB is rather smooth and show no signs of periodicity. Hence there is no temporal correlation between the CMB heat flux and the plume periodicity. With time, multiple pulses form in the upper mantle, and the pile shifts leftwards, albeit at varying rate, but in general, slower than during the initial pulse event (Figure 6.6c). The heat flux at the base of the plume also decreases with time effectively weakening the plume tail. It has two-fold effect on the dynamics of the pile: 1) the height of the pile decreases compared to the height during the first pulse (Figure 6.4d, Figure 6.6b) The rate of decrease of pile volume also lowers with time indicating less effectiveness of the plume to drag pile material with it.

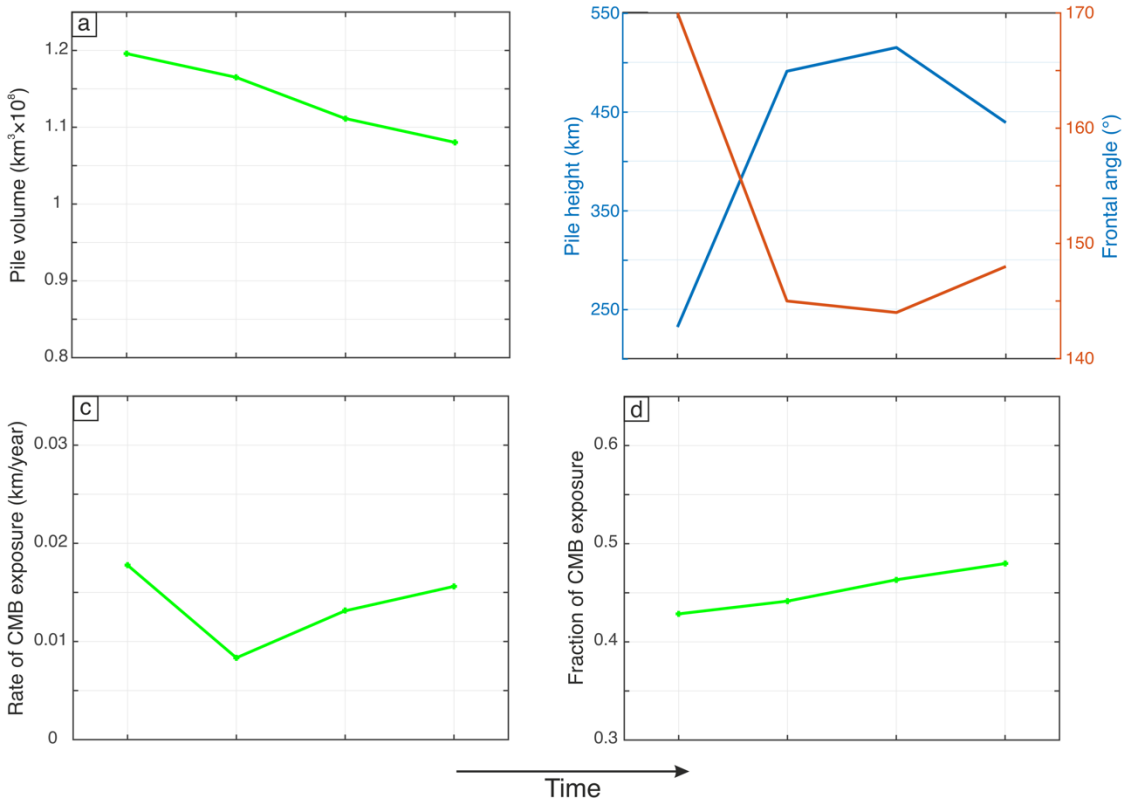

Figure 6.6: Change in pile volume (a); pile height, frontal angle (b); rate of CMB exposure (c); and fraction of CMB exposure (d) from our reference experiments.

In summary, the pile morphology changes more or less gradually. Before the formation of the plumes, compression causes a dome to form within the vicinity of mantle flow, apart from the dome, the pile maintains almost uniform thickness with the exception being the left boundary, where materials get accumulated forming a swell. The pile, thus has an asymmetric shape, with the left side of the pile being more elevated than the other. Hot thermal anomalies are found on left side of the pile, which cause large positive residual buoyancy on the left edge of the pile edge. With time the thermal anomaly on the left side of the pile forms a plume at the crest of the pile, and the pile is slightly elevated beneath the plume. This creates a depression beneath the main frontal dome with its trough adjacent to it. Also noticeable is the change in the structure of the frontal crest. Apart from the increase in the height of pile, the angle of the pile front decreases, indicating an unstable state of the pile. The dome follows the plume tail creating a sharp peak via which pile material get dragged with the plume tail creating a crevasse behind it. With time, as the strength of the tail decreases which now drags the pile less efficiently, causing the pile height to decrease.

6.3.2 Effect of model parameters

I studied the influences of model parameters such as pile height (h_{pile}), viscosity ratio (μ), buoyancy number (B) and heat producing element concentration (c_{HPE}) on the pile morphology, dynamic topography of CMB, pile height and angle and plume formation. Previous studies have shown how plume formation, pile morphology and CMB heat flux are related to the density contrast and volume of the pile on a larger time scale (i.e., more than tens of hundreds of million year) (Citron et al., 2020; Li et al., 2018). This study focuses on their effect on a shorter time scale variation of pile to help us understand the shorter-scale dynamics of pile.

Effect of Buoyancy

Buoyancy has the Most prominent effect on pile dynamics, parameterized by buoyancy number (B). Figure 6.7 shows the effect of B on the pile geometry for $h_{pile} = 150$ km, $\mu = 100$, and $c_{HPE} = 6.034 \times 10^{-9}$. Decreasing B to 0.8, changes the frontal dome geometry to a tent like structure with the peak representing the location of the plume tail by which the pile is connected to the upper mantle. The tent-like structure is asymmetric with the steeper side being exposed to mantle flow. Behind the tent like frontal dome, the

pile depression is more well-defined. With time the depression gets even more pronounced with the pile material concentrating on the frontal dome and on the left boundary (Figure 6.7b). It is also seen that the proportion of exposed CMB has increased drastically compared to the reference model (Figure). Overall, the pile height is more and the frontal angle is less than that of $B = 1$ (Figure 6.9), indicating unstable nature of the pile. This is also reflected in the temporal change in pile volume (Figure 6.10) suggesting more efficient erosion of pile material by the thermal plume. The overall dynamic topography of CMB remains similar but the amplitude is much higher (both negative and positive). This is demarcated here as Type 1asymmetric (*Type 1a*) pile geometry.

Figure 6.7: Evolution of pile geometry for $h_{pile} = 150$ km, $\mu = 100$, $c_{HPE} = 6.034 \times 10^{-9}$, and $B = 0.8$ (Type-1a).

Further decrease in B to 0.6 makes the pile completely unstable with very high positive dynamic topography of CMB near the plume formation (Figure 6.8). The pile material is effectively eroded due to its own buoyancy as evidenced by the rapid change in pile volume with time (Figure 6.10a). Pile geometry takes the shape of typical thermal plume but with wider tails which effectively transports the pile material to the upper mantle. Due to the unstable nature of the pile, its vertical motion hinders the rapid horizontal shortening of the pile after the formation of the first plume, which eventually leads to an exposed CMB proportion similar to that of $B \sim 0.8$. This pile geometry is described here as *Type 0*.

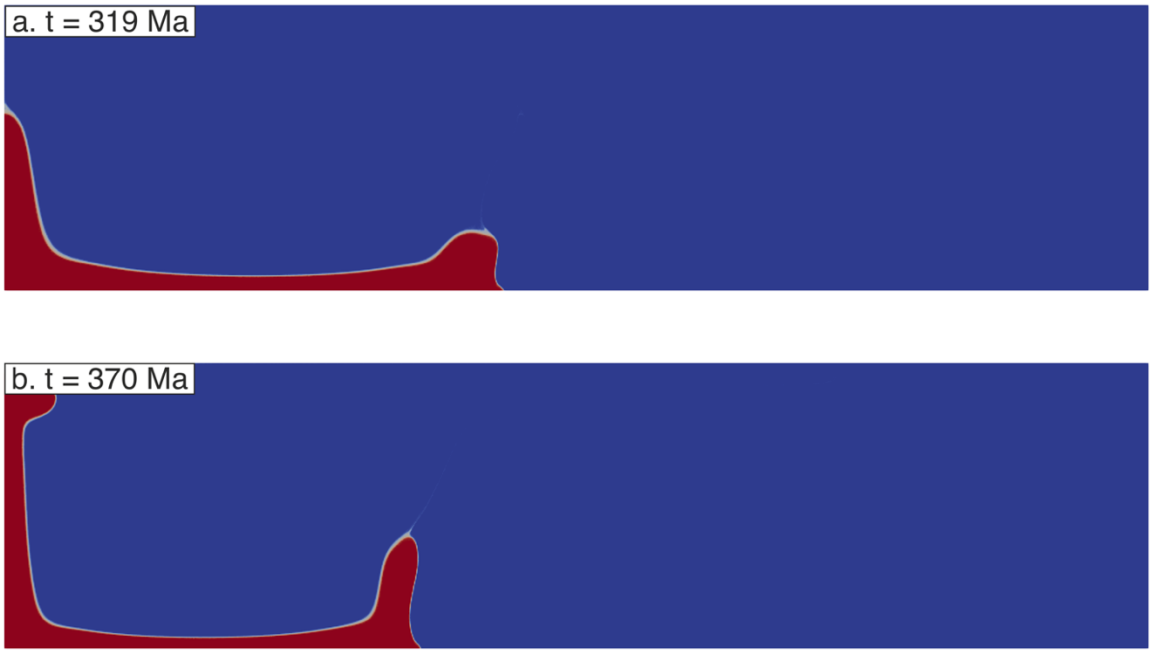

Figure 6.8: Evolution of pile geometry for $h_{pile} = 150$ km, $\mu = 100$, $c_{HPE} = 6.034 \times 10^{-9}$, and $B = 0.6$ (Type-0).

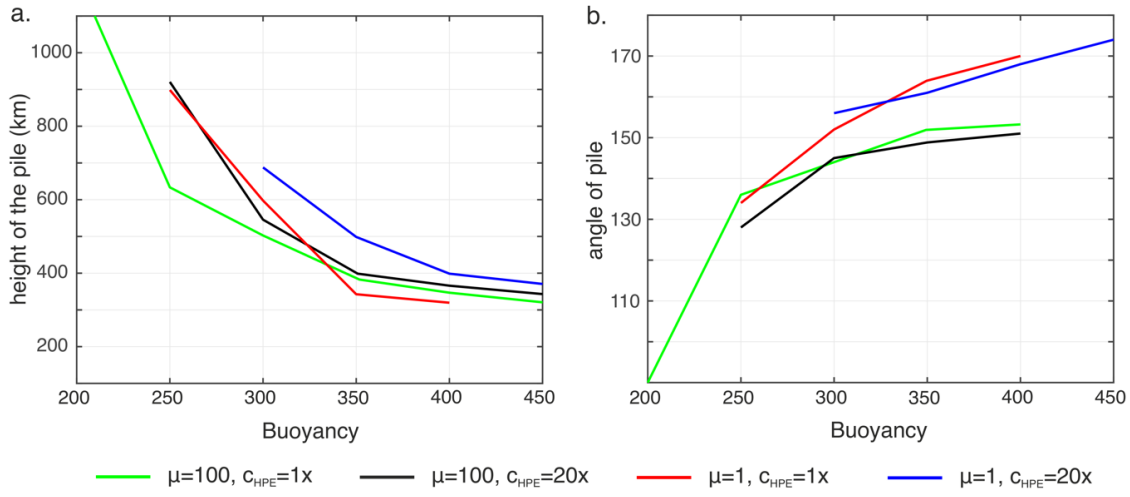

Figure 6.9: Plots of maximum pile height (a) and frontal angle of pile (b) from numerical models for different parametric values with $h_p = 150$ km.

Increasing B to ~1.4, on the other hand, further stabilizes the pile as compared to the reference model. As a result, the maximum pile height is lower than that of the model with $B \sim 1.0$ (Figure 6.9a). Similarly, the angle of the pile is higher than the reference indicating stable nature of the pile (Figure 6.9b). Overall, the pile geometry remains similar to the reference model but frontal dome is less pronounced and the depression behind the dome is less obvious. The time dependent change of the pile is also less prominent as the change in pile volume with time is much less compared to models with $B \leq 1.0$. The proportion

and rate of change of exposed CMB, on the other hand, is similar to the model with $B \sim 1$ (Figure 6.10c, d). We see a further lowering in the amplitude of dynamic topography near the plume rise and the exposed CMB adjacent to the pile. This pile geometry is labeled in this work as *Type 2asymetric* (*Type 2a*). The reference model also falls under the *Type 2* pile geometry. With Further increase in B completely stabilizes the pile which now acts almost passively owing to its high density and viscosity compared to the ambient mantle. The pile is much more resistant to the leftward mantle flow induced by the downwelling. This causes low CMB exposure throughout the course of the model run (Figure 6.10d). As a result, the maximum pile height is very low (Figure 6.9a) and the frontal angle is very high (Figure 6.9a). The pile volume, as a result, remains almost unchanged with time (Figure 6.10a). We call this *Type 3* pile (Figure 6.11).

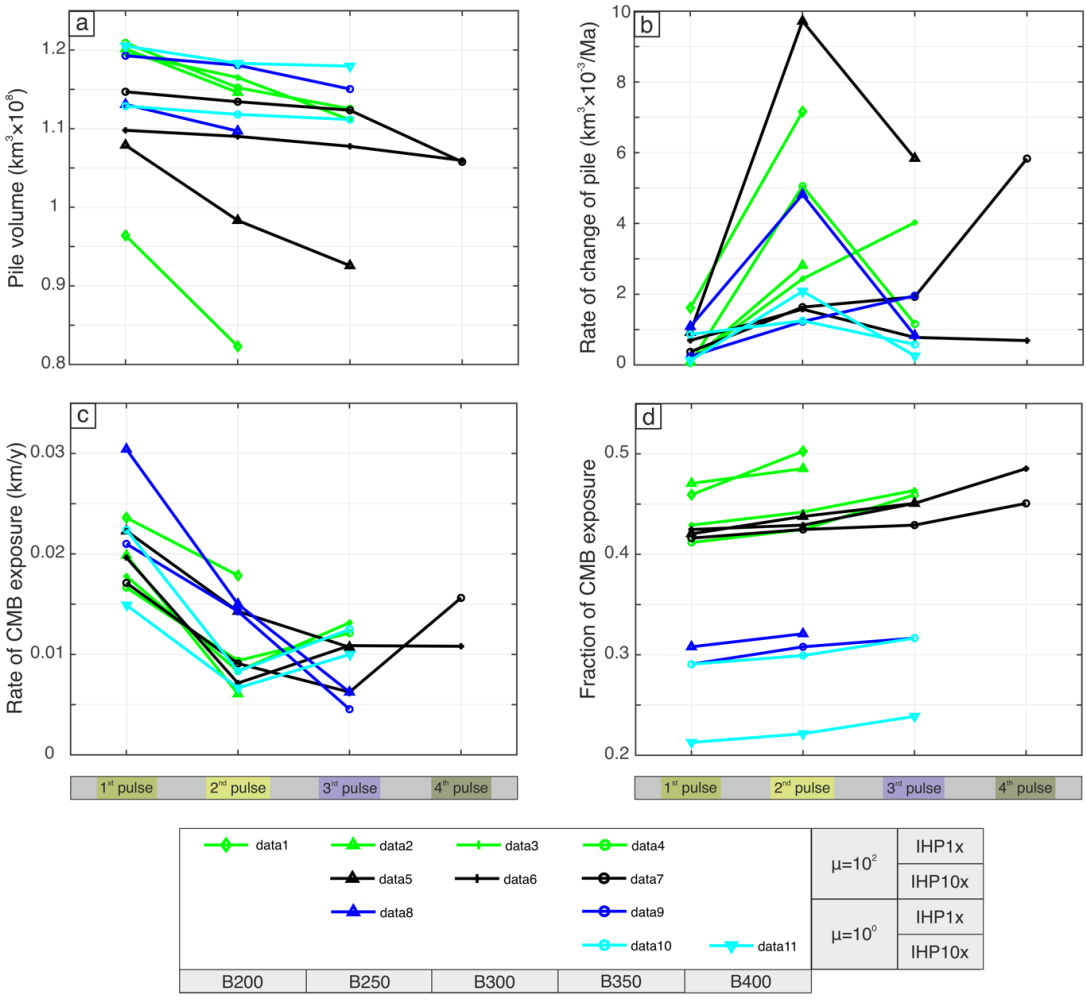

Figure 6.10: Calculated plots from numerical models for different parametric values with $h_p = 150$ km. (a) Decreasing trends of pile volumes. (b) & (c) Rate of change of pile volume and CMB exposure. (d)Variation in the exposed fraction of the core mantle boundary (CMB) for different model parameters. The x-axis represents successive pulses, which in turn reflect progressive time. The symbols stand for the parameter B, and the colors denote μ and c_{HPE}. Their details are provided in the legend.

Figure 6.11: Evolution of pile geometry for $h_{pile} = 150$ km, $\mu = 100$, $c_{HPE} = 6.034 \times 10^{-9}$, and $B = 1.4$ (Type-3).

Effect of viscosity

To see the effect of viscosity on its geometry, the pile viscosity was decreased to $\mu = 1$ while keeping all other parameters constant. The most prominent difference is in the structure of the frontal dome of the pile which gradually becomes symmetric as we decrease the pile viscosity. Another important difference can be identified by examining the dynamic topography of CMB. Unlike the model runs with $\mu = 100$, where there is a sharp depression behind the maxima, models with $\mu = 1$ leads to a gradual decrease in topography beneath the frontal dome. This difference is due to the greater distribution of velocity gradient near the pile margin owing to its comparable viscosity with the background (Heyn et al., 2020a). Other important thing to notice is that the exposed proportion of CMB is much less for $\mu = 1$ compared to that of $\mu = 100$ keeping other parameters constant (Figure 6.10d). This can again be explained by more diffused CMB parallel velocity gradient making the plie retreat much less effective, which results in lower rate of CMB exposure.

For $B \sim 0.8 - 1.0$ with $\mu = 1$, very prominent tent like symmetric frontal dome is seen to develop with plume tail forming at the its crest (Figure 6.12). The depression behind the frontal dome has now changed to symmetric domes and basins with a wavelength of $\sim$3000 km. Unlike the frontal domes, these domes are dormant and their height is lower.

Overall, the height of the frontal dome is more and the its angle is less compared to the model with $\mu = 100$ (Other parameters being the same) indicating the decreasing pile viscosity makes the pile more unstable (Figure 6.9). This results in lower pile volume with time as more pile materials are transported to the upper mantle (Figure 6.10a). We describe this pile geometry as *Type 1symmetric* (*Type 1s*). Increasing B to $1.2 - 1.4$ while keeping $\mu = 1$ we see a more stable pile with a symmetric frontal dome (Figure 6.13). Although the secondary domes are less pronounced, there is a clear visible wavelength of ~km. The height of frontal dome is now highly reduced and the angle is increased substantially. I call this pile geometry *Type 2symmetrical* (*Type 2s*). $B < 0.8$ and $B > 1.4$ makes the pile absolutely unstable (*Type 0*) and passive (*Type 3*), respectively.

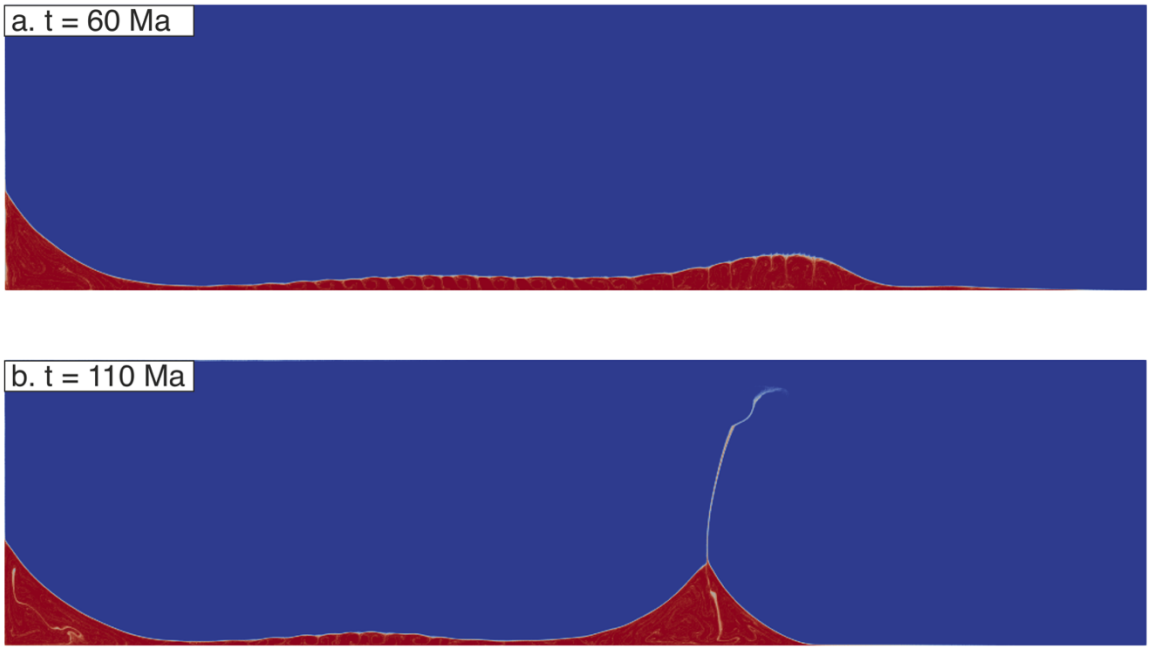

Figure 6.12: Evolution of pile geometry for $h_{pile} = 150$ km, $\mu = 1$, $c_{HPE} = 6.034 \times 10^{-9}$, and $B = 1$ (Type-1s).

Effect of c_{HPE}

To study the effect of the concentration of heat producing element on the pile dynamics I increased the c_{HPE} of the pile up to 20 times that of the ambient lower mantle. The most prominent difference in pile geometry is that for higher values of c_{HPE} the pipe of pile connecting the pile to the upper mantle becomes thicker, effectively transporting more pile material to upper mantle (Figure 6.10a) compared to models with $c_{HPE} = 6.034 \times 10^{-9}$. This is also reflected in lower values of pile volume with time indicating more effecting entrainment. Also noticeable is that higher c_{HPE} does not change the overall pile geometry.

The shape of the frontal dome remains almost similar to that of the lower c_{HPE}. Although, increasing c_{HPE} do increase the dome height more and the frontal angle is also lower (Figure 6.9).

Figure 6.13: Evolution of pile geometry for $h_{pile} = 150$ km, $\mu = 1$, $c_{HPE} = 6.034 \times 10^{-9}$, and $B = 1.4$ (Type-2s).

Effect of thickness of pile (h_p)

Thickness of the pile has a significant effect of the pile dynamics, its geometry and its volume. I varied the thickness between 150 km to 300 km with an interval of 50 to see how the total volume of pile material affects the pile geometry with time. Unlike the models with $h_p = 150$ km, models with $h_p = 300$ km show that for $B = 1, \mu = 100$ and $c_{HPE} = 1x$, the pile becomes passive with *Type 3* geometry. Although the maximum height of the pile is higher, if we examine the height difference from h_p (i.e., $h_{max} - h_p$) we see that the pile height actually decreases by increasing thickness (Figure 6.15a). Similarly, the frontal angle increases with increasing pile thickness (Figure 6.15b) indicating more stable pile for higher thickness. Within the range of $0.8 < B < 1$, *Type 2a* like pile geometry prevails as compared to *Type 1a* geometry for lower pile thickness. Other important feature is that the frontal dome is not well developed and the depression behind the dome is absent (Figure 6.14). We think of this as a manifestation of higher volume of high-density material making it much more resistant to internal deformation against gravity or also against lateral mantle

flow. As a result, it yields lower normalized rate of change of pile volume (Figure 6.16a) and higher CMB fraction (Figure 6.16c) compared to models with lower pile volume. Decreasing B further to 0.6, the pile geometry enters the *Type 1a* like geometry, again with an ill developed frontal dome. This drastically decreases the pile volume and the fraction of exposed CMB (Figure 6.16a, c) compared to the models with higher B. But when compared to the models with same values of B but lower thickness, the rate of CMB exposure and rate of change of pile volume decreases. Any further decrease in B value will lead to absolute unstable pile with *Type 0* geometry.

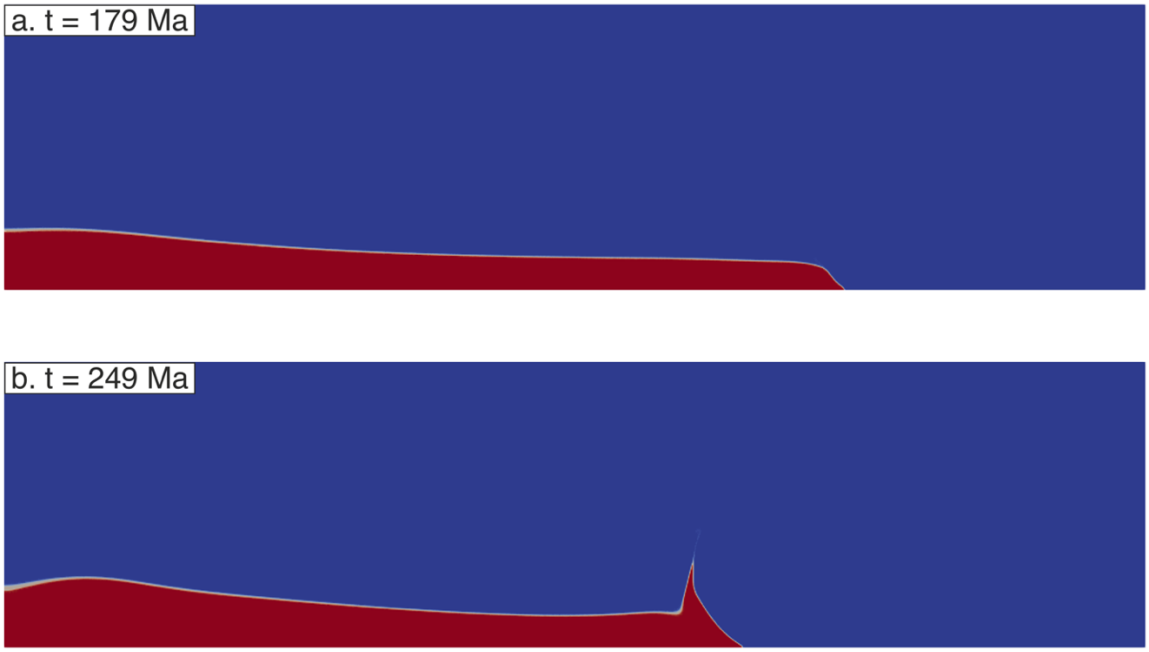

Figure 6.14: Evolution of pile geometry for $h_{pile} = 300$ km, $\mu = 100$, $c_{HPE} = 6.034 \times 10^{-9}$, and $B = 0.8$

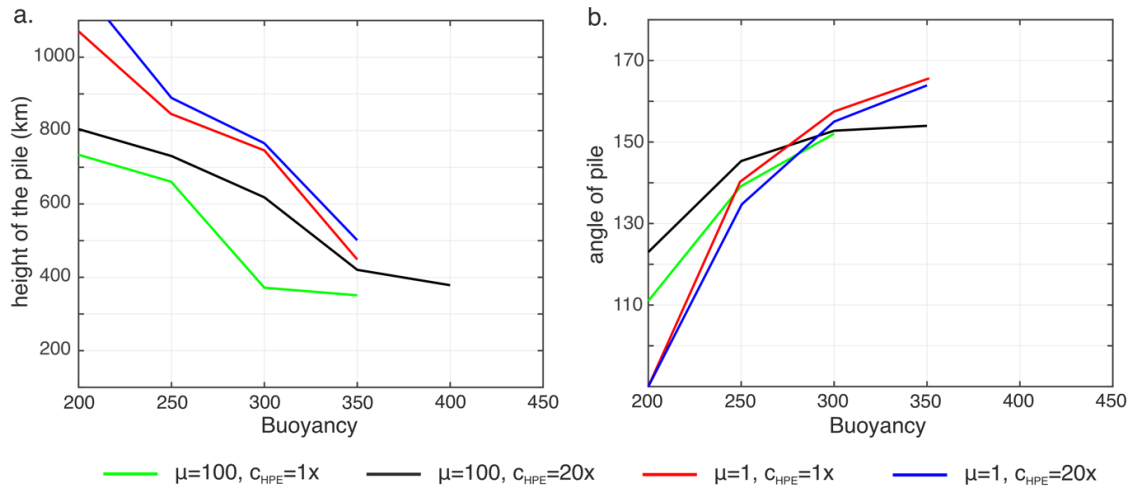

Figure 6.15: Plots of maximum pile height (a) and frontal angle of pile (b) from numerical models for different parametric values with $h_p = 300$ km.

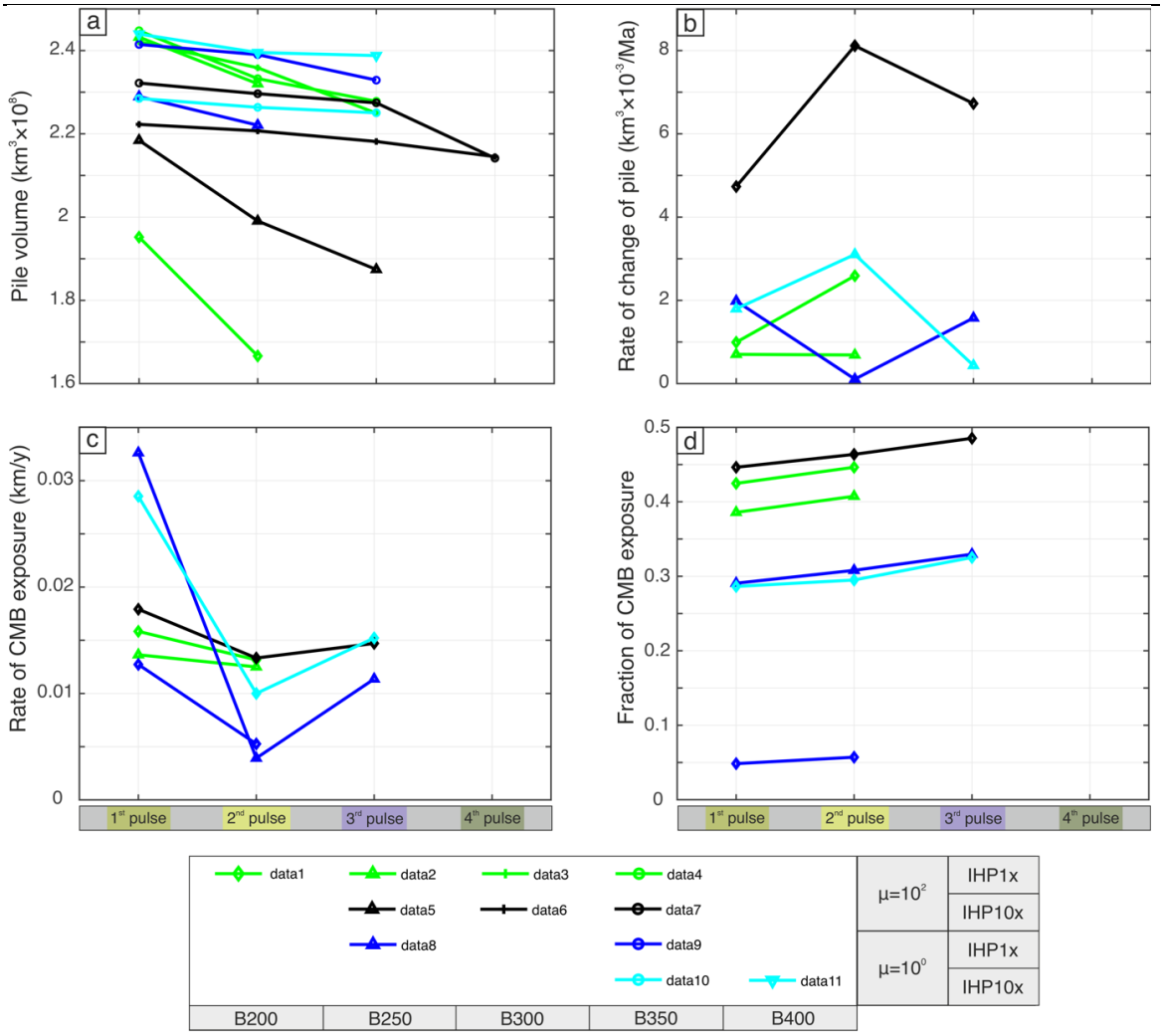

Figure 6.16: Calculated plots from numerical models for different parametric values with $h_p = 300$ km. (a) Decreasing trends of pile volumes. (b) & (c) Rate of change of pile volume and CMB exposure. (d)Variation in the exposed fraction of the core mantle boundary (CMB) for different model parameters. The x-axis represents successive pulses, which in turn reflect progressive time. The symbols stand for the parameter B, and the colors denote μ and c_{HPE}. Their details are provided in the legend.

Decreasing μ, however, makes the pile relatively unstable, similar to the models with lower h_p. E.g., for $B = 0.6$, decreasing μ to 1 makes the pile completely unstable producing *Type 0* geometry instead of *Type 2a* geometry. For $B = 0.8 - 1.0$, however, the pile takes a *Type 1s* geometry for $\mu = 1$. They also show lower pile volume with time and lower CMB fraction (Figure 6.16a, c) compared to models with higher μ indicating comparatively unstable nature of the pile. Then it transforms to *Type 2s* for $1.0 < B < 1.2$ with $\mu = 1$, before becoming passive (*Type 3*) for higher values of B. Similarly, both CMB fraction and pile volume increases (Figure 6.16a, c) as we decrease viscosity. Comparing it to models with lower h_p, a decrease in the rate of change of pile volume is observed. Increasing c_{HPE}

up to 20x, on the hand, does not change the type of the pile but it increases the overall supply of pile material to plume tail. This is evident from the lower pile volume as c_{HPE} is increased (Figure 6.16a). But compared to the same model with lower h_p, a reduction in the rate of change of pile volume (Figure 6.16b) and lower rate of CMB exposure (Figure 6.16c) is noticed.

6.4 Relevance of model parameters

Geochemical observations on oceanic island basalts (OIBs) support the presence of an enriched mantle reservoir represented by lower $^{40}\mathrm{Ar}/^{39}\mathrm{Ar}$ and a higher $^{3}\mathrm{He}/^{4}\mathrm{He}$ compared to MORB, indicating mantle heterogeneity and/or variable mantle reservoirs (White, 2015). Some of these sources are less degassed and hence, are more enriched in HPEs (Citron et al., 2020). One possibility is that such reservoirs are present within LLSVPs since they are primarily composed of primordial material (Deschamps et al., 2011), subducted Hadean crust (Tolstikhin et al., 2006), or recycled oceanic crust remnants from decomposed subducted plate(Mulyukova et al., 2015). Studies show that they constitute almost ~9% of total mantle mass and even if they constituted only ~2% of mantle by mass, they must be enriched in HPEs. Thus, it is a valid assumption that the LLSVPs are enriched in HPEs and based on heat budget calculations (Citron et al., 2020) it is estimated that the c_{HPE} can be as high as 20-25 times that of the background mantle. Now the plumes originated from the edges of LLSVPs will entrain enriched pile material, which explains the characteristic isotope ratios of various OIBs. It is obvious that such enrichment will alter the buoyancy of the pile over time which might ultimately lead to a gravitationally unstable state of the pile. Nonetheless, all these conclusions are based on a limited number of simulations and their model has c_{HPE} only $5x$ to $10x$ that of the ambience. A recent study by Citron et al., (2020), on the other hand has performed systematically a series of model to show the effect of c_{HPE} up to $25x$ on the long-term dynamics of piles. There results show that the for higher intrinsic density of the pile, we need to have a higher c_{HPE} to form a pile-like morphology rather than a stable layer (Type 3 in our model). But this work does not incorporate plate velocity and primarily focuses on the dynamics of the pile on a 100 Ma scale. In this work we incorporated c_{HPE} up to $20x$, and introduced plate velocity to examine pile dynamics on a sub-100Ma scale. We show that the effect of c_{HPE} is much less pronounced than that of other parameters such as viscosity ratio (μ) or pile thickness (h_p) in that they cannot change of type of pile geometry.

However, they affect the dynamic topography and more importantly the material supply to thermochemical plumes associated with a pile. Increasing c_{HPE} increases the dynamic topography and material supply to the plume, especially at lower value of buoyancy number (B) and h_p. Moreover, the thickness of plume tail increases with increasing c_{HPE}.

The thickness of the pile atop CMB is not well constrained because of its heterogeneous nature. Early tomographic models found 3% anomalies in shear-velocity and strong lateral gradients beneath southern Africa and is related to a pile height of ~1000 km (Ni and Helmberger, 2003; Ritsema and van Heijst, 2002). Later studies confirm stronger anomalies of 1–10% S-wave velocity at 2800 km below the southeastern Atlantic and southern Indian Ocean, over a thickness of 300 km above CMB. It is thus postulated that upward extent of LLSVP in their model is 800-1200 km in the central region and < 300 km at the flanks for African LLSVP. Similar height of LLSVP flanks have also been estimated from the Pacific LLSVP and newly discovered Eurasian LLSVP. I thus varied the average thickness of the pile between 150 km to 300 km at an interval of 50 km as we are primarily considering the flank of the piles.

The excess density of LLSVP is rather well constrained from various geophysical studies. Moulik and Ekström, (2016), applying various seismological observations have predicted the presence of large and dense anomalies that are anticorrelated with piles exhibiting low shear wave velocity above the CMB. Using measurements of semi-diurnal body tide deformation Lau et al., 2017 have constrained lower mantle buoyancy. Using a probabilistic approach, they have concluded that the bottommost 200-300 km is enriched with high-density materials derived by subduction leading to a mean density $\sim 0.5\%$ higher than the surrounding mantle. Koelemeijer et al., (2017), on the other hand, have shown using splitting of Stoneley modes that although the lowermost 100 km of the LLSVP is denser than the average CMB mantle density, the rest of the LLSVP is actually lighter than the surrounding mantle. We thus vary our basal layer excess density between $150 - 450$ kg/m^3 to get an idea of how it can affect the dynamics of the pile.

Unlike the aforementioned properties, the pile viscosity is not well-constrained as there is no straightforward way of calculating viscosity from geophysical observations. Although the thermal viscosity factors can be predicted, it is also highly dependent composition and mineral assemblage present. Moreover, additional problem is posed by the fact that the higher density of the pile is often attributed to phases with higher Fe/Mg ratio inside the pile. For example, if a high concentration of Bridgmanite is considered

within the pile, it should contain high proportion of Fe, which will ultimately create Ferropericlase and post-Bridgmanite (Trønnes et al., 2019). Although this can justify the higher density of the pile, both the Post-bridgmanite and ferropericlase have considerably lower viscosity compared to Bridgmanite (Ammann et al., 2010). Due to these uncertainties, I choose to vary the viscosity ratio (μ) between $0.1 - 100$ to see how they affect the lower mantle dynamics and the dynamic topography at the CMB.

Using all the aforementioned parameters, I separated out all the different pile geometries obtained from the model runs to create regime diagrams. Let us first focus on the effect of initial pile thickness (h_p) for a constant viscosity ratio (μ) of 100 on different types of piles (Figure 6.17). For low values of B, we see that increasing h_p decreases the stability field of Type 0 pile where it becomes unstable only if $B < 0.5$ for $h_p = 300$ km. For intermediate values of B we notice that the field of Type 1a shrinks rapidly with increasing h_p where for $h_p > 250$ km, Type 1a is completely replaced by Type 2a. For higher values of B, on the other hand, the stability field of Type 3 increases rapidly with increasing h_p. For $h_p > 300$ km, pile can become passive for B value as low as 0.9. Overall, the field of Type 2a also increases on the lower B side but decreases on the other end with increasing h_p.

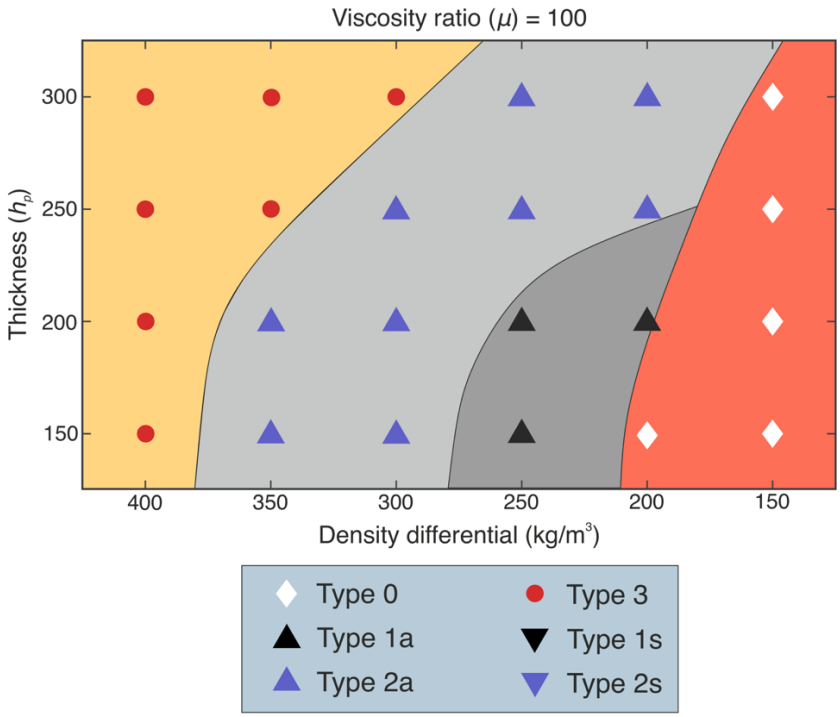

Figure 6.17: A regime diagram of the different modes of pile geometry for various values of $h_p$at constant μ of 100.

Next, I investigate the effect of viscosity ratio (μ) for a given value of $h_p = 150$ km (Figure 6.18). Decreasing μ for low values of B results in destabilization of the pile, where for $\mu < 1$, we get unstable pile (Type 0) for B value as high as 0.8. For intermediate values of B, a total of four fields are observed who are separated by the line $\mu = 1$. For $\mu \leq 1$, the frontal lobe becomes symmetrical and we get Type 1s and Type 2s pile geometry with increasing B. For $\mu \geq 1$, on the other hand, we get pile geometry with asymmetric frontal lobe (Type 1a and Type 2a). Overall, the fields of Type 1 and Type 2 shifts toward higher B side with decreasing μ. For higher values of B, the stability field of Type 3 pile decreases with decreasing μ with Type 2s replacing Type 3 for $\mu < 0.5$ even at very high values of B.

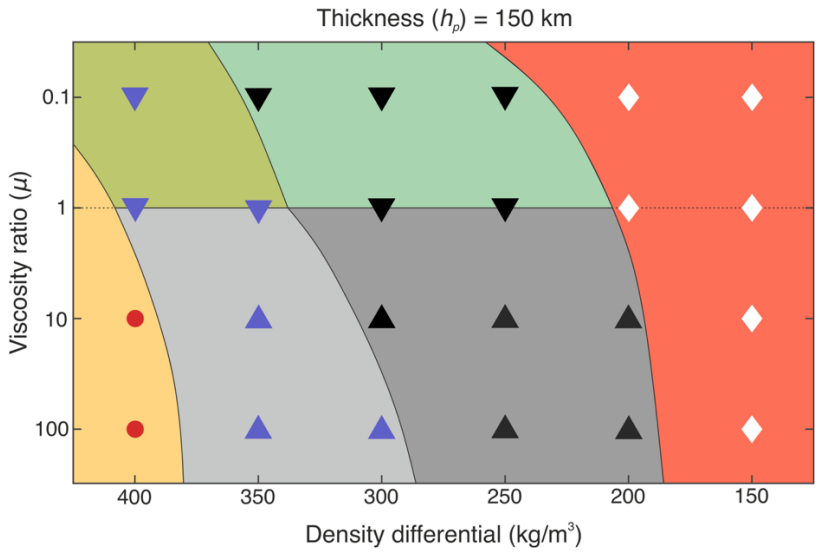

Figure 6.18: A regime diagram of the different modes of pile geometry for various values of μ at constant h_p of 150.

6.5 Pulsating rise of thermochemical plumes

I will now consider pile density, viscosity, concentration of heat-producing elements, and major phase transitions in the mantle to obtain a reasonable plume model for the Deccan LIP evolution in the geodynamic framework of the Réunion hotspot. In this modelling, the buoyancy number (B), which measures density contrast of the pile with the ambient lower mantle, accounts for varying relative proportions of eclogite and peridotite within the basal layer. As the viscosity and heat-producing element concentration of the pile are not well constrained, we varied them within a plausible range of their values found in the literature

(Citron et al., 2020; Dannberg and Sobolev, 2015; Heyn et al., 2020b; Li et al., 2018). A velocity boundary condition is imposed at the upper model boundary to replicate the lithospheric plate kinematics that prevailed during Réunion hotspot activities. The details of the model domain is provided in Figure 6.19.

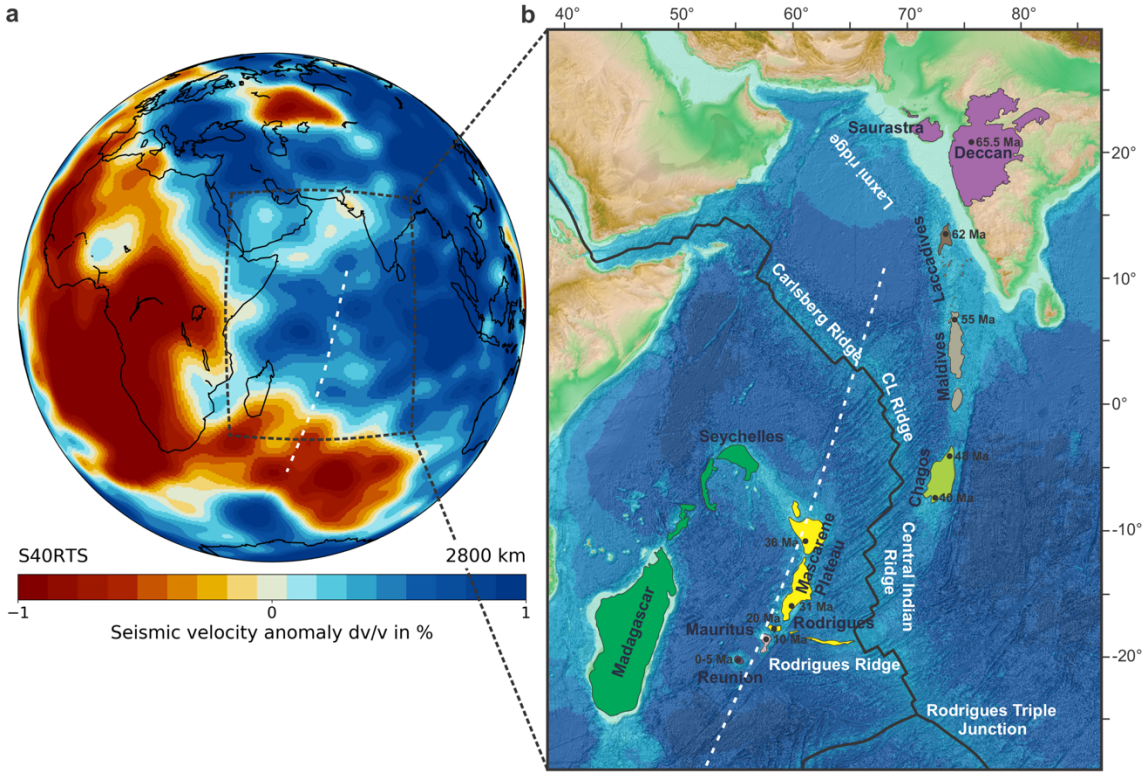

Figure 6.19: Details of the study area in a global perspective. (a) Tomography-Depth slice at 2800 km, showing the present-day location of the eastern flank of African LLSVP using S40RTS model (data generated using SubMachine). (b) Satellite bathymetry map of the western Indian Ocean showing the complete Réunion hotspot track (Deccan Traps to Réunion Island). Aerial extent of the Deccan volcanic province is demarcated in purple within the Indian subcontinent. Crustal age estimates for Réunion plume activity (in Ma) indicate plume positions. Black lines delineate the plate boundaries. The base map is reproduced from BODC data. www.bodc.ac.uk. The white dashed line represents the trace of our model section.

The plate velocity induces downwelling flow in the mantle, which forces the thermal boundary layer (TBL) at the CMB to pile up laterally and increase its thickness (h_{TBL}~300 km) (Figure 6.20a). The TBL is pushed towards the pile to increase h_{TBL} further (Figure 6.20b), amplifying the Rayleigh number (Ra) in the TBL to locally exceed the critical Ra. Under this threshold condition, the buoyancy head becomes high enough to force the material to flow vertically against gravity, forming a thermochemical plume (Figure 6.20c, d). Due to its strong buoyancy flux, the plume grows mainly in the vertical direction within the lower mantle. However, on encounter with the upper mantle, it faces two processes that significantly hinder its continuous growth: 1) influence of the plate

velocity and 2) phase transition between 300 and 400 km (Dannberg and Sobolev, 2015). At this stage, the plate-driven flow extends to a depth of 660 km and exert drags to the plume head (Figure 6.20e), detaching it from the tail counterpart. The buoyancy ultimately takes over the drag, allowing the head to move vertically upward in the form of a solitary pulse (Figure 6.21a i-iv). The ascending head undergoes phase transformations: coesite to stishovite and pyroxene to garnet, increasing the plume density. Ultimately, inherent high excess temperatures enable plumes to overcome this density-enhancing barrier to reach the lithosphere-asthenosphere boundary (LAB), where they spread laterally in the horizontal direction. This stagnation process facilitates thermal mixing and mechanical entrainment within the mantle.

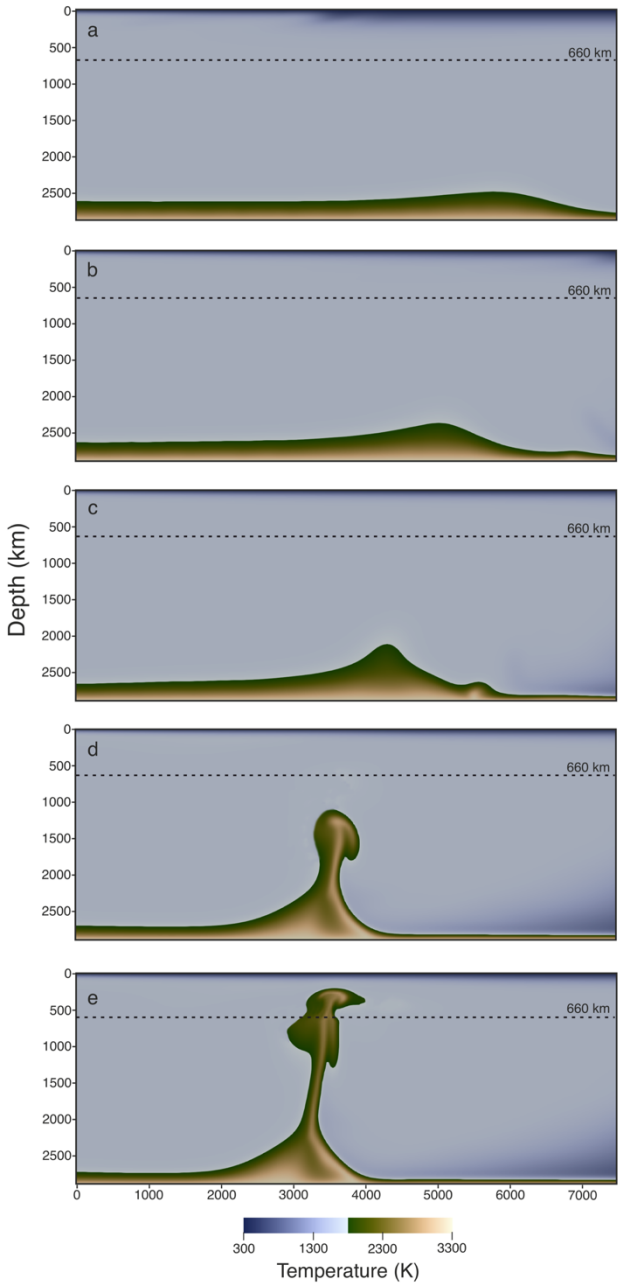

Figure 6.20: Evolution of a thermochemical plume in the reference model ($B = 0.8, \mu = 100$, and $c_{\mathrm{HPE}} = X$). (a) Piling up of TBL due to forcing by a downwelling flow in mantle. (b) Growth of a small instability on the extreme right side of the TBL. (c) Lateral advection and climb of the instability to the pile crest. (d) Development of a mature plume from the instability with increasing buoyancy flux. (e) Perturbation of the plume head at the mid mantle transition zone to produce a primary pulse. Note that the pulse in the upper mantle deflect to the right under the influence of plate velocity.

The model run shows that the plume upwells in a pulsating fashion to produce multiple heads in the course of the ascent event (Figure 6.21a i-iv). The primary head gives rise to the first pulse following its detachment from the main body after crossing the 660 km boundary (Figure 6.21a i). The initiation of the plume destabilizes the pile margin (Figure 6.21a i, ii), as indicated by reducing pile volumes and high rates of its lateral migration (~ 10 km/Ma) (Figure 6.21b ii, iii), that produces relatively high eclogite proportions (~ 10%) and heat-producing element concentration in the plume (Figure 6.22a). A large buoyancy head due to the high excess temperature (> 500 K) and density contrast (> -50 kg/m^3) (Figs. Figure 6.22b, c) facilitates the surface to attain high dynamic topography with an elevation of ~1600 m (Figure 6.21a i inset) and inflates the pulse volume ($\sim 1.5 \times 10^7$ km^3) (Figure 6.21b i). The pile margin remains unstable (Figure 6.21a ii), forcing a large volume of material to upwell through the plume tail and produce a second pulse (Figure 6.21b ii) as time elapses after the first pulse allowing new materials to accumulate in a threshold volume at 660 km. Unlike the first pulse, the second pulse evolves with a moderate amount of eclogite and heat-producing elements (HPE) to form significantly lower pulse volume (0.9×10^7 km^3) and dynamic topography (~800 m) (Figure 6.21a ii inset) owing to its lower excess temperature (~400 K) and density contrast (> -40 kg/m^3) (Figure 6.224b, c). With time the pile moves further away from the plume axis but the rate of the movement reduces to ~5-6 km/Ma. It sustains the periodic material supply to the 660 km boundary to produce tertiary pulses (Figure 6.21a iii, iv; b iii). The pile eventually attains a stable state, and unstable to stable transition results in a drastic reduction in material volume supply to the plume (Figure 6.21b ii), marked by much lower pulse volume ($\sim 0.5 \times 10^7$ km^3) and a low positive dynamic topography (~100-200 m) (Figure 6.21a iii, iv insets) with low excess temperature (~ 250 K) and density contrast (~-20 kg/m^3). Although all the sequential pulses ultimately reach the LAB and take part in melting and subsequent volcanism, the primary (first) pulse, owing to its sufficient excess temperature (> 500 K), and volume ($\sim 1.5 \times 10^7$ km^3) takes the lead role in forming LIPs. The thermochemical pile, which is the primary material feeder for the pulses, stratifies a

specific set of physio-chemical parameters to generate a reasonable melt volume and dynamic topography required for the formation of Deccan LIP.

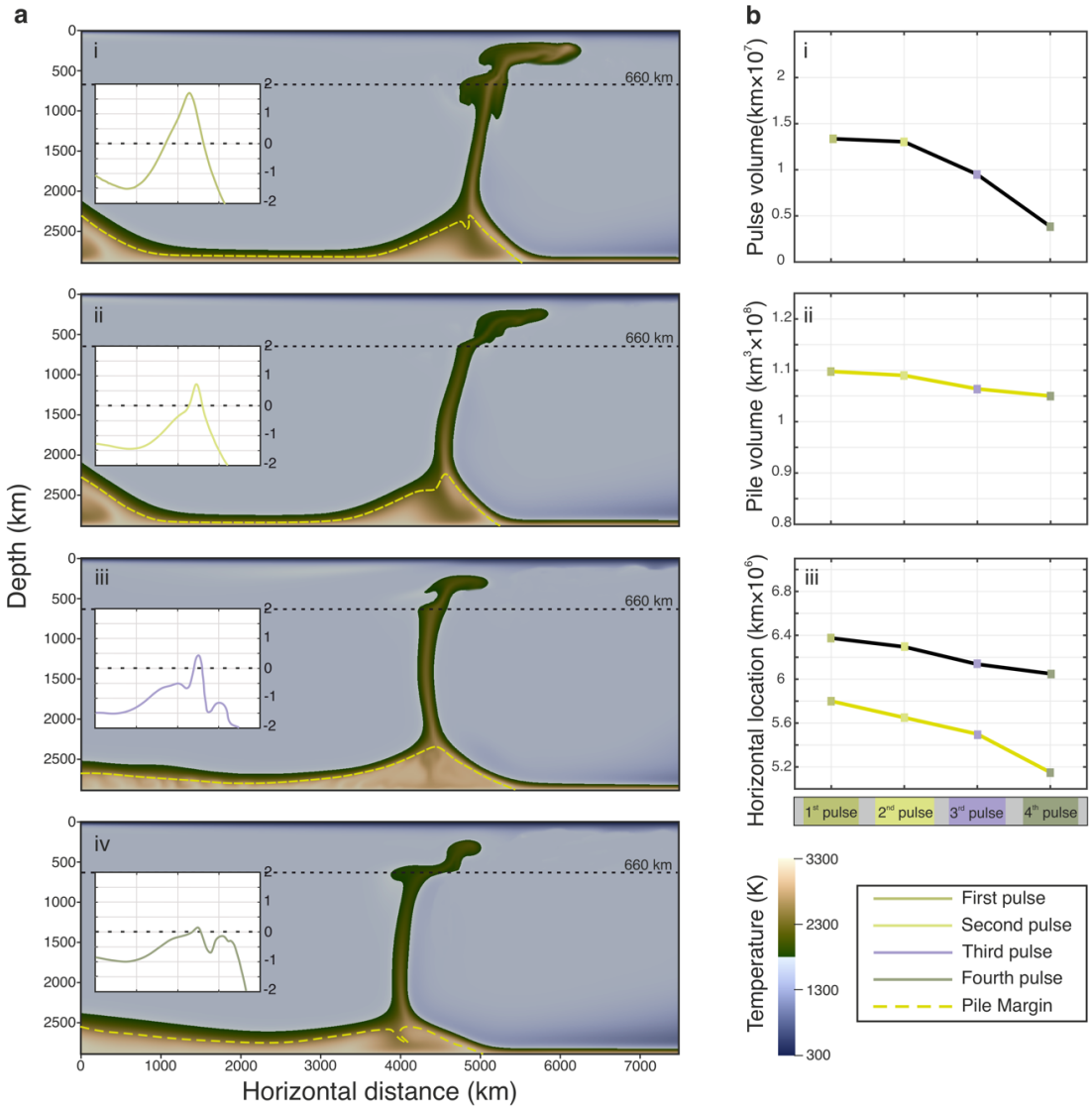

Figure 6.21: Pulsating ascent dynamics of thermochemical plume at mid-mantle transition zone. (**a**) Development of successive four pulses (i-iv) from a thermochemical plume in models with buoyancy number (B) = 0.8, viscosity ratio (μ) = 100 and heat producing element concentration (c_{HPE}) same as the background mantle. Colors (Crameri et al., 2020) represent the temperature and dashed yellow lines delineate the pile margin. Insets show the dynamic topography (in km) corresponding to each pulse. **(b)** Calculated plots of the pulse volume **(i)**, the pile volume **(ii)**, and the locations of plume (black) and pile margin (yellow) **(iii)** during the four pulse events (denoted in different colors).

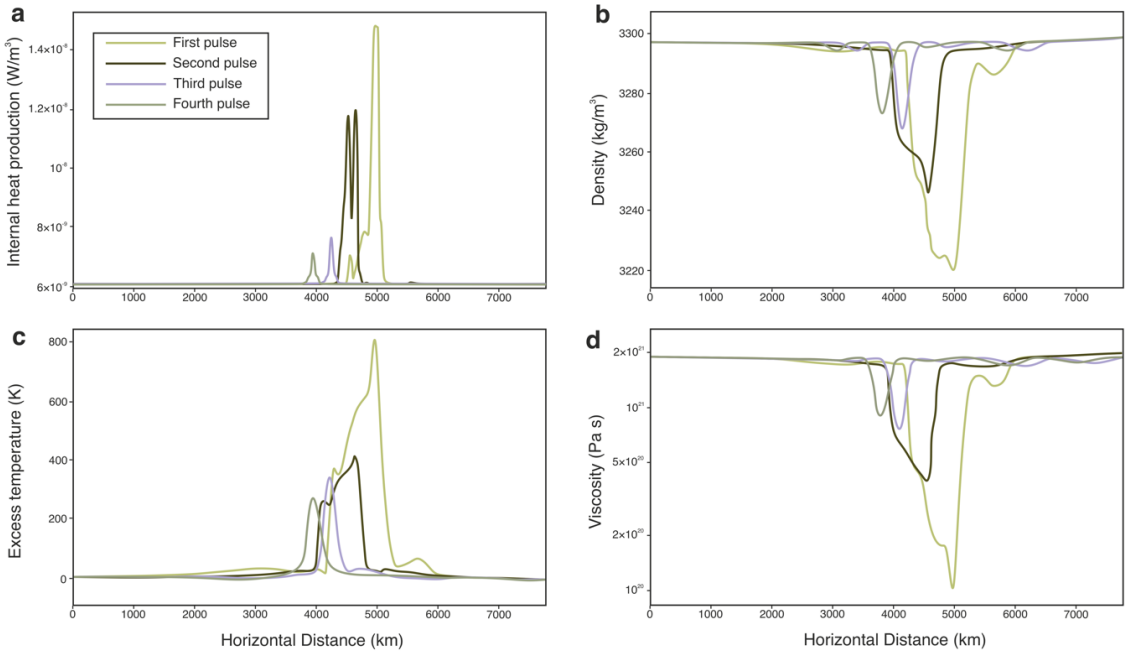

Figure 6.22: Horizontal variation of the physico-chemical properties in four successive plume pulses produced at the mid-mantle transition zone. The graphical plots correspond to a depth of 400 km. (a) Variations of internal heat production showing a maximum peak value for the first pulse (yellow curve). Note that the next pulses consistently reduce their peak values. The secondary pulse (Brown) contains considerable amount of HPE, as reflected from its high internal heating production, which weakens with the tertiary pulses (blue and green curves). Their reducing trend indicates decrease in HPE concentration due to less entrainment of pile materials by the plume. (b) Density profiles. The first pulse shows the highest negative density anomaly reflecting strong buoyancy head. The density anomalies significantly weaken in the secondary and tertiary pulses. (c)-(d) Excess temperature and viscosity profiles for the pulses, the patterns of which agree with the HPE concentration and the density profiles in (a) and (b), respectively.

Buoyancy effects on plume rise dynamics

A series of simulations was performed to investigate how the buoyancy number (B) of the pile influenced the process of pulse generation at the mid-mantle transition zone for a given viscosity ratio (μ ~1) and HPE concentration. For low B values (< 1), the mantle flow efficiently drags the pile horizontally to widen the exposed CMB fraction, causing both h_{TBL} and pile height (h_{pile}) to increase at high rates (Figure 6.23a, c; Figure 6.24a). Consequently, the pile becomes unstable (Figure 6.23a) to accelerate material flux into the plume and gives rise to initial pulses with large volumes ($> 1.5 \times 10^7$ km^3) and dynamic topography (> 1500 m) (Figure 6.23a, c inset; Figure 6.24b). Increasing B weakens the interaction of mantle flow with the pile due to a high intrinsic density of the basal layer, leading to TBL thickening at slow rates. (Figure 6.23b, d; Figure 6.24a). As a result, the plume having the same initial excess temperature produces pulses of much smaller volumes ($< 1.1 \times 10^7$ km^3) (Figure 6.24b) and dynamic topography (<1100 m) (Figure 6.23b, d

insets). Moreover, the volume difference in primary, secondary, and tertiary pulses are much more pronounced at a lower B value (Figure 6.24a).

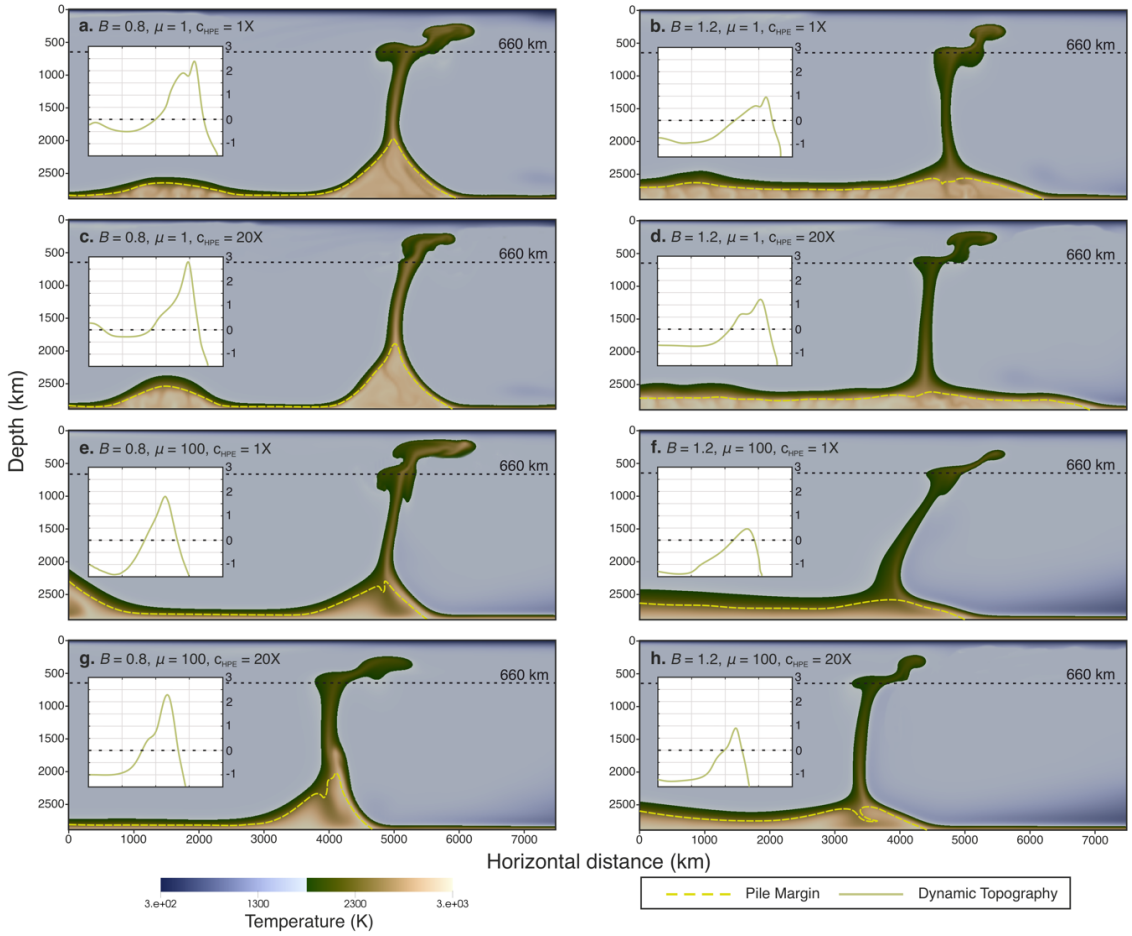

Figure 6.23: Effects of the model parameters on pulse and pile dynamics**.** Geometry and locations of the pulses generated from a plume head and the pile in different models with varying parameters: **(a)** B = 0.8, μ = 1, and c_{HPE} = 1X; **(b)** B = 1.2, μ = 1, and c_{HPE} = 1X; **(c)** B = 0.8, μ = 1, and c_{HPE} = 20X; **(d)** B = 1.2, μ = 1, and c_{HPE} = 20X; **(e)** B = 0.8, μ = 100, and c_{HPE} = 1X; **(f)** B = 1.2, μ = 100, and c_{HPE} = 1X; **(g)** B = 0.8, μ = 100, and c_{HPE} = 20X; **(h)** B = 1.2, μ = 100, and c_{HPE} = 20X, where X denote c_{HPE} value for the background mantle. Color scale are same as in Figure 6.21. Inset of each figure shows the dynamic topography (in km) at the surface for the pulses presented in the respective snapshot.

Viscosity effects on pulse-driven processes

Geophysical studies suggest that the viscosity of thermochemical piles can be up to 1000 times higher than the ambient mantle (Heyn et al., 2020b). It is found that an increase in the viscosity ratio (μ) from 1 to 100 considerably dampens the vertical growth of piles, allowing them to remain stable for given values of B and HPE concentration (Figure 6.23e-h), as reflected from the lower rates of pile volume changes (Figure 6.24c). This increase in μ, on the other hand, strengthens the interaction of mantle flow with the pile, as

evidenced from large exposed CMB areas (Figure 6.24a). Such a strong interaction increases the horizontal shortening of the pile at the cost of vertical growth, eventually reducing pulse volumes by up to 12 % (Figure 6.24b) and widening the time periodicity of pulse generation. μ also significantly influences the dynamic topography. The model estimates for $\mu = 1$ yield a large dynamic topography (> 3000 m) when B is low (< 0.8), which is considered unrealistic for thermochemical plumes. Increasing μ to 100 depresses the topography to < 2000 m for lower values of B which can be correlated with Deccan volcanic events.

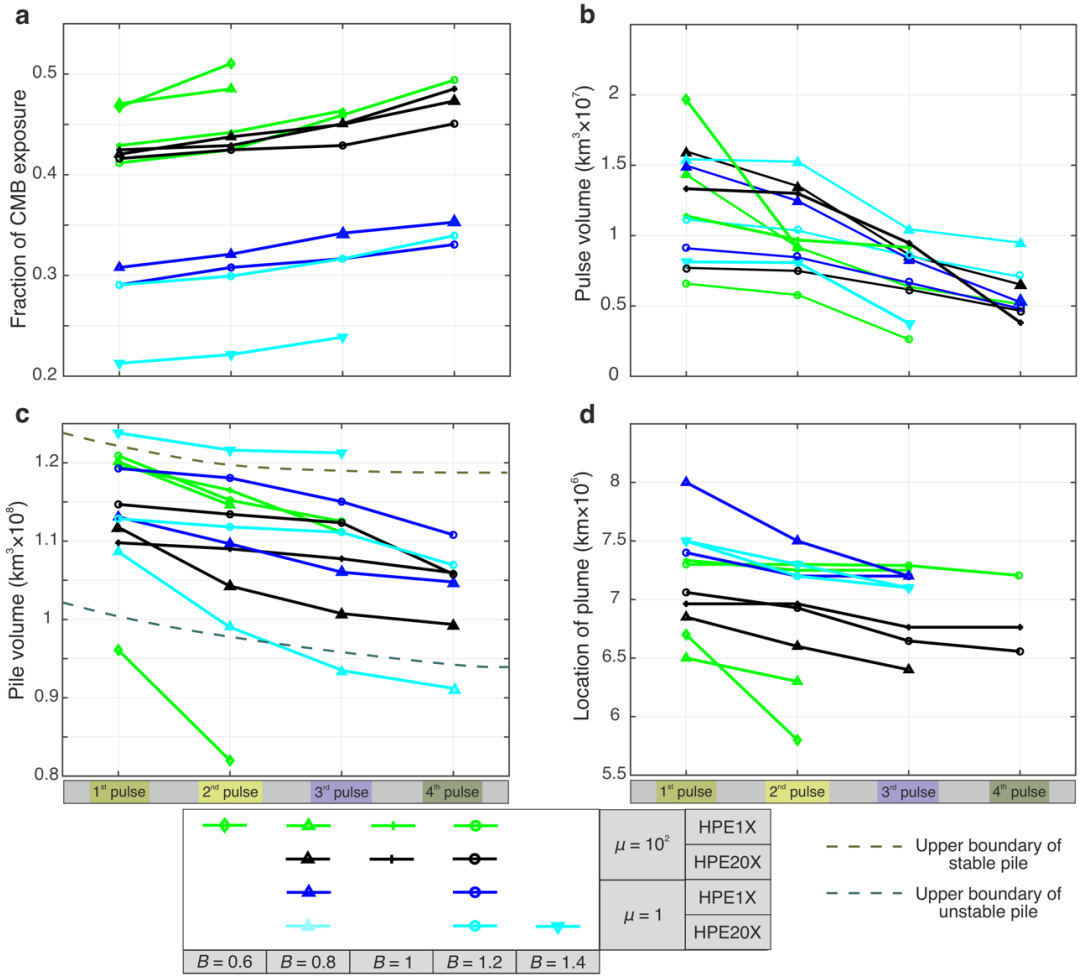

Figure 6.24: Calculated plots from numerical models of successive pulses for different parametric values. (**a**) Variation in the exposed fraction of the core mantle boundary (CMB) for different model parameters. **(b) - (c)** Decreasing trends of successive pulse and pile volumes. **(d)** Varying plume head locations for successive pulses. The x-axis represents successive pulses, which in turn reflect progressive time. The symbols stand for the parameter B, and the colors denote μ and c_{HPE}. Their details are provided in the legend. Also provided are the fields of passive, stable and unstable piles using dashed curves.

Effect of internal heat production on plume dynamics

Geochemical observations on OIBs support the presence of enriched mantle reservoirs as mantle heterogeneity and/or variable mantle reservoirs (Peters and Day, 2017). Some of these sources are less degassed and hence, are more enriched in HPEs. One possibility is that such reservoirs could be present within LLSVPs since they are primarily composed of primordial material, subducted Hadean crust, or recycled oceanic crust remnants from a decomposed subducted plate (Deschamps et al., 2011). Previous estimates, based on heat budget calculations, show that the heat-producing element concentrations (c_{HPE}) can be as high as 20 to 25 times that of the background mantle (Citron et al., 2020). To study the role of this factor on the pile dynamics, I increased c_{HPE} of the pile by up to 20 times that of the ambient lower mantle. Such enrichment augments the pile buoyancy with time to set a gravitationally unstable state of the pile even under a high B condition. Plumes that originate from pile edges in our models entrain HPE-enriched pile materials to increase its excess temperature. However, c_{HPE} has relatively weak effects, as compared to other parameters, such as viscosity ratio (μ) (Figure 6.23 c-d, g-h). c_{HPE} primarily affects the dynamic topography and, more importantly, the material supply to thermochemical plumes (Figure 6.24b, c). Increase in c_{HPE} amplifies the dynamic topography and also enhances material supply to the plume, especially at a lower value of the buoyancy number (B). The other remarkable effect of c_{HPE} on plume geometry is that the plume develops a thick tail, which facilitates pile material transport to the mid-mantle region in larger volumes (Figure 6.23g), compared to that produced in a lower c_{HPE} condition. This is also reflected in higher rate of reduction in pile volumes with time (Figure 6.24c), which implies a more effective pile material entrainment into the plume tail. In addition, high c_{HPE} causes the plume to gain a higher excess temperature that results in dynamic topography with a realistic elevation of ~1600 m for the primary pulse for μ = 100 (Figure 6.23g inset).

6.6 Melt transport from a thermochemical plume

To develop partial melting models, I used a 2D Cartesian box with a vertical depth of 350 km from Earth's surface and a horizontal length of 700 km (Figure 6.25a). The dimensions are reduced to achieve a high-resolution analysis of the melting phenomena. Unlike the whole mantle model, compressibility of both the solid and the melt phases within a two-phase model are considered. The top thermal boundary layer represents the thermal

structure of the Indian shield during the Late Mesozoic with a LAB depth of ~160 km. A thermal perturbation of 250-500 K is added at the bottom boundary to represent the excess temperature (non-adiabatic temperature) derived by the plume head from the whole mantle model (Figure 6.25b ii). The boundary velocity condition is the same as in the previous model, except for the bottom boundary, where mass can flow in and out, thus supplying plume material to generate successive melt pulses. Initially, the system is considered to be free from porosity. Mesh deformation was used at the upper boundary to track the surface topography generated in the successive melting events. The details of the model parameters is given in Table 6.2.

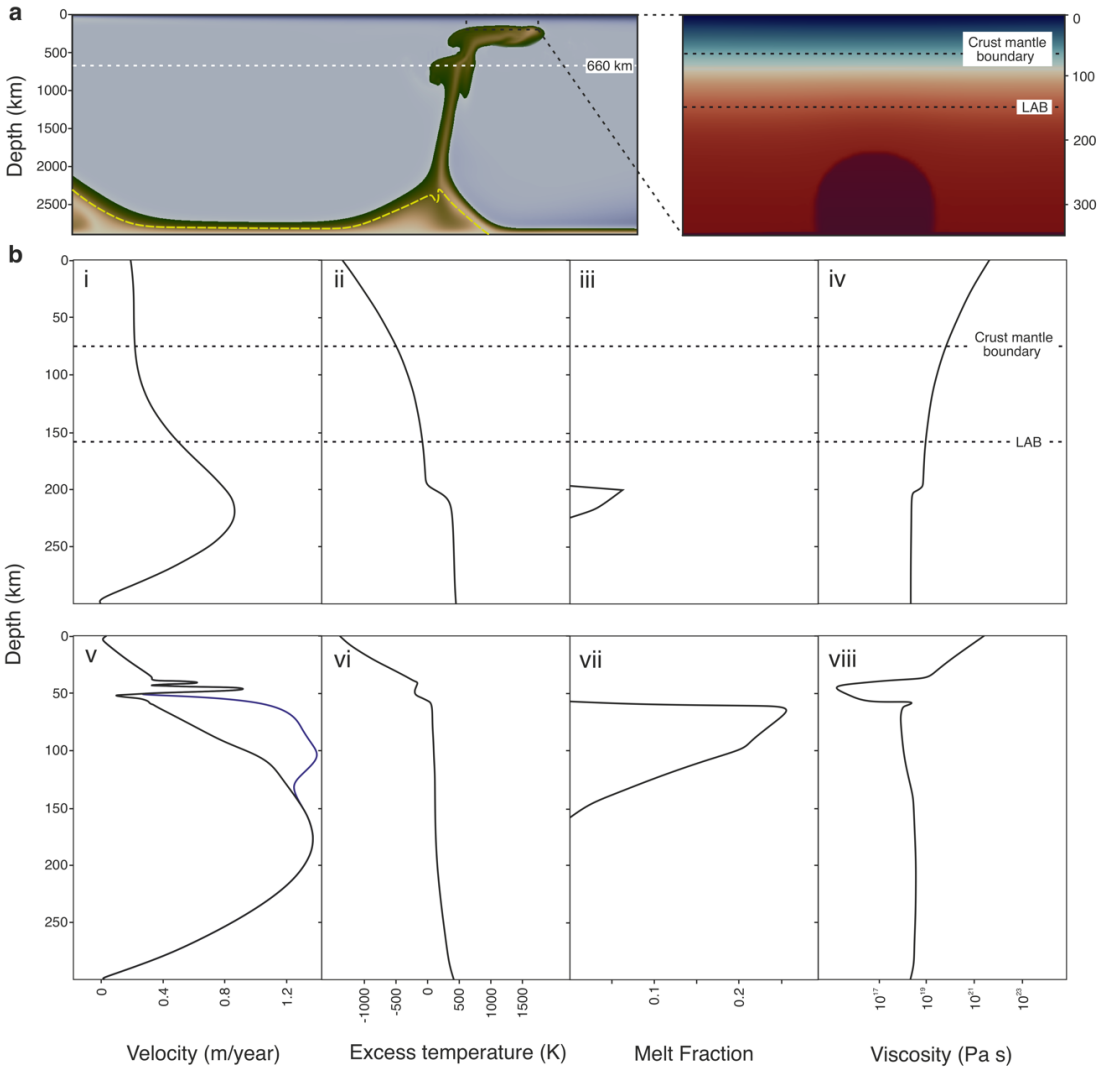

Figure 6.25: Model simulations of the melt transport processes. (a) Model domain (inset) chosen within the plume model (left panel). (b) Depth dependent variations of the physical parameters: flow velocity, excess temperature, melt-fraction and viscosity at the time of melt initiation (i-iv) and at the onset of thermal erosion of the lithosphere by the partial melts (v-viii).

The melting model is implemented in ASPECT by separating out the fluid phase from its solid counterpart, which is related by compaction pressure as,

$$p_c = (1-\phi)\big(p_s - p_f\big), \tag{6.16}$$

where ϕ is porosity, p_s is the solid pressure and p_f is the fluid pressure. After computing the stokes equation, the fluid velocity is calculated from Darcy's equation,

$$u_f = u_s - \frac{K_D}{\phi}\big(\nabla p_f - \rho_f g\big), \tag{6.17}$$

where u_f is the fluid velocity and u_s is the solid velocity, K_D is the Darcy coefficient, and ρ_f is fluid density. The porosity is advected using the following relation,

$$\frac{\partial \phi}{\partial t} + u_s \cdot \nabla \phi = \frac{\Gamma}{\rho_s} + (1-\phi)\nabla . u_s, \tag{6.18}$$

Γ is the rate of melting. Permeability is then calculated from

$$k_\phi = k_0 \phi^2 (1-\phi)^3, \tag{6.19}$$

k_0 is the reference permeability.

Table 6.2: Physical parameters and their values used to model partial melting in plumes

Model Parameters	Reference values
Melt density ρ_f	2700 kg/m^3
Reference shear viscosity η_o	5×10^{18} Pa s
Melt viscosity η_f	10 Pa s
Reference permeability k_0	5×10^{-9} m^2
Reference porosity ϕ_0	0.05
Melt weakening factor α	10
Thermal viscosity exponent β	5
Thermal expansion coefficient $\alpha_{thermal}$	3×10^{-5} K^{-1}
Solid compressibility κ_s	3×10^{-12} Pa^{-1}
Melt compressibility κ_f	3.8×10^{-11} Pa^{-1}
CFL number	1

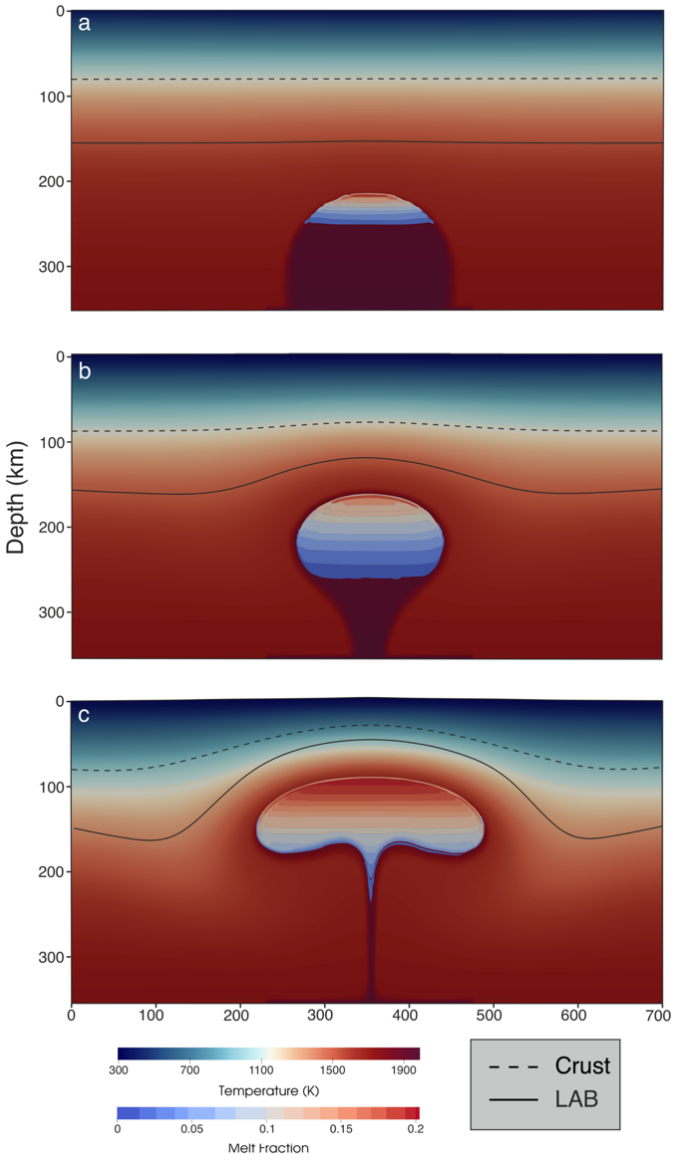

Figure 6.26: Time evolution of models showing melt production by partial melting. (a) Melt initiation at the crest of the plume head. (b)-(c) Progressively increasing melt fraction as the plume head interacts with the LAB.

When the plume head approaches the LAB, the temperature inside the plume exceeds the local solidus to initiate the melting process in the plume materials. This phenomenon inevitably increases the porosity of the system, which thereby enhances permeability in the top region of the plume head (

Figure 6.26). The Indian shield (a stable craton) had a thickness of 150-200 km before it started to interact with the plume (Naganjaneyulu and Santosh, 2012), implying a deep upper thermal boundary layer. Depending upon the initial temperature, composition, and volume of the plume head, the melting process is onset at a depth varying from ~ 150 to 250 km. During the initial phase of ascent, the magnitudes of melt and plume

velocities lie compatibly in a range of $0.4 - 0.6$ m/year (Figure 6.25b i), but as the plume ascends to a shallower depth, the melts owing to their lower density (2700 kg/m^3), gain a much higher velocity (> 1.2 m/year) to segregate from the plume materials at the LAB (Figure 6.25b v). The model results suggest that the melt-ascent velocity is directly proportional to the porosity in the system, which increases steadily with the plume evolution. Unlike the plume head, the segregated melts always ascend nearly in a vertical direction, implying that the plate velocity hardly affects the upward melt flow dynamics. At a depth of ~60-80 km, the segregated melts start to spread laterally, forming a melt pool below the lithosphere (a permeability barrier) (Figure 6.27a). The melt front interacts with the lithosphere to produce horizontal shear that sets in small-scale downwelling and causes thinning of the TBL. Upwelling of the melt front within the lithosphere ultimately gives rise to volcanism. The following parameters: melt volume, velocity, time scale of the melt rise, and dynamic topography were evaluated as a function of the initial plume volume, temperature, and density, which are presented in Figure 6.27 and Figure 6.25b.

Since the primary plume pulse has the highest volume (~1.5×10^7 km^3), it contains a high concentration of HPEs. This condition, aided with a high excess temperature (~500 K) (Figure 6.25), enables the pulse to overcome the upper-mantle buoyancy barriers. Model results show that the higher excess temperatures and HPE concentrations result in a greater melting depth (~250 km) of the initial melt pulse (Figure 6.27a i), and also enhance the excess buoyancy, that accelerates the upward flow of melts to reach a depth of 50 km within 150-180 kyr (Figure 6.27b). The porosity evolution, coupled with a high excess temperature, facilitates melt generation during the plume ascent to produce an enormous volume (~0.28×10^6km^3) of melts at the LAB (Figure 6.27b). This melt pool then efficiently incorporates lithospheric materials by thermal erosion to increase the melt volume further (~0.35×10^6km^3), ultimately giving rise to massive volcanism. Following this melt pulse generation, the plume head is then significantly depleted in HPE concentration. Secondly, the heat dissipation to the ambient mantle lowers the excess temperature (~300 K) in the plume. The thermal change by these mechanisms relocates the melting depth at a shallower level (150 to 180 km) during the subsequent pulses, where a moderate excess temperature, a relatively low HPE concentration, and smaller plume volume set the upward melt flows at slow rates (~ 0.5 m/year), taking up to 300 kyr to reach the LAB. These second-generation pulses reduce their melt volumes to $< 0.2 \times 10^6$ km^3. In addition, the thermal erosion of the lithosphere at the LAB by the melt pools

becomes less effective and fails to substantially increase the melt volumes (Figure 6.27a ii). Thus, they produced erupted volumes significantly lower than those produced in the first pulse. The smaller pulses are manifested in relatively low topographic elevations (Figure 6.27b, c). The tertiary melt pulses further reduce their volumes and their excess temperatures (~ 250 K) and lose their capacity for large-scale thermal erosion of the lithosphere and attaining a stagnation state at a depth of ~50 km (Figure 6.27a iii).

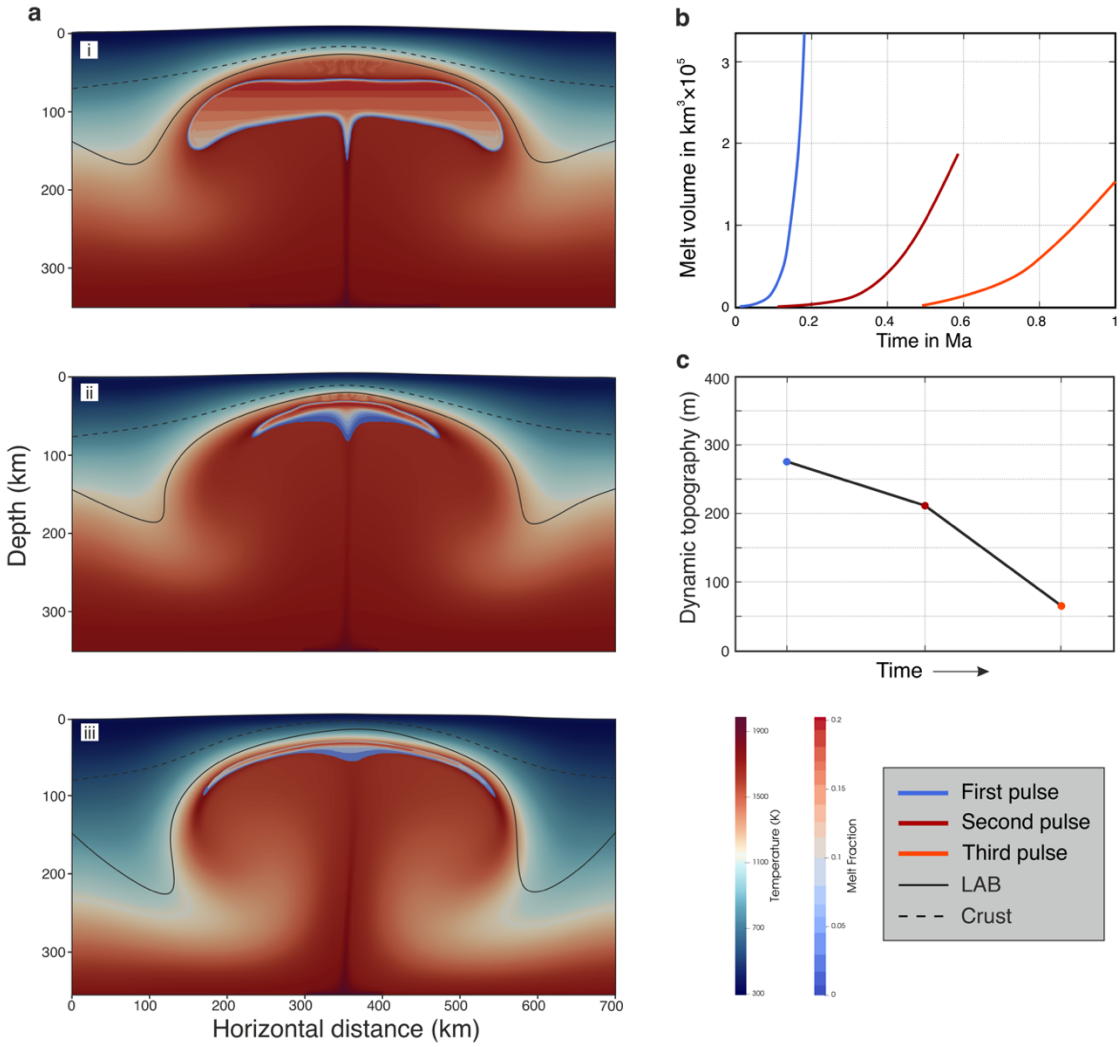

Figure 6.27: Melt production by partial melting of plume head in the model. (**a**) Melt localization in three successive melt pulses (**i-iii**) at lithosphere-asthenosphere boundary (LAB). They originate from a single major pulse obtained from the whole mantle model. Colors represent the temperature and the colored contours represent melt fraction. Black line delineate the deformed LAB geometry. The slight tilt in the plume axis results from plate movement. The first two pulses (i-ii) involve intense thermal erosion at the contact between the melt front and the LAB, resulting in thinning of the thermal boundary layer. The top boundary is deflected to produce topography during the successive melting events. **(b)** Calculated plots of melt volume formed in successive melt pulses. **(c)** Melt driven dynamic topography for three successive pulses. The colors used to represent the pulses in (b) and (c) are shown in the legend.

6.7 Model limitations

The model treats the lithosphere as an upper thermal boundary layer, which doesn't account for visco-plastic rheology in our simulations. This is a limitation as the model excludes any failure criterion in the plume-lithosphere interaction. Secondly, the creep processes that are often activated in the upper mantle, could influence the shape and the ascent rate of the plume head, which are not explored in this study. In addition, the primary model excludes any compressibility effect of the solid phases. The plume melting models considers a reaction time scale of 10^3 years due to computational constraints. This might overshoot the overall timescale of melting and melt migration.

Chapter 7

Rayleigh-Taylor Instability versus Porous flow in two-phase fluid systems

7.1 Introduction

The mechanism of melting and melt migration is of wide interests, ranging from the basic science to chemical engineering. Examples are metallurgical studies that include melting of metals (Cahn, 1986; Frenken and Van Der Veen, 1985), thermal analysis of moving spacecraft for aerodynamics study(Gadalla et al., 2019), and incongruent melting during peritectic reaction (Maiwa et al., 2003), ablation type Stefan problems (Mitchell and Vynnycky, 2012), melting and interface migration of wire anode (Sripada et al., 2003). Since, mantle phases often undergo partial melting under different circumstances, geoscientists are trying to understand the melting and melt migration phenomena under various pressure-temperature conditions for the past few decades (Kohlstedt and Holtzman, 2009; Riley and Kohlstedt, 1991). Many geodynamical phenomena such as mid oceanic ridge (Behn and Grove, 2016; Yang et al., 1998), underplating (Bergantz, 1989), and hotspot activity (Bredow et al., 2017) are closely associated with melting. In general, silicate melts have lower density than the source rock, which, in turn, facilitates melt migration either via Rayleigh-Taylor (RT) instability where gravitational force play the primary role or via interfacial instability where surface tension plays the main role. The interplay between the two often becomes important in different geodynamic condition such as the formation of Earth's core (Chabot and Agee, 2003; Olson and Weeraratne, 2008) or subsurface flow of hydrocarbons in porous formation (Cornell and Katz, 1953). Such complicated problem can only be explored if one considers multiphase fluid flow in porous media where dynamics of two or more fluid phases need to be considered inside a porous network. These flows are governed both by the properties of the porous media such as porosity, permeability as well as the physical properties of the liquids like density, viscosity, mixing energy of two fluids and interface properties such as surface tension and adhesive and cohesive properties. The mechanism of melt migration is often shown to be interface migration to channeling instability in Earth science literature (Daines and

Kohlstedt, 1994; Pec et al., 2017). Using analogue and numerical experiment as well as theoretical analysis, they showed that at greater depth, reaction instability prevails that promote melting of the solid phases. Owing to the lower density, the melt then percolates upwards and form channels upon reaching a lower depth.

The porous media is considered as a solid matrix with void spaces between the grains that acts as either pores or channels via which fluid phase can move. These flows often produce melt fracture instabilities to migrate away from the source (Shore et al., 1997). In other cases the melt progresses through the solid matrix as a melt-front via interconnected networks (Baruah et al., 2014). The density inversion and associated RT instability makes the system even more complex where the melt migration pattern is now determined by the interplay of gravity and surface tension driven instability.

Such multiphase system is composed of two or more distinct phases which themselves may be fluids or solids. From fluid dynamics point of view, this problem is complicated by the proper choice of momentum equation. In a melt rich system, the dynamics of the interface is explicitly described by the Naiver-Stokes equation which is primarily pressure driven, but in a completely porous media, the same will be described by Darcy equation that includes porosity and permeability into consideration. Things get further complicated where both fluid and solid are almost equal in proportion to form a *mushy zone* (Mandal et al., 2018). The dynamics of such mushy zone cannot be fully described by either of the two aforementioned formulations. Moreover, instead of using the absolute values, averaged properties must be employed for all physical properties such as density and viscosity (Bercovici et al., 2001).

Despite the advancement of the melt initiation and migration phenomenon in various discipline of science and engineering as discussed, the underlying dynamics of interface generation via melting and its subsequent migration is yet to be fully explored. Moreover, the difference in melt migration pattern from a line source versus a point source of melting were never thoroughly investigated from a geodynamic point of view. Lastly, although both interfacial and RT instability is studied extensively in porous media, the interplay between the two is yet to be dealt with in a comprehensive manner. This work is dedicated to meet this gap. The study is divided into two parts: the first part is dedicated to melting phenomena where, using laboratory experiments, we study dynamics of a progressive melting and associated solid-melt interaction via transformation from one phase to another and lead to various melt-front patterns depending on the line or point source if melting. The other part focuses on melt migration where we consider an experimental setup with

multiple phases in a porous media to study the various melt migration pattern generated by the interplay of RT and interfacial instabilities. In the end it is pertinent to understand the dynamics of mushy flows and how the melt is transported through this region to reach mid oceanic ridges.

7.2 Method

For the melting experiments, I took pure laboratory grade organic crystalline material in ambient condition. This material was chosen because of its well-defined crystalline structure and low melting point that made the experimental setup reasonably simple. The material is in the form of crystalline powder, and it was sieved through a moderately fine mesh to remove coarse foreign particles as well as to obtain a uniform size of the powder. A layer of crystals with a uniform thickness is taken in a rectangular plate. Heat plate was used for experiments with line source of heat and soldering kit was used for point source of heat. Thermocouples were used to continuously monitor the temperature at the contact point or line of the heat source and is kept above the melting point but below the decomposition temperature. This way the material didn't crystallized back to its original form, neither did it get decomposed during the course of the experimental run.

To conduct the fluid flow experiments, a porous media is constructed using glass beads of uniform diameter of 4.5mm in a glass aquarium having dimensions of $30\ \text{cm} \times 30\ \text{cm} \times 10\ \text{cm}$ $(L \times H \times W)$. Two different fluids with different density, viscosity and contact angle are used, the properties of which is given in Table 7.1. The lighter fluid used is PDMS (Polydimethylsiloxane) and the heavier fluid is distilled water. Inorganic salt is used in specific proportion to vary the density contrast of the two fluids. A dying agent is used to color the PDMS.

Table 7.1: Model parameters for the materials used for analogue experiments.

Fluids	Rheology	Density (kg/m^3)	Viscosity (Pa. s)	Contact angle (Solids)	Contact angle (Fluids)
PDMS	Non-Newtonian	925	50	$> 90°$	
Water	Newtonian	997	8.9×10^{-4}	$< 90°$	$54°$
Salt Water	Newtonian	$1000 - 1200$	1.8×10^{-3}	$< 90°$	

PDMS (Polydimethylsiloxane) of specific thickness is taken in the container and left to rest for two hours so that the air bubbles are completely removed. Glass beads are then added to form a thick layer of porous media overlying the PDMS layer. Finally, water is added from the top and it gets percolated through the porous media down to the PDMS forming a three-phase interface. PDMS being lighter that the overlying fluid and porous media, the interface starts to deform to form instabilities. With time these instabilities grow and interface moves upward. The progressive change of the interface was monitored using a Nikon camera with a constant focal length of 18 mm at regular intervals.

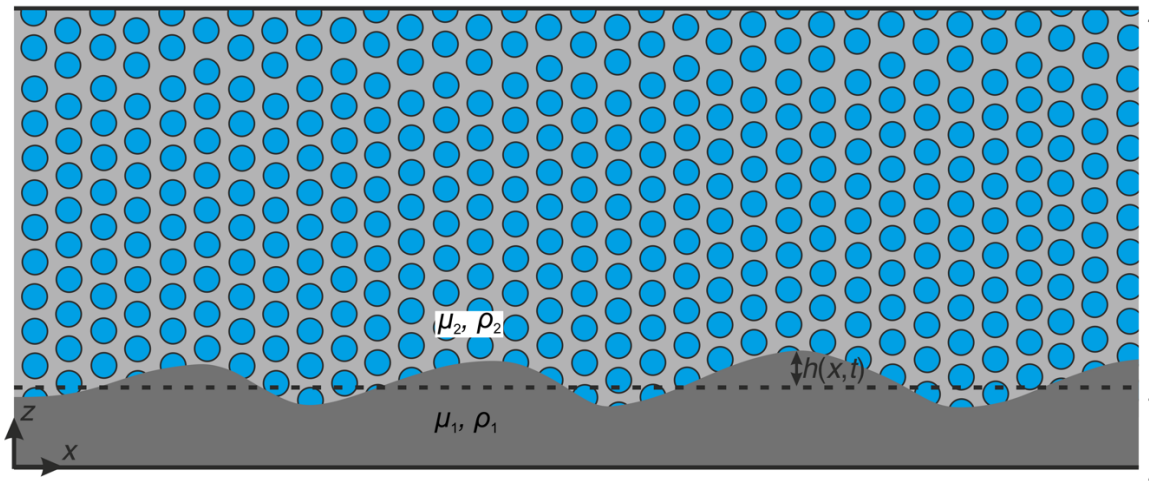

Figure 7.1: Schematics for the experimental setup.

7.3 Results

7.3.1 Melting experiments

During experimental run the crystalline solids underwent partial melting when the temperature of the heat contact reached melting point of the crystals. Now depending on the nature of the heat source, the contact formed a thin film of melt (when there is a line source of heat) or a small pool of melt (in case of point source heating) at the solid-melt interface. With time, the interface advected to generate irregular geometric patterns. The advection pattern varies based on the type of heat source. For line source heating, the solid-liquid boundary creates a melt front) with irregular pattern (Figure 7.2a). The melt-front showed second-order irregularities with the first order being the global front and the higher order being interface driven local migration of the melt along the grain boundaries. With time, the overall volume of melt increases and both the interface irregularities advect further upwards albeit at different velocities. The melt-front remains closer to the melting

zone and thus advect at a lower velocity whereas the higher order irregularities move faster and spread out form the source. This is done via partial resorption of the solid crystal by the higher-order irregularities (Figure 7.2b). This suggests that with progressive melting, the local fluctuations spreads determining the ultimate melt-front geometry. This also implies that the first order geometry of the front is linear in time whereas the higher-order irregularities grow in a non-linear manner. Thus, the melting process was steady.

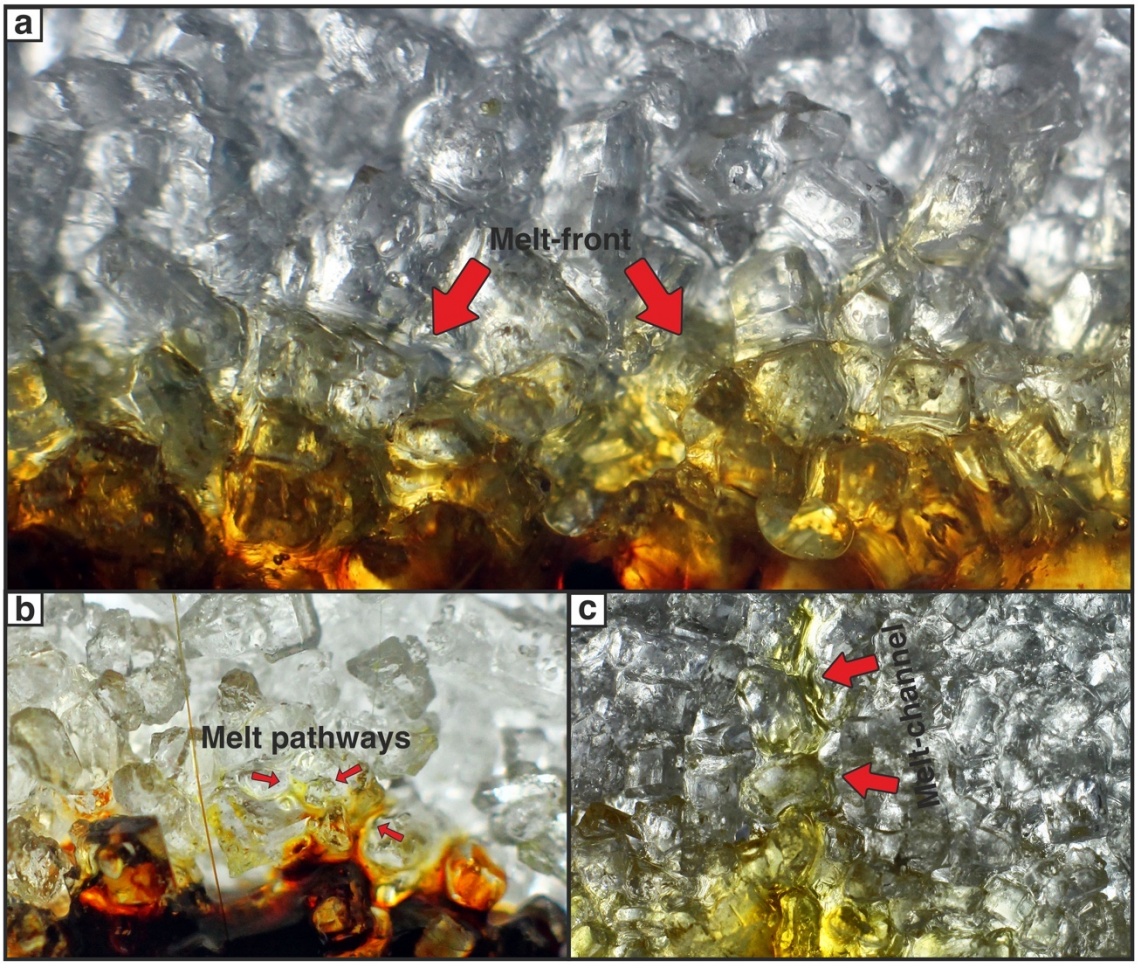

Figure 7.2: Formation of various melt advection patterns. (a) Melt-front generation and advection for line source of heating. (b) Growth of melt pathways by partial melting. (c) Melt migration via channel formation for point source of melting.

Point source melting, on the other hand, produced a different melt geometry with no prominent melt-front. Rather, the initial melt is concentrated around the melt source and it tries to spread out by creating melt pathways. With time, these pathways extend further away from the source creating a melt channel (Figure 7.2c) that is connected at its base to the melt source region. Unlike the previous case, the melt front expands at the very slow

speed but the higher order instabilities grow much more rapidly and spontaneously. Thus, the overall growth of the interface in this case is thus driven by nonlinear dynamics.

7.3.2 Porous media experiments

For these experiments, the density contrast between the two fluids was varied by changing the overlying layer density while keeping the PDMS layer fixed. I noticed very different outcomes in our results as we increase the density contrast, both in the dynamics as well as the geometry of the interface. To better understand this, I analyzed the number and change in frequency of interfacial instability with time from various experiments and compared them. I also determined the fractal nature of the patterns that incorporates determination of fractal dimension (D) using box count method. Furthermore, the growth rate of individual fingers as well as the interface was calculated to quantitatively differentiate the RT driven versus the surface tension driven instabilities. The details of the results along with the outcomes of the analysis are described below.

Models with low $\Delta\rho$

For this experiment I used pure water of density 970 kg/m^3 and PDMS of density 925 kg/m^3 creating a density inversion where the wetting phase is slightly denser than the non-wetting phase. Under these conditions, the interface is deformed by interfacial instabilities without any RT instability (Figure 7.3i). With time small fingers move upward either via pore space or via displacing the adjacent beads to create melt pathways (Figure 7.3ii). The number of fingers also increases as the interface grows (Figure 7.3ii, middle panel). Other interesting feature is that the interface grows as a whole with time at a faster rate, leading to small difference between the melt-front and melt-interface. As time progresses, the fingers branch out to form multiple interfacial instability from a single one to increase laterally while also maintaining vertical growth (Figure 7.3iii). Moreover, the width of the individual fingers increases on average and they rise at a higher velocity than the overall interface. As time progresses further, the distance between the interface and fingers increases giving rise to an overall dendritic structure (Figure 7.3iv). with time, the number of fingers increases further to cover almost the entirety of the domain.

Thus, although the interface growth is linear, the fingers grow non-linearly to form the dendritic structure. Fractal analysis suggests that the growth of interfacial instabilities is turned out to be fractal in nature with fractal dimension varying between 1.84 to 1.92.

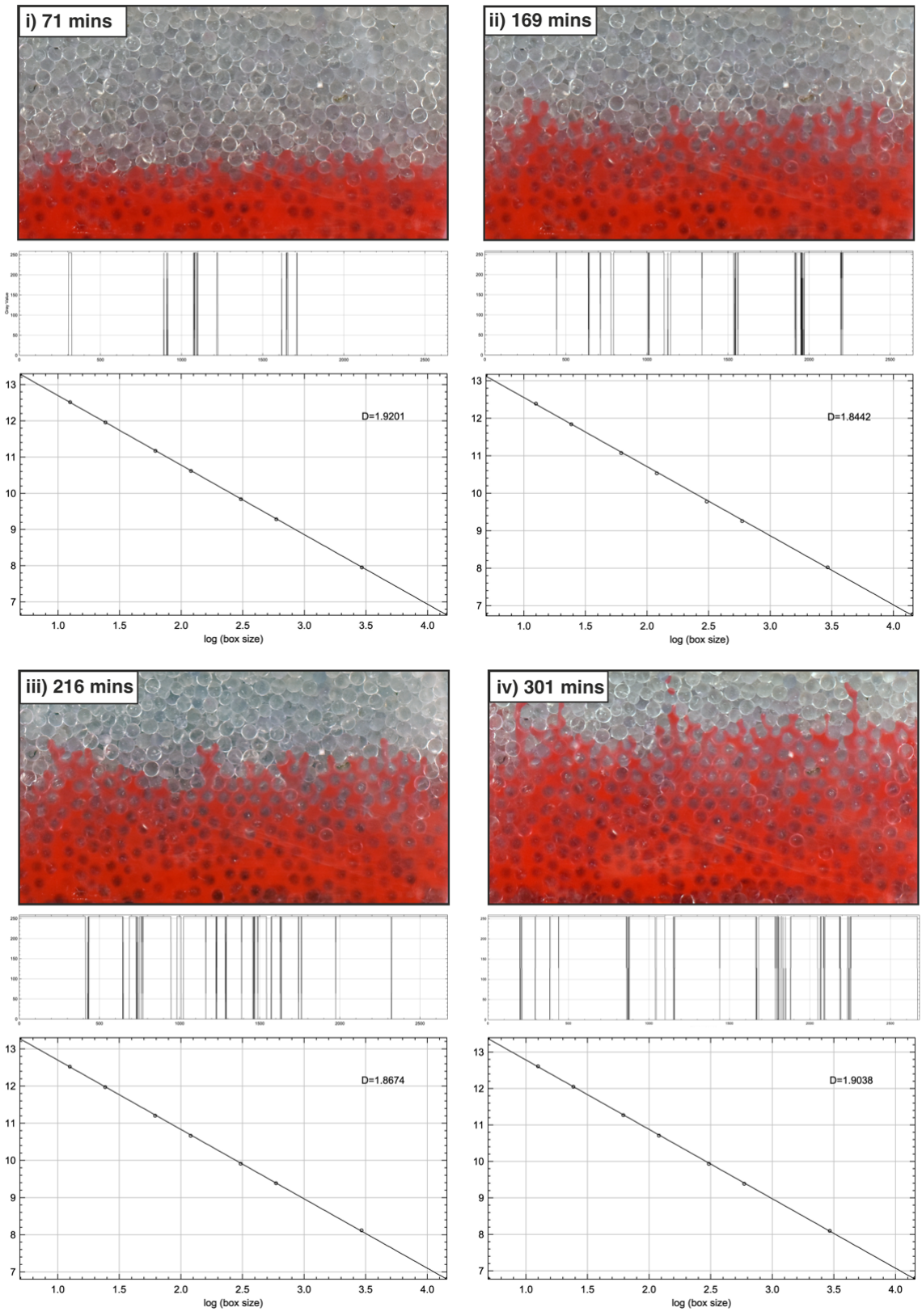

Figure 7.3: Experimental results for low $\Delta\rho$. (i-iv) The top panel shows the snapshot of the experimental result at a particular time. The middle panel shows the profile plot along a representative horizontal line of the snapshot. The bottom panels show fractal analysis of the melt migration pattern using box counting method.

Models with moderate $\Delta\rho$

The overlying fluid density was systematically increased by mixing table salt in a specific proportion. Now the wetting phase has a density of 1050 kg/m^3 and the non-wetting PDMS has a density 925 kg/m^3 creating a moderate density contrast between the two. Under these circumstances, the interface is deformed primarily by interfacial instabilities with a minor undulation due to RT instability (Figure 7.4i). As a consequence, the number of fingers generated due to interfacial instabilities are lower compared to the previous case. With time small fingers move upward either via pore space or via displacing the adjacent beads to create melt pathways (Figure 7.4ii). The number of fingers also increases as the interface grows (Figure 7.4ii, middle panel) but the interface moves at lower rate than the previous case. This is because the interface is affected by RT instability and now the interface location also depends on the nature and geometry of the RT waves. And the fingers are generally very narrow with a width of < 0.1mm. As time progresses, the viscous fingering becomes more prominent (Figure 7.4iii) with their width becoming thicker. As time progresses further, both the fingers and interface advects slower due to the presence of RT instabilities and the distance between the interface and fingers increases further as compared to our previous results. Initially the wavelength of the RT instability was almost comparable to the distance of the fingers, but with time, as the number of fingers increases, the wave breaks down to generate multiple interfacial instabilities (Figure 7.4iii-iv). Other remarkable thing to notice is the number of fingers, which is lesser as compared to the experiments of low $\Delta\rho$.

Thus, although the interface growth is linear due to RT instability, the fingers grow non-linearly to form the viscous fingering. The growth follows a fractal pattern, where the fractal dimension varies between 1.83 to 1.90.

Model with high $\Delta\rho$

To increase the overlying fluid density further, I mixed higher proportion table salt to the point of saturation. Now the wetting phase has a density of 1200 kg/m^3 and the non-wetting PDMS has a density 925 kg/m^3 creating a high-density contrast between the two. The results are drastically different as the interface takes the form of a wave with their wavelength covering more than half of the length of the container (Figure 7.5i). At this stage the interfacial instabilities are almost negligible with the interface being determined completely by RT instability which grows very slowly.

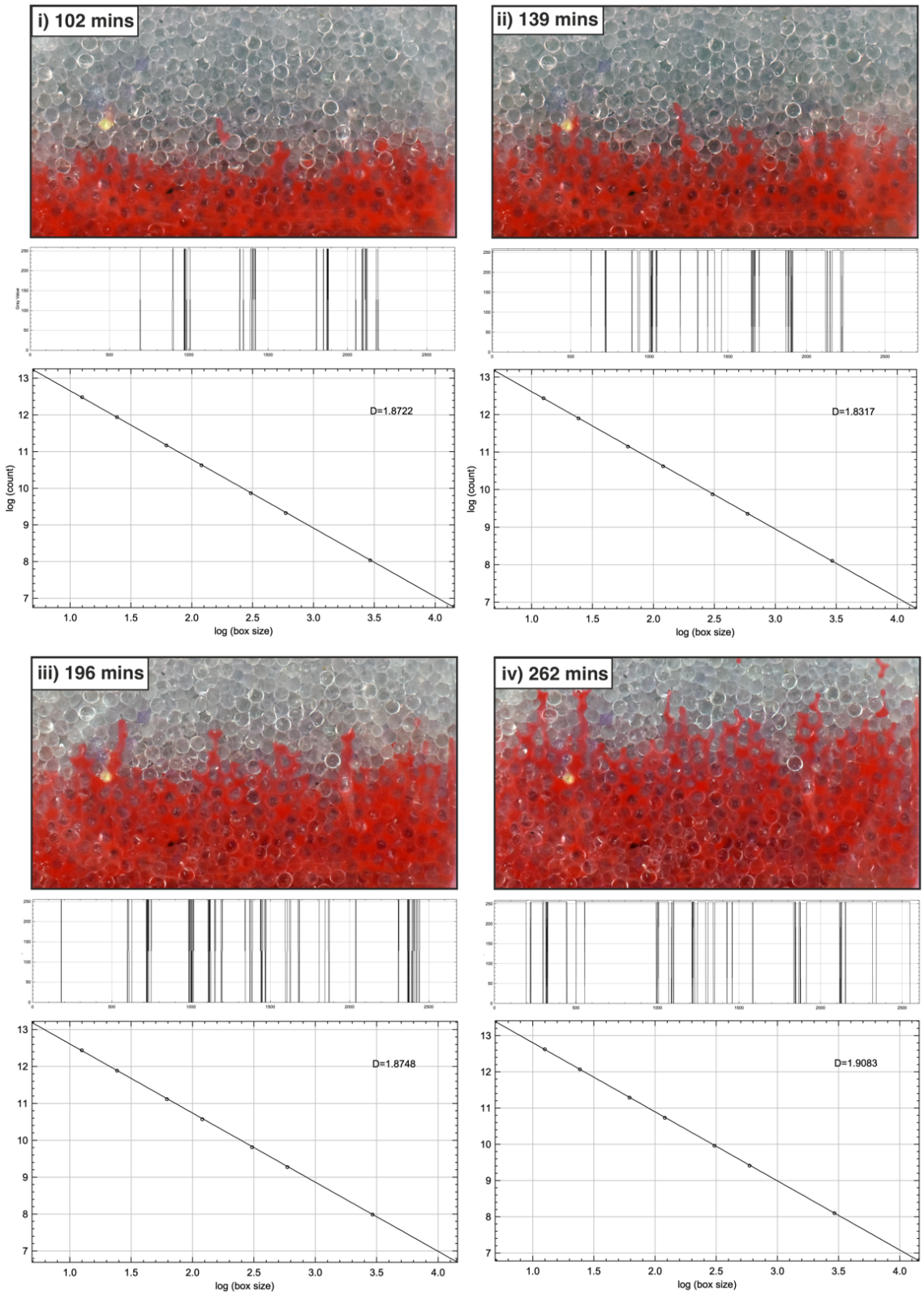

Figure 7.4: Experimental results for moderate $\Delta\rho$. (i-iv) The top panel shows the snapshot of the experimental result at a particular time. The middle panel shows the profile plot along a representative horizontal line of the snapshot. The bottom panels show fractal analysis of the melt migration pattern using box counting method.

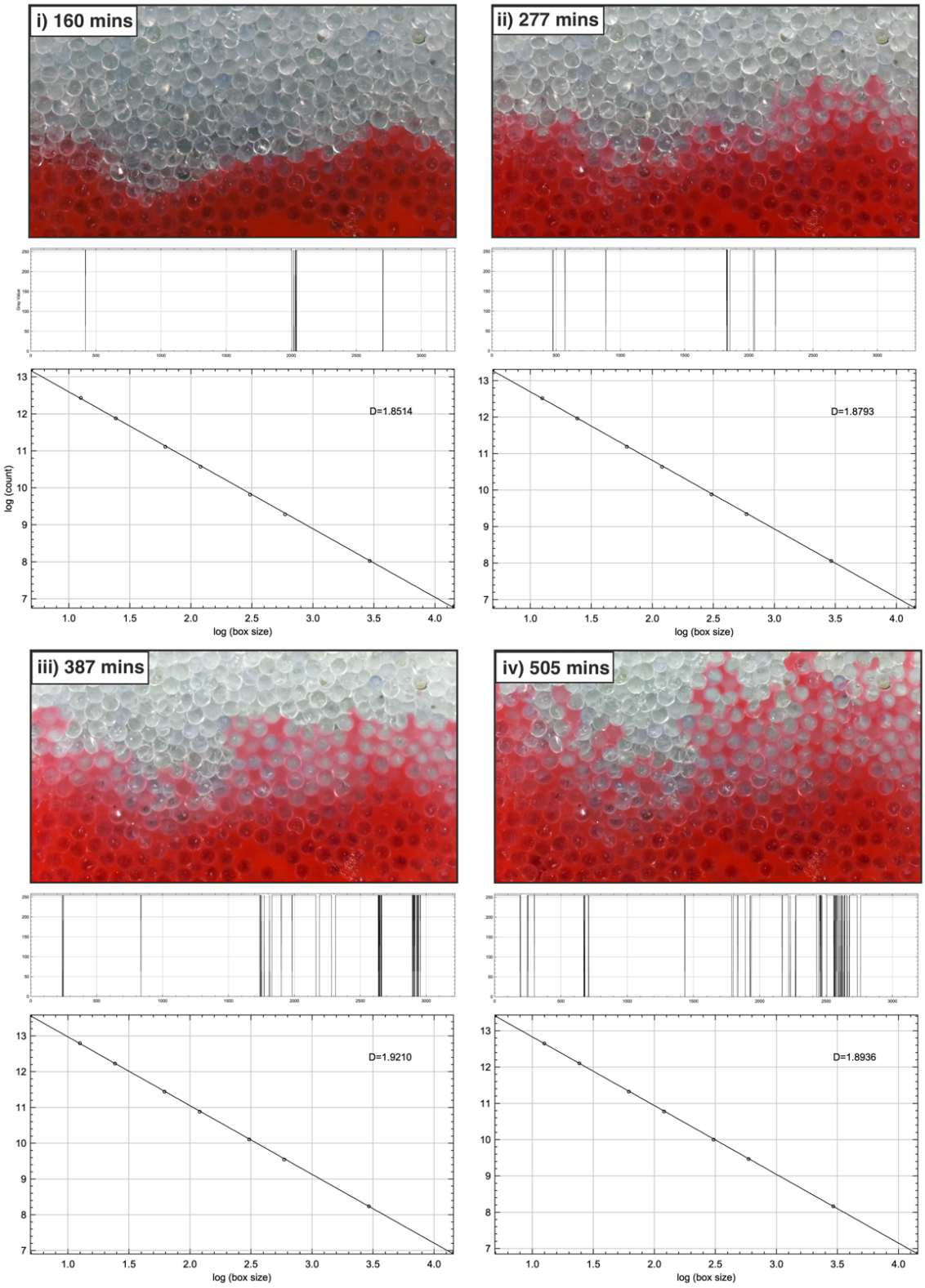

Figure 7.5: Experimental results for high $\Delta\rho$. (i-iv) The top panel shows the snapshot of the experimental result at a particular time. The middle panel shows the profile plot along a representative horizontal line of the snapshot. The bottom panels show fractal analysis of the melt migration pattern using box counting method.

With time, small fluid conduits or fingers form, but the displacement from the initial surface is more in the crest region as they are the locations of high pressure as compared to the trough regions where the pressure difference is low (Figure 7.5ii). Overall, the number of interfacial instabilities is still very low as compared to the experiments with lower $\Delta\rho$ values. As time progresses these small fingers move upward via displacing the adjacent beads to create melt pathways and the fingers branch out laterally to form multiple interfacial instability from a single one to increase laterally while also maintaining vertical growth (Figure 7.5iii). The growth of the fingers become more prominent as time progresses further, with numerous narrow fluid conduits have formed and the pattern they fluid conduits are arranged in dendritic typical of viscous fingering at low capillary numbers. The fingerings are more enhanced at the boundary due to surface tension acting along the fluid wall interface, but inside porous space various fingers are also seen. If enough time is given the wetting denser materials settles below and the lighter phase rises to the top. It can be thought as a self-reciprocating system that is initially unstable and then tries to attain stability by forming small conduits.

Unlike the previous results, in this set of experiments, the interface growth is linear for the first half of the experimental run due to RT instability and once the fingers start growing, the non-linearly takes over. The end result is very different with fingers brunching out of the crest of the RT waves to reach the top of the domain. The distance between the melt-front and the interface is maximum in these experiments out of all set of experiments. The fractal dimension of the fingering pattern ranges from 1.85 to 1.92.

7.3.3 Analysis

The results presented in the preceding section clearly show a marked difference in front migration pattern in a two-phase flow in porous media with a density inversion. When the density contrast between the fluids is low, we observe the overall dynamics of the system is controlled by interfacial instabilities driven by surface tension. For high density contrast, on the other hand, RT instability prevails giving the interface between the two fluid a curvature. These two end-member dynamics not only determines the geometry of the mushy zone but also affects the kinematic aspects of the system.

To better understand this, the growth of the melt front as well as the interface with time were analyzed for various experiments (Figure 7.6). The results show that for a surface tension dominated system, the melt front grows at a much faster rate with the fast-growing

interface. This leads a minimal height difference between the two. With an increase in density contrast, RT instability comes into play and it restricts the growth of the interface. The front still grows owing to the interfacial instabilities. This leads to a scenario where the front moves much faster ahead of the interface and the RT crests act as the feeder to the fingers from a much greater depth.

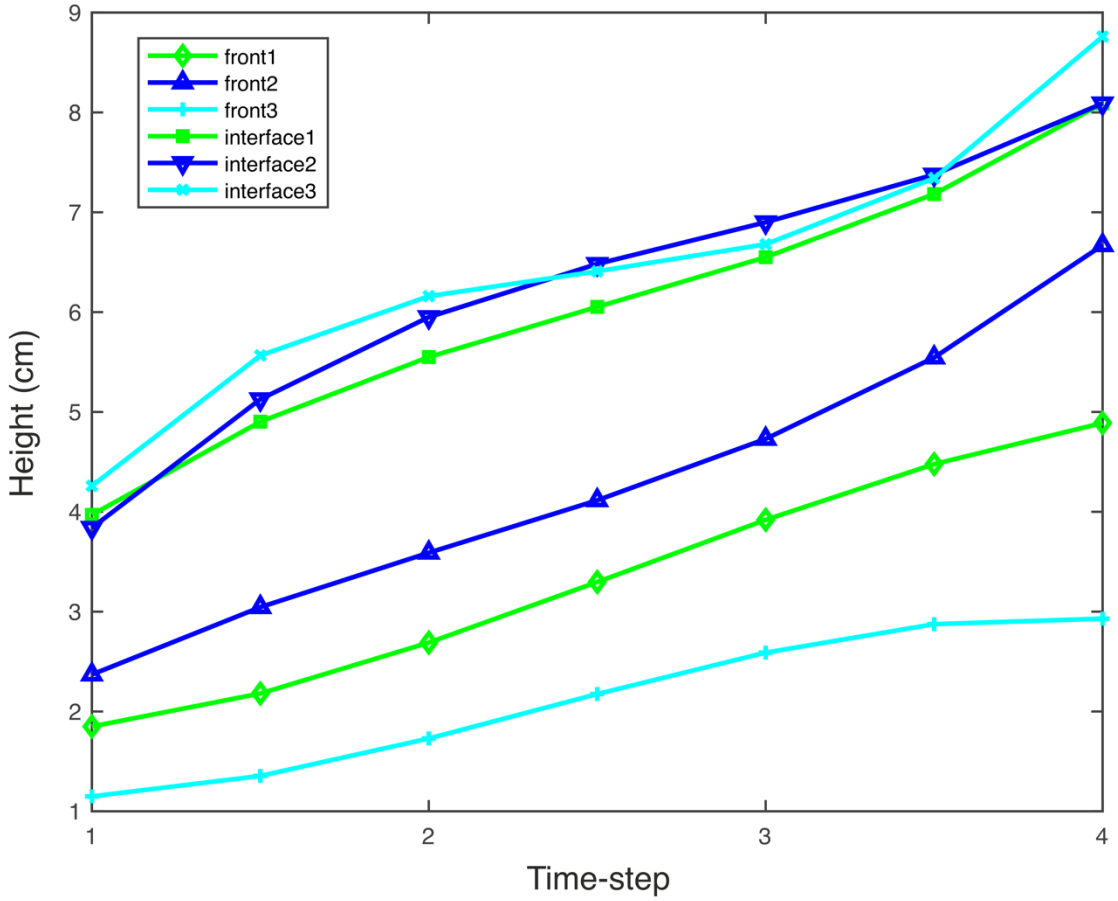

Figure 7.6: Progressive change in melt-front and melt interface for the conducted set of experiments.

The velocity analysis of the fingers from each set of experiments and the results are shown in Figure 7.7. The analysis show that for very high density constant, finger growth is hindered by the RT instabilities. For low density contrast, however, surface tension helps the fingers to move upward via the pore spaces. As a result, the mean velocity of the fingers is much higher. In reality, however, other factors such as the viscosity contrast, adhesive and cohesive properties, pore geometry and dimensions will also play a role key role in determining the dynamics and geometry of the instability growth which is beyond the scope of the present study.

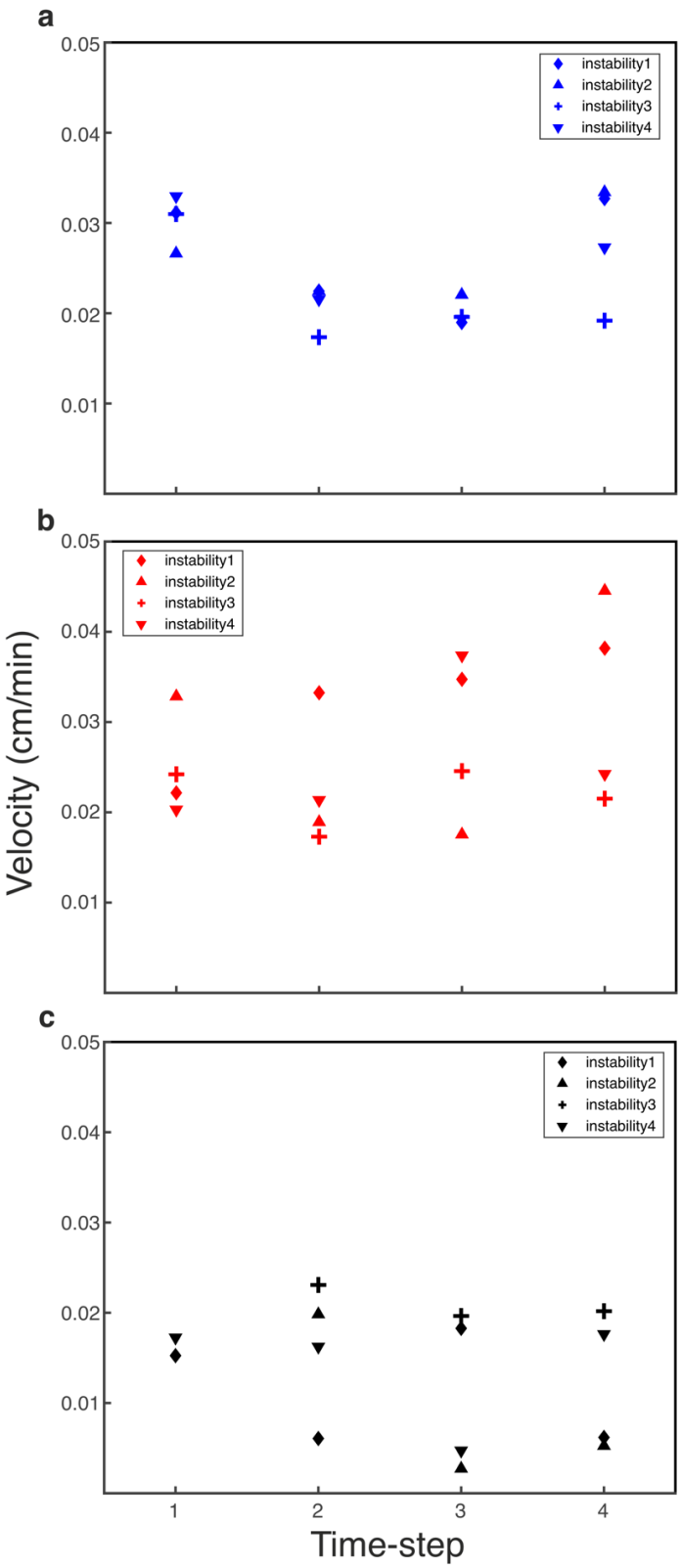

Figure 7.7: Calculated plot of instability growth rate for the conducted set of experiments. (a) experiments dominated by instability. (b) Experiments with both RT and interfacial instabilities. (c) Experiments dominated by RT instabilities.

Such a system is expected to be represent a mushy zone in mid oceanic ridge system. Thus, our finding will help understand the dynamics of the mush and the melt migration in mid oceanic ridge system in general.

Chapter 8

Discussion and conclusions

8.1 General remarks

This chapter is dedicated to the application of the theory and experiments discussed in the previous chapters to various natural geodynamic settings. The following sections contain discussions and conclusions regarding each of the following topics: In § 8.2 I present the application of Rayleigh-Taylor instability on an inclined plane (Chapter 3, and 4) to investigate the spatiotemporal arc volcano distribution patterns in different subduction zones. The validity of the model findings is tested in the Andean, Central American and Java-Sumatra subduction systems. § 8.3 discusses the potential applicability of 3D Rayleigh-Taylor instability (Chapter 5) in various natural settings. This includes discussion on the implications of our theoretical results presented in Chapter 5 the light of experimental observations. In § 8.4 I discuss the possible correlation of Deccan volcanism periodicity with the Réunion Hotspot and how their origin is related to the eastern flank of African LLSVP using the numerical experiments presented in Chapter 6.

8.2 Volcanic arc patterns in subduction settings

The *Andean subduction system* offers an excellent opportunity to study the control of slab dip in interpreting the volcanic distributions in space and time. This system presently involves Nazca plate, subducting with laterally varying slab dips along the N-S trending trench on the western margin of the South American overriding plate (Figure 8.1a, b). There are three flat-slab segments: Bucaramanga, Peruvian and Pampean, which separate the arc segments with high-angle slab dips ($\alpha > 35°$-$50°$), marked by localization of three distinct volcanic belts: The Northern, the Central and the Southern volcanic zones. Each of these segments displays a trench-parallel linear distribution of closely spaced volcanic spots (Ramos and Folguera, 2009). Both our laboratory experiments and CFD simulations suggest that they originated from Mode 2 plumes. By reconstructing the past subducting plate configuration of the Andean subduction zone, we find a completely different slab

configuration of the Andes, which provides indications for past flat-slab subduction. Based on geological evidence, Ramos and Floguera (2009) have established a series of flat-slab segments, covering the entire stretch of the Andean system. From North to South, these are Bucaramanga, Carnegie, Peruvian, Altiplano, Puna, Pampean, Payenia flat-slab segments. The three segments: Bucaramanga, Peruvian, and Pampean maintained a low-angle slab dip from 13, 11, and 12 Ma, respectively, to the present day, whereas the other segments were flat during different time intervals (Carnegie: < 3 Ma; Altiplano: 40-32 to 27-18 Ma; Puna: 18-12 Ma; Payenia: 13-5 Ma). For the present discussion, we specifically choose three segments: Puna, Pampean, and Payenia to compare their volcanic distribution patterns with those observed in our models. The Pampean flat-slab segment, flanked by the Puna segment on its north shows a contrasting volcanic arc pattern (Figure 8.1a). The Puna segment was flat during 16-12 Ma (Kay and Coira, 2009; Martinod et al., 2010; Ramos and Folguera, 2009), and steepened after 12 Ma to attain the current dip of 30° (Martinod et al., 2010). On the other hand, the Pampean had a high-angle slab dip before 16 Ma, and continuously lowered its slab dip to achieve an almost flat present configuration. These two segments evolved through opposite trends in their slab dips, which are shown by their contrasting temporal volcano distributions. The volcanic spots in the Puna segment are more densely clustered than those in the Pampean segment. During the period of flat subduction (>12 Ma; Figure 8.1a, X2) the slab beneath the Puna segment produced Mode 1 plumes. Slab dip steepening after 12 Ma facilitated domes to updrift and form Mode 2 plumes (Figure 8.1a, X1). The volcanic activities presently focus into a narrow region constituting a sharp volcanic arc in front of the Peru-Chile trench (Figure 8.1a). In contrast, the Pampean segment had a high-angle slab dip prior to 12 Ma which focused the volcanic activities into a narrow frontal region. The onset of slab flattening after 12 Ma prompted the volcanic spots to spread down the slab (Figure 8.1a, Y3-Y1) (Kay et al., 1991; Ramos et al., 2002; Ramos and Folguera, 2009). We interpret this switch over as a consequence of Mode 2 to Mode 1 transition in plume dynamics in response to a progressively reducing slab dip. The age distributions of volcanoes support this proposition. The segment displays a line of 15 Ma volcanic spots that possibly indicates the phase of focused volcanism by Mode 2 plumes (Figure 8.1a, Y3). All the younger volcanic spots < 12 Ma are strongly scattered, showing no consistent space-time correlation. Our laboratory models produce matured Mode 1 plumes randomly in space and time, which are in agreement with the scattered age distribution of volcanic spots in the Pampean segment.

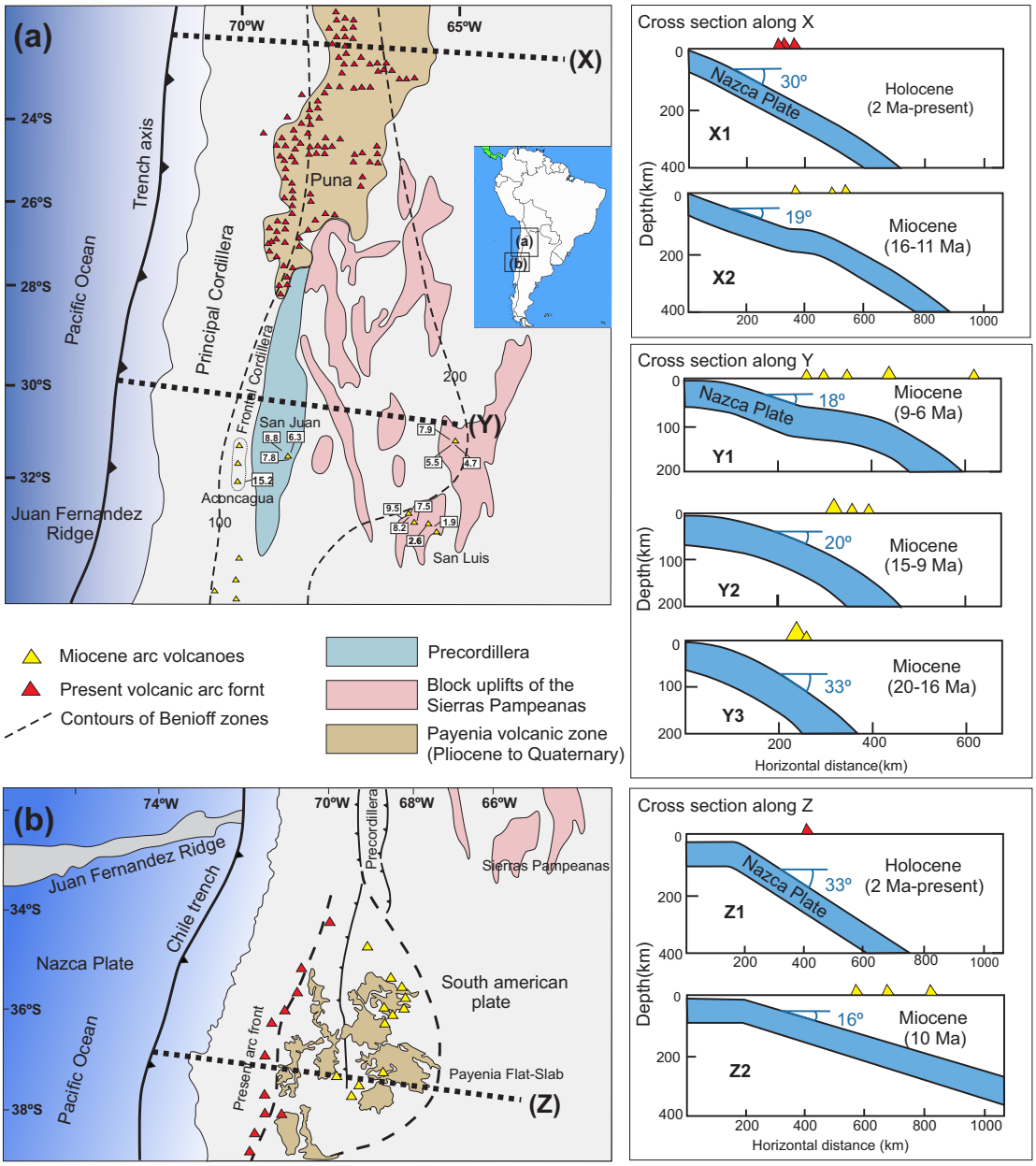

Figure 8.1: Spatio-temporal distributions of arc volcanisms in the Puna, Pampean and Payenia region of the Andes. a) Locations of the Puna and Pampean flat-slab segment in the Central Andes with 100km and 200km isobaths of the Nazca plate and with an outline of main basement uplifts of Sierras Pampeans, and location of the Precordillera fold and thrust belt and representative ages of volcanoes (modified after Ramos et al. 2002, 2009). X1) Cross-section shows the present-day subducting plate configuration and associated volcanic locations. X2) The 16-11 Ma configuration of the same plate with distributed volcanic spots (after Kay et al. 2009). Y) Schematic cross-sections of the plate segment between 30 to 31°S. Three sections (Y1, Y2 and Y3) show transformation of arc volcanism from localized to distributed arc volcanisms with decreasing subduction dips through time (20-16 to 9-6 Ma) (reconstructed from Kay et al. 1991). b) Variation of the magmatic arc pattern from Miocene (10 Ma) to Holocene (2 Ma) in the Payenia region. Z1: Present configuration of the subducting plate at 37°S, Z2: its Miocene reconstruction (after Gianni et al. 2017).

The Payenia segment displays two distinct patterns. Late Miocene arc volcanoes are scattered in both trench parallel and trench perpendicular direction, covering a horizontal

distance of ~400 km (Figure 8.1b, Z2). By contrast, the present-day volcanic arc defines an excellent trench parallel linear front (Figure 8.1b, Z1). These two patterns correspond to Mode 1 and Mode 2 plumes, respectively similar to our model results. During the period (13-5 Ma) of flat-slab subduction in the Payenia segment, Mode 1 plumes formed randomly as observed in models with $\alpha < 30°$. With steepening in slab dips, the updip advection became a dominating process to promote Mode 2 plumes in the upper fringe of the partially molten layer. Our experimental models produced Mode 2 plumes with a regular spacing, controlled by λ_L wave periodicity. We invoke this plume dynamics to explain the regular pattern of the volcanic arc front. The average spacing of volcanic spots in the front is estimated in the order of 40-60 km, which is in agreement with the scaled-up values of longitudinal plume spacing (35 to 70 km) obtained from the laboratory models.

The *Central American trench* and the *Java trench,* and their current subducting plate configurations are well constrained from seismic sections that can be used to demonstrate the effects of slab dip on the volcano distributions. I choose the Central American subduction system as our case study because it displays a spectacular variation in the distribution pattern of active volcanoes. In this subduction system the Cocos and Rivera plates, separated by a trench-normal tear fault subduct beneath the North American plate to produce a series of volcanic arcs, namely the Mexican and the central American volcanic arcs (Figure 8.2). I will focus specifically upon the Mexican volcanic arcs, marked by the Trans-Mexican Volcanic Belt (TMVB), a ~1000 km long, and 90 to 230 km wide discontinuous series of volcanic fields. In its north-western part, the Rivera plate subducts at a dip of 40°-50° beneath the Jalisco block, but steepens to a dip of ~ 70° below the TMVB (Dougherty and Clayton, 2014; Ferrari and Lunati, 2013). The central Cocos plate, on the other side of the tear fault, subducts at a slightly lower dip angle (~ 40°). Moving towards the north-east sector (Michoacán area), the plate flattens to a dip, ~15° at a depth of 40 km, continuing up to about 250 km, suddenly changing its dip to 70°. To further southeast (beneath Guerrero), the Cocos slab shows a higher inclination, ~25°, which ultimately steepens to 70-75°(Manea et al., 2013).

In the central part of TMVB, the active volcanoes are not spatially scattered, but distributed roughly along a trench-parallel linear trend. This pattern suggests melt focusing to the updip region in the subduction zone (Figure 8.2b-i), which we can relate to the slab-parallel advection mechanism in our laboratory experiments. In contrast, the north-eastern Cocos plate with a gentle α beneath Guerrero causes a global RTI in the melt-rich layer to

produce spatially scattered active volcanoes in TMVB (Figure 8.2b-ii). The present theoretical solution shows a critical α of ~28°, where $\alpha > 28°$ would suppress the RTI to facilitate the advection mechanism. This theoretical prediction explains the contrasting scenarios of arc-volcanism in the central and the eastern part of the Cocos plate with a steep (>> 28°) and a gentle (< 28°) slab-dip (Castellanos *et al.* 2018). We thus find an excellent correlation of the volcanic distribution with the varying slab dips. The high-angle slab dip segment has a relatively focused distribution of volcanic spots along a trench parallel narrow linear trend and is consistent with the experimental models for slab dip >30°, showing Mode 2 plumes. The low-angle dip segment of the trench displays distributed volcanic spots scattered in the slab dip direction, which again matches closely with the formation of Mode 1 plumes and their distributions in our experimental models with low slab dips (10°- 20°)(Currie et al., 2002; Riller et al., 2006; Stubailo et al., 2012).

The Java trench also delineates a spectacular arcuate chain of active volcanism, covering a large distance, nearly 4000 km (Figure 8.3). The trench has two segments, defined by Sumatra and Java islands in the overriding plate. These two islands are dotted with numerous volcanic spots but well organized to form a linear belt, trending more or less parallel to the trench. However, it is possible to recognize visually a difference in their distribution patterns. The Sumatra Island that lies on the NW flank of the trench localizes the volcanic spots along a trench-parallel line running for about 1750 km. Their trench normal scattering is virtually absent. On the other side, Java Island displays a scattered distribution of the volcanic spots. Available seismic sections reveal that the Indo-Asian plate subducts along the Java trench with varying slab dips, i.e., high-angle slab dip (~ 60°) beneath the Sumatra Island (Figure 8.3, X), and relatively low-angle slab dip (~20°) beneath some portion of the Java Island (Figure 8.3, Y). The present study suggests that the high-angle-slab condition favored the plume processes to occur in Mode 2, which caused focusing of the volcanic spots along a trench parallel linear trend in the Sumatra segment with an average spacing of 46 to 54 km (Figure 8.3), which is consistent with the experimental longitudinal spacing (~ 35-70 km). Flattening of slab dips resulted in a Mode 2 to 1 transition, giving rise to a scattered distribution of the volcanic spots in the Java Island. However, the degree of scattering is not as strong as in the case of Andes flat segments discussed above. We interpret such weak scattering in the Java Island as a direct consequence of a sharp change in the slab dip (20° to 40°) with increasing depth. The steeper slab segment promotes advection of partial melt up the slab and forced plumes to form a cluster. The stretch along which the slab dip sharply steepens limits the range of

trench-perpendicular scattering in the direction of slab dip (Chiu et al., 1991; Hall and Spakman, 2015).

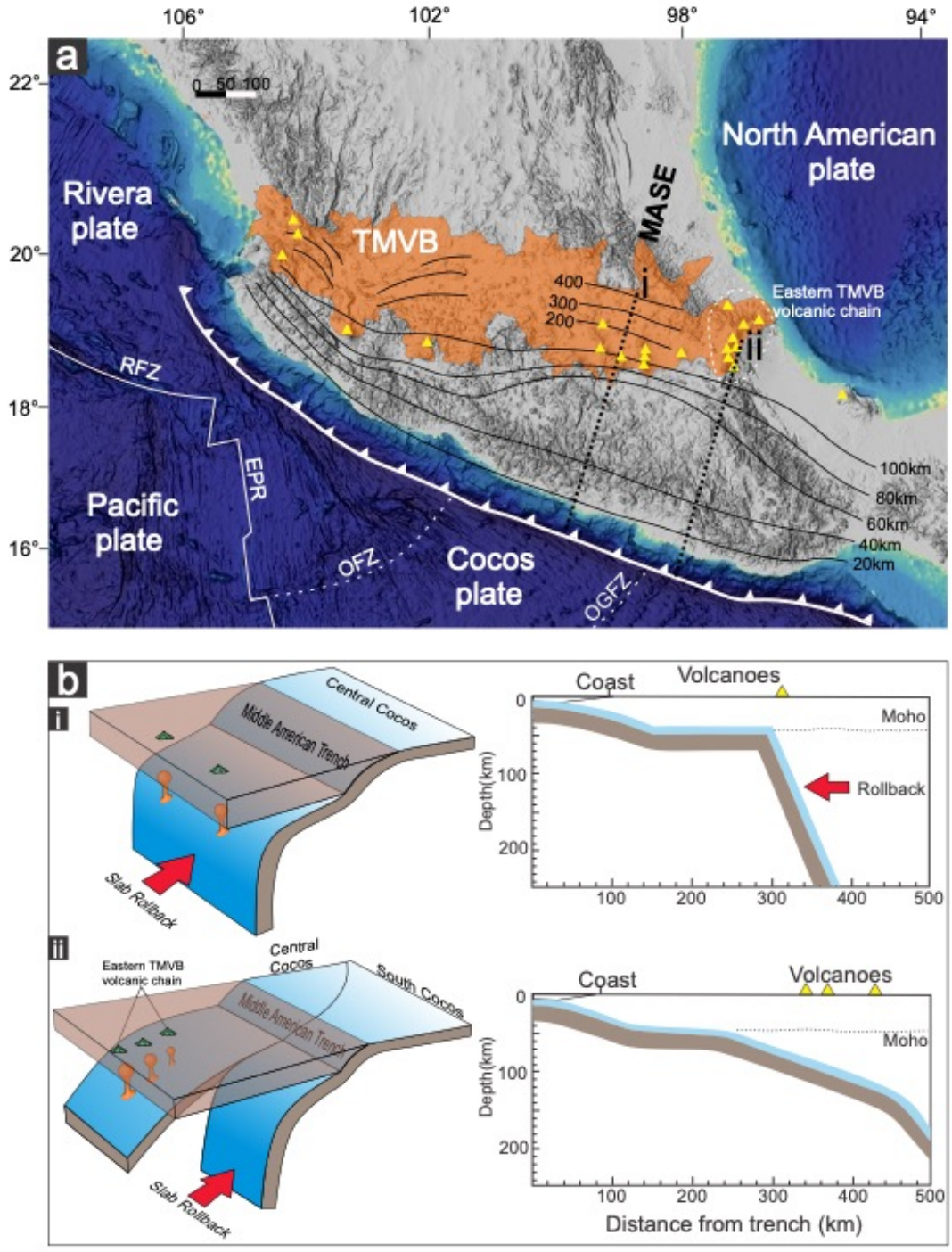

Figure 8.2: a) Spatial distributions of the active volcanoes in the Trans-Mexico volcanic belt (TMVB). The contours show the isobaths of subducting Cocos plate obtained from Ferrari et al, 2012. Locations of the main volcanoes are marked by yellow triangles. b) The subduction system (left panels) and the corresponding 2D cross sections (right panels) of central (i) (after Manea et al, 2013) and eastern (ii) (after Castellanos et al, 2018) TMVB, depicting contrasting distributions of the volcanoes, attributed to steep and gentle slab-dips of the subducting Cocos plate.

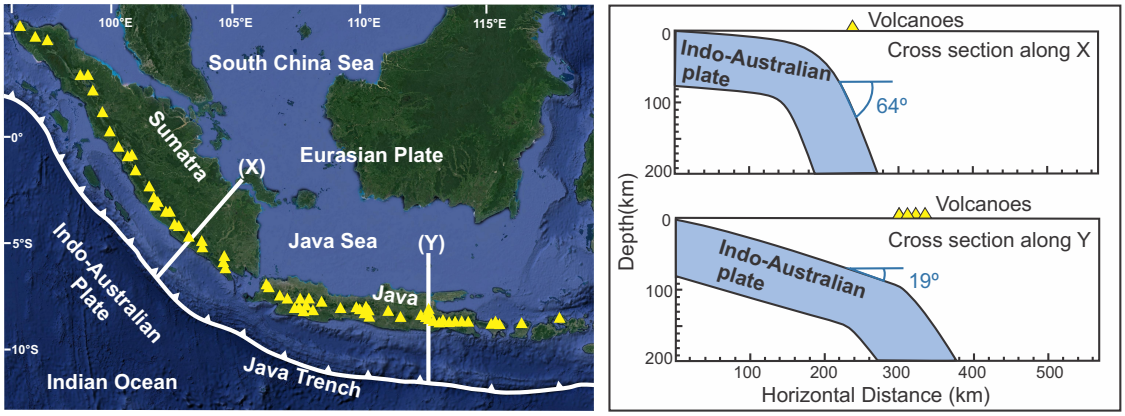

Figure 8.3: Present-day volcanic spot distributions in the Java-Sumatra trench (Hall et al. 2015). Locations of active volcanoes are shown as yellow triangles. The corresponding trench perpendicular sections (right side) show lateral variations of their subducting slab dips, and associated arc volcanism patterns.

8.2.1 Conclusions

This study provides a synthesis of scaled laboratory experiments and CFD simulations to explain the origin of contrasting arc volcanisms in subduction zones, where the cold plumes are initiated by Rayleigh-Taylor instabilities (RTIs) in the buoyant partially molten layer atop the dipping slabs. The slab dip (α) is found to play a key role in determining the modes of plume growth, leading to either a focused (linear) or a scattered (areal) distribution of the arc volcanoes. Dipping slabs develop two distinct sets of trench-perpendicular and trench-parallel RTI waves in the partially-molten layers: *longitudinal waves* (λ_L) directed along the slab dip, and *transverse waves* (λ_T) along the slab strike. For low slab dips ($\alpha <$ 30°), the λ_T/λ_L interference is the dominant mechanism in controlling the plume dynamics. Slab dips, exceeding a threshold value ($\alpha^* \sim 30°$) dampen the λ_T wave growth and promote the λ_L waves to capture the plume dynamics. We identify two principal modes of plume growth. In Mode 1, they initiate from melt-rich domes produced by λ_T/λ_L interference and grow randomly to form plumes distributed throughout the source layer, as observed in many subduction settings, e.g., the Mexico subduction system. On the other hand, Mode 2 plumes localize at the upper fringe of a partially molten layer above the subducting slab, and they are mostly controlled by λ_L-driven advection of buoyant materials in the updip direction. Unlike Mode 1 plumes, they grow spontaneously with a regular spacing (~ 35-70 km) to form a trench-parallel array, resembling the linear trench parallel volcanic arcs in many subduction zones, such as the Caribbean subduction zone. This study underscores

the role of α in governing the Mode 1 versus Mode 2 plume growth; the steepening of α results in a Mode 1 to 2 transitions at a threshold value (~30°). It can thus be proposed that the migration of the arc magmatism through time reflects changes in slab dip (α). Thickness (T_s) of the partially molten zone is another factor in plume dynamics. Increasing T_s facilitates partial melt advection along slab dip, which in turn accelerates the upward drift of vertically growing melt-rich domes. This mechanism eventually gives rise to Mode 2 plume clusters in the updip slab region. Based on our model estimates, we predict a ~ 200–500 kiloyear periodicity of plume pulses, which explains the periodic nature of arc volcanism in subduction zone settings.

8.3 Rayleigh-Taylor instability patterns in 3D: Conclusions and outlook

The experiments presented in this thesis provides an insight into the three-dimensional evolution of Rayleigh-Taylor instability (RTI) in a thin viscous layer on an inclined substrate, overlain by a denser fluid medium. Based on the experimental findings, the RTI mechanics in the inclined layer is theorized in the framework of interfering double Fourier modes. The 3D RTI geometry at the fluid interface evolves by the interference of two sets of mutually orthogonal waves, where one of them is oriented in the inclination direction. The two wave trains grow simultaneously but at different wavelengths depending on the substrate inclination (α). For $\alpha < 30^o$, they have competitive wavelengths, and their interference gives rise to periodic elongate dome-like structures oriented in the direction of substrate inclination. For higher α ($\geq 30°$), the double mode is replaced by a single Fourier mode of instability to form a series of cylindrical rivulet like structures down the substrate slope. The upward advection of buoyant fluids through the cylindrical channels results in the growth of vertical plumes at their upper extremities.

The RTI pattern on a horizontal substrate develops with hexagonal symmetry, as extensively reported in the literature. My study demonstrates that inclined orientations of the substrate break the hexagonal symmetry and gives rise to characteristic patterns as a function of the inclination (α). For moderate inclinations ($10° \leq \alpha < 30°$), the hexagonal symmetry transforms into a rectangular symmetry with the long and short axes to represent the two wavenumbers of the double Fourier mode of instability. Balestra et al., (2018) have shown a similar change in symmetry for a thin layer on the underside of a curved substrate in the presence of surface tension. Recently, Lerisson et al., (2020) have also demonstrated

such steady patterns in the presence of forced flow and surface tension. On the other hand, for a two-layer system, such a geometrical transformation of the interface instability can occur solely under the influence of vertical gravity components modulated by the substrate inclination, without any prior forcing in the flow or surface tension. The substrate inclination entirely decides the relative growth of instability waves along and across the slope direction of the substrate and their corresponding wavenumbers.

The linear analysis deals with a single normal mode to predict the amplitude growth of instabilities as an exponential function of time. The non-linear solution for small values of time (t) also suggest that the first-order term, η_{11} dominates to control the amplification. Comparing the graphical plots, the temporal variations of the normal mode obtained from the linear theory is found to be consistent with the first-order solution of our non-linear theory (Figure 8.4). The experimental results validate the theoretical prediction. The amplification predicted from our linear and non-linear theory are found to converge well with one another at a small growth time. However, the linear theory fails to accurately predict the amplification behaviour of the interface instability on a larger time scale. I thus consider the secondary modes (η_{21} , η_{31}) and their interactions with the primary mode to predict the instability growth in advanced stages of this process. Figure 8.4 show the amplitude of primary mode as a function of t for $\alpha = 20°$, deduced from the linear theory and weakly non-linear theory. With increase in t, the two solutions develop a large difference, which continues to occur till a maximum is attained. The maximum value marks the limit of validity of the non-linear analysis. The solutions for $\alpha = 40°$ show a similar result, but yields the growth rate of amplitudes increasing with t at significantly higher rates.

For $\alpha < 10$, the interface instability is initiated with a hexagonal pattern, as shown in Figure 5.13c and Figure 5.14c. At a small normalized time (t), the interface develops 3D topography with rounded crests and thoughts on all sides, forming a regular hexagonal cell structure. In general, each cell is surrounded by six equidistant cells. The linear solution reproduces the instability pattern produced at this stage of short time, implying that the primary Fourier mode dominates to control the 3D instability growth at the initial stage. With time the rounded crests transform their geometry with sharp curvatures, often showing asymmetrical shapes point to the up-dip direction. Overall, the interface topography consists of periodic spherical domes and depressions of uniform heights. The evolved geometry suggests the role of higher harmonics in the instability growth, which

can no longer be fully described by the linear theory. The results obtained from the weakly non-linear theory closely matches with the deformed interface geometry in our experiments. For $10° < \alpha < 30°$, the interface instability is initiated with a rectangular cell pattern with the longer wavelengths oriented down the substrate slope (Figure 5.13b). Each cell consists of a dome at the centre, surrounded by four troughs. In this case also, the primary mode governs the instability growth at the initial stage, as evident from the sinusoidal wave geometry in both x and y directions, which can also be predicted from the linear theory. However, the growth behavior progressively turns to be nonlinear with increasing effects of higher harmonics on the amplification process. During this time, the crests become sharper, whereas the troughs grow wider to increase their spherecity. Despite the strong nonlinear effects, the instability structure retains arrays of rectangular cells containing ellipsoidal depressions at their centers, surrounded by two sets of elongate ridges oriented parallel to the inclination direction.

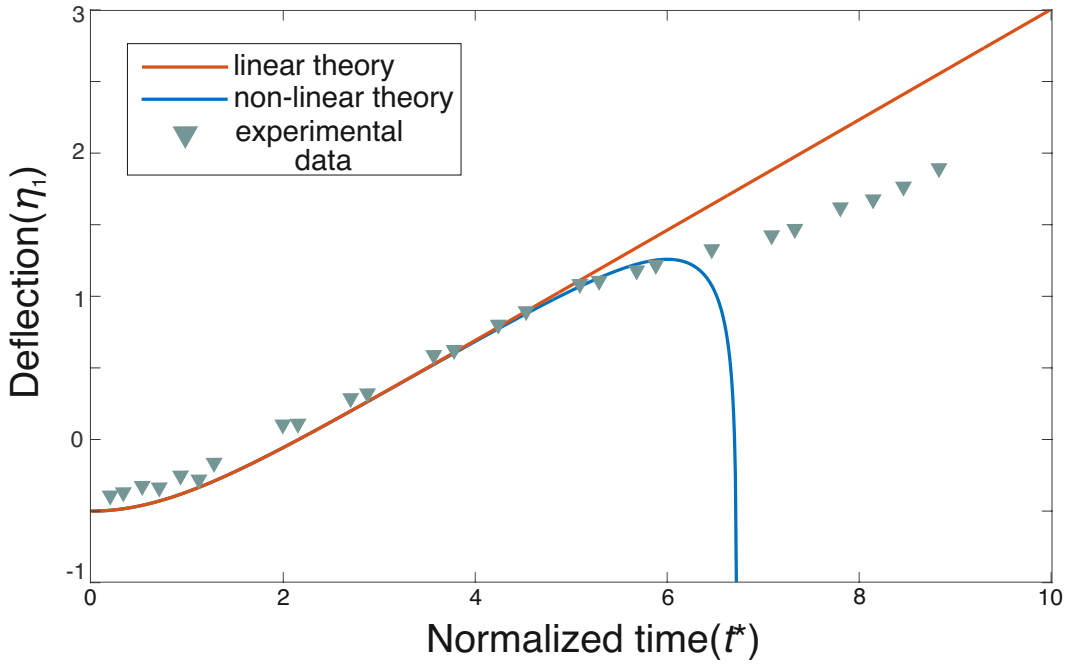

Figure 8.4: Interface deflection (η) of instabilities (logarithmic scale) as a function of normalized time (t^*) as calculated from linear and non-linear theory for $\alpha = 20°$. The values measured from experiments are also provided.

The mode of interfacial instability undergoes a dramatic transformation when $\alpha >$ 30°, and produces a roll or rivulet geometry of a single Fourier mode with a laterally persistent wavelength in the direction perpendicular to the substrate inclination (Figure

5.13a). The instability eventually grow into a train of cylindrical ridges, separated by long depressions, wherewith time the ridges grow linearly in the expense of the depressions. Substrate parallel advection in the up-dip direction is polarized along the crests, which in turn sets in a secondary instability to produce solitary domes at their upper extremities. The shape of the ridges remains constant throughout the runtime; hence, the difference between linear and nonlinear theory is rather insubstantial.

The effects of substrate inclination on the three-dimensional RTI evolution we report in this study can provide new insights into the gravity-driven flows in large-scale geophysical fluid systems. For example, warm, buoyant deep seawater undergoes upwelling against the continental slope. The present findings can be used to predict the modes of upwelling as a function of the continental slope. A typical along-slope upwelling is possible only when the continental slope exceeds a critical value. The experiments suggest that the upwelling in such a condition will be partitioned into a set of parallel linear zones with strong flow velocity. On the other hand, gentle continental slopes will facilitate 3D instabilities in the upwelling seawater layer, resulting in local vertical upwelling of buoyant water and their mixing with the ambient medium.

8.4 Deccan volcanism-African superplume connection: key findings

It is now a well-accepted hypothesis that the existence of African LLSVP dates back to at least the Pangea event (Zhang et al., 2010). During the Gondwana-proto-Laurussia convergence, several cold subducting slabs assembled in the lower mantle beneath the African continental lithosphere, forming this distinct layer above the CMB whose current location and shape is driven by the post-Pangea subduction history. Recent mantle convection models with continuously evolving plate boundaries (Hassan et al., 2016; Müller et al., 2016) decipher positional changes of the African LLSVP through time considering subduction driven mantle flow due to Neo-Tethys Ocean closure, which is illustrated in Figure 8.5a, b. The model results suggest that the western margin of African LLSVP has remained almost stable during the entire Cretaceous period, but the eastern flank has continuously changed its position during this time. The time-dependent effect of subduction on the north (closure of Tethys) produced a strong southward lower-mantle poloidal flow (Figure 8.5a), leading to mantle upwelling in the south. This upwelling dynamics in turn induced a convective mantle “roll” that forced the eastern flank of the

African LLSVP boundary to migrate southward and the Indian plate to move northward at a higher velocity (Glišović and Forte, 2017). These inferences are further validated by geophysical observations that predict deformation and southward movement of African LLSVP under east Africa (Ford and Long, 2015).

The modelling domain chosen in this study considers a north-south cross-section of the mantle, replicating the Indian plate movement in late Mesozoic and Cenozoic (past 130 Ma) to reconstruct the eastern flank position of the African LLSVP relative to the Indian subcontinent. The model simulations suggest that a large mantle roll formed as a consequence of the subduction in the north (*cf.* Glisovic *et al*.), forced the pile to move in the southward direction at a rate of 17-19 km/Ma in the beginning of the Late Cretaceous (Figure 8.5c ii). This postulate is consistent with the inferences from other studies that claimed the southward movement of African LLSVP due to the presence of deep-mantle southward poloidal flow as a consequence of the Tethyan subduction over the past 130 Ma (Hassan et al., 2020). The poloidal flow resulted in the formation of thermal instability within the exposed CMB north of the LLSVP, which subsequently migrated towards the African LLSVP amplifying the pile at its eastern flank to attain a thickness of ~800-1000 km. The laterally migrating TBL instabilities climbed up the pile edge to finally reach the pile crest and form a mature plume. The positional reconstruction of the African LLSVP and Indian plate for this time period allows us to conclude that the north-eastern flank of African LLSVP coincided with the Indian plate location in a time frame of 70-65 Ma (Figure 8.5b). This plume then generated successive pulses upon reaching the mid-mantle transition zone through the late Mesozoic and Cenozoic, where the first pulse corresponds to the Deccan events at 66 Ma. The plume initiation led to a drop in the rate of southward pile migration to ~ 6-7 km/Ma (Figure 8.5c ii) as the pile material now effectively upwells with the plume, hindering its horizontal movement. Subsequently, the pile migrated further south-westward, whereas the Indian plate itself moved north-eastward. The plume periodically formed the secondary and tertiary pulses at mid-mantle depth at an interval of 5-8 Ma, giving rise to successive eruptions from the Réunion hotspot. The plume process eventually reduced pulse volumes and involved a sharp change in the chemical characteristics of the Réunion lava flows during the post-Deccan volcanism period. With time, the eastern margin shifted its position to further southwest to reach the current location (Figure 8.5b). The present model suggests that the process of sequential plume-head detachment at the mid-mantle transition zone modulated the periodic pulse generation and determines the time scale, volume, and topography associated with each of these

pulses. Considering a CMB temperature of 3300 K and an initial pile thickness of 150 − 200 km, the model results for B in a range $0.8 - 1.2$ yield a periodicity of 5-8 Ma, similar to that of Réunion activity throughout the Cenozoic. To tally the dynamic topography, the pile also needs to be ~ 100 times viscous (μ~100) and ~ 20 times HPE enriched than the ambient lower mantle. This condition produces a primary pulse volume of $14 - 15.5 \times 10^6$ km^3 and dynamic topography of ~2000 m related to the Deccan event, followed by the next generation of pluses with volumes of 12×10^6 km^3, 7×10^6 km^3, 3.5×10^6 km^3 and topography of ~1400 m, ~700 m, and ~200 m.

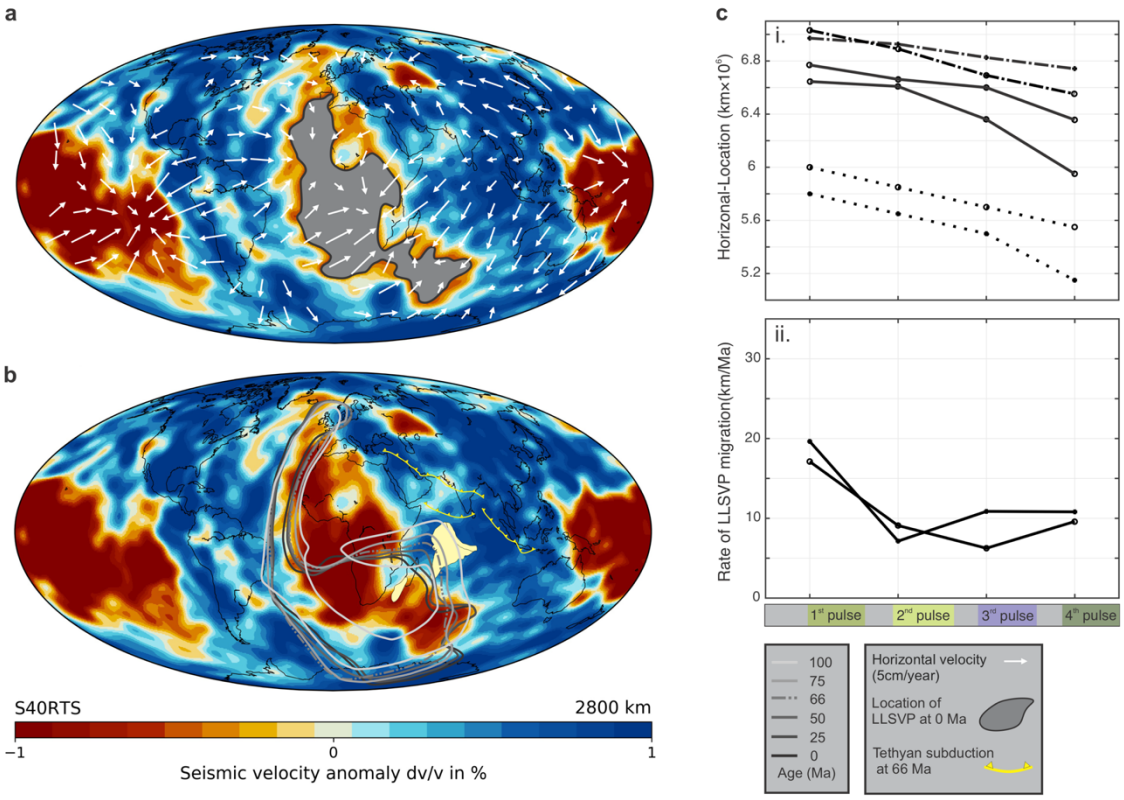

Figure 8.5: African LLSVP and its connection to the Réunion hotspot and the Deccan volcanism. (**a**) Global map showing present-day location of African LLSVP (gray shade) along with the poloidal velocity components at a level 150 km above CMB constructed from Ford and Long, 2015. Strong south-westward velocity can be noticed at the eastern flank of the LLSVP. **(b)** Contours of 75% chemical concentration corresponding to a time series, 100 Ma to present day. The contour plots depict positional changes of African LLSVP through geologic time. The contours are redrawn from Hassan et al., 2016, 2020 expect that for 66 Ma (dashed contour) which is interpolated. The figure also shows location of the Tethyan subduction system and Indian plate (yellow) during the Deccan volcanism at 66 Ma. At this time the western margin of Indian plate was located directly above the eastern flank of the African LLSVP. The base map has been produced using S40RTS (Ritsema et al., 2011) depth slice at 2800 km on SubMachine. **(c)** Plots of the locations of African LLSVP (solid lines), Réunion plume tail (dotted lines) and plume head (dashed lines) **(i)**, the rate of southward migration of LLSVP and **(ii)** those calculated from two of our representative models (see text) for each successive pulsation events.

8.4.1 Timescale of the Deccan volcanic periodicity

To study the time periodicity of Deccan volcanism, I will focus on the melting process in the primary plume head obtained from our thermochemical model (Figure 6.26). The model results suggest that the plume head locally underwent melting within the asthenosphere to set in three eruptive events within a time scale of 1 Ma (Figure 8.6), where the first event of the eruption occurred within 0.15 Ma from the plume head stagnation with a cumulative volume of 0.32×10^6 km^3 (Figure 6.26b), correlated with the lowermost seven formations produced during the period ~ 66.5-66.3 Ma. The second event took place after a quiescent period of ~ 0.3 Ma with a volume of 0.18×10^6 km^3, which corresponds to the ~ 66.0 Ma Poladpur Formation. Finally, the third pulse that initiated after 0.4 Ma produced a volume of 0.15×10^6 km^3, which can be equated with the Ambanali and later formations deposited during ~ 65.6-65-3 Ma. Based on these model calculations, we estimate a volume flux of ~8-9 km^3/year for the first event, subsequently reduced to $\sim 5 - 5.5$ km^3/year and $\sim 4 - 4.5$ km^3/year, respectively, for the second and third events. This estimate implies that the rate of Deccan volcanic eruption in a pulse (time scale ≤ 100 Ka) exceeded the global value (3 to 4 km^3/year) by a factor of 1.5 to 3. Moreover, there must be hiatuses in the order of tens of thousands of kiloyears within the pulses to balance the total volume estimates. Geochemical proxies also suggest a sharp increase of mantle contributions to later volcanic formations, such as Poladpur and Ambenali, indicating a reduction of magma-crust interface area (Renne et al., 2015). The higher rates of thermal erosion at the LAB during the first two events effectively thinned the lithosphere and weakened the vigorousity crust-mantle interaction during the subsequent melt pulse events, as revealed from our models (Figure 6.26a).

Although our model estimates broadly agree with the time gaps between different episodes of the Deccan volcanism, they somewhat underestimate the erupted volumes predicted from petrological and geochemical studies (Schoene et al., 2019). Groups of flows within the Poladpur and Mahabaleshwar Formations, each potentially comprising > 50,000 km^3, lack any secular variation of paleomagnetic poles, suggesting the eruption at high rates, ~ 1000 km^3/year on decadal to centuries scales. Our volume and flux estimates for eruptions prior to the KPB tally well with the available data; however, they do not account for either the high melt volumes or the rate of eruption for the post-KPB eruptions. We thus conclude that there is a transition in the nature of volcanism across the KPB, the explanation of which demands the possible effects of other internal or external

factors. One possible explanation could be that the Chicxulub bolide impact accelerated the eruption rates, as suggested by the previous studies (Renne et al., 2015).

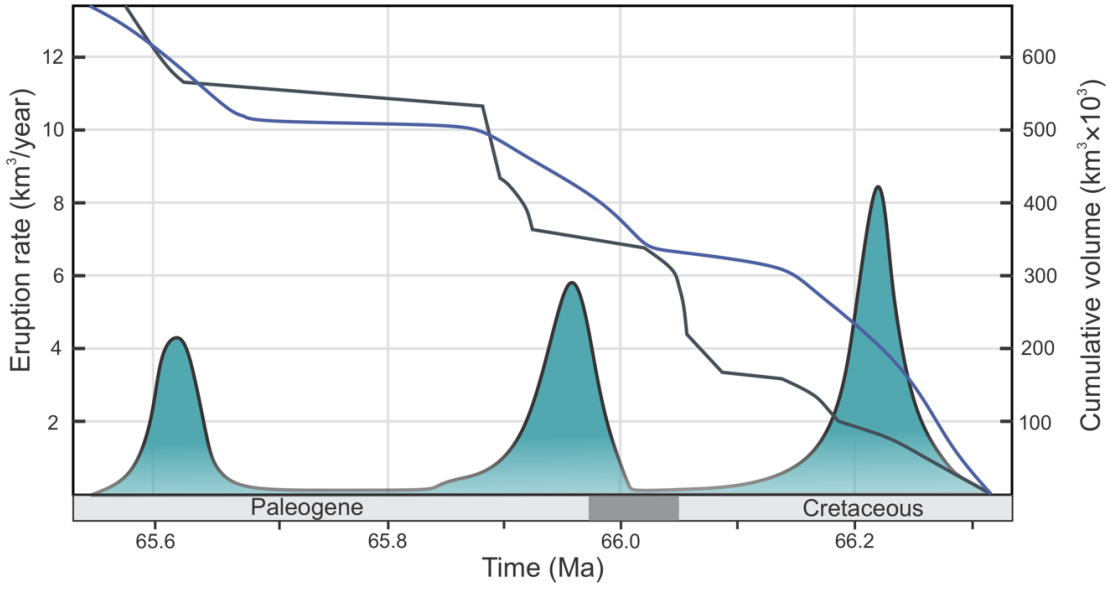

Figure 8.6: Comparison of the duration and cumulative volume of Deccan pulses between this study (blue curve) and the geochemical study by Schoene et al., (2019) (black curve).

8.4.2 Comparison with major global LIP events

We will now discuss the periodicity of Deccan volcanism that occurred sequentially in three major pulses in the context of similar episodic volcanic events from other LIPs and hotspots, such as Cobb, Hawaii, Kerguelen, Réunion, and others (Morrow and Mittelstaedt, 2021). They show the periodicity of the volcanic events on varied timescales (Figure 8.7). For example, the Hawaii-Emperor hotspot track records a sequence of magmatic pulses at around 64 Ma, 50 Ma, 42 Ma, and at 28 Ma, implying a pulsating time scale of about 10 Ma (Van Ark and Lin, 2004). On the other hand, from bathymetry analysis Wessel (2016) has established a much shorter pulsating time scale (< 2 Ma) for the post-22 Ma volcanism, as observed in the Deccan volcanism. The Yellowstone LIP started its volcanism at around 18 Ma (Schutt et al., 2008), followed by two distinct magmatic peak events at around 11 Ma and 5 Ma (Stachnik et al., 2008; Waite et al., 2006). In a recent study of the Yellowstone super-volcano the tomographic P-wave model has detected hot pulses in the upper mantle (Huang et al., 2015). These discrete bodies, most probably pockets of partial melts represent episodic pulses, produced by a large plume source in the mantle, as predicted from our numerical model simulations. The Réunion hotspot displays a major emplacement in Deccan traps at 66-68 Ma, with later magmatic peaks at 57 Ma, 48 Ma, 35 Ma, 8 Ma, and 2 Ma (Mjelde et al., 2010).

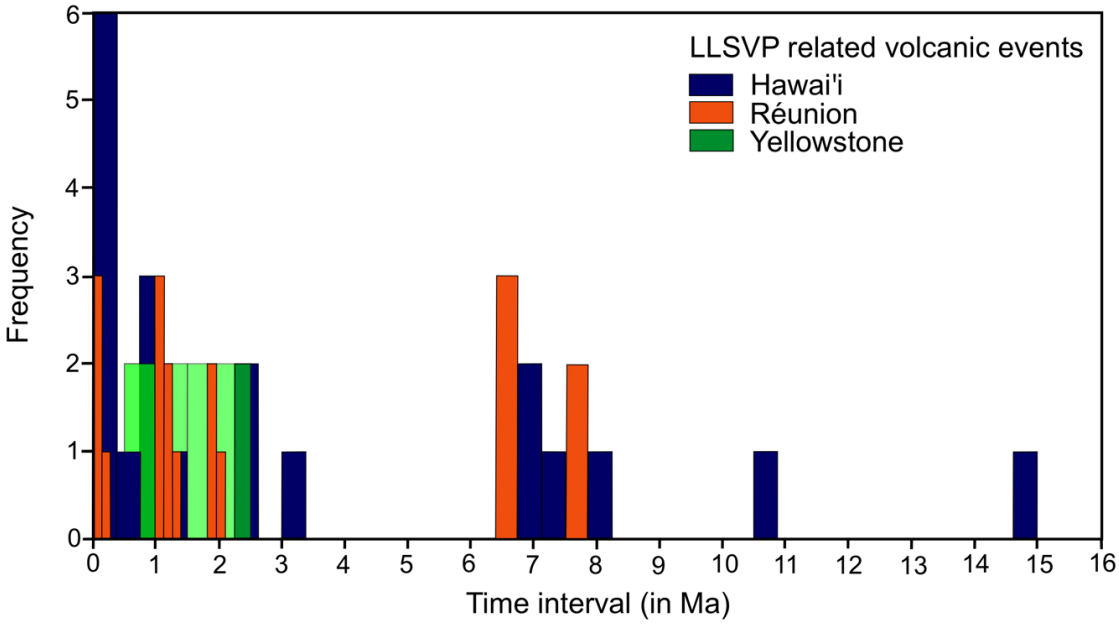

Figure 8.7: A timescale analysis of global LLSVP related volcanic events. Histogram analysis of the periodic variations of volcanism in Hawai'i (Blue), Réunion (Saffron) and Yellowstone (Green). Short-term (< 1.5-2 Ma oscillations) and long-term (> 3 Ma oscillations) temporal variations are distinct in the plots (see discussion).

Bibliography

Aharonov, E., Whitehead, J.A., Kelemen, P.B., Spiegelman, M., 1995. Channeling instability of upwelling melt in the mantle. J. Geophys. Res. Solid Earth 100, 20433–20450. https://doi.org/10.1029/95JB01307

Alvarez, L., Alvarez, W., Asaro, F., Michel, H. V., 1980. Extraterrestrial Cause for the Cretaceous-Tertiary Extinction. Science (80-.). 208, 1095–1108.

Ammann, M.W., Brodholt, J.P., Wookey, J., Dobson, D.P., 2010. First-principles constraints on diffusion in lower-mantle minerals and a weak D″ layer. Nature 465, 462–465. https://doi.org/10.1038/nature09052

Andikagumi, H., Macpherson, C.G., McCaffrey, K.J.W., 2020. Upper Plate Stress Controls the Distribution of Mariana Arc Volcanoes. J. Geophys. Res. Solid Earth 125, 1–27. https://doi.org/10.1029/2019jb017391

Antolik, M., Gu, Y., Ekstrom, G., Dziewonski, A., 2003. J362D28: a new joint model of compressional and shear velocity in the Earth's mantle. Geophys. J. Int. 153, 443–466.

Arcay, D., Tric, E., Doin, M.P., 2005. Numerical simulations of subduction zones. Effect of slab dehydration on the mantle wedge dynamics. Phys. Earth Planet. Inter. 149, 133–153. https://doi.org/10.1016/j.pepi.2004.08.020

Babchin, A.J., Frenkel, A.L., Levich, B.G., Sivashinsky, G.I., 1983. Nonlinear saturation of Rayleigh-Taylor instability in thin films. Phys. Fluids 26, 3159–3161. https://doi.org/10.1063/1.864083

Balestra, G., Kofman, N., Brun, P.T., Scheid, B., Gallaire, F., 2018. Three-dimensional Rayleigh-Taylor instability under a unidirectional curved substrate. J. Fluid Mech. 837, 19–47. https://doi.org/10.1017/jfm.2017.817

Baruah, A., Roy, M.K., Sarkar, S., Mandal, N., 2014. Dynamics of solid-melt front migration from a reaction-diffusion model. Heat Mass Transf. und Stoffuebertragung 50, 31–38. https://doi.org/10.1007/s00231-013-1221-0

Behn, M.D., Grove, T.L., 2016. Melting systematics in mid-ocean ridge basalts: Application of a plagioclase-spinel melting model to global variations in major

element chemistry and crustal thickness. J. Geophys. Res. Solid Earth 3782–3803. https://doi.org/10.1002/2015JB011885.Received

Bellman, R., Pennington, R.H., 1954. Effects of surface tension and viscosity on Taylor instability. Q. Appl. Math. 12, 151–162.

Benes, V., Davy, P., 1996. Modes of continental lithospheric extension: Experimental verification of strain localization processes. Tectonophysics 254, 69–87. https://doi.org/10.1016/0040-1951(95)00076-3

Bercovici, D., Ricard, Y., Schubert, G., 2001. A two-phase model for compaction and damage 1. General Theory. J. Geophys. Res. Solid Earth 106, 8887–8906. https://doi.org/10.1029/2000jb900430

Bergantz, G.W., 1989. Underplating and partial melting: Implications for melt generation and extraction. Science (80-.). 245, 1093–1095. https://doi.org/10.1126/science.245.4922.1093

Biot, M.A., Ode, H., 1965. Theory of gravityinstability with variable overburden and compaction. Geophysics xxx, 213–227.

Bisshopp, F.E., 1960. On two-dimensional cell patterns. J. Math. Anal. Appl. 1, 373–385. https://doi.org/10.1016/0022-247X(60)90011-1

Bond, D.P.G., Wignall, P.B., 2014. Large igneous provinces and mass extinctions: An update. Spec. Pap. Geol. Soc. Am. 505, 29–55. https://doi.org/10.1130/2014.2505(02)

Bose, K., Ganguly, J., 1995. Experimental and theoretical studies of the stabilities of talc, antigorite and phase A at high pressures with applications to subduction processes. Earth Planet. Sci. Lett. 136, 109–121.

Bredow, E., Steinberger, B., Gassmöller, R., Dannberg, J., 2017. How plume-ridge interaction shapes the crustal thickness pattern of the Réunion hotspot track. Geochemistry, Geophys. Geosystems 18, 2930–2948. https://doi.org/10.1002/2017GC006875

Brun, P., Damiano, A., Rieu, P., Balestra, G., Gallaire, F., 2015. Rayleigh-Taylor instability under an inclined plane. Phys. fluids 084107, 1–10. https://doi.org/10.1063/1.4927857

Buffett, B.A., Garnero, E.J., Jeanloz, R., 2000. Sediments at the top of earth's core. Science (80-.). 290, 1338–1342. https://doi.org/10.1126/science.290.5495.1338

Bull, A.L., McNamara, A.K., Ritsema, J., 2009. Synthetic tomography of plume clusters and thermochemical piles. Earth Planet. Sci. Lett. 278, 152–162. https://doi.org/10.1016/j.epsl.2008.11.018

Burgess, J.M., Juel, A., McCormick, W.D., Swift, J.B., Swinney, H.L., 2001. Suppression

of dripping from a ceiling. Phys. Rev. Lett. 86, 1203–1206. https://doi.org/10.1103/PhysRevLett.86.1203

Cahn, R.W., 1986. Materials science: Melting and the surface. Nature 323, 668–669. https://doi.org/10.1038/323668a0

Campbell, I.H., Griffiths, R.W., 1990. Implications of mantle plume structure for the evolution of flood basalts. Earth Planet. Sci. Lett. 99, 79–93. https://doi.org/10.1016/0012-821X(90)90072-6

Cande, S.C., Stegman, D.R., 2011. Indian and African plate motions driven by the push force of the Réunion plume head. Nature 475, 47–52. https://doi.org/10.1038/nature10174

Canright, D., Morris, S., 1993. Buoyant instability of a viscous film over a passive fluid. J. Fluid Mech. 255, 349–372. https://doi.org/10.1017/S0022112093002514

Chabot, N.L., Agee, C.B., 2003. Core formation in the Earth and Moon: New experimental constraints from V, Cr, and Mn. Geochim. Cosmochim. Acta 67, 2077–2091. https://doi.org/10.1016/S0016-7037(02)01272-3

Chandrasekhar, S., 1961. Hydrodynamic and Hydromagnetic Stability.

Chenet, A.L., Courtillot, V., Fluteau, F., Gérard, M., Quidelleur, X., Khadri, S.F.R., Subbarao, K. V., Thordarson, T., 2009. Determination of rapid Deccan eruptions across the Cretaceous-Tertiary boundary using paleomagnetic secular variation: 2. Constraints from analysis of eight new sections and synthesis for a 3500-m-thick composite section. J. Geophys. Res. Solid Earth 114. https://doi.org/10.1029/2008JB005644

Chenet, A.L., Quidelleur, X., Fluteau, F., Courtillot, V., Bajpai, S., 2007. 40K-40Ar dating of the Main Deccan large igneous province: Further evidence of KTB age and short duration. Earth Planet. Sci. Lett. 263, 1–15. https://doi.org/10.1016/j.epsl.2007.07.011

Chiu, J., Isacks, B.L., Cardwell, R.K., 1991. 3-D configuration of subducted lithosphere in the western Pacific. Geophys. J. Int. 106, 99–111.

Cimpeanu, R., Papageorgiou, D.T., G., P.P., 2013. On the control ans suppresssion of Rayleigh-Taylor instability using electric fields 1–31.

Citron, R.I., Lourenço, D.L., Wilson, A.J., Grima, A.G., Wipperfurth, S.A., Rudolph, M.L., Cottaar, S., Montési, L.G.J., 2020. Effects of Heat-Producing Elements on the Stability of Deep Mantle Thermochemical Piles. Geochemistry, Geophys. Geosystems 21, 1–17. https://doi.org/10.1029/2019GC008895

Cloos, E., 1955. Experimental analysis of fracture patterns. Bull. Geol. Soc. Am. 66, 241–

256. https://doi.org/10.1130/0016-7606(1955)66[241:EAOFP]2.0.CO;2

Codillo, E.A., Le Roux, V., Marschall, H.R., 2018. Arc-like magmas generated by mélange-peridotite interaction in the mantle wedge. Nat. Commun. 9. https://doi.org/10.1038/s41467-018-05313-2

Coffin, M.F., Duncan, R.A., Eldholm, O., Fitton, J.G., Frey, F.A., Larsen, H.C., Mahoney, J.J., Saunders, A.D., Schlich, R., Wallace, P.J., 2006. Large igneous provinces and scientific ocean drilling: Status quo and a look ahead. Oceanography 19, 150–160. https://doi.org/10.5670/oceanog.2006.13

Conder, J.A., Wiens, D.A., Morris, J., 2002. On the decompression melting structure at volcanic arcs and back-arc spreading centers. Geophys. Res. Lett. 29, 14–17. https://doi.org/10.1029/2002gl015390

Cornell, D., Katz, D.L., 1953. Flow of Gases through Consolidated Porous Media. Ind. Eng. Chem. 45, 2145–2152. https://doi.org/10.1021/ie50526a021

Crameri, F., Shephard, G.E., Heron, P.J., 2020. The misuse of colour in science communication. Nat. Commun. 11, 1–10. https://doi.org/10.1038/s41467-020-19160-7

Currie, C.A., Hyndman, R.D., Wang, K., Kostoglodov, V., 2002. Thermal models of the Mexico subduction zone: Implications for the megathrust seismogenic zone. J. Geophys. Res. Solid Earth 107, ETG 15-1-ETG 15-13. https://doi.org/10.1029/2001JB000886

Daines, M.J., Kohlstedt, D.L., 1994. The transition from porous to channelized flow due to melt/rock reaction during melt migration. Geophys. Res. Lett. 21, 145–148. https://doi.org/10.1029/93GL03052

Dannberg, J., Gassmöller, R., 2018. Supporting Information. Proc. Natl. Acad. Sci. 1–5.

Dannberg, J., Heister, T., 2016. Compressible magma/mantle dynamics: 3-D, adaptive simulations in ASPECT. Geophys. J. Int. 207, 1343–1366. https://doi.org/10.1093/gji/ggw329

Dannberg, J., Sobolev, S. V., 2015. Low-buoyancy thermochemical plumes resolve controversy of classical mantle plume concept. Nat. Commun. 6, 1–9. https://doi.org/10.1038/ncomms7960

Davies, J.H., Stevenson, D.J., 1992. Physical model of source region of subduction zone volcanics. J. Geophys. Res. 97, 2037–2070. https://doi.org/10.1029/91JB02571

Deschamps, F., Kaminski, E., Tackley, P.J., 2011. A deep mantle origin for the primitive signature of ocean island basalt. Nat. Geosci. 4, 879–882.

https://doi.org/10.1038/ngeo1295

Deville, E., Mascle, A., Callec, Y., Huyghe, P., Lallemant, S., Lerat, O., Mathieu, X., Padron de Carillo, C., Patriat, M., Pichot, T., Loubrieux, B., Granjeon, D., 2015. Tectonics and sedimentation interactions in the east Caribbean subduction zone: An overview from the Orinoco delta and the Barbados accretionary prism. Mar. Pet. Geol. 64, 76–103. https://doi.org/10.1016/j.marpetgeo.2014.12.015

Dobson, D.P., Brodholt, J.P., 2005. Subducted banded iron formations as a source of ultralow-velocity zones at the core-mantle boundary. Nature 434, 371–374. https://doi.org/10.1038/nature03430

Dougherty, S.L., Clayton, R.W., 2014. Seismicity and structure in central Mexico : Evidence for a possible slab tear in the South Cocos plate. J. Geophys. Res. Solid Earth 119, 3424–3447. https://doi.org/10.1002/2013JB010883.1.

Drake, R.E., 1976. Chronology of cenozoic igneous and tectonic events in the central Chilean Andes - latitudes 35° 30′ to 36°S. J. Volcanol. Geotherm. Res. 1, 265–284. https://doi.org/10.1016/0377-0273(76)90011-1

Dutta, U., Baruah, A., Mandal, N., 2016. Role of source-layer tilts in the axi-asymmetric growth of diapirs triggered by a Rayleigh-Taylor instability. Geophys. J. Int. 206, 1814–1830. https://doi.org/10.1093/gji/ggw244

El Jaouahiry, A., Aniss, S., 2020. Linear stability analysis of a liquid film down on an inclined plane under oscillation with normal and lateral components in the presence and absence of surfactant. Phys. Fluids 32. https://doi.org/10.1063/1.5138982

England, P.C., Katz, R.F., 2010. Melting above the anhydrous solidus controls the location of volcanic arcs. Nature 467, 700–703. https://doi.org/10.1038/nature09417

Escher, B.G., Kuenen, P.H., 1929. Experiments in connection with salt domes. Leidsche Geol. Meded. 151–182.

Evans, M.A., Fischer, M.P., 2012. On the distribution of fluids in folds: A review of controlling factors and processes. J. Struct. Geol. 44, 2–24. https://doi.org/10.1016/j.jsg.2012.08.003

Farnetani, C.G., 1997. Excess temperature of mantle plumes: The role of chemical stratification across D″. Geophys. Res. Lett. 24, 1583–1586. https://doi.org/10.1029/97GL01548

Farnetani, C.G., Richards, M.A., 1994. Numerical investigations of the mantle plume initiation model for flood basalt events. J. Geophys. Res. 99. https://doi.org/10.1029/94jb00649

Fedotov, S.A., 1975. Mechanism of magma ascent and deep feeding channels of island arc volcanoes. Bull. Volcanol. 39, 241–254. https://doi.org/10.1007/BF02597830

Fermigier, M., Limat, L., Wesfreid, J.E., Boudinet, P., Quilliet, C., 1992. Two-dimensional patterns in rayleigh-taylor instability of a thin layer. J. Fluid Mech. 236, 349–383. https://doi.org/10.1017/S0022112092001447

Fernandez, N., Kaus, B.J.P., 2015. Pattern formation in 3-D numerical models of down-built diapirs initiated by a Rayleigh–Taylor instability. Geophys. J. Int. 202, 1253–1270. https://doi.org/10.1093/gji/ggv219

Ferrari, A., Lunati, I., 2013. Direct numerical simulations of interface dynamics to link capillary pressure and total surface energy. Adv. Water Resour. 57, 19–31. https://doi.org/10.1016/j.advwatres.2013.03.005

Flück, P., Hyndman, R.D., Lowe, C., 2003. Effective elastic thickness Te of the lithosphere in western Canada. J. Geophys. Res. Solid Earth 108. https://doi.org/10.1029/2002JB002201

Fontaine, F.R., Barruol, G., Tkalčić, H., Wölbern, I., Rümpker, G., Bodin, T., Haugmard, M., 2015. Crustal and uppermost mantle structure variation beneath La Réunion hotspot track. Geophys. J. Int. 203, 107–126. https://doi.org/10.1093/gji/ggv279

Ford, H.A., Long, M.D., 2015. A regional test of global models for flow, rheology, and seismic anisotropy at the base of the mantle. Phys. Earth Planet. Inter. 245, 71–75. https://doi.org/10.1016/j.pepi.2015.05.004

French, S.W., Romanowicz, B., 2015. Broad plumes rooted at the base of the Earth's mantle beneath major hotspots. Nature 525, 95–99. https://doi.org/10.1038/nature14876

Frenken, J.W.M., Van Der Veen, J.F., 1985. Observation of surface melting. Phys. Rev. Lett. 54, 134–137. https://doi.org/10.1103/PhysRevLett.54.134

Fumagalli, P., Poli, S., 2005. Experimentally determined phase relations in hydrous peridotites to 6.5 GPa and their consequences on the dynamics of subduction zones. J. Petrol. 46, 555–578. https://doi.org/10.1093/petrology/egh088

Gadalla, M., Ghommem, M., Bourantas, G., Miller, K., 2019. Modeling and thermal analysis of a moving spacecraft subject to solar radiation effect. Processes 7, 1–15. https://doi.org/10.3390/pr7110807

Gailler, A., Charvis, P., Flueh, E.R., 2007. Segmentation of the Nazca and South American plates along the Ecuador subduction zone from wide angle seismic profiles. Earth Planet. Sci. Lett. 260, 444–464. https://doi.org/10.1016/j.epsl.2007.05.045

Gallaire, F., Brun, P., 2017. Fluid dynamic instabilities: theory and application to pattern forming in complex media. Philos. Trans. R. Soc. A Math. Phys. Eng. Sci. 375. https://doi.org/10.1098/rsta.2016.0155

Ganerød, M., Torsvik, T.H., van Hinsbergen, D.J.J., Gaina, C., Corfu, F., Werner, S., Owen-Smith, T.M., Ashwal, L.D., Webb, S.J., Hendriks, B.W.H., 2011. Palaeoposition of the seychelles microcontinent in relation to the deccan traps and the plume generation zone in late cretaceous-early palaeogene time. Geol. Soc. Spec. Publ. 357, 229–252. https://doi.org/10.1144/SP357.12

Garnero, E.J., McNamara, A.K., Shim, S.H., 2016. Continent-sized anomalous zones with low seismic velocity at the base of Earth's mantle. Nat. Geosci. 9, 481–489. https://doi.org/10.1038/ngeo2733

Gerya, T., Connolly, J.A.D., Yuen, D.A., Gorczyk, W., Capel, A.M., 2006. Seismic implications of mantle wedge plumes. Phys. Earth Planet. Inter. 156, 59–74. https://doi.org/10.1016/j.pepi.2006.02.005

Gerya, T., Yuen, D.A., 2003a. Rayleigh - Taylor instabilities from hydration and melting propel "cold plumes" at subduction zones. Earth Planet. Sci. Lett. 212, 47–62. https://doi.org/10.1016/S0012-821X(03)00265-6

Gerya, T., Yuen, D.A., Sevre, E.O.D., 2004. Dynamical causes for incipient magma chambers above slabs. Geology 321, 89–92. https://doi.org/10.1130/G20018.1

Ghosh, D., Maiti, G., Mandal, N., Baruah, A., 2020. Cold Plumes Initiated by Rayleigh-Taylor Instabilities in Subduction Zones, and Their Characteristic Volcanic Distributions: The Role of Slab Dip. J. Geophys. Res. Solid Earth 125, 1–23. https://doi.org/10.1029/2020JB019814

Glišović, P., Forte, A.M., 2017. On the deep-mantle origin of the Deccan Traps. Science (80-.). 355, 613–616. https://doi.org/10.1126/science.aah4390

Griffiths, R.W., Campell, I.H., 1990. Stirring and struture in mantle starting plumes. Earth Planet. Sci. Lett. 99, 66–78.

Griggs, D., 1939. A Theory of Mountain Building. Am. J. Sci. https://doi.org/10.1111/j.1365-246X.1961.tb00435.x

Grove, T., Chatterjee, N., Parman, S.W., Médard, E., 2006. The influence of H2O on mantle wedge melting. Earth Planet. Sci. Lett. 249, 74–89. https://doi.org/10.1016/j.epsl.2006.06.043

Grove, T., Till, C.B., 2019. H2O-rich mantle melting near the slab–wedge interface. Contrib. to Mineral. Petrol. 174, 1–22. https://doi.org/10.1007/s00410-019-1615-1

Grove, T., Till, C.B., Krawczynski, M.J., 2012. The Role of H2O in Subduction Zone Magmatism. Annu. Rev. Earth Planet. Sci. 40, 413–439. https://doi.org/10.1146/annurev-earth-042711-105310

Grove, T., Till, C.B., Lev, E., Chatterjee, N., Médard, E., 2009. Kinematic variables and water transport control the formation and location of arc volcanoes. Nature 459, 694–697. https://doi.org/10.1038/nature08044

Gudmundsson, A., 1986. Possible effects of aspect ratios of magma chambers on eruption frequency. Geology 14, 991–994.

Hall, J., 1815. II. On the Vertical Position and Convolutions of certain Strata, and their relation with Granite. Trans. R. Soc. Edinburgh 7, 79–108. https://doi.org/10.1017/S0080456800019268

Hall, Kincaid, C., 2001. Diapiric flow at subduction zones: A recipe for rapid transport. Science (80-.). 292, 2472–2475. https://doi.org/10.1126/science.1060488

Hall, Spakman, W., 2015. Mantle structure and tectonic history of SE Asia. Tectonophysics 658, 14–45. https://doi.org/10.1016/j.tecto.2015.07.003

Hansen, U., Yuen, D.A., 1996. Potential role played by viscous heating in thermal-chemical convection in the outer core. Geochim. Cosmochim. Acta 60, 1113–1123. https://doi.org/10.1016/0016-7037(96)00025-7

Hansen, U., Yuen, D.A., 1995. Formation of layered structures in double-diffusive convection as applied to the geosciences. Geophys. Monogr. Ser. 94, 135–149. https://doi.org/10.1029/GM094p0135

Hasenclever, J., Morgan, J.P., Hort, M., Rüpke, L.H., 2011. 2D and 3D numerical models on compositionally buoyant diapirs in the mantle wedge. Earth Planet. Sci. Lett. 311, 53–68. https://doi.org/10.1016/j.epsl.2011.08.043

Hassan, R., Müller, R.D., Gurnis, M., Williams, S.E., Flament, N., 2016. A rapid burst in hotspot motion through the interaction of tectonics and deep mantle flow. Nature 533, 239–242. https://doi.org/10.1038/nature17422

Hassan, R., Williams, S.E., Gurnis, M., Müller, D., 2020. East African topography and volcanism explained by a single, migrating plume. Geosci. Front. 11, 1669–1680. https://doi.org/10.1016/j.gsf.2020.01.003

He, L., 2014. Numerical modeling of convective erosion and peridotite-melt interaction in big mantle wedge: Implications for the destruction of the North China Craton. J. Geophys. Res. Solid Earth 120, 1195–1209. https://doi.org/10.1002/2014JB011376.Received

Heister, T., Dannberg, J., Gassmöller, R., Bangerth, W., 2017. High accuracy mantle convection simulation through modern numerical methods - II: Realistic models and problems. Geophys. J. Int. 210, 833–851. https://doi.org/10.1093/gji/ggx195

Herzberg, C., Gazel, E., 2009. Petrological evidence for secular cooling in mantle plumes. Nature 458, 619–622. https://doi.org/10.1038/nature07857

Heyn, B.H., Conrad, C.P., Trønnes, R.G., 2020a. Core-mantle boundary topography and its relation to the viscosity structure of the lowermost mantle. Earth Planet. Sci. Lett. 543. https://doi.org/10.1016/j.epsl.2020.116358

Heyn, B.H., Conrad, C.P., Trønnes, R.G., 2020b. How Thermochemical Piles Can (Periodically) Generate Plumes at Their Edges. J. Geophys. Res. Solid Earth 125. https://doi.org/10.1029/2019JB018726

Hirose, K., Takafuji, N., Sata, N., Ohishi, Y., 2005. Phase transition and density of subducted MORB crust in the lower mantle. Earth Planet. Sci. Lett. 237, 239–251. https://doi.org/10.1016/j.epsl.2005.06.035

Hofmann, A.W., 2007. Sampling Mantle Heterogeneity through Oceanic Basalts: Isotopes and Trace Elements, Treatise on Geochemistry. https://doi.org/10.1016/B0-08-043751-6/02123-X

Horiuchi, S.S., Iwamori, H., 2016. A consistent model for fluid distribution, viscosity distribution, and flow-thermal structure in subduction zone. J. Geophys. Res. Solid Earth 121, 3238–3260. https://doi.org/10.1002/2015JB012384

Houseman, G.A., Molnar, P., 1997. Gravitational (Rayleigh-Taylor) instability of a layer with non-linear viscosity and convective thinning of continental lithosphere. Geophys. J. Int. 128, 125–150. https://doi.org/10.1111/j.1365-246X.1997.tb04075.x

Hu, Q., Kim, D.Y., Yang, W., Yang, L., Meng, Y., Zhang, L., Mao, H.K., 2016. FeO2 and FeOOH under deep lower-mantle conditions and Earth's oxygen-hydrogen cycles. Nature 534, 241–244. https://doi.org/10.1038/nature18018

Huang, H., Lin, F., Schmandt, B., Farrell, J., Smith, R.B., Tsai, V.C., 2015. The Yellowstone magmatic system from the mantle plume to the upper crust. Science (80-.). 348, 773–776.

Hubbert, M., 1951. Mechanical basis for certain familiar geologic structures. Bull. Geol. Soc. Am. 62, 355–372. https://doi.org/10.1130/0016-7606(1951)62[355:MBFCFG]2.0.CO;2

Hubbert, M., 1937. Theory of scale models as applied to the study of geologic structures. Bull. Geol. Soc. Am. 48, 1459–1520. https://doi.org/10.1130/GSAB-48-1459

Huerre, P., Monkewitz, P.A., 1990. Local and Global Instabilities in Spatially Developing Flows. Annu. Rev. Fluid Mech. 22, 473–537. https://doi.org/10.1146/annurev.fl.22.010190.002353

Ishii, M., Tromp, J., 2004. Constraining large-scale mantle heterogeneity using mantle and inner-core sensitive normal modes. Phys. Earth Planet. Inter. 146, 113–124. https://doi.org/10.1016/j.pepi.2003.06.012

Ito, E., Stern, R.J., 1986. Oxygen- and strontium-isotopic investigations of subduction zone volcanism: the case of the Volcano Arc and the Marianas Island Arc. Earth Planet. Sci. Lett. 76, 312–320. https://doi.org/10.1016/0012-821X(86)90082-8

Iwamori, H., 1998. Transportation of H2O and melting in subduction zones. Earth Planet. Sci. Lett. 160, 65–80. https://doi.org/10.1016/S0012-821X(98)00080-6

Jacobs, J. W., Catton, I., 1988. Three-dimensional rayleigh-taylor instability part 1. weakly nonlinear theory. J. Fluid Mech. 187, 329–352. https://doi.org/10.1017/S002211208800045X

Jacobs, J W, Catton, I., 1988. Three-dimensional Rayleigh-Taylor instability Part 2. Experiment. J. Fluid Mech. 187, 353–371.

Jacoby, W.R., 1976. Paraffin model experiment of plate tectonics. Tectonophysics 35, 103–113. https://doi.org/10.1016/0040-1951(76)90031-7

Jones, T.D., Davies, D.R., Campbell, I.H., Wilson, C.R., Kramer, S.C., 2016. Do mantle plumes preserve the heterogeneous structure of their deep-mantle source? Earth Planet. Sci. Lett. 434, 10–17. https://doi.org/10.1016/j.epsl.2015.11.016

Kale, V.S., Bodas, M., Chatterjee, P., Pande, K., 2020. Emplacement history and evolution of the Deccan Volcanic Province, India. Episodes 43, 278–299. https://doi.org/10.18814/EPIIUGS/2020/020016

Katia, R., Berzak, L., Boyle, D., Gray, T., Granstedt, E., 2010. Experiments with Liquid Metal Walls: Status of the Lithium Tokamak Experiment. Fusion Eng. Des.

Kay, S.M., Coira, B.L., 2009. Shallowing and steepening subduction zones, continental lithospheric lithospheric loss, magmatism, and crustal flow under the central Andean Altiplano-Puna Plateau. Geol. Soc. Am. Mem. 204, 1–32. https://doi.org/10.1130/2009.1204(11).

Kay, S.M., Mpodozis, C., Ramos, V.A., Munizaga, F., 1991. Magma source variations for mid-late Tertiary magmatic rocks associated with a shallowing subduction zone and a thickening crust in the central Andes (28 to 33 S). Geol. Soc. Am. Spec. Pap. 265, 113–137.

Keller, G., Adatte, T., Bhowmick, P.K., Upadhyay, H., Dave, A., Reddy, A.N., Jaiprakash, B.C., 2012. Nature and timing of extinctions in Cretaceous-Tertiary planktic foraminifera preserved in Deccan intertrappean sediments of the Krishna-Godavari Basin, India. Earth Planet. Sci. Lett. 341–344, 211–221. https://doi.org/10.1016/j.epsl.2012.06.021

Kelly, A., Bercovici, D., 1997. The clustering of rising diapirs and plume heads. Geophys. Res. Lett. 24, 201–204. https://doi.org/10.1029/96GL03904

Kimura, J.-I., Nagahashi, Y., Satoguchi, Y., Chang, Q., 2015. Origins of felsic magmas in Japanese subduction zone: Geochemical characterizations of tephra from caldera-forming eruptions <5Ma. Geochemistry Geophys. Geosystems 16, 267–300. https://doi.org/10.1002/2014GC005684.Key

Koelemeijer, P., Deuss, A., Ritsema, J., 2017. Density structure of Earth's lowermost mantle from Stoneley mode splitting observations. Nat. Commun. 8, 1–10. https://doi.org/10.1038/ncomms15241

Kohlstedt, D.L., Holtzman, B.K., 2009. Shearing melt out of the earth: An experimentalist's perspective on the influence of deformation on melt extraction. Annu. Rev. Earth Planet. Sci. 37, 561–593. https://doi.org/10.1146/annurev.earth.031208.100104

Koppers, A.A.P., Becker, T.W., Jackson, M.G., Konrad, K., Müller, R.D., Romanowicz, B., Steinberger, B., Whittaker, J.M., 2021. Mantle plumes and their role in Earth processes. Nat. Rev. Earth Environ. 2, 382–401. https://doi.org/10.1038/s43017-021-00168-6

Kuenen, P.H., 1936. The negative isostatic anomalies in the East Indies (with Experiments). Leidse Geol. Meded. 8, 169–214.

Kuenen, P.H., Sitter, L.U. DE, 1938. Experimental investigation of into the mechanism folding. Leidse Geol. Meded. 217–239.

Kutterolf, S., Jegen, M., Mitrovica, J.X., Kwasnitschka, T., Freundt, A., Huybers, P.J., 2013. A detection of Milankovitch frequencies in global volcanic activity. Geology 41, 227–230. https://doi.org/10.1130/G33419.1

Labrosse, S., Hernlund, J.W., Coltice, N., 2007. A crystallizing dense magma ocean at the base of the Earth's mantle. Nature 450, 866–869. https://doi.org/10.1038/nature06355

Lallemand, S., Heuret, A., Boutelier, D., 2005. On the relationships between slab dip, back-arc stress, upper plate absolute motion, and crustal nature in subduction zones. Geochemistry, Geophys. Geosystems 6. https://doi.org/10.1029/2005GC000917

Lapuerta, V., Mancebo, F.J., Vega, J.M., 2001. Control of Rayleigh-Taylor instability by vertical vibration in large aspect ratio containers. Phys. Rev. E - Stat. Physics, Plasmas, Fluids, Relat. Interdiscip. Top. 64, 17. https://doi.org/10.1103/PhysRevE.64.016318

Lassak, T.M., McNamara, A.K., Garnero, E.J., Zhong, S., 2010. Core-mantle boundary topography as a possible constraint on lower mantle chemistry and dynamics. Earth Planet. Sci. Lett. 289, 232–241. https://doi.org/10.1016/j.epsl.2009.11.012

Lay, T., Garnero, E.J., 2011. Deep mantle seismic modeling and imaging. Annu. Rev. Earth Planet. Sci. 39, 91–123. https://doi.org/10.1146/annurev-earth-040610-133354

Lee, C.T.A., Luffi, P., Höink, T., Li, J., Dasgupta, R., Hernlund, J., 2010. Upside-down differentiation and generation of a primordial lower mantle. Nature 463, 930–933. https://doi.org/10.1038/nature08824

Lerisson, G., Ledda, P.G., Balestra, G., Gallaire, F., 2020. Instability of a thin viscous film flowing under an inclined substrate: Steady patterns. J. Fluid Mech. 898. https://doi.org/10.1017/jfm.2020.396

Li, C., Van Der Hilst, R.D., Engdahl, E.R., Burdick, S., 2008. A new global model for P wave speed variations in Earth's mantle. Geochemistry, Geophys. Geosystems 9. https://doi.org/10.1029/2007GC001806

Li, M., McNamara, A.K., 2013. The difficulty for subducted oceanic crust to accumulate at the Earth's core-mantle boundary. J. Geophys. Res. Solid Earth 118, 1807–1816. https://doi.org/10.1002/jgrb.50156

Li, M., Zhong, S., Olson, P., 2018. Linking lowermost mantle structure, core-mantle boundary heat flux and mantle plume formation. Phys. Earth Planet. Inter. 277, 10–29. https://doi.org/10.1016/j.pepi.2018.01.010

Liang, Y., Schiemenz, A., Hesse, M.A., Parmentier, E.M., Hesthaven, J.S., 2010. High-porosity channels for melt migration in the mantle: Top is the dunite and bottom is the harzburgite and lherzolite. Geophys. Res. Lett. 37, 1–5. https://doi.org/10.1029/2010GL044162

Lin, S.C., Van Keken, P.E., 2006. Dynamics of thermochemical plumes: 1. Plume formation and entrainment of a dense layer. Geochemistry, Geophys. Geosystems 7. https://doi.org/10.1029/2005GC001071

Lin, T.S., Kondic, L., 2010. Thin films flowing down inverted substrates: Two dimensional flow. Phys. Fluids 22, 1–10. https://doi.org/10.1063/1.3428753

Lin, T.S., Kondic, L., Filippov, A., 2012. Thin films flowing down inverted substrates:

Three-dimensional flow. Phys. Fluids 24. https://doi.org/10.1063/1.3682001

Lingenfelter, R.E., Schubert, G., 1974. Hot spot and trench volcano separations. Nature 249, 820.

Link, T.A., 1930. Experiments Relating to Salt-Dome Structures. Am. Assoc. Pet. Geol. Bull. 14, 483–508. https://doi.org/10.1306/3d9328c6-16b1-11d7-8645000102c1865d

Lister, J.R., Kerr, R.C., Russell, N.J., Crosby, A., 2011. Rayleigh-Taylor instability of an inclined buoyant viscous cylinder. J. Fluid Mech. 671, 313–338. https://doi.org/10.1017/S0022112010005689

Maiwa, K., Nakamura, H., Kimura, H., Miyazaki, A., 2003. In situ observation of the crystallization via incongruent melting and peritectic reaction in Sr(NO3)-H2O system. J. Cryst. Growth 255, 379–385. https://doi.org/10.1016/S0022-0248(03)01306-X

Mancktelow, N.S., 1999. Finite-element modelling of single-layer folding in elasto-viscous materials: The effect of initial perturbation geometry. J. Struct. Geol. 21, 161–177. https://doi.org/10.1016/S0191-8141(98)00102-3

Mandal, N., Sarkar, S., Baruah, A., Dutta, U., 2018. Production, pathways and budgets of melts in mid-ocean ridges: An enthalpy based thermo-mechanical model. Phys. Earth Planet. Inter. 277, 55–69. https://doi.org/10.1016/j.pepi.2018.01.008

Manea, V.C., Manea, M., Ferrari, L., 2013. A geodynamical perspective on the subduction of Cocos and Rivera plates beneath Mexico and Central America. Tectonophysics 609, 56–81. https://doi.org/10.1016/j.tecto.2012.12.039

Mao, W.L., Mao, H., Sturhahn, W., Zhao, J., Prakapenka, V.B., Meng, Y., Shu, J., Fei, Y., Hemley, R.J., 2006. Origin of Ultralow-Velocity Zones 312, 564–566.

Marques, F.O., Mandal, N., 2016. Post-buckling relaxation of an elastic layer and its geological relevance: Insights from analogue experiments in pure shear. Tectonophysics 668–669, 82–91. https://doi.org/10.1016/j.tecto.2015.12.004

Marschall, H.R., Schumacher, J.C., 2012. Arc magmas sourced from mélange diapirs in subduction zones. Nat. Geosci. 5, 862–867. https://doi.org/10.1038/ngeo1634

Marsh, 1979. Island arc development: some observations, experiments, and speculations. J. Geol. 87, 687–713.

Marsh, 1975. Plume spacing and source. Nature 256, 240.

Marsh, Carmichael, I., 1974. Benioff zone magmatism. J. Geophys. Res. 79.

Martinod, J., Husson, L., Roperch, P., Guillaume, B., Espurt, N., 2010. Horizontal subduction zones, convergence velocity and the building of the Andes. Earth Planet.

Sci. Lett. 299, 299–309. https://doi.org/10.1016/j.epsl.2010.09.010

Matyska, C., Moser, J., Yuen, D.A., 1994. The potential influence of radiative heat transfer on the formation of megaplumes in the lower mantle. Earth Planet. Sci. Lett. 125, 255–266. https://doi.org/10.1016/0012-821X(94)90219-4

Mead, W., 1920. Notes on the Mechanics of Geologic Structures. J. Geol. 28, 505–523.

Miller, N.C., Behn, M.D., 2012. Timescales for the growth of sediment diapirs in subduction zones. Geophys. J. Int. 190, 1361–1377. https://doi.org/10.1111/j.1365-246X.2012.05565.x

Mitchell, S.L., Vynnycky, M., 2012. An accurate finite-difference method for ablation-type Stefan problems. J. Comput. Appl. Math. 236, 4181–4192. https://doi.org/10.1016/j.cam.2012.05.011

Mjelde, R., Wessel, P., Müller, R.D., 2010. Global pulsations of intraplate magmatism through the Cenozoic. Lithosphere 2, 361–376. https://doi.org/10.1130/L107.1

Morgan, W.J., 1972. Deep Mantle Convection Plumes and Plate Motions. Am. Assoc. Pet. Geol. Bull. https://doi.org/10.1306/819A3E50-16C5-11D7-8645000102C1865D

Morgan, W.J., 1971. Convection plumes in the lower mantle. Nature 230, 42–43. https://doi.org/10.1038/230042a0

Morishige, 2015. A new regime of slab-mantle coupling at the plate interface and its possible implications for the distribution of volcanoes. Earth Planet. Sci. Lett. 427, 262–271. https://doi.org/10.1016/j.epsl.2015.07.011

Morrow, T.A., Mittelstaedt, E.L., 2021. Quantifying Periodic Variations in Hotspot Melt Production. J. Geophys. Res. Solid Earth 126. https://doi.org/10.1029/2021JB021726

Moulik, P., Ekström, G., 2016. The relationships between large-scale variations in shear velocity, density, and compressional velocity in the Earth's mantle. J. Geophys. Res. Solid Earth 121, 2737–2771. https://doi.org/10.1002/2015JB012679

Müller, R.D., Seton, M., Zahirovic, S., Williams, S.E., Matthews, K.J., Wright, N.M., Shephard, G.E., Maloney, K.T., Barnett-Moore, N., Hosseinpour, M., Bower, D.J., Cannon, J., 2016. Ocean Basin Evolution and Global-Scale Plate Reorganization Events since Pangea Breakup. Annu. Rev. Earth Planet. Sci. 44, 107–138. https://doi.org/10.1146/annurev-earth-060115-012211

Mulyukova, E., Steinberger, B., Dabrowski, M., Sobolev, S. V., 2015. Survival of LLSVPs for billions of years in a vigorously convecting mantle: Replenishment and destruction of chemical anomaly. J. Geophys. Res. Solid Earth 120, 3824–3847. https://doi.org/10.1002/2014JB011688

Naganjaneyulu, K., Santosh, M., 2012. The nature and thickness of lithosphere beneath the Archean Dharwar Craton, southern India: A magnetotelluric model. J. Asian Earth Sci. 49, 349–361. https://doi.org/10.1016/j.jseaes.2011.07.002

Nayfeh, A.H., 1969. On the non-linear Lamb-Taylor instability. J. Fluid Mech. 38, 619–631.

Ni, S., Helmberger, D. V., 2003. Seismological constraints on the South African superplume: Could be the oldest distinct structure on earth. Earth Planet. Sci. Lett. 206, 119–131. https://doi.org/10.1016/S0012-821X(02)01072-5

Niu, Y., 2018. Origin of the LLSVPs at the base of the mantle is a consequence of plate tectonics – A petrological and geochemical perspective. Geosci. Front. 9, 1265–1278. https://doi.org/10.1016/j.gsf.2018.03.005

Olson, P., Singer, H., 1985. Creeping plumes. J. Fluid Mech. 158, 511–531. https://doi.org/10.1017/S0022112085002749

Olson, P., Weeraratne, D., 2008. Experiments on metal-silicate plumes and core formation. Philos. Trans. R. Soc. A Math. Phys. Eng. Sci. 366, 4253–4271. https://doi.org/10.1098/rsta.2008.0194

Olsson, E., Kreiss, G., 2005. A conservative level set method for two phase flow. J. Comput. Phys. 210, 225–246. https://doi.org/10.1016/j.jcp.2005.04.007

Oron, A., Rosenau, P., 1989. Nonlinear evolution and breaking of interfacial Rayleigh-Taylor waves. Phys. Fluids A 1, 1155–1165. https://doi.org/10.1063/1.857340

Osher, S., Sethian, J.A., 1988. Fronts propagating with curvature-dependent speed: Algorithms based on Hamilton-Jacobi formulations. J. Comput. Phys. 79, 12–49. https://doi.org/10.1016/0021-9991(88)90002-2

Pacey, A., Macpherson, C.G., McCaffrey, K.J., 2013. Linear volcanic segments in the central Sunda Arc, Indonesia, identified using Hough transform analysis: implications for arc lithosphere control upon volcano distribution. Earth Planet. Sci. Lett. 369, 24–33. https://doi.org/10.1063/1.2756072

Panda, D., Senapati, B., Tyagi, B., Kundu, B., 2019. Effects of Rayleigh-Taylor instability and ionospheric plasma bubbles on the global navigation satellite System signal. J. Asian Earth Sci. 170, 225–233. https://doi.org/10.1016/j.jseaes.2018.11.006

Parker, T., McDowel, A., 1955. Model studies of salt-dome tectonics. Am. Assoc. Pet. Geol. Bull. 39. https://doi.org/10.1306/5CEAE2DD-16BB-11D7-8645000102C1865D

Pec, M., Holtzman, B.K., Zimmerman, M.E., Kohlstedt, D.L., 2017. Reaction infiltration

instabilities in mantle rocks: An experimental investigation. J. Petrol. 58, 979–1003. https://doi.org/10.1093/petrology/egx043

Perrin, A., Goes, S., Prytulak, J., Rondenay, S., Davies, D.R., 2018a. Mantle wedge temperatures and their potential relation to volcanic arc location. Earth Planet. Sci. Lett. 501, 67–77. https://doi.org/10.1016/j.epsl.2018.08.011

Perrin, A., Goes, S., Prytulak, J., Rondenay, S., Davies, D.R., 2018b. Mantle wedge temperatures and their potential relation to volcanic arc location. Earth Planet. Sci. Lett. 501, 67–77. https://doi.org/10.1016/j.epsl.2018.08.011

Peters, B.J., Day, J.M.D., 2017. A geochemical link between plume head and tail volcanism. Geochemical Perspect. Lett. 5, 29–34. https://doi.org/10.7185/geochemlet.1742

Petersen, S. V., Dutton, A., Lohmann, K.C., 2016. End-Cretaceous extinction in Antarctica linked to both Deccan volcanism and meteorite impact via climate change. Nat. Commun. 7, 1–9. https://doi.org/10.1038/ncomms12079

Poli, S., Schmidt, M.W., 2002. Petrology of Subducted Slabs. Annu. Rev. Earth Planet. Sci. 30, 207–235. https://doi.org/10.1146/annurev.earth.30.091201.140550

Pozrikidis, C., 2004. Instability of Multi-Layer Channel and Film Flows. Adv. Appl. Mech. 40, 179–239. https://doi.org/10.1016/s0065-2156(04)40002-7

Prueher, L.M., Rea, D.K., 2001. Tephrochronology of the Kamchatka-Kurile and Aleutian arcs: Evidence for volcanic episodity. J. Volcanol. Geotherm. Res. 106, 67–84. https://doi.org/10.1016/S0377-0273(00)00266-3

Putirka, K., 2008. Excess temperatures at ocean islands: Implications for mantle layering and convection. Geology 36, 283–286. https://doi.org/10.1130/G24615A.1

Rajappa, N.R., 1970. Non-linear theory of Taylor instability of superposed fluids. J. Phys. Soc. Japan 28.

Ramberg, H., 1981. The role of gravity in orogenic belts. Geol. Soc. London, Spec. Publ. 9, 125–140. https://doi.org/10.1144/GSL.SP.1981.009.01.11

Ramberg, H., 1972. Theoretical models of density stratification and diapirisn in the earth. J. Geophys. Res. 77, 877–889.

Ramberg, H., 1968. Fluid dynamics of layered systems in the field of gravity, a theoretical basis for certain global structures and isostatic adjustment. Phys. Earth Planet. Inter. 1, 63–87.

Ramberg, H., 1955. Natural and Experimental Boudinage and Pinch-and-Swell Structures. J. Geol. 63, 512–526.

Ramos, V.A., Cristallini, E.O., Perez, D.J., 2002. The Pampean flat-slab of the Central Andes. J. South Am. Earth Sci. 15, 6–8.

Ramos, V.A., Folguera, A., 2009. Andean flat-slab subduction through time. Geol. Soc. London, Spec. Publ. 327, 31–54. https://doi.org/10.1144/SP327.3

Rayleigh, 1882. Investigation of the character of the equilibrium of an incompressible heavy fluid of variable density. Proc. London Math. Soc. s1-14, 170–177. https://doi.org/10.1112/plms/s1-14.1.170

Renne, P.R., Sprain, C.J., Richards, M.A., Self, S., Vanderkluysen, L., Pande, K., 2015. State shift in Deccan volcanism at the Cretaceous-Paleogene boundary, possibly induced by impact. Science (80-.). 350, 76–78.

Ribe, N.M., 1998. Spouting and planform selection in the Rayleigh-Taylor instability of miscible viscous fluids. J. Fluid Mech. 377, 27–45. https://doi.org/10.1017/S0022112098002912

Ribe, N.M., Davaille, A., 2013. Dynamical similarity and density (non-) proportionality in experimental tectonics. Tectonophysics 608, 1371–1379. https://doi.org/10.1016/j.tecto.2013.06.005

Richards, M.A., Alvarez, W., Self, S., Karlstrom, L., Renne, P.R., Manga, M., Sprain, C.J., Smit, J., Vanderkluysen, L., Gibson, S.A., 2015. Triggering of the largest Deccan eruptions by the Chicxulub impact. Bull. Geol. Soc. Am. 127, 1507–1520. https://doi.org/10.1130/B31167.1

Richards, M.A., Duncan, R.A., Courtillot, V.E., 1989. Flood basalts and hot-spot tracks: Plume heads and tails. Science (80-.). 246, 103–107. https://doi.org/10.1126/science.246.4926.103

Richter, F., 1978. Mantle convection Model. Annu. Rev. Earth Planet. Sci. 6, 9–19.

Riley, G.N., Kohlstedt, D.L., 1991. Kinetics of melt migration in upper mantle-type rocks. Earth Planet. Sci. Lett. 105, 500–521. https://doi.org/10.1016/0012-821X(91)90188-N

Riller, U., Scheuber, E., Hongn, F.D., 2006. The Time-Space Distribution of Cenozoic Volcanism in the South-Central Andes: a New Data Compilation and Some Tectonic Implications. https://doi.org/10.1007/978-3-540-48684-8_2

Ritsema, J., Deuss, A., Van Heijst, H.J., Woodhouse, J.H., 2011. S40RTS: A degree-40 shear-velocity model for the mantle from new Rayleigh wave dispersion, teleseismic traveltime and normal-mode splitting function measurements. Geophys. J. Int. 184, 1223–1236. https://doi.org/10.1111/j.1365-246X.2010.04884.x

Ritsema, J., van Heijst, H.J., 2002. Constraints on the correlation of P- and S-wave velocity heterogeneity in the mantle from P, PP, PPP and PKPab traveltimes. Geophys. J. Int. 149, 482–489. https://doi.org/10.1046/j.1365-246X.2002.01631.x

Rohlfs, W., Pischke, P., Scheid, B., 2017. Hydrodynamic waves in films flowing under an inclined plane. Phys. Rev. Fluids 2, 1–23. https://doi.org/10.1103/PhysRevFluids.2.044003

Rost, S., Garnero, E.J., Wiliams, Q., 2006. Fine-scale ultralow-velocity zone structure from high-frequency seismic array data. J. Geophys. Res. Solid Earth 111, 1–14. https://doi.org/10.1029/2005JB004088

Ryu, I.C., Lee, C., 2017. Intracontinental mantle plume and its implications for the Cretaceous tectonic history of East Asia. Earth Planet. Sci. Lett. 479, 206–218. https://doi.org/10.1016/j.epsl.2017.09.032

Scheid, B., Kofman, N., Rohlfs, W., 2016. Critical inclination for absolute / convective instability transition in inverted falling films. Phys. fluids 044107, 1–15. https://doi.org/10.1063/1.4946827

Schindlbeck, J.C., Jegen, M., Freundt, A., Kutterolf, S., Straub, S.M., Mleneck-Vautravers, M.J., McManus, J.F., 2018. 100- kyr cyclicity in volcanic ash emplacement: Evidence from a 1.1 Myr tephra record from the NW Pacific. Sci. Rep. 8, 1–9. https://doi.org/10.1038/s41598-018-22595-0

Schmalholz, S.M., Schmid, D.W., 2012. Folding in power-law viscous multi-layers. Philos. Trans. R. Soc. A Math. Phys. Eng. Sci. 370, 1796–1826. https://doi.org/10.1098/rsta.2011.0421

Schmidt, A., Skeffington, R.A., Thordarson, T., Self, S., Forster, P.M., Rap, A., Ridgwell, A., Fowler, D., Wilson, M., Mann, G.W., Wignall, P.B., Carslaw, K.S., 2016. Selective environmental stress from sulphur emitted by continental flood basalt eruptions. Nat. Geosci. 9, 77–82. https://doi.org/10.1038/ngeo2588

Schmidt, M.W., Poli, S., 1998. Experimentally based water budgets for dehydrating slabs and consequences for arc magma generation. Earth Planet. Sci. Lett. 163, 361–379. https://doi.org/10.1016/S0012-821X(98)00142-3

Schoene, B., Eddy, M.P., Samperton, K.M., Keller, C.B., Keller, G., Adatte, T., Khadri, S.F.R., 2019. U-Pb constraints on pulsed eruption of the Deccan Traps across the end-Cretaceous mass extinction. Science (80-.). 363, 862–866. https://doi.org/10.1126/science.aau2422

Schoene, B., Samperton, K.M., Eddy, M.P., Keller, G., Adatte, T., Bowring, S.A., Khadri,

S.F.R., Gertsch, B., 2015. U-Pb geochronology of the Deccan Traps and relation to the end-Cretaceous mass extinction. Science (80-.). 347, 182–184. https://doi.org/10.1126/science.aaa0118

Schulte, P., Alegret, L., Arenillas, I., Arz, J.A., Barton, P.J., Bown, P.R., Bralower, T.J., Christeson, G.L., Claeys, P., Cockell, C.S., Collins, G.S., Deutsch, A., Goldin, T.J., Goto, K., Grajales-Nishimura, J.M., Grieve, R.A.F., Gulick, S.P.S., Johnson, K.R., Kiessling, W., Koeberl, C., Kring, D.A., MacLeod, K.G., Matsui, T., Melosh, J., Montanari, A., Morgan, J. V., Neal, C.R., Nichols, D.J., Norris, R.D., Pierazzo, E., Ravizza, G., Rebolledo-Vieyra, M., Reimold, W.U., Robin, E., Salge, T., Speijer, R.P., Sweet, A.R., Urrutia-Fucugauchi, J., Vajda, V., Whalen, M.T., Willumsen, P.S., 2010. The chicxulub asteroid impact and mass extinction at the cretaceous-paleogene boundary. Science (80-.). 327, 1214–1218. https://doi.org/10.1126/science.1177265

Schutt, D.L., Dueker, K., Yuan, H., 2008. Crust and upper mantle velocity structure of the Yellowstone hot spot and surroundings. J. Geophys. Res. Solid Earth 113, 1–14. https://doi.org/10.1029/2007JB005109

Self, S., Schmidt, A., Mather, T.A., 2014. Emplacement characteristics, time scales, and volcanic gas release rates of continental flood basalt eruptions on Earth. Spec. Pap. Geol. Soc. Am. 505, 319–337. https://doi.org/10.1130/2014.2505(16)

Seton, M., Müller, R.D., Zahirovic, S., Gaina, C., Torsvik, T., Shephard, G., Talsma, A., Gurnis, M., Turner, M., Maus, S., Chandler, M., 2012. Global continental and ocean basin reconstructions since 200Ma. Earth-Science Rev. 113, 212–270. https://doi.org/10.1016/j.earscirev.2012.03.002

Shemenda, A.I., Grocholsky, A.L., 1994. Physical modeling of slow seafloor spreading the order The jumps normally occur in the wall of a rift valley resulting in. J. Geophys. Res. 99, 9137–9153.

Shore, J.D., Ronis, D., Piché, L., Grant, M., 1997. Theory of melt fracture instabilities in the capillary flow of polymer melts. Phys. Rev. E - Stat. Physics, Plasmas, Fluids, Relat. Interdiscip. Top. 55, 2976–2992. https://doi.org/10.1103/PhysRevE.55.2976

Sobolev, S. V., Sobolev, A. V., Kuzmin, D. V., Krivolutskaya, N.A., Petrunin, A.G., Arndt, N.T., Radko, V.A., Vasiliev, Y.R., 2011. Linking mantle plumes, large igneous provinces and environmental catastrophes. Nature 477, 312–316. https://doi.org/10.1038/nature10385

Spiegelman, M., Kelemen, P.B., Aharonov, E., 2001. Causes and consequences of flow organization during melt transport : The reaction infiltration instability in compactible

media. J. Geophys. Res. 106, 2061–2077.

Sprain, C.J., Renne, P.R., Clemens, W.A., Wilson, G.P., 2018. Calibration of chron C29r: New high-precision geochronologic and paleomagnetic constraints from the Hell Creek region, Montana. Bull. Geol. Soc. Am. 130, 1615–1644. https://doi.org/10.1130/B31890.1

Sprain, C.J., Renne, P.R., Vanderkluysen, L., Pande, K., Self, S., Mittal, T., 2019. The eruptive tempo of deccan volcanism in relation to the cretaceous-paleogene boundary. Science (80-.). 363, 866–870. https://doi.org/10.1126/science.aav1446

Sripada, S.S., Cohen, I.M., Ayyaswamy, P.S., 2003. Melting of a wire anode followed by solidification: A three-phase moving interface problem. J. Heat Transfer 125, 661–668. https://doi.org/10.1115/1.1576811

Stachnik, J.C., Dueker, K., Schutt, D.L., Yuan, H., 2008. Imaging Yellowstone plume-lithosphere interactions from inversion of ballistic and diffusive Rayleigh wave dispersion and crustal thickness data. Geochemistry, Geophys. Geosystems 9. https://doi.org/10.1029/2008GC001992

Sterman-Cohen, E., Bestehorn, M., Oron, A., 2017. Rayleigh-Taylor instability in thin liquid films subjected to harmonic vibration. Phys. Fluids 29. https://doi.org/10.1063/1.4984082

Stuart, J.T., 1964. On the cellular patterns in thermal convection. J. Fluid Mech. 18, 481–498. https://doi.org/10.1017/S0022112064000362

Stubailo, I., Beghein, C., Davis, P.M., 2012. Structure and anisotropy of the Mexico subduction zone based on Rayleigh-wave analysis and implications for the geometry of the Trans-Mexican Volcanic Belt. J. Geophys. Res. Solid Earth 117, 1–16. https://doi.org/10.1029/2011JB008631

Suetsugu, D., Isse, T., Tanaka, S., Obayashi, M., Shiobara, H., Sugioka, H., Kanazawa, T., Fukao, Y., Barruol, G., Reymond, D., 2009. South Pacific mantle plumes imaged by seismic observation on islands and seafloor. Geochemistry, Geophys. Geosystems 10. https://doi.org/10.1029/2009GC002533

Sun, Y., Lai, X., Wignall, P.B., Widdowson, M., Ali, J.R., Jiang, H., Wang, W., Yan, C., Bond, D.P.G., Védrine, S., 2010. Dating the onset and nature of the Middle Permian Emeishan large igneous province eruptions in SW China using conodont biostratigraphy and its bearing on mantle plume uplift models. Lithos 119, 20–33. https://doi.org/10.1016/j.lithos.2010.05.012

Syracuse, E.M., Abers, G.A., 2006. Global compilation of variations in slab depth beneath

arc volcanoes and implications. Geochemistry, Geophys. Geosystems 7. https://doi.org/10.1029/2005GC001045

Tackley, P.J., 2012. Dynamics and evolution of the deep mantle resulting from thermal, chemical, phase and melting effects. Earth-Science Rev. 110, 1–25. https://doi.org/10.1016/j.earscirev.2011.10.001

Tamura, Y., Tatsumi, Y., Zhao, D., Kido, Y., Shukuno, H., 2002. Hot fingers in the mantle wedge: New insights into magma genesis in subduction zones. Earth Planet. Sci. Lett. 197, 105–116. https://doi.org/10.1016/S0012-821X(02)00465-X

Tapponnier, P., Peltzer, G., Le Dain, A.Y., Armijo, R., Cobbold, P., 1982. Propagating extrusion tectonics in Asia: new insights from simple experiments with plasticine. Geology 10, 611–616. https://doi.org/10.1130/0091-7613(1982)10<611:PETIAN>2.0.CO;2

Tatsumi, Y., 1989. Migration of fluid phases and genesis of basalt magmas in subduction zones. J. Geophys. Res. 94, 4697–4707.

Taylor, G., 1950. The Instability of Liquid Surfaces when Accelerated in a Direction Perpendicular to their Planes. II. Proc. R. Soc. A Math. Phys. Eng. Sci. 202, 81–96. https://doi.org/10.1098/rspa.1950.0086

Thompson, P.F., Tackley, P.J., 1998. Generation of mega-plumes from the core-mantle boundary in a compressible mantle with temperature-dependent viscosity. Geophys. Res. Lett. 25, 1999–2002. https://doi.org/10.1029/98gl01228

Till, C.B., Grove, T., Withers, A.C., 2012. The beginnings of hydrous mantle wedge melting. Contrib. to Mineral. Petrol. 163, 669–688. https://doi.org/10.1007/s00410-011-0692-6

Tolstikhin, I., Hofmann, A.W., 2005. Early crust on top of the Earth's core. Phys. Earth Planet. Inter. 148, 109–130. https://doi.org/10.1016/j.pepi.2004.05.011

Tolstikhin, I.N., Kramers, J.D., Hofmann, A.W., 2006. A chemical Earth model with whole mantle convection: The importance of a core-mantle boundary layer (D″) and its early formation. Chem. Geol. 226, 79–99. https://doi.org/10.1016/j.chemgeo.2005.09.015

Trønnes, R.G., Baron, M.A., Eigenmann, K.R., Guren, M.G., Heyn, B.H., Løken, A., Mohn, C.E., 2019. Core formation, mantle differentiation and core-mantle interaction within Earth and the terrestrial planets. Tectonophysics 760, 165–198. https://doi.org/10.1016/j.tecto.2018.10.021

Tsekhmistrenko, M., Sigloch, K., Hosseini, K., Barruol, G., 2021. A tree of Indo-African mantle plumes imaged by seismic tomography. Nat. Geosci. 14, 612–619.

https://doi.org/10.1038/s41561-021-00762-9

Turcotte, D., Schubert, G., 2014. Geodynamics, 3rd edition. https://doi.org/10.1002/1521-3773(20010316)40:6<9823::AID-ANIE9823>3.3.CO;2-C

Ulmer, P., Trommsdorff, V., 1995. Serpentine stability to mantle depths and subduction-related magmatism. Science (80-.). 268, 858–861. https://doi.org/10.1126/science.268.5212.858

Umeda, K., Ban, M., Hayashi, S., Kusano, T., 2013. Tectonic shortening and coeval volcanism during the Quaternary, Northeast Japan arc. J. Earth Syst. Sci. 122, 137–147. https://doi.org/10.1007/s12040-012-0245-z

Van Ark, E., Lin, J., 2004. Time variation in igneous volume flux of the Hawaii-Emperor hot spot seamount chain. J. Geophys. Res. Solid Earth 109, 1–18. https://doi.org/10.1029/2003JB002949

van Keken, P.E., 1997. Evolution of starting mantle plumes: a comparison between Numerical and Laboratory Models. Earth Planet. Sci. Lett. 148, 1–11.

Vogt, P.R., 1974. Volcano spacing, fractures, and thickness of the lithosphere. Earth Planet. Sci. Lett. 21, 235–252. https://doi.org/10.1016/0012-821X(74)90159-9

Waite, G.P., Smith, R.B., Allen, R.M., 2006. VP and VS structure of the Yellowstone hot spot from teleseismic tomography: Evidence for an upper mantle plume. J. Geophys. Res. Solid Earth 111, 1–21. https://doi.org/10.1029/2005JB003867

Wang, H., Huismans, R.S., Rondenay, S., 2019. Water Migration in the Subduction Mantle Wedge: A Two-Phase Flow Approach. J. Geophys. Res. Solid Earth 124, 9208–9225. https://doi.org/10.1029/2018JB017097

Weatherley, S.M., Katz, R.F., 2012. Melting and channelized magmatic flow in chemically heterogeneous, upwelling mantle. Geochemistry, Geophys. Geosystems 13, 1–23. https://doi.org/10.1029/2011GC003989

Weijermars, R., Schmeling, H., 1986. Scaling of Newtonian and non-Newtonian fluid dynamics without inertia for quantitative modelling of rock flow due to gravity (including the concept of rheological similarity). Phys. Earth Planet. Inter. 43, 316–330. https://doi.org/10.1016/0031-9201(86)90021-X

Weis, D., Garcia, M.O., Rhodes, J.M., Jellinek, M., Scoates, J.S., 2011. Role of the deep mantle in generating the compositional asymmetry of the Hawaiian mantle plume. Nat. Geosci. 4, 831–838. https://doi.org/10.1038/ngeo1328

White, R.S., McKenzie, D., 1995. Mantle plumes and flood basalts. J. Geophys. Res. 100. https://doi.org/10.1029/95jb01585

White, W.M., 2015. Isotopes, DUPAL, LLSVPs, and Anekantavada. Chem. Geol. 419, 10–28. https://doi.org/10.1016/j.chemgeo.2015.09.026

Whitehead, J., 1986. Buoyancy-Driven Instabilities of Low-Viscosity Zones as Models of Magma-Rich Zones. J. Geophys. Res. 91, 9303–9314. https://doi.org/10.1029/JB091iB09p09303

Whitehead, J.A., 1982. Instabilities of fluid conduits in a flowing earth- are plates lubricated by the asthenosphere. Geophys. J. R. Astron. Soc. 70, 415–433.

Whitehead, J.A., Luther, D.S., 1975. Dynamics of laboratory diapir and plume models. J. Geophys. Res. 80, 705–717. https://doi.org/10.1029/jb080i005p00705

Wicks, J.K., Jackson, J.M., Sturhahn, W., Zhang, D., 2017. Sound velocity and density of magnesiowüstites: Implications for ultralow-velocity zone topography. Geophys. Res. Lett. 44, 2148–2158. https://doi.org/10.1002/2016GL071225

Wignall, P.B., 2001. Large igneous provinces and mass extinctions. Earth Sci. Rev. 53, 1–33. https://doi.org/10.1016/S0012-8252(00)00037-4

Wilcock, W.S.D., Whitehead, J.A., 1991. The Rayleigh-Taylor instability of an embedded layer of low-viscosity fluid. J. Geophys. Res. 96.

Williams, C.D., Li, M., McNamara, A.K., Garnero, E.J., Van Soest, M.C., 2015. Episodic entrainment of deep primordial mantle material into ocean island basalts. Nat. Commun. 6, 1–7. https://doi.org/10.1038/ncomms9937

Williams, Q., Revenaugh, J., Garnero, E., 1998. A correlation between ultra-low basal velocities in the mantle and hot spots. Science (80-.). 281, 546–549. https://doi.org/10.1126/science.281.5376.546

Wilson, C.R., Spiegelman, M., van Keken, P.E., Hacker, B.R., 2014. Fluid flow in subduction zones: The role of solid rheology and compaction pressure. Earth Planet. Sci. Lett. 401, 261–274. https://doi.org/10.1016/j.epsl.2014.05.052

Wilson, G.P., 2014. Mammalian extinction, survival, and recovery dynamics across the Cretaceous-Paleogene boundary in northeastern Montana, USA. Spec. Pap. Geol. Soc. Am. 503, 365–392. https://doi.org/10.1130/2014.2503(15)

Wilson, J.T., 1963. A possible origin of the Hawaiian Islands. Can. J. Earth Sci. https://doi.org/10.1139/cjes-2014-0036

Yang, H.J., Sen, G., Shimizu, N., 1998. Mid-ocean ridge melting: Constraints from lithospheric xenoliths at Oahu, Hawaii. J. Petrol. 39, 277–295. https://doi.org/10.1093/petroj/39.2.277

Yiantsios, S.G., Higgins, B.G., 1989. Rayleigh-Taylor instability in thin viscous films.

Phys. Fluids A 1, 1484–1501. https://doi.org/10.1063/1.857327

Yoo, S., Lee, C., 2020. Correlation of Quaternary Volcano Clusters with Partial Melting of Mantle Wedge , Northeast Japan : A Numerical Model Study. Geophys. Res. Lett. https://doi.org/10.1029/2019GL086205

Yuen, D.A., Peltier, W., 1980. Mantle plume and the thermal stability of the D'' layer. Geophys. Res. Lett. 7, 625–628.

Zhang, N., Behn, M.D., Parmentier, E.M., Kincaid, C., 2020. Melt Segregation and Depletion during Ascent of Buoyant Diapirs in Subduction Zones. J. Geophys. Res. Solid Earth 1–21. https://doi.org/10.1029/2019jb018203

Zhang, N., Zhong, S., Leng, W., Li, Z.X., 2010. A model for the evolution of the Earth's mantle structure since the Early Paleozoic. J. Geophys. Res. Solid Earth 115, 1–22. https://doi.org/10.1029/2009JB006896

Zhao, D., Mishra, O.P., Sanda, R., 2002. Influence of fluids and magma on earthquakes: Seismological evidence. Phys. Earth Planet. Inter. 132, 249–267. https://doi.org/10.1016/S0031-9201(02)00082-1

Zhao, D., Wang, Z., Umino, N., Hasegawa, A., 2009. Mapping the mantle wedge and interplate thrust zone of the northeast Japan arc. Tectonophysics 467, 89–106. https://doi.org/10.1016/j.tecto.2008.12.017

Zheng, Y., Chen, R.X., Xu, Z., Zhang, S., 2016. The transport of water in subduction zones. Sci. China Earth Sci. 59, 651–682. https://doi.org/10.1007/s11430-015-5258-4

Zhu, G., Gerya, T., Yuen, D.A., Honda, S., Yoshida, T., Connolly, J.A.D., 2009. Three-dimensional dynamics of hydrous thermal-chemical plumes in oceanic subduction zones. Geochemistry, Geophys. Geosystems 10, 1–20. https://doi.org/10.1029/2009GC002625

List of Publications

Ghosh, D., Maiti, G., and Mandal, N. (2020). Slab-parallel advection versus rayleigh-taylor instabilities in melt-rich layers in subduction zones: A criticality analysis. *Physics of the Earth and Planetary Interiors*, 307, 106560. https://doi.org/10.1016/j.pepi.2020.106560

Ghosh D., Maiti, G., Mandal, N., and Baruah, A. (2020). Cold plumes initiated by rayleigh-taylor instabilities in subduction zones, and their characteristic volcanic 188 distributions: The role of slab dip. *Journal of Geophysical Research: Solid Earth*. https://doi.org/10.1029/2020jb019814

Ghosh, D., and Mandal, N. "Rayleigh-Taylor instability patterns in viscous layers controlled by their substrate inclination." *Journal of Fluid Mechanics*. (Under Revision)

Ghosh, D., Sen, J. and Nibir Mandal, N. "Periodicity in the Deccan volcanism modulated by plume perturbations at the midmantle transition zone." *Earth and planetary science letters*. (Under Revision)

Roy, A., **Ghosh, D.**, and Mandal, N. "Effects of global flow on Rayleigh-Taylor instabilities: Implications for plume formation in Earth's mantle" Geophysical journal international. (In Preparation)

Abstracts

Ghosh, D., and Mandal, N. Dynamics of partially molten layers on subducting slabs in subduction zones: Insights from theory and experiments, *AGU Fall Meeting Abstracts*, 2020

Ghosh, D., Maiti, G., and Mandal, N. Late Cenozoic volcano distribution patterns in the Andean subduction system: a consequence of gravitational instabilities in melt-rich source layer, *Rock Deformation and Structure Conference (RDS-VI)*, 2021

Online Article

Rayleigh-Taylor instability in geodynamics, *European Geoscience Union, Geodynamics division Blog*, 2021